# *ULTRASOUND IMAGE ANALYSIS OF THE CAROTID ARTERY*

*CHRISTOS P. LOIZOU*

*A THESIS SUBMITTED IN PARTIAL FULLFILMENT OF THE REQUIREMENTS OF THE UNIVERSITY FOR THE DEGREE OF DOCTOR OF PHILOSOPHY (PhD)*

*SCHOOL OF COMPUTING AND INFORMATION SYSTEMS*

*KINGSTON UNIVERSITY*

*LONDON, UK*

Collaborating Establishments: Intercollege, Cyprus; University of Cyprus; Kingston University, UK; Cyprus Institute of Neurology and Genetics; Academic Vascular Surgery, Imperial College, Faculty of Medicine, Division of Surgery, Anesthetics and Intensive Care, Saint Mary's Hospital, UK.

*Submitted: September, 2005*

# Abstract

Stroke is one of the most important causes of death in the world and the leading cause of serious, long-term disability. There is an urgent need for better techniques to diagnose patients at risk of stroke based on the measurements of the intima media thickness (IMT) and the segmentation of the atherosclerotic carotid plaque.

The objective of this work was to carry out a comparative evaluation of despeckle filtering on ultrasound images of the carotid artery, and develop a new segmentation system, for detecting the IMT of the common carotid artery and the borders of the athrerosclerotic carotid plaque in longitudinal ultrasound images of the carotid artery. To the best of our knowledge no similar system has been developed for segmenting the atherosclerotic carotid plaque, although a number of techniques have been proposed for IMT segmentation.

A total of 11 despeckle filtering methods were evaluated based on texture analysis, image quality evaluation metrics, and visual evaluation made by two experts, on 440 ultrasound images of the carotid artery bifurcation. Furthermore, the proposed IMT and plaque segmentation techniques were evaluated on 100 and 80 longitudinal ultrasound images of the carotid bifurcation respectively based on receiver operating chatracteristic (ROC) analysis.

The despeckle filtering results showed that a despeckle filter based on local statistics (*lsmv*) improved the class separation between asymptomatic and symptomatic classes, gave only a marginal improvement in the percentage of correct classifications success rate, and improved the visual assessment carried out by the experts. It was also found that the *lsmv* despeckle filter can be used for despeckling asymptomatic images where the expert is interested mainly in the plaque composition and texture analysis, whereas a geometric despeckle filter (*gf4d*) can be used for despeckling of symptomatic images where the expert is interested in identifying the degree of stenosis and the plaque borders.

The IMT snakes segmentation results showed that no significant difference was found between the manual and the snakes segmentation measurements. Better segmentation results were obtained for the normalized despeckled images. The plaque segmentation results showed that, the Lai&Chin snakes segmentation method gives results comparable to the manual delineation procedure. The IMT and plaque snakes segmentation method may be therefore used to complement and assist the final expert's evaluation.

The proposed despeckling and segmentation methods will be further evaluated on a larger number of ultrasound images and on multiple experts' evaluation. Furthermore, it is expected that both methods will be incorporated into an integrated system enabling the texture analysis of the segmented plaque, providing an automated system for the early diagnosis and the assessment of the risk of stroke.

# Contents

Page

**List of Tables** ..... vii

**List of Figures** ..... x

**List of Symbols** ..... xvi

**List of Abbreviations** ..... xxii

**Acknowledgements** ..... xxvi

**Chapter 1: Vascular Ultrasound Imaging and Digital Image Processing** ..... 1

1.1 Introduction ..... 2

1.1.1 Risk of stroke ..... 2

1.1.2 IMT measurements ..... 6

1.1.3 Plaque characteristics ..... 7

1.2 A brief review of ultrasound imaging ..... 8

1.2.1 Basic principles of ultrasound ..... 10

1.2.2 Ultrasound modes ..... 12

1.2.3 Image quality and resolution ..... 13

1.2.4 Limitations of ultrasound ..... 14

1.3 Image processing of the carotid artery ..... 15

1.3.1 Despeckle filtering ..... 16

1.3.2 IMT segmentation ..... 18

1.3.3 Plaque segmentation ..... 19

1.4 Original aspects of the work ..... 20

1.5 Guide to thesis contents ..... 22

**Chapter 2: Despeckle Filtering** ..... 24

2.1 Introduction ..... 25

2.2 Speckle modelling in ultrasound images ..... 29

2.3 Despeckle filters ..... 31

2.3.1 Local statistics filters ..... 35

2.3.1.1 First order statistics filtering (*lsmv, lsmv_lee, lsmvminmax, lemva, wiener*) ..... 35

2.3.1.2 Local statistics filtering with higher moments (*lsmvske1d, lsmvsk2d*) . 36

2.3.1.3 Homogeneous mask areas filtering (*lsminv, lsminsc, lsminv1d*) ..... 37

2.3.1.4 Local statistics 1D filtering (*lsmv1d*) ..... 38
2.3.2 Median filtering (*median*) ..... 39
2.3.3 Linear scaling filtering (*ca*, *lecasort*, *ls*) ..... 39
2.3.4 Maximum homogeneity over a pixel neighbourhood filtering (*homog*) ..... 39
2.3.5 Geometric filtering (*gf4d*, *gfminmax*) ..... 40
2.3.6 Homomorphic filtering (*homo*) and logarithmic point operation filtering (*lslog*) ..... 41
2.3.7 Diffusion filtering ..... 42
2.3.7.1 Anisotropic diffusion filtering (*ad*) ..... 43
2.3.7.2 Lee diffusion and speckle reducing anisotropic diffusion filtering (*lsmedcd*, *adsr*) ..... 44
2.3.7.3 Exponential damp kernel filters utilizing diffusion (*lsmedc*) ..... 45
2.3.7.4 Coherent nonlinear anisotropic diffusion (*nldif*) ..... 46
2.3.8 Wavelet filter (*waveltc*) ..... 47

**Chapter 3: IMT and Plaque Segmentation ..... 50**

3.1 Introduction ..... 51
3.2 Previous work on carotid IMT segmentation ..... 53
3.2.1 On the difference between manual and automated IMT measurements ..... 56
3.3 Previous work on carotid plaque segmentation ..... 57
3.4 Active contours (snakes) ..... 60
3.4.1 Approximation of the first order differential ..... 63
3.4.2 Approximation of the second order differential ..... 63
3.4.3 Approximation of the image energy term ..... 65
3.4.4 Approximation of the external energy term ..... 67
3.5 Other snakes approaches ..... 67
3.5.1 Balloon snake ..... 68
3.5.2 Lai&Chin snake ..... 69
3.5.3 Gradient vector flow (GVF) snake ..... 70
3.6 Snake initialization ..... 71
3.6.1 IMT contour initialization ..... 72
3.6.2 Plaque contour initialization ..... 73

**Chapter 4: Image Quality, Texture Analysis, and ROC Analysis ..... 74**

4.1 Image quality ..... 75

4.2 Optical perception testing procedures ..... 77
4.3 Image quality metrics ..... 78
4.4 Texture analysis ..... 81
4.4.1 Texture measures ..... 82
4.4.2 Feature selection ..... 83
4.4.3 kNN Classifier ..... 83
4.5 ROC analysis ..... 84
4.5.1 Performance metrics for detection problems ..... 84
4.5.2 Evaluation of the plaque segmentation ..... 87

**Chapter 5: Methodology ..... 89**

5.1 Material ..... 90
5.2 Acquisition ..... 91
5.3 Image normalisation ..... 92
5.4 Generation of an artificial carotid image ..... 94
5.5 Image quality of two ultrasound scanners ..... 94
5.6 Despeckle filtering ..... 94
5.6.1 Visual perception evaluation ..... 95
5.6.2 Texture analysis ..... 97
5.6.3 Image quality evaluation metrics ..... 97
5.7 IMT segmentation ..... 98
5.7.1 Manual measurements and visual perception evaluation ..... 98
5.7.2 IMT initialisation ..... 100
5.7.3 IMT segmentation ..... 102
5.7.4 Univariate statistical analysis ..... 105
5.7.5 Correlation analysis ..... 107
5.8 Plaque segmentation ..... 107
5.8.1 Manual measurements and visual perception evaluation ..... 107
5.8.2 Plaque initialisation using the blood flow image ..... 111
5.8.3 Plaque segmentation ..... 113
5.8.4 ROC analysis of plaque segmentation methods ..... 114

**Chapter 6: Results ..... 116**

6.1 Image quality evaluation of two ultrasound scanners ..... 117
6.1.1 Visual perception ..... 117

6.1.2 Statistical and texture features ..... 120
6.1.3 Quality evaluation metrics ..... 122
6.2 Despeckle filtering ..... 124
6.2.1 Despeckle filtering on an artificial and a real carotid image ..... 124
6.2.2 Texture analysis ..... 129
6.2.3 Image quality evaluation metrics ..... 133
6.2.4 Visual perception by experts ..... 134
6.2.5 Additional comments by experts ..... 135
6.3 IMT segmentation ..... 138
6.3.1 An example of IMT segmentation ..... 138
6.3.2 Univariate statistical analysis ..... 140
6.3.3 Regression and correlation analysis ..... 148
6.4 Plaque segmentation ..... 155
6.4.1 Examples of plaque segmentation ..... 155
6.4.2 Evaluation of plaque segmentation methods ..... 161

**Chapter 7: Discussion ..... 165**

7.1 Image quality evaluation of two ultrasound scanners ..... 166
7.1.1 Visual perception ..... 166
7.1.2 Statistical and texture measures ..... 166
7.1.3 Quality evaluation metrics ..... 167
7.1.4 Summary findings on image quality evaluation ..... 167
7.2 Despeckle filtering ..... 168
7.2.1 Despeckle filtering on an artificial and a real carotid image ..... 169
7.2.2 Texture analysis ..... 171
7.2.3 Image quality evaluation metrics ..... 172
7.2.4 Visual perception and additional comments by experts ..... 174
7.2.5 Summary findings on despeckle filtering ..... 175
7.3 IMT segmentation ..... 179
7.3.1 IMT snakes segmentation ..... 179
7.3.2 Univariate statistical analysis ..... 182
7.3.3 Regression and correlation analysis ..... 187
7.3.4 Summary findings on IMT segmentation ..... 189
7.4 Plaque segmentation ..... 190
7.4.1 Plaque snakes segmentation ..... 190
7.4.2 Evaluation of plaque segmentation methods ..... 193

7.4.3 Summary findings on plaque segmentation ..... 195
7.5 Proposed system ..... 196

**Chapter 8: Conclusions and Future Work ..... 198**

8.1 Conclusions ..... 199
8.2 Future work ..... 201

**Appendix I: Statistics of Speckle ..... 204**

**Appendix II: Optical Perception Testing Procedure Evaluations ..... 208**

**Appendix III: Texture Measures ..... 212**

**Appendix IV: Complete Snake Implementation ..... 224**

**Appendix V: List of Publications ..... 230**

**References ..... 307**

# List of Tables


| | | PAGE |
|---|---|---|
| TABLE 2.1 | AN OVERVIEW OF DESPECKLE FILTERING TECHNIQUES | 33 |
| TABLE 3.1 | AN OVERVIEW OF ULTRASOUND SEGMENTATION TECHNIQUES IN VASCULAR IMAGING | 53 |
| TABLE 3.2 | AN OVERVIEW OF PLAQUE SEGMENTATION TECHNIQUES IN VASCULAR IMAGING | 58 |
| TABLE 6.1 | VISUAL PERCEPTION EVALUATION FOR THE IMAGE QUALITY ON 80 IMAGES PROCESSED FROM EACH SCANNER FOR THE ORIGINAL (NF), DESPECKLED (DS), NORMALIZED (N), AND NORMALIZED DESPECKLED (NDS). SCORES ARE EXPRESSED IN PERCENTAGE FORMAT | 120 |
| TABLE 6.2 | STATISTICAL AND TEXTURE FEATURES (MEAN VALUES FOR 80 IMAGES PROCESSED FROM EACH SCANNER) FOR THE ORIGINAL (NF), DESPECKLED (DS), NORMALIZED (N) AND NORMALIZED DESPECKLED (NDS) IMAGES | 121 |
| TABLE 6.3 | IMAGE QUALITY EVALUATION METRICS BETWEEN THE ORIGINAL-DESPECKLED (NF-DS), THE ORIGINAL-NORMALIZED (NF-N), THE ORIGINAL-NORMALIZED DESPECKLED (NF-NDS) AND THE NORMALIZED-NORMALIZED DESPECKLED (N-NDS) IMAGES | 122 |
| TABLE 6.4 | SELECTED STATISTICAL FEATURES FOR FIG. 6.3A BEFORE AND AFTER DESPECKLE FILTERING. BOLDED VALUES SHOW IMPROVEMENT AFTER DESPECKLE FILTERING | 127 |
| TABLE 6.5 | FEATURE DISTANCE (4.13) AND SCORE_DIS (4.14) FOR SF, SGLDM RANGE OF VALUES, AND NGTDM TEXTURE FEATURES SETS BETWEEN ASYMPTOMATIC AND SYMPTOMATIC CAROTID PLAQUE ULTRASOUND IMAGES. BOLDED VALUES SHOW IMPROVEMENT AFTER DESPECKLE FILTERING | 130 |
| TABLE 6.6 | WILCOXON RANK SUM TEST FOR THE SGLDM RANGE OF VALUES TEXTURE FEATURES APPLIED ON THE 440 ULTRASOUND IMAGES OF CAROTID PLAQUE BEFORE AND AFTER DESPECKLE FILTERING. THE TEST SHOWS WITH S SIGNIFICANT DIFFERENCE AFTER FILTERING AT $p<0.05$ AND NS NO SIGNIFICANT DIFFERENCE AFTER FILTERING AT $p>=0.05$. THE P VALUE IS ALSO GIVEN IN PARENTHESIS | 131 |

| | | |
|---|---|---|
| TABLE 6.7 | PERCENTAGE OF CORRECT CLASSIFICATIONS SCORE FOR THE KNN CLASSIFIER WITH K=7 FOR THE ORIGINAL AND THE DESPECKLED IMAGE SETS. BOLDED VALUES INDICATE IMPROVEMENT AFTER DESPECKLING | 132 |
| TABLE 6.8 | IMAGE QUALITY EVALUATION METRICS COMPUTED FOR THE 220 ASYMPTOMATIC AND 220 SYMPTOMATIC IMAGES | 133 |
| TABLE 6.9.1 | PERCENTAGE SCORING OF VISUAL EVALUATION OF THE ORIGINAL AND DESPECKLED IMAGES (50 ASYMPTOMATIC (A) AND 50 SYMPTOMATIC (S)) BY THE EXPERTS | 134 |
| TABLE 6.9.2 | PERCENTAGE SCORING OF VISUAL EVALUATION OF THE ORIGINAL AND DESPECKLED IMAGES (50 ASYMPTOMATIC (A) AND 50 SYMPTOMATIC (S)) BY THE EXPERTS ONE YEAR AFTER THE FIRST VISUAL EVALUATION | 135 |
| TABLE 6.10 | ADDITIONAL COMMENTS ON DESPECKLE FILTERING MADE BY THE EXPERTS | 137 |
| TABLE 6.11 | COMPARISON BETWEEN THE MANUAL AND THE SNAKES SEGMENTATION MEASUREMENTS FOR THE CASES B-H IN FIGURE 6.6. MEASUREMENTS ARE IN MILLIMETERS (MM) | 138 |
| TABLE 6.12.1 | COMPARISON BETWEEN MANUAL AND SNAKES SEGMENTATION MEASUREMENTS FOR THE 100 ULTRASOUND IMAGES OF THE CAROTID ARTERY. MEASUREMENTS ARE IN MILLIMETRES (MM). BOLDED VALUES SHOW BEST PERFORMANCE | 141 |
| TABLE 6.12.2 | IMT MANUAL MEASUREMENTS (IN MM) FOR THE 100 ULTRASOUND IMAGES OF THE CAROTID ARTERY PERFORMED BY THE TWO VASCULAR EXPERTS | 141 |
| TABLE 6.12.3 | WILCOXON RANKSUM TEST FOR THE IMT MANUAL SEGMENTATION MEASUREMENTS. THE TEST SHOWS WITH S SIGNIFICANT DIFFERENCE AFTER FILTERING AT P<0.05 AND NS NO SIGNIFICANT DIFFERENCE AFTER FILTERING AT P>=0.05. THE P VALUES ARE ALSO SHOWN IN PARENTHESIS. | 142 |
| TABLE 6.13.1 | TESTS AND MEASURES COMPUTED ON 100 ULTRASOUND IMAGES OF THE CAROTID ARTERY FROM THE FIRST EXPERT. LEFT COLUMN UPPER TRIANGLE: WILCOXON RANK SUM TEST (S=SIGNIFICANTLY DIFFERENT AFTER FILTERING AT P<0.05, NS=NOT SIGNIFICANTLY DIFFERENT AFTER FILTERING AT P>=0.05). THE P VALUES ARE ALSO SHOWN IN PARENTHESIS. LEFT COLUMN LOWER TRIANGLE: VARIATION OF THE | 144 |

| | | |
|---|---|---|
| | HAUSDORFF DISTANCE (*$10^{-3}$). RIGHT COLUMN UPPER TRIANGLE: COVARIANCE, $c_{m,a}$. RIGHT COLUMN LOWER TRIANGLE: MEAN-SQUARE ERROR (*$10^{-3}$). BOLDED VALUES SHOW BEST PERFORMANCE. THE LEVEL OF SIGNIFICANCE IS ALSO SHOWN IN BRACKETS. | |
| TABLE 6.13.2 | TESTS AND MEASURES COMPUTED ON 100 ULTRASOUND IMAGES OF THE CAROTID ARTERY FROM THE SECOND EXPERT. LEFT COLUMN UPPER TRIANGLE: WILCOXON RANK SUM TEST (S= SIGNIFICANTLY DIFFERENT AFTER FILTERING AT p<0.05, NS=NOT SIGNIFICANTLY DIFFERENT AFTER FILTERING AT p>=0.05). THE p VALUE IS ALSO SHOWN IN PARENTHESIS. LEFT COLUMN LOWER TRIANGLE: VARIATION OF THE HAUSDORFF DISTANCE (*$10^{-3}$). RIGHT COLUMN UPPER TRIANGLE: COVARIANCE, $c_{m,a}$. RIGHT COLUMN LOWER TRIANGLE: MEAN-SQUARE ERROR (*$10^{-3}$). BOLDED VALUES SHOW BEST PERFORMANCE. THE LEVEL OF SIGNIFICANCE IS ALSO SHOWN IN BRACKETS. | 144 |
| TABLE 6.14 | PEARSON CORRELATION TEST AND CORRELATION COEFFICIENT FOR THE 100 ULTRASOUND IMAGES OF THE CAROTID ARTERY. VALUES ABOVE 0.1654 SHOW SIGNIFICANT CORRELATION AT p<0.05. BOLDED VALUES SHOW BEST PERFORMANCE. BOLDED VALUES SHOW BEST PERFORMANCE | 149 |
| TABLE 6.15 | NUMBER OF ITERATIONS AND COMPUTATIONAL TIME FOR THE FOUR DIFFERENT SNAKES SEGMENTATION METHODS | 158 |
| TABLE 6.16 | ROC ANALYSIS FOR THE FOUR DIFFERENT PLAQUE SEGMENTATION METHODS AND THE MANUAL DELINEATIONS MADE BY AN EXPERT ON 80 ULTRASOUND IMAGES OF THE CAROTID ARTERY | 162 |
| TABLE 6.17 | ROC ANALYSIS FOR THE FOUR DIFFERENT PLAQUE SEGMENTATION METHODS AND THE MANUAL DELINEATIONS MADE BY AN EXPERT ON 80 ULTRASOUND IMAGES OF THE CAROTID ARTERY BASED ON THE SENSITIVITY, R, SPECIFICITY, Sp, PRECISION, P, AND EFFECTIVENESS MEASURE, 1-E | 162 |
| TABLE 7.1 | SUMMARY FINDINGS OF IMAGE QUALITY EVALUATION IN ULTRASOUND IMAGING OF THE CAROTID ARTERY | 168 |
| TABLE 7.2 | SUMMARY FINDINGS OF DESPECKLE FILTERING IN ULTRASOUND IMAGING OF THE CAROTID ARTERY | 169 |

# List of Figures


| | | PAGE |
|---|---|---|
| Fig. 1.1 | World leading causes of death (US CDC National center of health statistics, vital statistics of the United States, Annual 2000). | 3 |
| Fig. 1.2 | (a) The carotid system [130], (b) longitudinal section of a carotid artery with plaque (left) and embolisation (right) [153] (c) transverse section of a carotid artery with plaque, (e) stable and unstable plaque. (From Heart Center online: http://www.heartcenteronline.com). | 4 |
| Fig. 1.3 | Ultrasound imaging scanners: (a) ATL HDI-3000, (b) ATL HDI-5000 [153]. | 9 |
| Fig. 1.4 | Longitudinal color flow duplex image of the carotid artery combined with Doppler ultrasound image. Highlighted image with white contour on top shows the carotid bifurcation. The 2D signal shows the velocity variation related to the cardiac cycle. Blood flow velocity spectrum is displayed with markings 1 and 2, where marking 1 represents the peak systolic velocity and marking 2 represents the end diastolic velocity. This is the duration of one cardiac cycle. Different colours represent blood flow direction. For the current picture, red represents the blood moving to the brain through the carotid artery, whereas blue represents the blood returning back from the brain. | 11 |
| Fig. 1.5 | Ultrasound B-mode longitudinal image of the carotid bifurcation with manually outlined plaque, which is usually confirmed with blood flow image. | 13 |
| Fig. 1.6 | Close view of manual measurement of the IMT: (1) 0.9 mm, (2) 0.8 mm, (3) 0.86 mm. | 16 |
| Fig. 1.7 | Results of despeckle filtering based on first order local statistics. Asymptomatic case: (a) original, (c) despeckled, (e) enlarged region marked in c) of the original, (g) enlarged region marked in c) of the despeckled image. Symptomatic case: (b) original, (d) despeckled, (f) enlarged region marked in d) of the original, (h) enlarged region marked in d) of the despeckled image. Regions were enlarged by a factor of three. | 17 |

| | | |
|---|---|---|
| Fig. 1.8 | Ultrasound image of the carotid artery for an asymptomatic case: (a) detected initial contours for the IMT, and (b) final contours after snakes deformation. $IMT_{mean}$ = 0.86 mm, $IMT_{\max}$ = 1.04 mm, $IMT_{\min}$ = 0.73 mm, $IMT_{median}$ = 0.83 mm. | 18 |
| Fig. 1.9 | Ultrasound image of the carotid artery: (a) plaque initial contour estimation, and (b) the final plaque contour after the snakes deformation. | 20 |
| Fig. 2.1 | The usual tissue model in ultrasound imaging, modified from [199]. | 26 |
| Fig. 2.2 | (a) The scattering in the sound beam, (b) one pulse (from [14]). | 27 |
| Fig. 2.3 | The processing steps of the RF-signal inside the ultrasound scanner, modified from [156]. | 28 |
| Fig. 2.4 | Schematical operation of the filters: (a) *lsmv* and (b) *lsminv1d* respectively. | 38 |
| Fig. 2.5 | (a) Directions of implementation of the *gf4d* geometric filter, (b) pixels selected for the NS direction (intensity of central pixel b is adjusted based on the values of intensities of pixels a, b, and c). | 41 |
| Fig. 3.1 | (a) Illustration of the intima-media (IM). IM contains the area between the intima and adventitia. The sub-intima region may cause problems in searching the adventitia layer due to speckle noise and due to its interference caused from the adventitia layer. (b) Intensity schematic illustration of a lumen-intima and media-adventitia interface at the far wall of the carotid artery. Modified from [253]. | 57 |
| Fig: 3.2 | Illustration of the snake contour deformation. Open circles represent snake points that are candidates to replace the original (solid) point. | 62 |
| Fig. 4.1 | DSCQS method: (a) the reference and the test sequence are presented twice in alternated fashion, (b) the order of the two is chosen randomly for each trial, and experts are not informed which is which. They rate each of the two separately on a continuous quality scale ranging from bad to excellent (Modified from [7] pp. 572, Fig. 10.1). | 78 |
| Fig. 4.2 | Definition of TP, FN, FP, and TN. | 85 |

Fig. 4.3 (a) Intersection, and (b) union of two variables, $AS$ and GT. 88

Fig. 5.1 Normalization of a carotid ultrasound image: two reference points are selected in order to normalize the image: (a) blood area is selected and, (b) adventitia area located over the plaque is selected. 93

Fig. 5.2 The graphical user interface for the visual image evaluation carried out by the experts. The screen illustrates four different despeckled images and their corresponding scores. 96

Fig. 5.3 Demonstration of the manual IMT segmentation module. 99

Fig. 5.4 IMT contour initialization procedure and final snakes contours: (a) Original ultrasound image with selected area, (b) cropped area, (c) despeckled area, (d) binary cropped area, (e) dilated cropped area, (f) dilated area after removal of small edges, (g) construction of the interpolating B-spline, (h) detected initial contours for the adventitia and the intima layers, and (i) final contours after the snake deformation. The $IMT_{mean}$, is shown with double line box, the $IMT_{\max}$, with a full line box and the $IMT_{\min}$, with dashed line box. 101

Fig. 5.5 Edge map of an artificial carotid image of the original image in Fig. 6.3a, and the detected initial contours for the IMT. 103

Fig. 5.6 Demonstration of the IMT segmentation module. 104

Fig. 5.7 Types of plaque: (a) blood flow image for the type I plaque, (b) type I plaque: the plaque is not visible, (c) type II plaque: bright echoes occupy < 50% of plaque, (d) type III: bright echoes occupy 50%-80% of plaque, (e) type IV: bright echoes occupy 80%-100% of plaque, (f) type V plaque: calcified plaque where borders cannot be visualized well. 109

Fig. 5.8 Selection of a plaque: (a) The gray scale image and the blood flow colour image are loaded, (b) expert has selected a log transform on the gray scale image for better visualising the plaque, and (c) the final selected plaque is saved. 110

Fig. 5.9 Plaque initialization using the blood flow image procedure: (a) 112

Original ultrasound B-mode image of a carotid artery with plaque at the far wall, (b) blood flow image, (c) initial blood flow edge contour with the area for the initial contour selected by the expert, (d) sampled initial snake contour, (e) snakes segmentation of plaque, and (f) manual segmentation of plaque.

Fig. 5.10 Demonstration of the plaque segmentation module. 113

Fig. 6.1 Ultrasound carotid artery images, taken from one patient at the Cyprus Institute of Neurology and Genetics, of the original (NF), despeckled (DS), normalized (N), and normalized despeckled (NDS) of the ATL HDI-3000, and ATL HDI-5000 shown in the left and right columns respectively. 118

Fig. 6.2 Line profiles for the NF, DS, N, and NDS images, for the ATL HDI-3000, and ATL HDI-5000 scanner, shown in the left and right columns respectively. The gray scale values, and the column 240, are shown in the y- and x-axis. 119

Fig. 6.3 Original noisy image of an artificial carotid artery given in (a), and the application of the 11 despeckle filters given in (b)-(l). (Vertical line given in (a) defines the position of the line intensity profiles plotted in Fig. 6.4). 125

Fig. 6.4 Line profiles of the line illustrated in Fig. 6.3a for the original noisy image (a), and the 11 despeckled images given in (b)-(l). 126

Fig. 6.5 Original ultrasound image of the carotid artery (2-3 cm proximal to bifurcation) given in (a), and the despeckled images given in (b)-(l). 128

Fig. 6.6 (a) Original longitudinal ultrasound image of the carotid artery, (b) manual delineation from the first expert, (c) manual delineation from the second expert, (d) initial contour estimation, and the segmentation results of the IMT for (e) no filtering (NF), (f) despeckled (DS), (g) normalized (N), and (h) normalized despeckled (NDS) images. The detected $IMT_{mean}$, $IMT_{\max}$, and $IMT_{\min}$ are shown with a double, single, and dashed line boxes respectively. 139

Fig. 6.7 Increase of $IMT_{mean}$ with: (a) age and (b) systolic blood pressure. 142

Fig. 6.8 Histograms of the $IMT_{mean}$ values for the: (a) manual first set of measurements from first expert (M1F), (b) manual normalized first set of measurements from first expert (MN1F), (c) manual first set of measurements from second expert (M2F), (d) manual normalised first set of measurements from second expert (MN2F), (e) no filtering (NF), (f) despeckle (DS), (g) normalised (N), and (h) normalized despeckled (NDS), images. 146

Fig. 6.9 Box plots for the $IMT_{mean}$ values in mm: (a) for the manual and manual normalized first set of measurements, from expert one (M1F, MN1F) and expert two (M2F, MN2F), and (b) for the Williams&Shah snakes segmentation cases NF, DS, N, and NDS respectively. 147

Fig. 6.10 A scatter plot with least squares regression line for the inter-observer variability of the manual IMT delineation between the two experts for 100 ultrasound images of the carotid artery, on: (a) the original (M), and (b) the normalised (MN) images. 148

Fig. 6.11 Comparison of manually and snakes segmented IMT borders with regression lines, showing the correlations between: (a) the NF-M1F, (b) NF-MN1F, (c) DS-MN1F, (d) N-MN1F, (e) NDS-MN1F, (f) DS-M1F, (g) N-M1F, and (h) NDS-M1F detected IMT boundaries. 150

Fig. 6.12 Regression lines (Bland-Altman plots) of manual versus Williams&Shah snakes segmentation method for the $IMT_{mean}$ for the first set of measurements for both experts. The middle line represents the mean difference, and the upper and lower two outside lines represent the limits of agreement between the two methods, which are the mean of the data $\pm 2sd$ for the estimated difference between the two methods. 154

Fig. 6.13 Segmentation results on a longitudinal ultrasound B-mode image of the carotid artery with plaque, with: (a) manual segmentation, (b) Williams&Shah, (c) Balloon, (d), Lai&Chin, (e) GVF snake, and (f) segmentation contours computed in (b)-(e) superimposed. 156

Fig. 6.14 Segmentation results on a longitudinal ultrasound B-mode image of the carotid artery with plaque, with: (a) manual segmentation, (b) Williams&Shah, (c) Balloon, (d), Lai&Chin, (e) GVF snake, and (f) 157

all segmentation contours computed in (b)-(e) superimposed.

Fig. 6.15 Segmentation results on a longitudinal ultrasound B-mode image of the carotid artery with plaque at the near wall, with: (a) manual segmentation, and (b) Williams&Shah (red line), Balloon (blue line), Lai&Chin (yellow line), and GVF (green line), snakes segmentation contours computed superimposed. 158

Fig. 6.16 Plots of the total snake energy for: (a) the Williams&Shah (TSEP), (b) Balloon (TSEB), (c) Lai&Chin (TSELC), and (d) GVF snake (TSEGVF) for the image in Fig. 6.14a. 159

Fig. 6.17 Plots of the snake energy terms versus the number of iterations for the Williams&Shah snakes segmentation method for the image in Fig. 6.14, for: (a) normalized total snake energy (NTSE), (b) normalized continuity energy (NCE), (c) normalized curvature energy (NCRE), and (d) normalized image energy (NIE) terms respectively. 160

Fig. 6.18 Plots for the $\alpha$ and $\beta$ snake parameters for the Lai&Chin snakes segmentation method versus the number of iterations. 161

Fig. 6.19 Box plots for the four snakes segmentation methods (Williams&Shah, Balloon, Lai&Chin, and GVF) for: (a) TPF, (b) TNF, (c) FPF, (d) FNF, (e) Williams index, KI and (f) overlap index. 163

Fig. 6.20 ROC curve analysis based on the TPF and FPF fractions for the four snakes segmentation methods. 164

# List of Symbols

| | |
|---|---|
| $A$ | Pentavector (matrix) |
| $A_{\max}$ , $A_{\min}$ | Maximum and minimum values of the signal A |
| $\overline{A}_i$ | Average gray-tone over a neighbourhood |
| A | Input ultrasound signal to the amplifier |
| $\alpha(s)$ | Snake tension parameter of the energy functional |
| $\alpha_{GVF}$ | GVF snake elasticity parameter |
| $a_{i,j}$ | Additive noise component on pixel $i, j$ |
| $\alpha_{visual}$ | Degrees of visual angle |
| $a$ | A non-zero parameter |
| $\alpha_{comp}, \beta_{comp}$ | Logarithmic compression parameters |
| $\beta(s)$ | Snake stiffness of the energy functional |
| $\beta_{GVF}$ | GVF snake rigidity parameter |
| $C$ | Speckle Index |
| $CV\%$ | Coefficient of variation |
| $Cov_{m,a}$ | Covariance between automated and manual measurements |
| $c_{m,a} = \frac{Cov_{m,a}}{\sigma_m \sigma_a}$ | Correlation, for the strength of the relationship between automated and manual methods |
| $cd(\|\nabla g\|)$ , $c_{i,j}$ | Diffusion coefficient |
| $c_{adsr}$ | Speckle reducing anisotropic diffusion coefficient |
| $c$ | Constant controlling the magnitude of the potential |
| $c_{ssin_1}, c_{ssin_2}$ | Constants used to calculate the SSIN |
| $c_2$ | Positive weighting factor |
| $\Gamma$ | Number of directions, which diffusion is computed |
| $\gamma(s)$ | Influence of image gradients on energy snake functional |
| $\gamma$ | Signal-to-noise radio (SNR) |
| $\frac{dv^2(s)}{ds^2}$ | Second order snake differential |
| $\frac{dv(s)}{ds}$ | First order snake differential |
| $D \in \Re^{2x2}$ | Symmetric positive semi-definite diffusion tensor representing |

| | |
|---|---|
| | the required diffusion in both gradient and contour directions |
| $D_f$ | Fractal dimension |
| $D$ | Matrix used to calculated the image energy of the snake, $E_{image}(v)$ |
| $D_{viewing}$ | Viewing distance |
| DR | Dynamic range of input ultrasound signal |
| $d(k)$ | Wavelet coefficient for the wavelet filtering |
| $d_{ICA,\min}$ | Minimum lumen diameter in the ICA |
| $d_{ICA,distal}$ | Lumen diameter in a distal diseased free portion of the ICA |
| $dis_{i,c}$ | Distance between asymptomatic and symptomatic images |
| $d$ | Average distance between snake vertices |
| $\Delta$ | Snake convergence scalar factor |
| $\delta(s)$ | Snake contour damping density |
| $\delta \equiv (\Delta x, \Delta y)$ | Displacement of a pixel at direction (x, y) |
| $\Delta f$ | Frequency shift (Doppler frequency shift) |
| $\Delta r$ | Distance between two pixels |
| $\nabla g$ | The gradient magnitude of image $g(x, y)$ (gradient) |
| $\nabla g_{i,j}$ | Directional derivative (simple difference) at location $i, j$ |
| $\nabla g_{\min}$ , $\nabla g_{\max}$ | Maximum and minimum gradient values in a pixel neighbourhood |
| $\Delta g$ | Intensity difference between two pixels |
| $E\{\}$ | Expectation operation |
| $E\{X\}$ | Expected value of the reflected ultrasound signal X |
| $E_{snake}(v)$ | Snake energy function |
| $E_{\text{int}}(v)$ | Snake internal energy |
| $E_{cont}(v)$ | Snake continuity energy |
| $E_{curv}(v)$ | Snake curvature energy |
| $E_{image}(v)$ | Snake image energy |
| $E_{external}(v)$ | External snake energy |
| $E_{line}(v)$ | Line energy of the snake |
| $E_{edge}(v)$ | Edge energy of the snake |
| $\varepsilon$ | Constant for the snake points length adjustment in $E_{\text{int}}(v)$ |

| | |
|---|---|
| $F_{normal}$ | Normal force, added to the energy snake functional |
| $f_1 \cdots f_{13}$ | SGLDM texture measures from Haralick |
| $f_x(x,y)$ | First order differential of the edge magnitude along the x-axis |
| $F_v$ | Vertical force, added to the snake energy functional |
| $f_{i,j}$ | Noise-free signal ultrasound signal in discrete form (the new image) on pixel $i, j$ |
| $f$ | Frequency of ultrasound wave |
| $f_0$ | Transmitted frequency of ultrasound signal |
| $f_{\max_spat}$ | Maximum spatial frequency |
| $feat_dis_i$ | Percentage distance |
| $g_{i,j}$ | Observed ultrasound signal in discrete formulation after logarithmic compression |
| $g(x,y)$ | Observed ultrasound signal after logarithmic compression, representing image intensity at location (x, y) |
| G | Linear gain of the amplifier |
| $G\sigma * g_{i,j}$ | Image convolved with Gaussian smoothing filter |
| $G\sigma$ | Gaussian smoothing filter |
| $\overline{g}_i$, $\overline{f}_i$ | Mean gravity of the searching pixel region in image $g$ or $f$ |
| $g_{\max}$, $g_{\min}$ | Maximum and minimum gray level values in a pixel neighbourhood |
| $Hz$, $KHz$, $MHz$ | Hertz, Kilohertz, Megahertz |
| $HX$, $HY$ | Entropies of $p_x$ and $p_y$ |
| $H^{(k)}$ | Hurst coefficients |
| $H(x,y)$ | Array of points of the same size for the HT |
| $H_{screen}$ | Screen height |
| $H(A)$ | Frequency response of the pentavector $A$ |
| $HD$ | Hausdorff distance |
| $h$ | Distance between two consecutive snake points $v_{i,j-1}$ and $v_{i,j}$ |
| $\eta_s$ | Spatial neighborhood of pixel $i, j$ |
| $\lvert\eta_s\rvert$ | Number of neighbors (usually four except at the image boundaries) |
| $\theta_i$ | Phase shift relative to the insonated ultrasound wave |

| | |
|---|---|
| $\theta$ | Angle between the direction of movement of the moving object and the ultrasound beam |
| $I$ | Identity matrix |
| $I_0(x)$ | Modified Bessel function of the first kind of order 0 |
| $I_1 - I_7$ | Echo boundaries describing the regions in carotid artery |
| $IMT_{mean}$ | Mean value of the IMT |
| $IMT_{\min}$ | IMT minimum value |
| $IMT_{\max}$ | IMT maximum value |
| $IMT_{median}$ | IMT median value |
| $id(k)$ | Average of the absolute intensity difference. |
| $K_\zeta(.)$ | Modified Bessel function of the second kind of order $\zeta$ |
| $K_\alpha(.)$ | Modified Bessel function of the second kind of order $\alpha$ |
| K | Damping factor |
| $k$ | Coefficient of variation for speckle filtering |
| $L$ | Snake contour length |
| $L_{scan}$ | Number of scan lines for a display (screen) |
| $lpg_{i,j}$ | Low passed filtered of the original image at location $i, j$ |
| $\lambda$ | Wavelength of ultrasound wave |
| $\lambda_\pi$ | Lai&Chin snake energy regularisation parameter, $E_{snake}(v)$ |
| $\lambda_d \in \Re^+$ | Rate of diffusion for the anisotropic diffusion filter |
| $mean_relative_error$ | Mean relative error |
| $m_{i1}, m_{i2}$ | Mean values of two classes (asymptomatic, symptomatic) |
| $m/s$, $cm/s$ | Metres per second, centimetres per second |
| $\mu$ | Mean |
| $\mu(s)$ | Snake contour mass density |
| $\mu_{GVF}$ | GVF snake regularisation parameter |
| N | Number of scatterers within a resolution cell |
| $N_{feat}$ | Number of features in the feature set |
| $N_g$ | Number of distinct gray levels in the quantized image |
| $n_{i,j}$ | Multiplicative noise component (independent of $g_{i,j}$ , with mean 0) on pixel $i, j$ |
| $nl_{i,j}$ | Multiplicative noise component after logarithmic compression |

| | |
|---|---|
| | on pixel $i, j$ |
| $n(s)$ | Normal force tensor |
| $\xi_i$ | Amount of ultrasound signal backscattered by scatterer $i$ |
| $p_{X_r X_i}(X_r, X_i)$ | Joint intensity distribution (density function) of the real and the imaginary part of the ultrasound signal X |
| $p_X(X)$ | Probability distribution of X |
| $P(v(s))$ | Snake scalar potential function |
| $p(i, j)$ | $(i, j)th$ entry in the normalised SGLDM |
| $p_r(x)$ | Rice distribution with variance $\sigma^2 x/\alpha$ |
| $p_\gamma(x)$ | Gamma distribution |
| $p_x(i)$ | $ith$ entry in the marginal probability matrix obtained by summing the rows of $p(i, j)$ |
| $Q$ | Mathematically defined universal quality index |
| $R = 1 - \frac{1}{1+\sigma^2}$ | Smoothness of an image |
| $r_{pearson}$ | Pearson product moment correlation coefficient |
| $\rho_{corel}$ | Correlation coefficient |
| $\rho$ | Normal force, $F_{normal}$ weighting factor |
| $Score_Dis$ | Score distance between two classes (asymptomatic, symptomatic) |
| $s_e = \sigma_{IMT}/\sqrt{2}$ | Inter-observer error |
| $s_{\max}$ | Maximum pixel value in the image |
| $s^2$ | Structural energy |
| $\sigma_{IMT}$ | IMT standard deviation |
| $\sigma_{fg}$ | Covariance between two images $f$ and $g$ |
| $\sigma$ | Standard deviation |
| $\sigma^2$ | Variance |
| $\sigma^3$ | Skewness |
| $\sigma^4$: | Kurtosis |
| $\sigma_{i1}, \sigma_{i2}$ | Standard deviations of two classes (asymptomatic, symptomatic) |
| $2\sigma^2$ | Diffuse energy |
| $\sigma_n$ | Standard deviation of the noise |

| | |
|---|---|
| $s$ | Arc length of the snake contour |
| $\tau$ | Time constant, controls the next iteration of the snake |
| $u_{sp}$ | Speed of sound through tissue |
| $v_{i,j-1}, v_{i,j}, v_{i,j+1}$ | Precedent, current and next snake contour points |
| $v$ | Velocity of ultrasound wave propagation |
| $v(s,t)$ | Element along the snake contour, $v(s) = [x(s), y(s)]$ |
| $window_variance$ | Variance of the gray values in a pixel window |
| X | Reflected ultrasound signal |
| $X_{\max}, X_{\min}$ | Maximum and minimum values of the signal X |
| $x_{i,j}$ | Noise free signal before logarithmic compression in discrete form on pixel $i, j$ |
| $X_r,\ X_i$ | Real and imaginary part of the reflected ultrasound signal X |
| $\lvert X \rvert$ | Amplitude of the reflected ultrasound signal |
| $(x, y) \in \Re^2$ | Spatial coordinates of an image |
| $z_{i,j}$ | Original ultrasound signal before logarithmic compression in discrete form on pixel $i, j$ |
| $Z_1 - Z_7$ | Echo zones describing the regions in carotid artery |
| $\omega_{line}$ | Sign of the line energy functional |
| $\omega_{edge}$ | Sign of the edge energy functional |
| $\cap$ | Intersection between two areas |
| $\cup$ | Union between two areas |
| # | Number of elements in a set |

# List of Abbreviations

| | |
|---|---|
| ACSRS | Asymptomatic Carotid Stenosis |
| *ad* | Perona and Malik anisotropic diffusion filter |
| *adsr* | Speckle reducing anisotropic diffusion filter |
| AS | Automatic segmented area |
| ASM | Angular second moment |
| ATL HDI-3000 | ATL 3000 ultrasound scanner |
| ATL HDI-5000 | ATL 5000 ultrasound scanner |
| *ca* | Linear scaling of the gray-levels despeckle filter |
| CAT | Computer assisted tomography |
| CCA | Common carotid artery |
| CSR | Contrast-to-speckle radio |
| CT | Computer tomography |
| CW | Continuous wave |
| DR | Dynamic range |
| DS | Despeckled |
| DSCQS | Double stimulus continuous quality scale |
| DSIS | Double stimulus impairment scale |
| DVD | Digital video |
| DWT | Discrete wavelet transform |
| E | Effectiveness measure |
| ECA | External carotid artery |
| ECST | European carotid surgery trial |
| EROS | Evaluation of risk of stroke |
| Err | Error summation in the form of the Minkowski metric |
| *fdf* | Frequency domain despeckle filter |
| FDTA | Fractal dimension texture analysis |
| FFT | Fast Fourier transform |
| FN | False negative |
| FNF | False negative fraction |
| FP | False positive |
| FPF | False positive fraction |
| FPS | Fourier power spectrum |
| GA | Genetic algorithms |
| GACs | Geometric active contours |
| GAE | Geometric average error |

| | |
|---|---|
| GF | Geometric filtering |
| *gf4d* | Geometric despeckle filter |
| *gfminmax* | Geometric despeckle filter utilising minimum maximum values |
| GGVF | Generalised gradient vector flow |
| GHT | Generalised Hough transform |
| GLDS | Gray level difference statistics |
| GT | Segmented area representing ground truth |
| GVF | Gradient vector flow |
| HD | Hausdorff distance |
| HDI Lab | QLAB quantification software |
| HF | Maximum homogeneity |
| HM | Homomorphic |
| *homo* | Homomorphic despeckle filter |
| *homog* | Most homogeneous neighbourhood despeckle filter |
| HT | Hough transform |
| HVS | Human visual system |
| ICA | Internal carotid artery |
| ICRU | International commission of radiation units and measurements |
| IDM | Inverse difference moment |
| IDV | Intensity difference vector |
| IMC | Intima media complex |
| IMT | Intima media thickness |
| IVUS | Intra Vascular ultrasound |
| KI | Similarity kappa index |
| kNN | The statistical k-nearest-neighbour classifier |
| *lecasort* | Linear scaling and sorting despeckle filter |
| *lemva* | Mean and variance local statistics despeckle filter |
| LS | Linear scaling |
| *ls* | Linear scaling of the gray level values despeckle filter |
| *lslog* | Linear scaling of gray values logarithmic despeckle filter |
| *lsmedc* | Diffusion exponential damp kernel despeckle filter |
| *lsmedcd* | Lee diffusion despeckle filter |
| *lsminsc* | Minimum speckle index homogeneous mask despeckle filter |
| *lsminv1d* | Minimum variance homogeneous 1D mask despeckle filter |
| *lsmv* | Mean and variance local statistics despeckle filter |
| *lsmv_lee* | Lee local statistics despeckle filter |
| *lsmvsk2d* | Mean variance, higher moments local statistics despeckle filter |

| | |
|---|---|
| *lsmvske1d* | Mean, variance, skewness, kurtosis 1D local statistics despeckle filter |
| M | Manual |
| *median* | Median despeckle filter |
| MF | Multi-resolution fractal |
| MMSE | Minimum mean-square error |
| MN | Manual normalised |
| MRI | Magnetic resonance imaging |
| MSE | Mean square error |
| N | Normalized |
| NASCET | North American symptomatic carotid endarterectomy trial |
| NCE | Normalised continuity energy |
| NCRE | Normalised curvature energy |
| ND | Normalized despeckled |
| NE | North east |
| NF | No filtering |
| NGTDM | Neighbourhood gray tone difference matrix |
| NIE | Normalised image energy |
| *nldif* | Non-linear coherent diffusion despeckle filter |
| NS | Not significant difference |
| NST | North south |
| NTSE | Normalised total snake energy |
| Overlap | Overlap value of two areas |
| P | Precision |
| PACs | Parametric active contours |
| PDE | Partial differential equation |
| PDF | Probability density function |
| PET | Positron emission tomography |
| PHT | Probabilistic Hough transform |
| PSNR | Peak signal-to-noise radio |
| PW | Pulsed wave |
| R | Sensitivity (or recall) |
| RF | Radio frequency |
| RHT | Randomised Hough transform |
| RMSE | Root mean square error |
| ROC | Receiver operating characteristic |
| S | Significant difference |

| | |
|---|---|
| Sp | Specificity |
| SAR | Synthetic aperture radar |
| SD | Simple statistical descriptors |
| SE | South east |
| SFM | Statistical feature matrix |
| SGLDM | Spatial gray level dependence matrices |
| SGLDMm | Spatial gray level dependence matrix mean values |
| SGLDMr | Spatial gray level dependence matrix range of values |
| SNR | Signal-to-noise radio |
| SPECT | Single photon emission computer tomography |
| SSCQE | Single continuous stimulus quality evaluation |
| SSIN | Structural similarity index |
| TEM | Laws texture energy measures |
| TGC | Time gain compensation |
| TIA | Transient ischemic attacks |
| TN | True negative |
| TNF | True negative fraction |
| TP | True positive |
| TPF | True positive fraction |
| TSEB | Total snake energy Balloon snake |
| TSEGVF | Total snake energy GVF snake |
| TSELC | Total snake energy Lai&Chin snake |
| TSEP | Total snake energy Williams&Shah snake |
| TV | Television |
| *waveltc* | Wavelet despeckle filter |
| WE | West east |
| *wiener* | Wiener despeckle filter |
| WN | West north |
| WRHT | Window randomised Hough transform |
| WS | West south |
| WT | Wavelet transform |
| $\overline{GT}$ | Complement area of $GT$ |
| $\beta_{err}$ | Minkowski error coefficient |
| 1D | One-dimensional |
| 2D | Two-dimensional |
| 3D | Three-dimensional |

# Acknowledgments

During my research, I received help, advice, and support from many people, who I would like to acknowledge here. First of all I would like to thank my director of research Prof. Robert Istepanian, who was always helpful and ready to give his support when requested, and my local supervisor in Cyprus, Prof. Constantinos Pattichis who supervised me during my PhD work. Their guidance, knowledge, and discussions were invaluable.

Furthermore, I would also like to thank Prof. Andrew Nicolaides, Emeritus Professor at the Faculty of Medicine at Imperial College and former director at the Cyprus Institute of Neurology and Genetics, Dr. Marios Pantziaris consultant neurologist, and Dr. Tyllis Theodosis consultant physician, from the Cyprus Institute of Neurology and Genetics. I am thankful to Dr. Efthivoulos Kyriakou, Dr. Christodoulos Christodoulou of the Cyprus Institute of Neurology and Genetics, and Prof. Marios Pattichis from the Department of Electrical and Computing Engineering at the University of New Mexico. Their research work and support helped me in numerous times to solve many problems and decide on the most appropriate research directions. Also, I would like to thank Prof. Christos Schizas of the Department of Computer Science at the University of Cyprus for his valuable support.

I would also like to thank the Director of Intercollege Mr. Stahis Mavros, and my colleagues at the Computer Science Department of Intercollege for their support in my research work.

Partial funding for this project was obtained from CDER (Cardiovascular Disease Educational and Research) Trust, and two projects (IASIS 104\5$^0$ ΠΕ-2002, TALOS ΠΑΗΡΟ\0603\05) funded form the Institute Promotion Foundation (IPF) of Cyprus.

Finally, I would like to thank my parents, all my friends and family, but especially my wife Phaedra who was so patient with me all those nights I was working late.

Christos P. Loizou

September 2005

# *Chapter 1*

# *Vascular Ultrasound Imaging and Digital Image Processing*

# CHAPTER 1: VASCULAR ULTRASOUND IMAGING AND DIGITAL IMAGE PROCESSING

According to an old Chinese proverb, "a picture is worth a thousand words". In the modern age, this concept is still significant for computer vision and image processing, where we aim to derive better tools that give us different perspectives on the same image thus allowing us to understand not only its content, but also its meaning and significance. Image processing cannot compete with the human eye in terms of accuracy but it can perform better on observational consistency and ability to carry out detailed mathematical operations. In the course of time, image-processing research has evolved from basic low-level pixel operations to high-level analysis that now includes sophisticated techniques for image interpretation and analysis. These new techniques are being developed in order to gain a better understanding of images based on the relationships between its components, context, history, and knowledge gained from a range of sources.

In this Chapter we introduce stroke, which is associated with the carotid artery disease, and present a brief review on ultrasound imaging. Section 1.3 presents an introduction for the processing of carotid artery ultrasound images, where examples on despeckle filtering and segmentation are given. In section 1.4 we present the original aspects of this work and explain how image processing helps in the assessment of the risk of stroke. Finally, at the end of the Chapter a guide to this thesis contents is presented.

## 1.1 Introduction

### *1.1.1 Risk of stroke*

Figure 1.1 presents the 10 leading causes of death in the world where stroke is the third leading cause after heart disease (42%), and cancer (30%), with 9% of death incidents worldwide per year.

According to the 2002 world health report [134] cardiovascular deaths in 2001 accounted for 36% of all deaths in women, and 30% of all deaths in men, and all predictions suggest growing figures for the next decade especially for the developing world. It was also reported from the Heart and Stroke Foundation of Canada [134], that each year in Canada, about 700,000 people develop a stroke, with 500,000 of these being first attacks, and 200,000 recurrent attacks. Stroke costs the Canadian government more than $40-$50 billion dollars per year. One of the most important causes of death in the world and the leading cause of serious, long-term disability in the United States today is cardiovascular disease [134]. Stroke killed 283,000 people in the United States in 2000 and accounted for about one of almost every 14 deaths. The

worldwide statistics for the year 2001 were 20.5 million strokes, 5.5 million of which were fatal [134].

Stroke accounts for some non-modifiable risk factors such as age, gender, family history and race and for some modifiable factors such as hypertension, cardiac disease, diabetes, hyperlipedemia, asymptomatic carotid stenosis (ACSRS), smoking, alcohol consumption, transient ischemic attacks (TIA's), physical inactivity, and others [134], [208].

Atherosclerosis is a disease of the large and medium sized arteries that is characterized by progressive intimal accumulation of lipid, protein, and cholesterol esters [48], which significantly reduces blood flow. Atherosclerosis may be present in different sites of the body, including the coronary arteries, the superficial femoral artery, the infarenal aorta, and the carotid arteries at the area of the common carotid bifurcation (see Fig. 1.2a). Atherosclerotic plaque formation, (see Fig. 1.2b-d), initially causes compensatory enlargement of the vessel with little or no compression of the lumen [352].

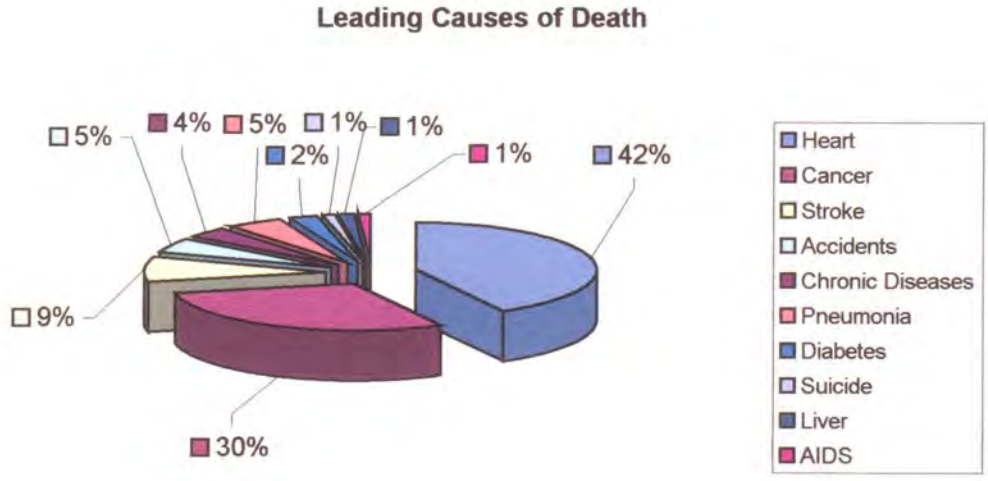


**Fig. 1.1**: World leading causes of death (US CDC National Center of Health Statistics, vital statistics of the United States, Annual 2000).

Figure 1.2a shows the carotid system, which is located in the neck and contains the common carotid artery (CCA), which branches into the internal carotid (ICA), and the external carotid artery (ECA). The ICA supplies blood to structures inside the skull like most of the cerebrum of the brain. It also supplies blood to the eyeballs, ears and external nose. The general distribution of the ECA is to structures external to the skull.

Carotid plaque is defined as a localized thickening involving the intima and media in the bulb, internal carotid, external carotid or common femoral arteries (see Fig. 1.2a, b). The risk of

stroke increases with the severity of carotid stenosis (the narrowing of the artery caused by plaque, see Fig. 1.2b), and is reduced after carotid endarterectomy [353]. The degree of internal carotid stenosis is the only well established measurement that is used to assess the risk of stroke [194], and it is mainly the current criterion used to decide whether carotid endarterectomy is indicated or not [208]. It is increasingly accepted that carotid artery plaque thickness measurements, can serve as early indicators of cardiovascular disease development. In other words, it is assumed that an increased plaque thickness in the carotid artery is a predictor of future cardiovascular events like heart attack and stroke [7] pp. 721, [208], [353].

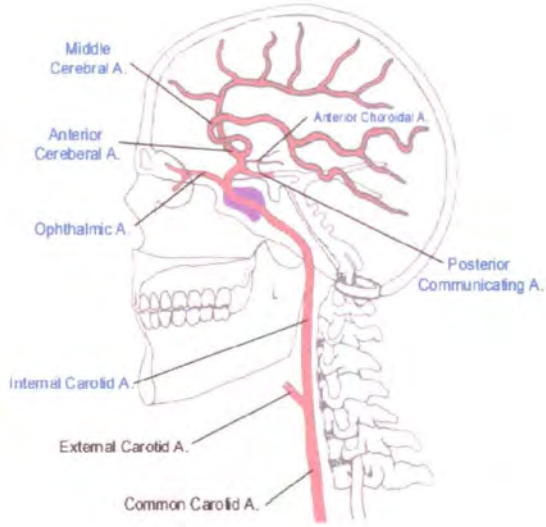


(a)

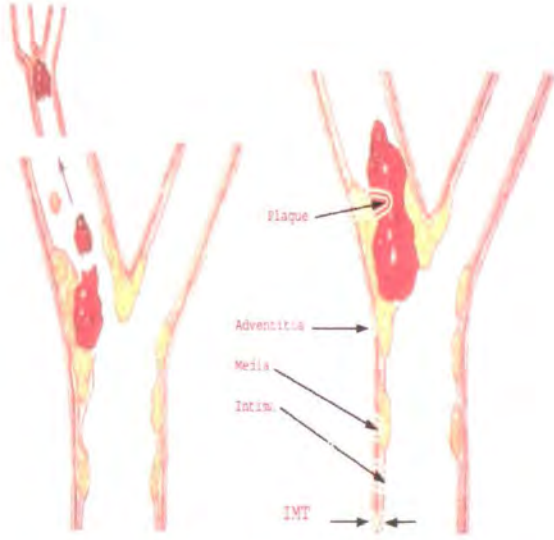


(b)

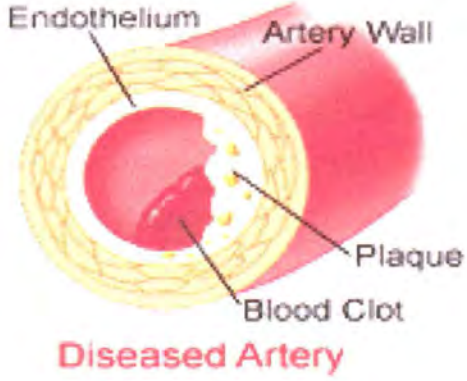


(c)

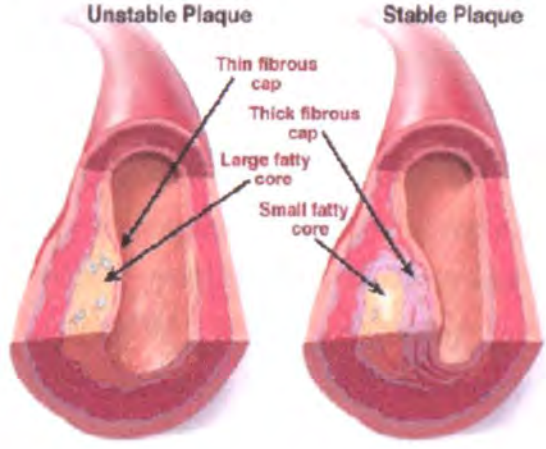


(d)

**Fig. 1.2**: (a) The carotid system [130], (b) longitudinal section of a carotid artery with plaque (right) and embolisation (left) [153] (c) transverse section of a carotid artery with plaque, (e) stable and unstable plaque. (From Heart Center online: http://www.heartcenteronline.com).

Recent studies involving angiography, high-resolution ultrasound, thrombolytic therapy, plaque pathology, coagulation studies, and more recently molecular biology, have implicated atherosclerotic plaque rapture as a key mechanism responsible for the development of cerebrovascular events [369]-[371]. Atherosclerotic disease has two main clinical manifestations, a) asymptomatic bruits and, b) cerebrovascular syndromes such as amaurosis fugax, TIA's or stroke which are often the result of plaque erosion or rupture with subsequent thrombosis producing occlusion or embolisation [367], [368] (see also Fig. 1.2b).

A stroke occurs usually when the blood supply to parts of the brain is suddenly interrupted or becomes blocked (Ischemic stroke). Ischemic strokes caused by artery stenosis, account for approximately 75% of all strokes. This blockage, caused by fatty build-up, is referred to as atherosclerosis [10], [51], [61], [100], [149]. Atherosclerosis changes the mechanical properties of the vessel walls and the build up of a plaque making the artery walls stiffer [99]. The plaque accumulates in the inner lining of blood vessels and results in narrowing and irregularity of the artery, (see Fig. 1.2b, d). When a blood vessel in the brain bursts, spilling of blood occurs into the spaces surrounding brain cells and we have a hemorrhagic stroke. For all types of stroke, treatment must be given immediately, as neuronal death processes quickly after the onset of symptoms.

The decision to treat narrowing of the carotid artery is not always straightforward. The potential benefit of the surgery must be weighted against the risk of the surgery. The degree of stenosis of the carotid artery, the intima-media thickness (IMT), which is the thickness of the artery walls (see also Fig. 1.2b), and the presence or absence of symptoms are some of the important factors to consider when taking this decision [71] pp. 334, [194], [208], [266], [353]. Measurements of IMT are better predictors of risk than any combination of conventional risk factors [149], [322], [372].

Compared to medical therapy alone, surgery (carotid endarterectomy) has been found highly beneficial for patients who have already had a stroke or experienced the warning signs of a stroke and have a severe degree of stenosis of 70-99% [208]. Usually these patients are considered to benefit from a carotid endarterectomy [52], [266]. Based on the evidence of the North American Symptomatic Carotid Surgery Trial (NASCET), and the European Carotid Surgery Trial (ECST), for a degree of stenosis of less than 30%, medical therapy is preferred [208], [353]. For a degree of stenosis between 30% and 70%, the best therapy has not been yet determined, since the risk/benefit ratio varies between the conditions of the patients. Patients that are at a high risk for a surgical procedure may be placed on medications to inhibit their blood from clotting [208], [266].

The primary aim of most digital carotid image-processing techniques is to provide human–independent aids for assessing the condition of the arteries and assessing the risk of stroke. In

normal individuals usually before the age of 40, there is no plaque present in the carotid artery. As atherosclerosis disease progresses due to various factors [48], [99], [266], [352], the IMT initially increases diffusely along the artery and then becomes more focal, forming plaques which gradually obstruct blood flow and causes a lumen stenosis. Furthermore the plaques may become unstable and rupture to block the artery suddenly if they develop internal pools of lipid and thrombus covered by a thin fibrous cap (see Fig. 1.2b-d). Lumen stenosis, the degree to which the vessel is narrowed as a result of plaque growth, is an indirect measure used to describe the sensitivity of the atherosclerosis, where the IMT and the presence of a plaque, are direct indicators of the risk of stroke [49], [99], [208]. Accurate measurements and understanding of the IMT and plaque in the carotid arteries are therefore important for the assessment and management of the risk of stroke [48], [65], [99], [322].

### *1.1.2 IMT measurements*

Measurements of the IMT in the CCA by ultrasound have been used in several clinical trials [44], [49], [82], [99], [227], [241], [253]-[256], to validate atherosclerosis disease [194], [314], where measurements from 0.2 mm-2.5 mm were reported. It was shown that increased IMT was correlated to coronary artery disease and stroke in older adults without a history of cardiovascular disease [99], [315], [320] and that, a strong correlation of the IMT with increasing age in both men and women exists, where the estimated change of IMT is 0.009 mm/year. The IMT of patients with a history of cardiovascular disease, such as stroke, myocardial infraction and angina was increased by 6-12% in comparison to those without symptomatic cardiovascular disease [320]. Increased IMT was also demonstrated to have a strong correlation with the presence of atherosclerosis elsewhere in the body. Risk factors like diabetes, smoking and high blood pressure also may cause an increase of 5-12% in the IMT [313], [322]. IMT measurements may be therefore used as an indicator of generalized atherosclerosis and future cardiovascular events.

The degree of the artery stenosis is defined as the percentage of the lumen diameter reduction relative to a reference vessel diameter. It is usually measured as the difference between the largest and smallest area of the artery in relation to the largest area [208], [372], and is defined by the NASCET study as [166]:

$$100\left[1-\frac{d_{ICA,\min}}{d_{ICA,distal}}\right] \tag{1.1.1}$$

where $d_{ICA,\min}$, is the minimum lumen diameter in the ICA (i.e. at the site of maximal stenosis) and $d_{ICA,distal}$, is the lumen diameter in a distal diseased free portion of the ICA. In practice, ICA stenosis is commonly estimated from blood velocity measurements made using Doppler ultrasound. Although this method has proven effective in identifying stenosis above the

threshold for carotid endarterectomy, it is widely considered to be unsuitable for accurate quantification of disease severity over a wide range of degrees of stenosis [49], [54], [99], [208].

### *1.1.3 Plaque characteristics*

Plaque characteristics may also be useful in determining high-risk plaques, which are more likely to cause thromboembolic events leading to heart attack or stroke [10], [39], [48], [56], [67]. There is an increasing body of medical research suggesting that differences in the structure and composition of individual atherosclerotic plaques (plaque morphology), may be linked to possible future health problems for patients [10], [51], [138], [209], [320], [368], [372]. The challenge for doctors and technology is to discover a way to identify which plaques can be referred to as "safe" and which has the potential to break off and threaten the patient's life. Homogeneous plaques are characterised by uniformly high- or medium level echoes, smooth surface, echogenicity, and are associated with stable plaques, whereas heterogeneous plaques are associated with advance stages of carotid plaque lesion, irregular surface, echolucency, [10], [51], [320], [322], which are characteristics of a potentially unstable plaque [208] (see also Fig. 1.2d). Echogenic plaques reflect strongly the ultrasound signal, whereas echolucent ones have less reflectivity ability. It has been shown that echolucent plaques, as evaluated by B-mode ultrasound, are more likely to lead to the development of neurological events than echogenic ones [93], [209], [266]. The ultrasonic characteristics of unstable (vulnerable) plaques have been determined [337], [358] and populations or individuals at increased risk for cardiovascular events can now be identified [99], [202], [320], [328]. In addition, high-resolution ultrasound enables the identification of the different ultrasonic characteristics of unstable carotid plaques associated with amaurosis fugax, TIAs, stroke and different patterns of computer tomography-brain infraction [337], [358]. This information has provided new insight into the pathophysiology of the different clinical manifestations of extracranial atherosclerotic cerebrovascular disease using non-invasive methods.

Different classifications have been proposed in the literature for the characterization of atherosclerotic plaque morphology, resulting in considerable confusion. For example, plaques containing medium or high level uniform echoes were classified as homogeneous by Reilly [303] and correspond closely to Johnson's dense and calcified plaques [281], to Gray-Weale's type 3 and 4 [277] and to Widder's type I and II plaques [275] (i.e echogenic or hyperechoic). A recent consensus on carotid plaque characterization has suggested that echodensity should reflect the overall brightness of the plaque with the term hypoechoic referring to echolucent plaques [274]. The reference structure to which plaque echodensity should be compared with is for hypoechoic plaques, blood; for the isoechoic, the sternomastoid muscle; and for the hyperechoic ones, the bone of the adjacent cervical vertebrae.

There is enough evidence published to support the clinical usefulness of ultrasonic plaque characterization, patients with hypoechoic carotid plaques being at increased risk of stroke. Polak has recently investigated the association between stroke and ICA plaque echodensity [266]. Plaque morphology may be subjectively characterized as hypoechoic, isoechoic or hyperechoic in relation to the surrounding soft tissues. The stroke rate for hypoechoic plaques was 2.78 times higher than for isoechoic and hyperechoic plaques. In addition to the subjective characterization of plaques, studies that presented computer assisted plaque characterization using ultrasound B-mode images of plaques taken from a duplex scanner with fixed instrument settings including time gain control, have been published. In a study by El-Barghouty et al. the median of the frequency distribution of gray-scale values of the pixels within the plaque is used as the measurement of echodensity [209]. It is also reported in the literature, that carotid endarterectomy in patients with asymptomatic carotid stenosis (ACSRS) will reduce the incidence of a stroke [208], [322]. However, as a result of the above, a large number of patients are operated on unnecessarily. For example, twenty patients have to be operated in order to prevent one stroke episode in 5 years, or 100 patients to prevent one stroke in one year [64], [353]. Therefore, it is necessary to identify patients with a high risk of developing a stroke (>4% stroke incidence per annum) who will be considered for carotid endarterectomy, and those patients with a low risk (<1% per annum), who will be spared from an unnecessary, expensive and often dangerous operation.

## 1.2 A brief review of ultrasound imaging

Medical imaging technology has experienced a dramatic change in the last 30 years [4]. Previously only X-ray radiographs were available, which showed the organs as shadows on photographic film. With the advent of modern computers, new imaging modalities like computer tomography (CT or CAT computer assisted tomography), magnetic resonance imaging (MRI), positron emission tomography (PET) and ultrasound, which deliver cross-sectional images of a patient's anatomy and physiology, have been developed. Among the imaging techniques employed are X-ray angiography, X-ray, CT, ultrasound imaging, MRI, PET, and single photon emission computer tomography (SPECT). MRI and CT have advantages compared to ultrasound, in the sense that higher resolution and clearer images are produced.

Imaging techniques have long been used for assessing and treating cardiac [4], [7], [8] and carotid disease [7], [93], [233]-[235]. Today's available imaging modalities produce a wide range of image data types for disease assessment which includes, 2D projection images, reconstructed three-dimensional (3D) images, 2D slice images, true 3D images, time sequences of 2D and 3D images, and sequences of 2D interior view (endoluminal) images.

The use of ultrasound in the diagnosis and assessment of imaging organs and soft tissue structures as well as human blood, is well established [4], [44], [50], [55], [136], [141]. Because of its non-invasive nature and continuing improvements in imaging quality, ultrasound imaging is progressively achieving an important role in the assessment and characterization of carotid plaques [51], [126], [255], and assessment of carotid artery disease [55], [56], [136]. The main disadvantage of ultrasound is that it does not work well in the presence of bone or gas, and the operator needs a high level of skill in both image acquisition and interpretation to carry out the clinical evaluation [136]. Standard angiography cannot give reliable information [8], [9], on the cross-sectional structure of the arteries. This makes it difficult to accurately assess the build-up of plaque along the artery walls. For some years, B-mode ultrasound imaging or intravascular ultrasound (IVUS) has emerged and it is used for visualizing carotid plaques and assessment of plaque characteristics related to the onset of neurological symptoms [57], [73], [217]. To perform IVUS, one inserts a catheter equipped with an ultrasonic transducer into a vessel of interest and real-time cross sectional images may be reproduced. However, reproducible measurements of the severity of the plaque in 2D and 3D ultrasound are made difficult because of the complex shapes, asymmetry of carotid plaques, and the speckle noise present in ultrasound images [2], [38], [141]. Furthermore, IVUS is invasive as a catheter is inserted in the artery and possesses therefore, a certain risk for the patient.

(a) (b)

**Fig. 1.3**: Ultrasound imaging scanners: (a) ATL HDI-3000, (b) ATL HDI-5000 [153].

The use of ultrasound in medicine began during the Second World War in various centres around the world. The work of Dr. Karl Theodore Dussik in Austria in 1942 [133] on transmission ultrasound investigation of the brain provides the first published work on medical ultrasonics. Although other researchers in the USA, Japan, and Europe have also been cited as pioneers, the work of Professor Ian Donald [200] and his colleagues in Glasgow, in the mid 1950s, did much to facilitate the development of practical technology and applications. This lead to the wider use of ultrasound in medical practice in subsequent decades.

From the mid sixties onwards, the advent of commercially available systems allowed the wider dissemination of the use of ultrasound. Rapid technological advances in electronics and piezoelectric materials provided further improvements from bistable to gray-scale images and from still images to real-time moving images. The technical advances at this time led to a rapid growth in the applications of ultrasound. The development of Doppler ultrasound [366] had been progressing alongside the imaging technology but the fusing of the two technologies in Duplex scanning [50] and the subsequent development of colour Doppler imaging [366] provided even more scope for investigating the circulation and blood supply to organs, tumours etc (see also sections 1.2.1, 1.2.2). The advent of the microchip in the seventies and the subsequent exponential increase in processing power facilitated the development of faster and more powerful systems incorporating digital beam forming, signal enhancement and new ways of interpreting and displaying data, such as power Doppler [81], [148] and 3D imaging [45]. Ultrasound has long been recognized as a powerful tool for use in the diagnosis and evaluation of many clinical entities. Over the past decade, as higher quality less expensive scanners were developed, ultrasound has proliferated throughout various specialties [65], [66].

Figure 1.3 illustrates the two ultrasound scanners used in this PhD work.

### *1.2.1 Basic principles of ultrasound*

Ultrasound is a sound wave with frequency that exceeds 20 $kHz$. It transports energy and propagates through several means as a pulsating pressure wave. It is described by a number of wave parameters such as pressure density, propagation direction, and particle displacement. If the particle displacement is parallel to the propagation direction then the wave is called longitudinal or a compression wave. If the particle displacement is perpendicular to the propagation direction, it is a shear or transverse wave. Interaction of ultrasound waves with tissue is subject to the laws of geometrical optics. It includes reflection, refraction, scattering, diffraction, interference and absorption. Except from interference all other interactions reduce the intensity of the ultrasound beam.

The main characteristic of an ultrasound wave is the wavelength $\lambda$, which is a measure of the distance between two adjacent maximum or minimum values of a sine curve and frequency $f$, which is the number of waves per unit of time. The product of these two measures give the velocity of ultrasound wave propagation, $v$, described with the equation $v = f\lambda$. Ultrasound techniques are mainly based on measuring the echoes transmitted back from a medium when sending an ultrasound wave to it. In the echo impulse ultrasound technique, the ultrasound wave interacts with tissue and blood, and some of the transmitted energy returns to the transducer to be detected by the instrument. If we know the velocity of propagation in the tissue being interrogated, we can determine the distance from the transducer at which the interaction occurred [156]. The characteristics of the return signal (amplitude, phase etc.) provide

information on the nature of the interaction, and hence they give some indication of the type of the medium in which they occurred. Mainly two principles are used in medical ultrasound diagnostics, the echo impulse technique and the Doppler technique [156].

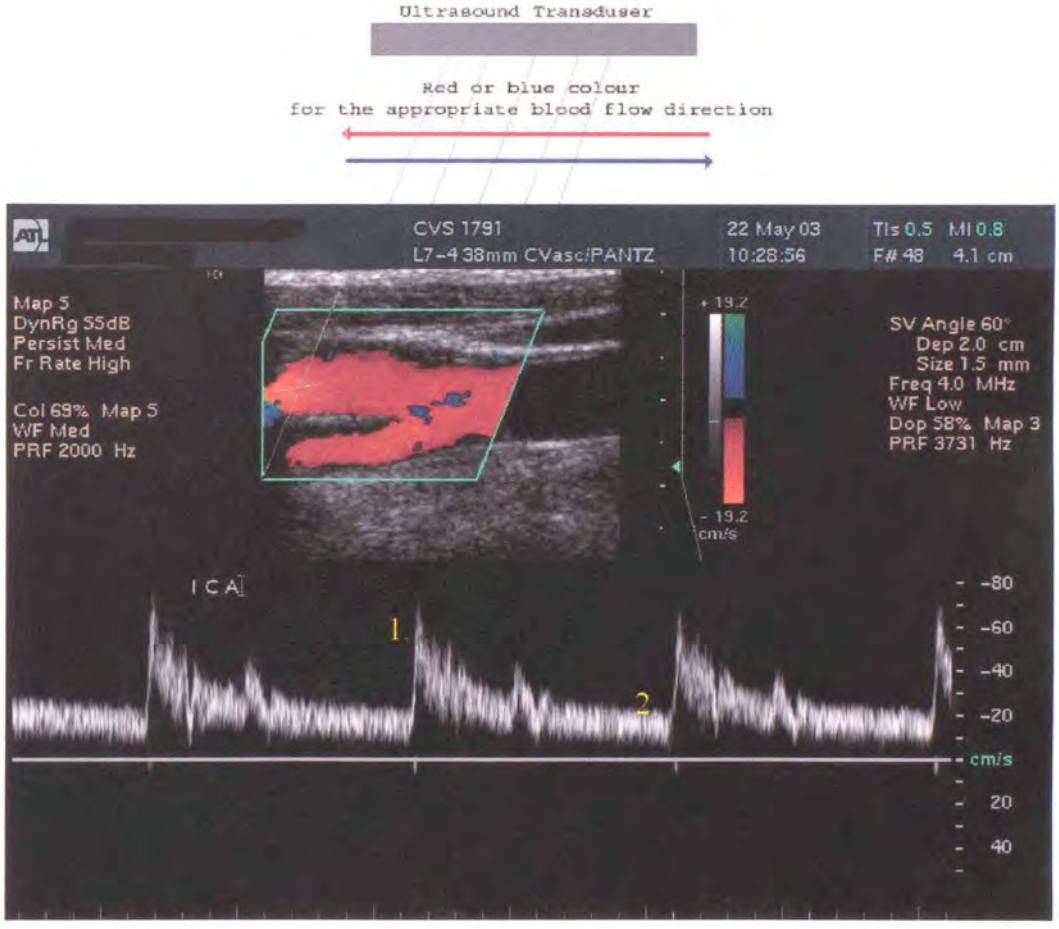


**Fig. 1.4**: Longitudinal color flow duplex image of the carotid artery combined with Doppler ultrasound image. Highlighted image with green contour on top shows the carotid bifurcation. The 2D signal shows the velocity variation related to the cardiac cycle. Blood flow velocity spectrum is displayed with markings 1 and 2, where marking 1 represents the peak systolic velocity and marking 2 represents the end diastolic velocity. This is the duration of one cardiac cycle. Different colours represent blood flow direction. For the current picture, red represents the blood moving to the brain through the carotid artery, whereas blue represents the blood returning back from the brain.

The second principle used in ultrasound diagnostics is the Doppler principle, named after the physicist Christian Doppler (1803-1853) [366]. This technique is based on the principle that the perceived frequency of sound echoes reflected by a moving target is related to the velocity of the target. The frequency shift (Doppler frequency shift) $\Delta f$, of the echo signal is proportional to the flow velocity $v$ $(cm/s)$, and the ultrasound transmission frequency $f$, $(MHz)$. The Doppler shift is described by the formula $\Delta f = 2 f_0 (v \cos\theta)/u_{sp}$, where $f_0$, is the transmitted frequency of the signal, $\theta$, is the angle between the direction of movement of

the moving object and the ultrasound beam and $u_{sp}$, is the speed of sound through tissue that is approximately 1540 m/s.

In Doppler ultrasound waves are produced by a vibrating crystal using the piezoelectric effect, whereas the returned echoes are displayed as 2D signal as shown in Fig. 1.4. When blood flow in a vessel is being examined sound reflections caused by the blood's corpuscular elements play a major role. Based on the fact that blood flow velocity varies in different areas of a vessel, the Doppler signal contains a broad frequency spectrum. In normal ICA the spectrum varies from 0.5 $kHz$ to 3.5 $kHz$ and $v$ is less than 120 $cm/s$ when an ultrasound beam of 4 $MHz$ is used.

### *1.2.2 Ultrasound modes*

The two main scanning modes are A- and B-mode. Other modes used are the M-mode, Duplex ultrasound, colour coded ultrasound, and power Doppler ultrasound, which will be briefly introduced below.

A-mode refers to amplitude mode scanning, which has mainly a historical interest. In this mode the strength of the detected echo signal is measured and displayed as a continuous signal in one direction. A-mode is a line, with strong reflections being represented as an increase of signal amplitude. This scanning technique has the limitation that the recorded signal is 1D with limited anatomical information. A-mode is no longer used, especially for the assessment of cardiovascular disease. Its use is restricted to specialist uses such as ophthalmology in order to perform very accurate measurements of distance.

B-mode refers to brightness mode. In B-mode echoes are displayed as a 2D gray scale image. The amplitude of the returning echoes is represented as dots (pixels) of an image with different gray values as Fig. 1.5 shows. The image is constructed by these pixels line by line. Advances in B-mode ultrasound have resulted in improved anatomic definition, which has enable plaque characterization [156], [330].

The M-mode is used in cardiology and it is actually an A-scan plotted against time. The result is the display of consecutive lines plotted against time. Using this mode, detailed information may be obtained about various cardiac dimensions and also the accurate timing of vascular motion.

Moving blood generates a Doppler frequency shift in the reflected sound from insonated red blood cells and this frequency shift can be used to calculate the velocity of the moving blood, using the Doppler equation [54], [366]. The invention of gated Doppler ultrasound in the late 1950s allowed velocity sampling at different depths and positions and its subsequent combination with B-mode real-time ultrasonic imaging led to the development of Duplex ultrasound. Stenosis in any vessel is characterised by an increase in systolic and diastolic

velocities. Several types of Doppler systems are used in medical diagnosis, Continuous Wave (CW) Doppler, Pulsed Wave (PW) Doppler, Duplex ultrasound and Color Flow Duplex. In CW Doppler, the machine uses two piezoelectric elements serving as transmitters and receivers. They transmit ultrasound beams continuously. Because of the continuous way that ultrasound is being transmitted, no specific information about depth can be obtained. PW Doppler is used in order to detect blood flow at a specific depth. Sequences of pulses are transmitted to the human body that are gated for a short period of time in order to receive the echoes. By selecting the time interval between the transmitted and received pulses, it is possible to examine vessels at a specific depth.

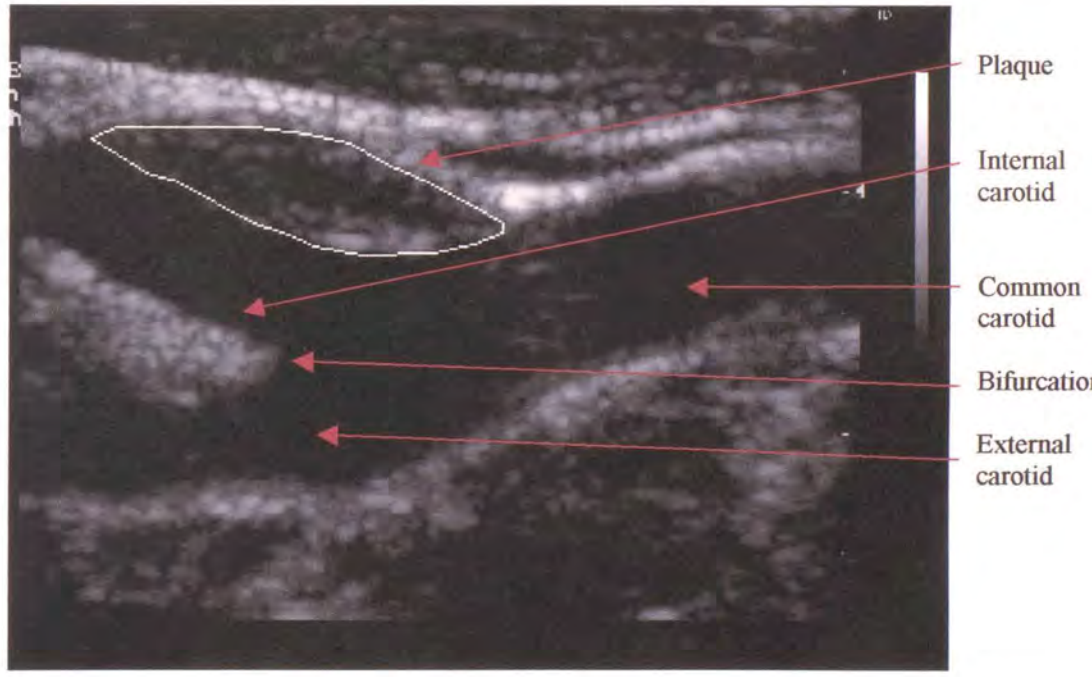


**Fig. 1.5**: Ultrasound B-mode longitudinal image of the carotid bifurcation with manually outlined plaque, which is usually confirmed with blood flow image.

In colour-coded ultrasound, every pixel is tested for Doppler shift. Using this technique, the movement of the red blood cells is finally depicted through colour. The final image results by superimposing the colour-coded image on the B-mode image.

Power Doppler is the depiction of flow, based on the integrated power of the Doppler spectrum rather than on the mean Doppler frequency. This modality results in an angle, which is independent of the resulting enhanced sensitivity in flow detection as compared to the colour-coded Doppler and therefore the detection of low flow is better viewed.

### *1.2.3 Image quality and resolution*

The quality of the produced ultrasound image depends on image resolution, axial and lateral. Resolution is defined as the smallest distance between two points at which they can be

represented as distinct. Axial resolution refers to the ability of representing two points that lie along the direction of ultrasound propagation. It depends on the wavelength of the beam. In B-mode ultrasound pulses consist of one to two sinusoidal wavelengths, and the axial resolution is dependent on the wavelength of the waveforms, and lies in the range of the ultrasound wavelength, $\lambda$ (0.21 mm). Resolution depends on the frequency of the beam waveforms. Since this value is reciprocal to the ultrasound frequency ($\lambda = v/f$), the axial resolution improves with increasing frequency.

Lateral resolution refers to the ability to represent two points that lie at right angle to the direction of ultrasound propagation. This is dependent on the width of the ultrasound wave (beam). To be able to resolve points that lie close together, the width of the ultrasound beam has to be kept reasonably small and the diameter of the transducer is kept as large as possible (i.e. small phase-array transducers have a worse lateral resolution than large linear or curved-array transducers).

In order to achieve the best results in vascular ultrasound imaging, the transmission frequencies are in the range of 1-10 *MHz*. The selected frequency depends on the application domain. For arteries located close to the human skin, frequencies greater than 7.5 *MHz* are used, whereas for arteries located deeper in the human body, frequencies from 3-5 *MHz* are used. For transcranial applications frequencies less than 2 *MHz* are used. Though when selecting a frequency, the user has to keep in mind that axial resolution is proportional to the ultrasound wavelength; while the intensity of the signal depends on the attenuation of the signal transmitted through the body, with the higher the frequency the higher the attenuation. Therefore, there is a trade off between higher resolution ultrasound images at smaller depth and lower resolution images at higher depths.

### *1.2.4 Limitations of ultrasound*

Variability in B-mode images (even when using the same ultrasonic equipment with fixed settings) does exist [79], [93], [172], [253]. Sources of variability are outlined below:

a) Geometrical and diffraction effects, where spatial compound imaging may be employed to correct the image [95].

b) Inter-patient variation due to depth dependence and inhomogeneous intervening tissue, where normalisation techniques may be applied to standardise the image [322] (see also Chapter 5.3).

c) Speckle is an important factor affecting the quality of ultrasound B-mode imaging. It is described as an ultrasound textural pattern that varies depending on the type of biological tissue. The presence of speckle, which is difficult to suppress [131], [141], [345], may obscure small structures thus degrading the spatial resolution of an

ultrasonic image [160]. Despeckle filtering may be applied to despeckle the image (see also Chapter 2).

d) The IMT and plaque borders generally have a very low contrast [57], [58], and a small thin size [44], [182], [338], which makes it more difficult to interpret.

e) Falsely low echogenicity due to shadowing effects. Such B-mode images, showing plaques or IMT structures, are not included in visual or objective plaque analysis [208], [337], (see also Chapter 5.7, and Chapter 5.8).

f) Low signal-to-noise ratio in anechoic components and difficulty in outlining the carotid plaque, where the difficulty may be overcome by employing the use of colour coded images [322].

g) Ultrasound images inspected by the same expert at different occasions will also be different (intra-observer variability) [253].

h) Ultrasound images inspected by two or more experts will be different (inter-observer variability), as each expert will interpret a specific tissue differently [79], [186].

It is noted that the entries g and h are applicable in any medical imaging modality. In order to overcome intra- and inter- observer variabilities, multiple observers should perform the image evaluation.

## 1.3 Image processing of the carotid artery

Ultrasound imaging provides a well-established technique in the diagnosis and assessment of cardiovascular disease, by visualising the IMT, vessel stenosis, plaque composition, and size [99]. Monitoring of the arterial characteristics, like the vessel lumen diameter, the IMT, and the morphology of atherosclerotic plaque, are very important in order to assess the severity of atherosclerosis and evaluate its progression [7], [93], [138]. Due to its non-invasive nature, and continuing advances in ultrasound transducer instrumentation, and digital image processing technology, vascular imaging is progressively achieving a more important role in helping the expert visualize the morphology of vascular structure, as well as measure blood velocity and flow, arterial wall changes, volume and texture of atherosclerotic plaque [8], [9]. Information that can be determined from visualizing carotid arteries with ultrasound includes: plaque compositions (such as necrotic lipid core and fibrous cap), total plaque area and volume, lumen area, IMT, and plaque distribution. Improved imaging techniques may help in determining the ideal treatment and clinical outcomes for asymptomatic or symptomatic patients by providing more information about carotid athrerosclerotic plaque and IMT.

In the area of the carotid artery for the evaluation of the risk of stroke, some researchers are concentrating in semi-automatic segmentation methods in order to measure the IMT [44], [178],

[227], [241], [253], or to segment the atherosclerotic carotid plaques [64], [184], [191], [220] from ultrasound images. Other researchers tried to identify the degree of artery stenosis and to classify arteries as being either as asymptomatic or symptomatic [194], [314], [322]. If ultrasound shows a stenosis of grater than 70%, magnetic resonance or CT angiography is recommended [208], [322], [353]. If the results correspond, no further investigation is needed for surgery. If they do not correspond then a carotid angiogram is required [67], [68].

Figure 1.5 shows a typical longitudinal ultrasound image from a normal adult subject. A close view of the IMT is shown in Fig. 1.6, with the far wall of the artery being depicted by a double line pattern, marked with asterisks by an expert. The upper set of asterisks corresponds to the echogenic lumen-intima and the lower set of asterisks corresponds to the media-adventitia, which are separated by a sonolucent region. One of our objectives is to apply despeckle filtering (see Chapter 2), to enhance the boundaries in the image and aid in the identification, localization, and extraction, of this important ultrasound structure which is associated with several risk factors for atherosclerosis [99], [202], [320], [328].

**Fig. 1.6**: Close view of manual measurements of the IMT:
(1) 0.9 mm, (2) 0.8 mm, (3) 0.86 mm.

### *1.3.1 Despeckle filtering*

Speckle noise, is considered to be the major performance-limiting factor in visual lesion detection in ultrasound imaging, which makes the lesions difficult to detect and diagnose by the expert [18]-[34]. Speckle is a multiplicative noise that reduces both image contrast and detail resolution, degrades tissue texture, reduces the visibility of small low-contrast lesions and makes continuous structures appear discontinuous. It also limits the effective application (e.g. edge detection) of automated computer analysis (e.g. volume rendering and 3D display) algorithms. It is caused by the interference between ultrasound waves reflected from microscopic scattering through the tissue. A characteristic speckle noise pattern observed in ultrasound images is shown in Fig. 1.7e and Fig. 1.7f after enlarging a portion of the images in Fig.1.7a and Fig. 1.7b respectively. Many authors have shown a reduction of lesion detectability of approximately a factor of eight due to the presence of speckle noise in the image [87], [89],

[163], [199]. This radical reduction in contrast resolution is responsible for the poorer effective resolution of ultrasound compared to X-ray and MRI [17], [92]. Despeckle filtering is therefore a critical pre-processing step in medical ultrasound images, provided that the features of interest for diagnosis are not lost.

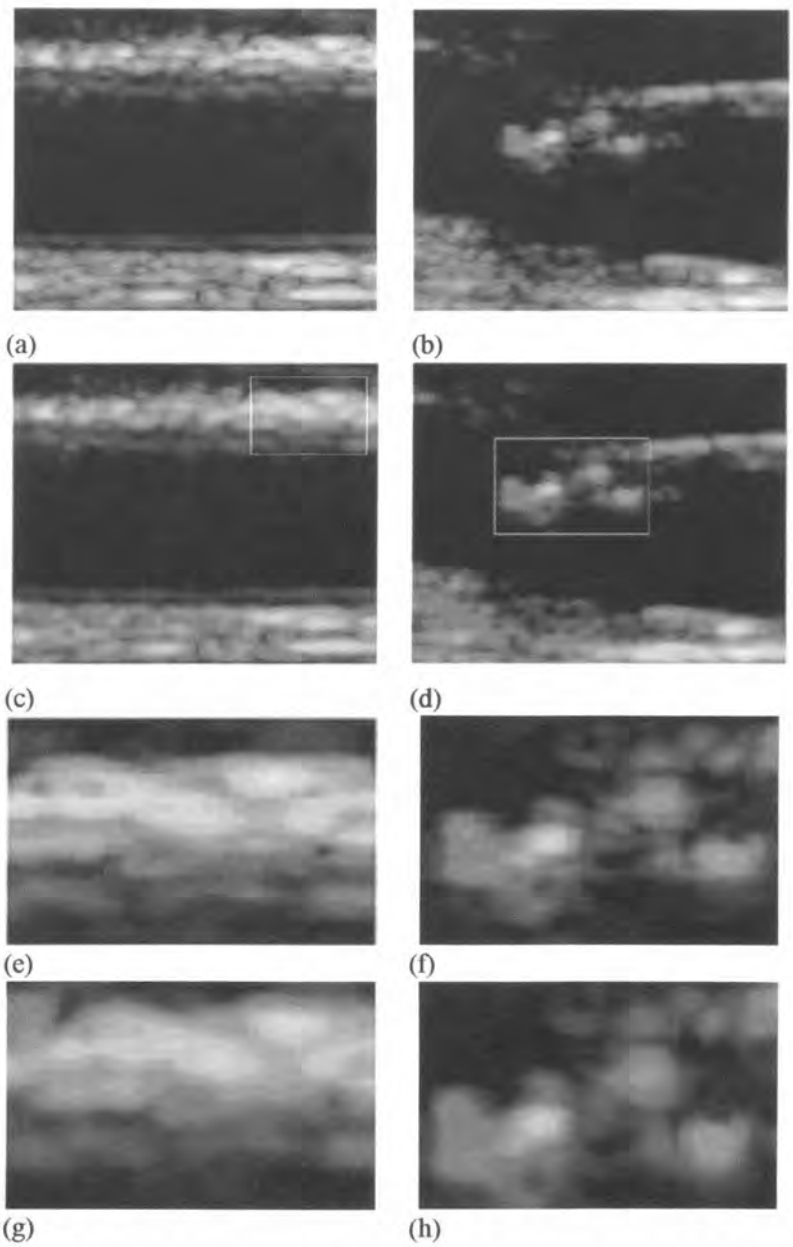


**Fig. 1.7**: Results of despeckle filtering based on first order local statistics. Asymptomatic case: (a) original, (c) despeckled, (e) enlarged region marked in c) of the original, (g) enlarged region marked in c) of the despeckled image. Symptomatic case: (b) original, (d) despeckled, (f) enlarged region marked in d) of the original, (h) enlarged region marked in d) of the despeckled image. Regions were enlarged by a factor of three.

Figure 1.7 illustrates an original longitudinal asymptomatic (see Fig. 1.7a) and symptomatic image (see Fig. 1.7b) and their despeckled images (see Fig. 1.7c and Fig. 1.7d) respectively.

Figure 1.7e through Fig. 1.7h shows an enlarged window from the original and despeckled images (shown in a rectangle in Fig. 1.7c, and Fig. 1.7d).

Despite significant advances in image quality over the past decade, only minimal progress has been made towards removing coherent radiation speckle from ultrasonic B-scan images [2], [17], [115], [181], [351]. Whether speckle is viewed as image signal or noise depends largely on the imaging context [2]. Some researchers [156] discussed the possibility that a despeckle filter might destroy subtle textural differences in tissue that may indicate pathology. Therefore our approach to despeckle filtering is that we consult with the clinical experts before improving the image formation process. The procedure is intended to be both an image enhancement process, that reduces speckle and thereby aids in the accurate interpretation of these images, and a means towards performing quantitative tissue characterization. Different despeckle filtering techniques have been introduced in the literature that are based on local statistics [22], linear scaling [3], pixel homogeneity [170], geometric filtering [19], homomorphic filtering [168], anisotropic [345]-[348], speckle anisotropic diffusion [38], coherence enhancing diffusion [345], and wavelet filtering [13], [88], [107], [142], [157], which will be presented in Chapter 2.

### *1.3.2 IMT segmentation*

Segmentation of the carotid artery is an important operation before further analysis of the image can take place. IMT borders are usually traced manually by experts but it is time consuming [58], [59], and results show poor reproducibility. Several studies have been presented in the literature for the detection of the IMT [55], [64], [178], [241] in the carotid artery. The development and testing of new methods for computing the IMT will greatly help the expert in the assessment of the carotid artery disease.

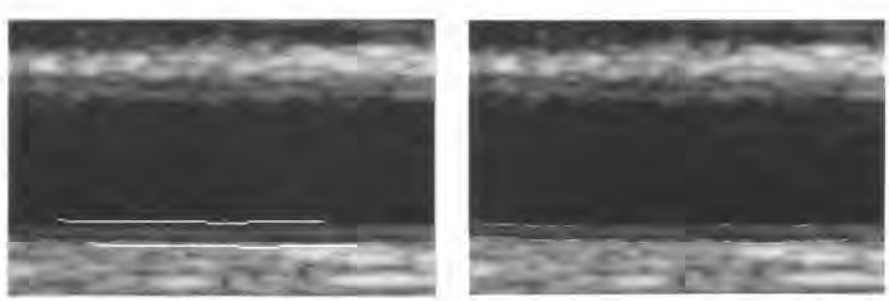

(a) (b)

**Fig. 1.8**: Ultrasound image of the carotid artery for an asymptomatic case: (a) detected initial contours for the IMT and, (b) final contours after snakes deformation. $IMT_{mean}$ = 0.86 mm, $IMT_{max}$ = 1.04 mm, $IMT_{min}$ = 0.73 mm, $IMT_{median}$ = 0.83 mm.

In the segmentation of an ultrasound image of the carotid artery, interest lies in identifying and measuring the IMT, determining the presence or absence of a plaque, and determining its contour provided that a plaque exists. The majority of the proposed segmentation methods developed, are suitable for delineating the lumen walls, and the IMT. For lumen delineation in transversal ultrasound imaging, the Hough transform (HT) was initially investigated [148] as well as to find an initial approximation of the lumen area in the left ventricle [218]. Dynamic programming [253] and cost function optimization [217] were applied for determining the optimal vessel wall. In IVUS imaging of the carotid artery for detecting the vessel wall the following methods were developed: texture based [220], morphology operators [215], optimal graph searching [72], and dynamic contour modeling [78]. Furthermore, snakes or deformable models to detect the IMT in 2D [241], and 3D [55], ultrasound images of the carotid artery were developed. These methods are based on the active contour model first introduced by Kass [243]. In general, the snake-based methods require that the initial snake contour must be specified by an expert, although recently a method that automatically detects an initial snake contour for the IMT [115], [252], [338], was introduced, as a first step towards the automated segmentation of the IMT and plaque in the carotid artery images.

Figure 1.8a shows a longitudinal ultrasound image of the CCA with computed initial contours at the far wall, of the intima and the adventitia layers based on despeckle filtering and morphology operators, whereas Fig. 1.8b shows the final result after the two contours were deformed using the Williams&Shah snakes segmentation method proposed in Chapter 3.

### *1.3.3 Plaque segmentation*

As it has been mentioned in the previous section on IMT segmentation, the segmentation of an ultrasound image of the carotid artery necessitates the need to identify and measure the IMT and determine the presence or absence of a plaque. If there is a plaque its contour should be determined. Although in ultrasound imaging, different segmentation methods were developed for IMT segmentation, no method was developed for segmenting the atherosclerotic carotid plaque in longitudinal ultrasound images.

Traditionally, X-ray angiography is used for measuring manually the percentage of stenosis of the carotid artery. However this measure may not be reliably estimated because this modality depicts only the lumen of the artery [10], [208], [322], [372]. Furthermore, X-ray angiography is not capable of visualising the vessel wall and cannot determine the size or composition of the atherosclerotic plaque [71], [93], [100], [320]. The use of ultrasound significantly helps in determining the size or composition of atherosclerotic carotid plaque.

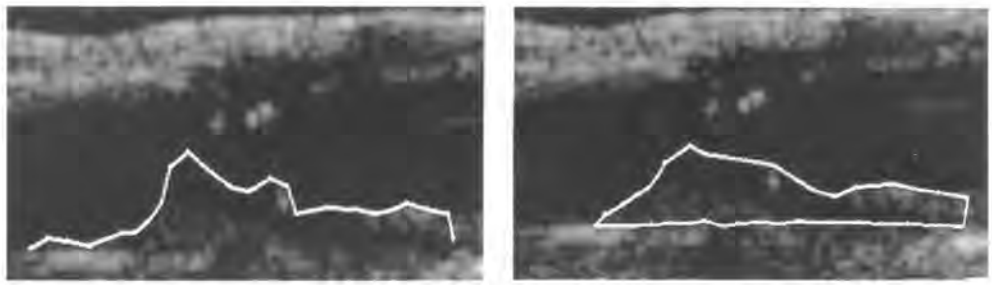

(a) (b)

**Fig. 1.9**: Ultrasound image of the carotid artery: (a) plaque initial contour estimation, and (b) the final plaque contour after the snakes deformation.

Some researchers have attempted to segment the carotid plaque from MRI, by using active contours [191], and dynamic programming [321]. Others have used a graph-searching approach to detect the wall and plaque in IVUS images [72]. Figure 1.9a shows an ultrasound image of the carotid artery, where an initial contour for the plaque was estimated, whereas in Fig. 1.9b the final plaque contour is shown after the deformation by the Williams&Shah snakes segmentation method proposed in Chapter 3.

## 1.4 Original aspects of the work

The original aspects of this work are the following:

a) *Quantitative image quality evaluation*: Investigate the usefulness of quantitative quality evaluation metrics in ultrasound imaging of the carotid artery. For this task we have evaluated the quality of ultrasound imaging of the carotid artery on two different ultrasound scanners, the HDI ATL-3000 and the HDI ATL-5000, before and after despeckle filtering, and after despeckle filtering and image normalization. Statistical and texture analysis was carried out on the above-mentioned preprocessed images and these findings were compared with the visual perception, carried out by two experts. Results showed that the normalised despeckled images were rated visually better on both scanners. Also, the texture analysis evaluation showed that the normalised despeckled images were better on both scanners.

b) *Despeckle filtering*: Develop and evaluate a number of despeckle filtering methods for the pre-processing of carotid ultrasound images. For this purpose, a total of 11 despeckle filters presented in Chapter 2, were developed based on local statistics, median filtering, linear scaling, pixel homogeneity, geometric filtering, logarithmic filtering, homomorphic filtering, anisotropic diffusion, speckle anisotropic diffusion, non-linear coherence diffusion and wavelet filtering. Despeckle filtering was evaluated on 440 (220 asymptomatic and 220 symptomatic) longitudinal ultrasound

images of the carotid artery bifurcation. Furthermore, despeckle filtering evaluation was investigated using the visual perception by two experts, statistical and texture analysis, as well as image quality evaluation metrics. Results showed that a despeckle filter based on local statistics (*lsmv*) improved the class separation between the asymptomatic and the symptomatic classes, gave only a marginal improvement in the percentage of correct classifications success rate, and improved the visual assessment by the experts. It was also found that the *lsmv* despeckle filter can be used for despeckling asymptomatic images where the expert is interested mainly in the plaque composition and texture analysis, whereas a geometric despeckle filter (*gf4d*) can be used for despeckling of symptomatic images where the expert is interested in identifying the degree of stenosis and the plaque borders.

c) *IMT snakes segmentation*: Develop and evaluate a new segmentation method to extract the IMT borders and measure the IMT from longitudinal ultrasound carotid artery images. The IMT snakes segmentation method, developed in this work is based on the Williams&Shah [124] snake and utilises an automatic initial contour estimation, so that the snake will be placed in a close proximity to the borders of interest. The initial contour estimation was performed on the ultrasound image after despeckle filtering and normalisation. Unlike classical based algorithms where experts place the initial contour manually we estimate the initial snake contour automatically using morphology operators. Segmentation was carried out on the original, despeckled, normalized and normalized despeckled images. We have tested and validated the Williams&Shah IMT snakes segmentation method on 100 images of the carotid artery based on univariate statistical analysis, correlation and regression analysis, and on visual perception by two experts. The IMT mean $\pm$ standard deviation snakes segmentation results were $0.7 \pm 0.14$ mm, $0.69 \pm 0.13$ mm, $0.67 \pm 0.13$ mm, $0.68 \pm 0.12$ mm, for the original, despeckled, normalized, and normalized despeckled images respectively. The manual $\pm$ standard deviation results for the first expert were, $0.67 \pm 0.16$ mm, $0.68 \pm 0.17$ mm, and for the second expert were, $0.65 \pm 0.18$ mm, $0.61 \pm 0.17$ mm on the original and normalized images respectively. The results showed that there was no significant difference between all the snakes segmentation measurements and the manual measurements. Furthermore snakes segmentation results were more reproducible than the manual measurements on the normalized despeckled ultrasound images.

d) *Plaque snakes segmentation*: Develop and evaluate four different plaque snakes segmentation methods on 80 ultrasound images of the carotid artery based on the Williams&Shah [124], the Balloon [333], the Lai&Chin [248], and the GVF [116] algorithms to extract the plaque borders from ultrasound longitudinal carotid artery

images. The four different plaque snakes segmentation methods, in order to find the initial plaque boundaries, utilise an automatic initial contour estimation and place it as close as possible to the borders of interest. The plaque snakes segmentation method, estimated the initial plaque contour, using the B-mode and the blood flow images. The initial contour was mapped on the original B-mode image, which was despeckled and normalized. The contour was then deformed by the snake for best fit of the plaque boundaries. We have validated the four plaque snakes segmentation methods using the manual measurements made by a vascular expert, the performance of the algorithms, and ROC (receiver operating characteristics) analysis. The plaque segmentation results showed that, the Lai&Chin segmentation method that is based on variable snake parameters, gave results closest to the manual delineation procedure, compared with the results given by the Williams&Shah, Balloon, and the GVF, snakes segmentation methods. Specifically the Lai&Chin segmentation method, gave a better true positive fraction (82.7%), and true negative fraction (80.89%), a better kappa index (80.66%), and overlap index (69.3%). Furthermore, the Lai&Chin snakes segmentation method gave the best sensitivity, R, and precision, P with 0.8270 and 0.9338 respectively. The Balloon snakes segmentation method gave the best specificity, Sp, and a goodness measure F, with 0.946 and 0.8882 respectively. The area below the ROC was 0.88, 0.85, 0.82, and 0.76 for the Lai&Chin, Balloon, Williams&Shah, and GVF snakes segmentation method respectively, with the largest area under the ROC curve obtained by the Lai&Chin snakes segmentation method.

e) *Integrated system for the despeckling and segmentation of atherosclerotic carotid images*: The proposed system should be designed, developed and implemented supporting the processing of atherosclerotic carotid plaque images based on the algorithms mentioned in a)-d). It should be simple and user-friendly, recording all processing and analysis steps carried out, illustrate to the expert the image analysis and measurements results, save the results in a database, display results of different methods and run in real time.

It should be emphasised that to the best of our knowledge no other studies carried out a comparative despeckle filtering on ultrasound imaging of the carotid artery, no other studies performed such a large scale analysis for the IMT segmentation as well as no other study performed a plaque segmentation on longitudinal ultrasound images of the carotid artery.

## 1.5 Guide to Thesis Contents

Chapter 2 introduces the theoretical concepts of the despeckle filters used in this work, where a multiplicative speckle noise model suitable for ultrasound images, is derived.

Chapter 3 presents the theoretical background of the IMT and plaque snakes segmentation method in ultrasound images of the carotid artery. A literature review of the IMT and plaque segmentation techniques is presented whereas a segmentation technique for the IMT and the plaque borders is developed using the Williams&Shah snake model [124]. The theoretical and mathematical derivation of the Williams&Shah, Balloon [333], Lai&Chin [248], and GVF [116], snakes segmentation methods, are furthermore explained. Finally a review on different snake initialization procedures used in the literature is presented.

Chapter 4 deals with the issue of image and segmentation quality evaluation in ultrasound images of the carotid artery. A number of evaluation metrics are presented for evaluating the despeckle and segmentation methods. Despeckle filtering is evaluated quantitatively using image quality evaluation metrics, and texture analysis, whereas segmentation is evaluated using the ROC curve analysis.

Chapter 5 presents the methodology of our work where the ultrasound scanners, material used, the process of image acquisition, and image normalization, is presented respectively. Furthermore, the process of generating an artificial carotid image, and the visual, and texture analysis evaluation for the despeckle filtering is presented. The protocols for the manual and the snakes segmentation for the IMT, and plaque are furthermore explained, whereas, statistical metrics are proposed for the segmentation evaluation.

Chapter 6 presents the results of our study with a comparison and discussion of the different despeckle filters. Furthermore, the segmentation results for the IMT and plaque in ultrasound images of the carotid artery are presented, using the evaluation metrics presented in Chapter 4. The evaluation of the proposed despeckle, and segmentation methods, was based on real ultrasound images of the carotid artery.

Discussion of findings of this work are reported in Chapter 7, together with a discussion of the despeckle filtering and segmentation results presented in Chapter 6. A comparison with other studies is attempted whenever possible. Based on the results obtained in this study, a short description of a proposed system is given.

The last Chapter, Chapter 8, presents the concluding remarks and gives suggestions for future work.

Five Appendices provide additional information. Appendix I presents the theory on speckle statistics. Appendix II presents procedures for optical perception evaluation. Appendix III includes the 55 texture features used in this work for texture analysis. Appendix IV describes the mathematical derivation of the snakes segmentation algorithm. Finally, Appendix V includes the publications made during this work.

# *Chapter 2*

# *Despeckle Filtering*

# CHAPTER 2: DESPECKLE FILTERING

Noise and artefacts can cause signal and image degradations for many medical image modalities. Different image modalities exhibit distinct types of degradation. Radiographs often exhibit low contrast while images formed with coherent energy, such as ultrasound, suffer from speckle noise. Image degradation can have a significant impact on image quality and thus affect human interpretation and the accuracy of computer-assisted methods. Poor image quality often makes feature extraction, analysis, recognition, and quantitative measurements problematic and unreliable. Therefore, image despeckling is a very important task, which motivated a considerable amount of research in medical imaging.

In this Chapter we introduce speckle noise as a major factor limiting the visual perception and processing of ultrasound images. A mathematical speckle model is introduced, where the statistics of speckle noise are presented, taking into consideration the log-compression of the ultrasound image, which is performed in order to match the image into the display device. Based on this speckle model, a number of despeckling techniques are derived and explained in detail. Specifically the following categories of despeckle filtering techniques are presented: local statistics, median filtering, linear scaling, homogeneity, geometric filtering, logarithmic, homomorphic, anisotropic diffusion, and wavelet filtering.

## 2.1 Introduction

Ultrasound images show a granular appearance known as speckle, which is a form of locally correlated multiplicative noise corrupting medical ultrasound imaging making visual observation and image analysis difficult [163], [164], [339]-[341]. The presence of speckle noise in ultrasound images has been documented since the early 1970's where researchers such as Goodman [163], Burckhardt [164], and Wagner [339], described its fundamentals and its statistical properties. Speckle noise is the primary factor, which limits the contrast resolution in diagnostic ultrasound imaging, thereby limiting the detectability of small, low contrast lesions and making the ultrasound images generally difficult, even for an expert to interpret [22]-[28], [163], [164], [339]. Speckle noise also limits the effective application of image processing and analysis algorithms (i.e. edge detection, segmentation) and display in 2D and volume rendering in 3D. Even expert radiologists with sufficient experience may not often draw useful conclusions from the images [87], [131], [132]. From an engineering point of view, speckle is most often considered a dominant source of noise in ultrasound imaging and therefore should be filtered out [25], [87], [107], [132], [152], [345]. For images that contain speckle, enhancing the image by removing the speckle without affecting important features is the goal.

The speckle pattern, visible as the typical light and dark spots the image is composed of, results from destructive interference of ultrasound waves scattered from different sites. The nature of speckle has been a major subject of investigation [163], [164], [167], [339]-[342], [351], [359]. When a fixed, rigid object is scanned twice under exactly the same conditions, one obtains identical speckle patterns. Although a random appearance, speckle is therefore not random in the same sense as electrical noise. However, if the same object is scanned under slightly different conditions, say with a different transducer aperture, pulse length or transducer angulation, the speckle patterns changes.

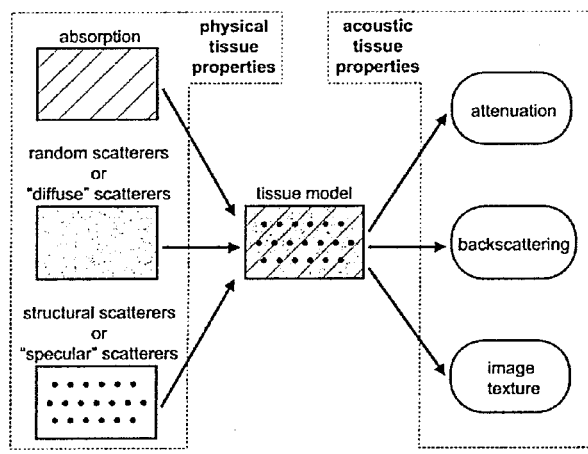


**Fig. 2.1**: The usual tissue model in ultrasound imaging, modified from [199].

The most popular model adopted in the literature to explain the effects that occur when a tissue is insonated is displayed in Fig. 2.1, where a tissue may be modeled as a sound absorbing medium containing scatterers, which scatter the sound waves [236]. These scatterers arise from inhomogeneities and structures approximately equal to or smaller in size than the wavelength of the ultrasound, such as tissue parenchyma, where there are changes in acoustic impedance over a microscopic level within the tissue. Tissue particles that are relatively small in relation to the wavelength (i.e. blood cells), and particles with differing impedance that lie very close to one another, cause scattering or speckling. Absorption of ultrasound tissue is an additional factor to scattering and refraction, responsible for pulse energy loss. The process of energy loss involving absorption, reflection, and scattering is referred to as attenuation, which increases with depth and frequency. Because higher frequency of ultrasound, results into increased absorption, the consequence is a decrease of the depth of visualisation.

Figure 2.2 illustrates the entire scattering procedure [14], [199]. Consider a transducer insonating a homogeneous medium containing four point-like scatterers, as depicted in Fig. 2.2a. These scatterers yield spherical waves that will arrive at the transducer at slightly different

times after the transmission of the ultrasound pulse. Usually the pulse envelope is approximately Gaussian as shown in Fig. 2.2b. If the pulse has a Gaussian shape then so has its spectrum. One chooses a Gaussian shape, because for a medium with linear attenuation coefficient this Gaussian shape of the spectrum is maintained while the pulse travels through the medium (although a shift of this Gaussian spectrum to lower frequencies occurs while the pulse travels through the medium, because the attenuation increases with the frequency).

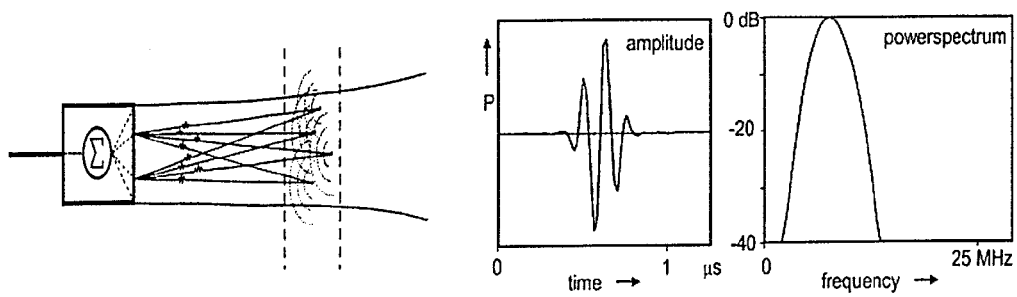


(a) (b)

**Fig. 2.2**: (a) The scattering in the sound beam, (b) one pulse (from [14]).

Upon reception of the reflected signal, the transducer produces an electrical signal (RF) that is the algebraic sum of the instantaneous sound pressures originating from the backscattered waves (four waves in Fig. 2.2a). The depth differences of the scatterers are smaller than the axial size of the resolution volume of the transducer (i.e., the pulse length). This is, in fact, the basic cause for the generation of tissue texture. The formed pattern is the so-called speckle pattern. Note, in particular, that the tissue texture resulting from this speckle pattern is in general not a true image of the histological structure of the tissue but rather an interference pattern that is mainly determined by the beam characteristics. Speckle is described as one of the more complex image noise models [163], [199], [351], it is signal dependent, non-Gaussian and spatially dependent.

In homogeneous tissue, the distribution of the scatterers throughout 3D space is assumed to be isotropic. As displayed in Fig. 2.1 one distinguishes random (or diffuse) scatterers, and structural (or specular) scatterers. The diffuse scatterers are assumed to be uniformly distributed over space. Diffuse scattering arises when there are a number of scatterers with random phase within the resolution cell of the ultrasound beam. This random nature of the location of the scatterers causes the statistical nature of the echo signals, and hence the resulting speckle pattern. Consequently, a statistical approach to its analysis seems obvious.

Other properties of the tissue that affect the ultrasound as it propagates through it are the propagation speed, the attenuation, and the backscattering. The absorption of ultrasound is caused by relaxation phenomena of biological macromolecules [354] that transfer mechanical

energy into heat. Another source of attenuation is the scattering, i.e., omni directional reflections by small inhomogeneities in the tissue. The overall attenuation is therefore the resultant of absorption and scattering, which are both frequency-dependent in such a way that the attenuation increases with frequency.

In analyzing speckle an important point to bear in mind is to make a clear distinction between the speckle as it appears in the image and the speckle in the received RF-signal. The block diagram in Fig. 2.3 explains the entire track of the RF-signal from the transducer to the screen inside the ultrasound imaging system. As set forth, the signal is subject to several transformations that severely affect its statistics. The most important of these is the log-compression of the signal, employed to reduce the dynamic range of the input signal to match the lower dynamic range of the display device. The input signal could have a dynamic range of the order of 50-70 dB whereas a typical display could have a dynamic range of the order of 20-30 dB. Such a relation is normally affected through an amplifier, which has a reducing amplification for a larger input signal.

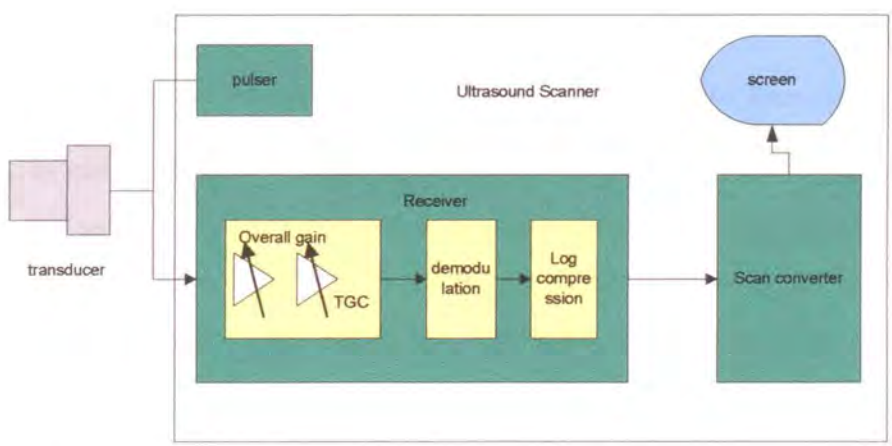


**Fig. 2.3**: The processing steps of the RF-signal inside the ultrasound scanner, modified from [156].

In addition, the expert has the possibility to adjust several machine settings manually. In Fig. 2.3 these are indicated as the slide contacts overall gain and time gain compensation (TGC). These machine settings control the amplification of the signal, the overall gain controls the overall amplification, and the TGC is a time-dependent amplification, and serves as tools for the expert to adjust the image for an optimal visual diagnosis. The TGC is adjusted by several (usually seven) slide contacts, each of which controls the gain in part of the image. For instance, if the slide contacts are placed in a vertical row, the top slide contact controls the gain in the top of the image, the bottom slide contact controls the gain in the bottom of the image, etc. This place specific gain in the image is realized by making the amplification of the signal dependent

on the exact time that the sound reflection is received. Since the place where a pixel is put on the screen is dependent on this time instant, the time dependent amplification of the received signal converts to a place dependent change in gray value of the pixels on the screen.

In the following section a speckle model, suitable for ultrasound images is derived, whereas in section 2.3 the despeckle filters derived in this work, are explained.

## 2.2 Speckle modeling in ultrasound images

The despeckle filtering methods described in this work are based on the noise model as proposed in [351], which is adopted for speckle noise in ultrasound B-mode carotid artery images. The speckle noise model may be approximated as multiplicative if the envelope signal which is received at the output of the beamformer of the ultrasound imaging system, is captured before logarithmic compression and may be defined as:

$$z_{i,j} = x_{i,j} n_{i,j} + a_{i,j}, \quad j,i \in N \tag{2.2.1}$$

where $z_{i,j}$, represents the noisy pixel in the middle of the moving window, $x_{i,j}$, represents the noise-free pixel, $n_{i,j}$, and $a_{i,j}$, represent the multiplicative and additive noise (independent of $z_{i,j}$, with mean 0), respectively, and $i, j$, are the indices of the spatial locations that belong in the 2D space of real numbers, $i, j \in \Re^2$. This model is particularly suitable for our purpose, as it can be applied on the images as displayed by the ultrasound machine rather than the envelope detected echo signal [271], [345], [351]. Despeckling consists in estimating the true intensity of $x_{i,j}$, as a function of the intensity of the pixel $z_{i,j}$, and some local statistics calculated on a neighbourhood of this pixel. Wagner et al. [339] has shown that the histogram of amplitudes within the resolution cells of the envelope detected RF-signal backscattered from a uniform area with a sufficiently high scatterer density has a Rayleigh distribution with $\mu$ proportional to the $\sigma$, $(\mu/\sigma = 1.91)$. This implies that speckle could be modelled as multiplicative noise. However, the signal processing stages inside the scanner, (mainly the logarithmic compression) in order to adjust the large echo dynamic range (50-70dB) to the 8-bits of the digitization in the scan converter, modify the statistics of the original signal. The model in (2.2.1) has been shown to be valid for images as displayed by the ultrasound scanner in studies [341], [345], [355], [360]. In particular it should be noted, that speckle is no longer multiplicative in the sense that on homogeneous regions, where $x_{i,j}$, can be assumed constant, the mean is proportional to the variance $(\mu \approx \sigma^2)$, rather than the standard deviation $(\mu \approx \sigma)$, [141], [345], [349], [351]. In this respect, the speckle index, C, which will be presented in Chapter 4 (see (4.9)), will be for the log-compressed ultrasound images, $C = \sigma^2 / \mu$.

The variance of the speckle noise, $\sigma_n^2$, may be calculated from the logarithmically compressed image, by computing the average noise variance over a number of windows with dimensions considerable larger than the filtering window. In each window the noise variance is computed as [351]:

$$\sigma_n^2 = \sum_{i=1}^{p} \sigma_p^2 / \overline{g}_p \tag{2.2.2}$$

where $\sigma_p{}^2$, and $\overline{g}_p$, are the variance and the mean of the noise in the selected windows respectively and $p$, is the index covering all windows in the whole image [345], [351]. We may therefore calculate the variance of the speckle noise, $\sigma_n^2$, from the noise image characteristics, namely from $\overline{g}_p$, and $\sigma_p{}^2$, over the image. The speckle noise variance, $\sigma_n^2$, will be used in some of the despeckle filters which are introduced in the following Chapters.

As shown earlier, nonlinear processing such as logarithmic compression, employed on ultrasound echo images, affects the speckle statistics in such a way that the local mean becomes proportional to the local variance rather than the standard deviation. More specifically, logarithmic compression affects the high intensity tail of the Rayleigh and Rician PDFs more than the low intensity part. As a result the speckle noise becomes very close to white Gaussian noise corresponding to the uncompressed Rayleigh signal [351]. The envelope at the output of the beamformer before logarithmic compression, may thus be approximated as shown in (2.2.1).

Since the effect of additive noise, such as sensor noise, is considerably smaller and less significant compared with that of the multiplicative noise component [141], [345] such as:

$$(\|\alpha_{i,j}\|^2 << \|n_{i,j}\|^2) \tag{2.2.3}$$

then the filters utilizing first order statistics such as the variance and the mean of the neighborhood, may be derived from (2.2.1) with the following multiplicative model as:

$$z_{i,j} \approx x_{i,j} n_{i,j}\,. \tag{2.2.4}$$

The logarithmic amplification transforms the model in (2.2.4) into the classical signal in additive noise form as:

$$\log(z_{i,j}) = \log(x_{i,j}) + \log(n_{i,j})\,, \tag{2.2.5a}$$

$$g_{i,j} = f_{i,j} + nl_{i,j}\,. \tag{2.2.5b}$$

For the rest of the work the term $\log(z_{i,j})$, which is the observed pixel on the ultrasound image display after logarithmic compression, is denoted as $g_{i,j}$, and the terms $\log(x_{i,j})$, and

$\log(n_{i,j})$, which are the noise free pixel and noise component after logarithmic compression, as $f_{i,j}$, and $nl_{i,j}$, respectively (see Eq. 2.2.5b).

## 2.3 Despeckle filters

Despeckling is always a trade-off between noise suppression and loss of information, something that experts are very concerned about. It is therefore attractive to keep as much of important information as possible. Despeckle filtering can be used as a pre-processing step for image segmentation [115], or image registration [81], techniques. By suppressing the speckle the performance of these techniques can be improved.

The despeckle filters originated from the Synthetic Aperture Radar (SAR) community [18], [22], [31]-[36], [107]. These techniques have later been applied to ultrasound imaging since the early 1980's [167], which may be described with the same statistical model as the one describing the SAR images. The most widely used filters in SAR and ultrasound imaging include the Frost [27], [28], Lee [22]-[26], and the Kuan [29], [30].

Most adaptive filters only use local statistical information related to the central pixel to be filtered [2], [21]-[26], [115]. Some additional information may be used from the despeckle window (see next subsection) to improve despeckling, by utilising the higher order statistics of the image. Many adaptive despeckling methods have been proposed, such as the Lee filter [22]-[26], Frost [27], [28], Kuan [29], [30], and Lopes [31], [32]. Furthermore, the Gaussian filter function [84] has been used for despeckling but it was shown [83], that this form of filtering is not suitable for speckle noise, as it does not take into consideration the true positions of object boundaries. However, the full removal of speckle noise without losing any information in ultrasound images is still a long way off. When additionally edges are present in the filtering window, the central pixel gray level replaced by the information from all its neighbourhood pixels will not be correct. Lee has therefore introduced [25] an edge detector, which was implemented in his old algorithm version [22].

Since the early 1980's, various researchers have presented the progress that has been made in quantitative ultrasound imaging and reported techniques that have been applied on ultrasound images for despeckling [167]. The majority of the despeckling filtering techniques presented in the literature, have certain limitations that can be briefly summarised as follows:

a) They are sensitive to the size and shape of the window [2], [23], [30], [38], [115], [345]. The use of different window sizes will greatly affect the quality of the processed images. If the window is too large over smoothing will occur, subtle details of the image will be lost in the filtering process and edges will be blurred. A small window will decrease the smoothing capability of the filter and will not reduce

speckle noise thus making the filter not effective. In homogenous areas, the larger the window size, the more efficient is the filter in reducing the speckle noise. In heterogeneous areas the smaller the window size, the more it is possible to keep subtle image details unchanged. Our experiments showed that a 7x7 window size is a fairly good choice. The images presented in this work have been processed either by 7x7 or by 5x5 pixel windows.

b) Some of the despeckling methods, based on window approaches [2], [19], [22], [131], require thresholds to be used in the filtering process, which have to be estimated empirically. The inappropriate choice of a threshold may lead to averaging filtering and noisy boundaries from leaving the sharp features unfiltered [19], [22], [131].

c) Most of the existing despeckle filters do not enhance edges but they only inhibit smoothing near the edges. When an edge is contained in the filtering window, the coefficient of variation will be high and smoothing will be inhibited. Therefore, speckle in the neighbourhood of an edge will remain after filtering. They are not directional in the sense that in the presence of an edge, all smoothing is precluded. Instead of inhibiting smoothing in directions perpendicular to the edge, smoothing in directions parallel to the edge is allowed.

d) Different evaluation criteria for evaluating the performance of despeckle filtering were used in different studies. Although most of the studies used quantitative criteria like the MSE and the speckle index, C, there are additional quantitative criteria, like texture analysis and classification, image quality evaluation metrics, and experts assessment that could be investigated (see Chapter 4).

Speckle reduction techniques that have been proposed in the literature and have also been used in our study, are shown in Table 2.1 and are summarized under the following categories: local statistics, median filtering, linear scaling, homogeneity, geometric, logarithmic, homomorphic, anisotropic diffusion, and wavelet filtering. These filters are presented in greater detail in the next section. Some of the local statistic filters are the Lee [22]-[26], the Frost [27], [28] and the Kuan [29], [30] filters. The Lee and Kuan filters have the same structure, where the Kuan is a generalization of the Lee filter.

Both filters form an output image by computing a linear combination of the central pixel intensity in a filter window with the average intensity of the window and a coefficient of variation inside the moving window. Kuan considered a multiplicative speckle model and designed a linear filter, based on the minimum-mean-square error (MMSE) criterion, optimal when the intensity image is Gaussian distributed. The Lee [22] MMSE filter was a particular case of the Kuan filter based on a linear approximation made for the multiplicative noise model.

The Frost [27] makes a balance between the averaging and the all-pass filters. It was designed as an adaptive Wiener filter that assumed an autoregressive exponential model for the image.

TABLE 2.1
AN OVERVIEW OF DESPECKLE FILTERING TECHNIQUES.

| Speckle Reduction Techniques | Investigator | Method | Filter Name |
|---|---|---|---|
| Local Statistics | [2], [21]-[34] | Moving window utilizing local statistics: a) Mean ($\mu$), variance ($\sigma^2$). | *lsmvminmax, lsmv, lemva, lsmv1d, lsmv_lee* |
| | [2], [21], [131] | b) Mean, $\sigma^2$, $\sigma^3$, $\sigma^4$. | *lsmvske1d, lsmvsk2d* |
| | [2], [165] | c) Homogeneous mask area filters. | *lsminsc,* |
| | [2], [323] | d) 1-D $\mu$, and $\sigma^2$ filter. | *lsminv1d,* |
| | [3], [8], [168] | e) Wiener filtering. | *wiener* |
| Median Filtering | [3], [8], [168] | Median filtering | *median* |
| Linear Scaling | [2] | Linear scaling of the gray level values. | *ls, ca, lecasort* |
| Homogeneity | [2], [132] | Based on the most homogeneous neighbourhood around each image pixel. | *homog* |
| Geometric | [19], [162] | Non-linear iterative filter. | *gf4d, gfminmax* |
| Logarithmic | [9], [324] | Image is logarithmically transformed then filtered for suppressing additive noise (wiener or median [21]). Image is then exponentially back transformed. | *lslog* |
| Homomorphic | [168], [324], [325] | The idea is similar to the logarithmic point operations used in histogram improvement: de-emphasize the dominant bright image pixels. | *homo* |
| Anisotropic Diffusion | [324]-[326], [167] | Non-linear filtering technique for simultaneously performing contrast enhancement and noise reduction. | *ad, lsmedcd,* |
| | [27], [38] | Exponential damp kernel filters utilising diffusion. | *lsmedc* |
| | [38], [345] | Anisotropic diffusion based on the coefficient of variation. | *adsr* |
| | | Coherence enhancing diffusion. | *nldif* |
| Wavelet | [107], [141], [152], [157], [324] | Realistic distribution of the wavelet coefficients. Only the useful wavelet coefficients are utilized. | *waveltc* |

In the linear scaling group the gray level values are linearly scaled to despeckle the image [131]. In the homogeneity group the despeckling is based on the most homogeneous neighbourhood around each image pixel [132]. Geometric filters [19], [162], are based on non-linear iterative algorithms, which increment or decrement the pixel values in a neighbourhood

based upon their relative values. The method of homomorphic filtering [168], [325], is similar to the logarithmic point operation used in histogram improvement, where dominant bright pixels are de-emphasised. In the homomorphic filtering the image is logarithmically transformed, the FFT of the image is calculated, then despeckled, the inverse FFT is calculated, and finally exponentially transformed back.

Some other despeckle filtering methods, such as anisotropic diffusion [37], [38], [326], [344]-[347], speckle reducing anisotropic diffusion [38], and coherence anisotropic diffusion [345], presented recently in the literature, are non-linear filtering techniques for simultaneously performing contrast enhancement and noise reduction by utilising the coefficient of variation [38]. Furthermore, in the wavelet category, filters for suppressing the speckle noise by making use of a realistic distribution of the wavelet coefficients [107], [141], [157], [348]-[350], where only the useful wavelet coefficients are utilised, were documented. Wavelet methods involve a pre-processing step consisting of a logarithmic transform to separate the noise from the original image. Then different wavelet shrinkage approaches are employed, based on Donoho's work [350].

Some other researchers have tried in the past to despeckle SAR images by averaging of uncorrelated images obtained from different spatial positions [343]. These temporal averaging and multi-frame methods aimed to increase the SNR by generating multiple uncorrelated images that are summed incoherently to reduce speckle [131], [324]. Despite being simple and fast, these approaches suffer from two limitations. First, in order to produce uncorrelated ultrasound images, the transducer has to be translated at least by about half its element width for each of the generated frames [164]. Second, temporal averaging based on transducer movement causes the loss of small details such as small vessels and texture patterns because of blurring. For the above reasons this procedure has been proved to be not suitable for despeckle filtering. It is most suitable for additive noise reduction [2], [12]. Another disadvantage of this method is that multiple images from the same object are required [19], [21], [23], [26]. Other researchers applied their techniques on ultrasound images of the kidney [141], echocardiograms [348], heart [345], abdomen [345], pig heart [349], liver [271], SAR images [16], [28], [30], [107], [152], [159], real world [29], [347], and artificial images [19], [285], [345], [349]. They used statistical measures like the mean, variance, median, C, MSE, image contrast, and visual perception evaluation made by experts, to evaluate their techniques. They compared their despeckling techniques with the Lee filter [22], homomorphic filtering [325], median filter [170], and diffusion filtering [346], [347]. A detailed discussion on different despeckle filtering methods will be presented in Chapter 7.

In the next section, we present the theoretical background of the despeckle filters presented in this dissertation whereas in Chapter 6, we compare all despeckle filters quantitatively. To

achieve such evaluation, we make use of an artificial carotid image, (see Fig. 6.3a) [261], [301], and real ultrasound images of the carotid artery (see Fig. 6.5a).

### *2.3.1 Local statistics filters*

Most of the techniques for speckle reduction proposed in the literature use local statistics. Their working principle may be described by a weighted average calculation using sub region statistics to estimate statistical measures over pixel windows varying from 3x3 up to 15x15. All these techniques assume that the speckle noise model has a multiplicative form [2], [19], [21]-[34], [345] as in (2.2.4)

#### *2.3.1.1 First order statistics filtering (lsmv, lsmv_lee, lsmvminmax, lemva, wiener)*

The filters utilizing first order statistics, such as the variance and the mean of the neighborhood may be described with the model as in (2.2.5). By taking in consideration (2.2.1)-(2.2.5), then the despeckle filters in this class may be traced back to the following equation [21], [27]-[30], [38], [131], [132]:

$$f_{i,j} = \overline{g} + k_{i,j}(g_{i,j} - \overline{g}) \tag{2.3.1}$$

where $f_{i,j}$, is the estimated noise free pixel, $g_{i,j}$, is the noisy pixel value in the moving window, $\overline{g}$, is the local mean value of a $N_1 x N_2$ region surrounding and including pixel $g_{i,j}$, $k_{i,j}$, is a weighting factor with $k \in [0..1]$, and $i, j$, are the absolute pixel coordinates. The factor $k_{i,j}$, is a function of the local statistics in a moving window. It can be found in the literature [2], [21]-[26], [29], and may be derived in different forms such that:

$$k_{i,j} = (1 - \overline{g}^2\sigma^2)/(\sigma^2(1+\sigma_n^2)) \tag{2.3.2a}$$

$$k_{i,j} = \sigma^2/(\overline{g}^2\sigma_n^2 + \sigma^2) \tag{2.3.2b}$$

$$k_{i,j} = (\sigma^2 - \overline{g}^2\sigma_n^2)/(\sigma^2 + \overline{g}^2\sigma_n^2) \tag{2.3.2c}$$

$$k_{i,j} = (\sigma^2 - \overline{g}^2\sigma_n^2)/(\sigma^2 + \sigma^2\sigma_n^2) \tag{2.3.2d}$$

$$k_{i,j} = (\sigma_n{}^2 - \sigma^2)/(\sigma + \overline{g}) \tag{2.3.2e}$$

$$k_{i,j} = (\overline{g}^2 - \sigma_n^2\overline{g}^2)/(g_{i,j} - \overline{g})^2 \tag{2.3.2f}$$

$$k_{i,j} = (1 + \sigma_n^2 - g_{\max})/(g_{\max} + g_{\min}) \tag{2.3.2g}$$

where $g_{\max}$, and $g_{\min}$, in (2.3.2g), are the maximum and the minimum gray level values from the whole image, and

$$k_{i,j} = (\sigma^2 - \sigma_n^2)/\sigma^2 . \quad (2.3.2h)$$

The *lsmv* despeckle filter uses the equations (2.3.2a)-(2.3.2c), (2.3.2e), *lemva* (2.3.2d), *lsmv_lee* (2.3.2f), *lsmvminmax* (2.3.2g), and *wiener* (2.3.2h), respectively. The values $\sigma^2$, and $\sigma_n^2$, are the variance in the moving window and the variance of the noise in the whole image respectively. The noise variance $\sigma_n^2$, may be calculated for the logarithmically compressed image, with (2.2.2). If the value of $k_{i,j}$, with $i, j$, the pixel coordinates in a moving window, is 1 (in edge areas) this will result to an unchanged pixel, however a value of 0 (in uniform areas) replaces the actual pixel by the local average $\overline{g}$, over a small region of interest. Equation (2.3.1) is applicable both for additive and multiplicative noise by using different calculations of $k_{i,j}$, as shown in (2.3.2a)-(2.3.2h) and it is based on the Lee filter [22]-[26]. The filter *wiener* uses a pixel-wise adaptive Wiener method [3], [8], [168], and is implemented as given in (2.3.1), with the weighting factor as shown in (2.3.2h). For all despeckle filters in this category the moving window size was 5x5.

*2.3.1.2 Local statistics filtering with higher moments (lsmvske1d, lsmvsk2d)*

As discussed earlier many of the despeckle filters proposed in the literature suffer from smoothing effects in edge areas. Because of their statistical working principle, the edges may be better detected by incorporating higher statistical variance moments (variance, skewness, kurtosis) [21], calculated from the local moving window. The variance in every window, $window_variance$, may thus be described as a function of the variance, $\sigma^2$, skewness, $\sigma^3$, and kurtosis, $\sigma^4$, in the sliding moving local window, and is calculated for the filter *lsmvske1d* as:

$$window_variance = (c_2\sigma^2 + c_3\sigma^3 + c_4\sigma^4)/(c_2 + c_3 + c_4) \quad (2.3.3)$$

The constants $c_2$, $c_3$, $c_4$, in (2.3.3) may be calculated using [2], [21], [131], [132]:

$$R = 1 - \frac{1}{1+\sigma^2} \quad (2.3.4)$$

which is the smoothness of the image [8], [9]. Specifically, the constants, $c_2$, $c_3$, $c_4$, are calculated, by replacing, $\sigma^2$, in (2.3.4), with the variance, $\sigma^2$, the skewness, $\sigma^3$, and the kurtosis, $\sigma^4$, in the moving pixel window respectively. The higher moments are each, weighted with a factor, $c_2$, $c_3$, $c_4$, which receives values, $0 < c < 1$. Equation (2.3.4), will be applied in areas where:

$$c_3\sigma^3 \le c_2\sigma^2 \le c_4\sigma^4. \tag{2.3.5}$$

In other areas where (2.3.5) is not valid, the window variance will be calculated as:

$$window_variance = (c_2\sigma^2 + c_4\sigma^4)/(c_2 + c_4). \tag{2.3.6}$$

The final value for the $window_variance$, will be used to replace the variance, $\sigma^2$, for calculating the coefficient of variation in (2.3.2b). The *lsmvske1d* despeckle filter operates in the 1D direction [21], [131], where the introduction of the higher moments in the filtering process should preserve the edges and should not smooth the image in areas with strong pixel variations. The $window_variance$ in (2.3.3), can be interpreted as a generalized moment weighting factor with the weighting coefficients $c_2$, $c_3$, $c_4$. The moving window size for the *lsmvske1d* filter was 5x5 and its operation is shown in Fig. 2.4b.

The *lsmvsk2d* [21], [131] is the 2D realization of the *lsmvske1d* utilizing the higher statistical moments, $\sigma^3$, and $\sigma^4$ of the image in a 5x5 pixel moving window.

*2.3.1.3 Homogeneous mask area filtering (lsminv, lsminsc, lsminv1d)*

The *lsminv* is a 2D filter operating in a 5x5 pixel neighbourhood by searching for the most homogenous neighbourhood area around each pixel, using 3x3 subset windows [2], [327], as shown in Fig. 2.4a. The middle pixel of the 5x5 neighbourhood is then substituted with the average gray level of the 3x3 mask with the lowest variance. The window with the lowest variance is the most homogenous semi-window, which does not contain any edge.

The *lsminv1d* [2] is a 1D filter and operates by calculating the mean and the variance of all rows and columns in a 5x5 pixel neighbourhood as shown in Fig. 2.4b. It is the 1D realization of the *lsminv* filter. The middle pixel in the window will be substituted with the average gray level values of the rows with the smallest variance.

Both filters *lsminv* and *lsminv1d* may be used for despeckle filtering; however, the use of sub windows is computationally very time consuming. The operation of the two despeckle filters shown in Fig. 2.4, may be described as follows:

a) Rotate a mask around the middle pixel of the window.

b) Detect the position of the mask for which the variance of the gray level is minimum.

c) Assign the average gray level of the mask at the selected position to the middle point.

d) Apply steps a) to c) to all pixels in the image.

e) Iterate the above process until the gray levels of almost all pixels in the image do not change.

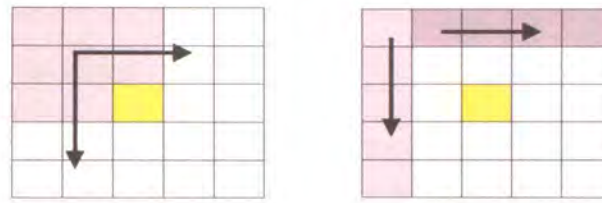

(a) (b)

**Fig. 2.4**: Schematical operation of the filters: (a) *lsmv* and (b) *lsminv1d* respectively.

The *lsminsc* is a 2D filter operating in a 5x5 pixel neighbourhood by searching for the most homogenous neighbourhood area around each pixel, using a 3x3 subset window [165] as shown in Fig. 2.4. The middle pixel of the 5x5 neighbourhood is substituted with the average gray level of the 3x3 mask with the smallest speckle index, C, where C for log-compressed images is given by, $C = \sigma_s^2 / \overline{g}_s$ (see also 4.9), where $\sigma_s^2$, and $\overline{g}_s$, represents the variance and mean of the 3x3 window. The window with the smallest C is the most homogenous semi-window, which presumably, does not contain any edge. The filter is applied iteratively until the gray levels of almost all pixels in the image do not change.

The operation of the *lsminsc* filter, may be described as follows (see also Fig. 2.4a):

a) Rotate a mask around the middle pixel of the window.

b) Detect the position of the mask for which C of the gray level is minimum.

c) Give the average gray level of the mask at the selected position to the middle pixel.

d) Apply steps a) to c) to all pixels in the image.

e) Iterate the above process until the gray levels of almost all points in the image do not change.

*2.3.1.4 Local statistics 1D filtering (lsmv1d)*

The 1D filter *lsmv1d*, is applied in four different directions in the whole image, namely in the horizontal, the vertical and the two diagonal directions [2], [323], where in the horizontal direction the filter is applied to the whole image. The output image of the horizontal direction is the input to the vertical direction. The output image of the vertical direction is the input image of the first diagonal direction and so forth. The disadvantage of this filter is that some small details of the edges will be blurred after filtering, but a significantly strong noise component is filtered away. If we consider the operation that is being applied in a 2D image as $f_{i,j} = T[g_{i,j}]$, then the operation that is being applied from the 1D filter in the image in four different directions will be described as, $f_{i,j} = T_{135°}[T_{45°}[T_{90°}[T_{0°}[g_{i,j}]]]]$, where the output image in each

direction is given by (2.3.1) with the coefficient of variation in (2.3.2h). The moving window was 5x5 pixels.

### *2.3.2 Median filtering (median)*

The filter *median* [3], [8], [168], [285] is a simple nonlinear operator and replaces the middle pixel in the window with the median value of its neighbours. The moving window was 7x7 pixels.

### *2.3.3 Linear scaling filtering (ca, lecasort, ls)*

The *ca* filter despeckles the image through linear scaling of the gray level values [2]. In a window of 5x5 pixels, compute the mean of all pixels whose difference in the gray level with the intensity $g_{i,j}$, (middle pixel in the window), is lower or equal to a given threshold $\vartheta$. Assign this value to the gray level $g_{i,j}$, with $\vartheta = \alpha * g_{\max}$, where $g_{\max}$, is the maximum gray level of the image and $\alpha = [0,1]$. Best results were obtained with $\alpha = 0.1$.

The *lecasort* filter takes $k$ points of a pixel neighbourhood, which are closest to the gray level of the image at point $g_{i,j}$, (middle point in window) including $g_{i,j}$, itself [2]. It then assigns the mean value of these points to the pixel $g_{i,j}$. (Usually N=9 in a 3x3 window, where k=6).

The *ls* filter, scales the pixel intensities by finding the maximum, $g_{\max}$, and the minimum, $g_{\min}$, gray level values in every moving window and then replaces the middle pixel with:

$$f_{i,j} = \frac{g_{\max} + g_{\min}}{2}. \tag{2.3.7}$$

### *2.3.4 Maximum homogeneity over a pixel neighbourhood filtering (homog)*

The filter *homog* is based on an estimation of the most homogeneous neighbourhood around each pixel [2], [165], [170]. It operates in a 7x7 moving window where the output image is formed by:

$$f_{i,j} = (c_{i,j} g_{i,j}) / \sum_{i,j} c_{i,j}, \text{ with } c_{i,j} = 1 \text{ if } (1-2\sigma_n)\bar{g} \le g_{i,j} \le (1+2\sigma_n)\bar{g} \tag{2.3.8}$$

$$\text{otherwise } c_{i,j} = 0 \tag{2.3.9}$$

The *homog* filter does not require any parameters or thresholds to be tuned, thus making the filter suitable for automatic interpretation.

### *2.3.5 Geometric filtering (gf4d, gfminmax)*

The geometric despeckle filter *gf4d,* works by passing an image through a speckle-removing filter, which uses the complementary hulling technique [19], [162], (raising pixels that are darker than their surrounding neighbours, then complementarily lowering pixels that are brighter than their surrounding neighbours) to reduce the speckle index, C, of that image. The filter uses a non-linear noise reduction technique, which compares the intensity of each pixel in an image with those of its 8 nearest neighbours (3x3 neighbourhood) and, based upon the relative values, increments or decrements the value of the pixel in question such that it becomes more representative of its surroundings. The filtering process involves a series of pair wise operations in which the value of the middle pixel within each neighbourhood window is compared, in turn, with each set of neighbours (N-ST, E-W, NW-STE, NE-STW, see Fig. 2.5) in a search for intensity spikes.

Suppose that the three consecutive pixels (*e.g.* on a N-ST column) that are being examined are $a$, $b$, $c$ (see Fig. 2.5). The operation of the geometric filter *gf4d* may be described with Fig. 2.5 and has the following form:

a) Select direction and assign pixel values. Select the direction be NST and the corresponding three consecutive pixels be $a$, $b$, $c$ (see Fig. 2.5a and b).

b) Carry out central pixel adjustments. Do the following intensity adjustments (see Fig. 2.5b)

$$\begin{aligned}
&\text{if } a \geq b+2 \text{ then } b = b+1,\\
&\text{if } a \succ b \text{ and } b \leq c \text{ then } b = b+1,\\
&\text{if } c \succ b \text{ and } b \leq a \text{ then } b = b+1,\\
&\text{if } c \geq b+2 \text{ then } b = b+1,\\
&\text{if } a \leq b-2 \text{ then } b = b-1,\\
&\text{if } a \prec b \text{ and } b \geq c \text{ then } b = b-1,\\
&\text{if } c \prec b \text{ and } b \geq a \text{ then } b = b-1,\\
&\text{if } c \leq b-2 \text{ then } b = b-1.
\end{aligned} \tag{2.3.10}$$

c) Repeat steps 1 and 2 for west-east (WE), west-north to south-east (WN-STE), and north-east to west-south (NE-WST) directions.

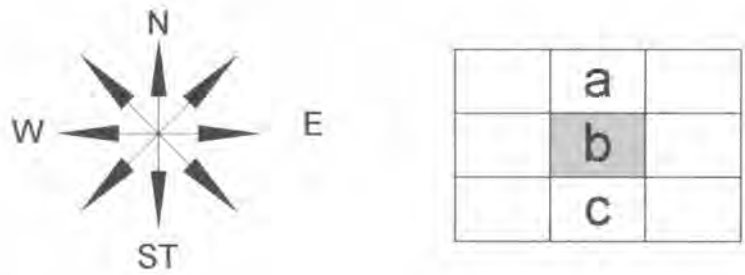


(a) (b)

**Fig. 2.5**: (a) Directions of implementation of the *gf4d* geometric filter, (b) pixels selected for the NS direction (intensity of central pixel b is adjusted based on the values of intensities of pixels a, b, and c).

The above procedure is applied in all four directions of a pixel neighbourhood, namely in the west-east (WE) direction, north to south (NST), west-north to south-east (WN-STE) and north-east to west-south direction (NE to WST). The advantage in geometric filtering is that the statistics of the noise are not required, thus making the filter applicable to a wide range of images.

The *gfminmax* is a non-linear despeckle filter initially used for SAR filtering [2], where the filtering is performed by averaging [19]. Pixels in the 7x7-moving window are grouped into two groups, according to their intensity level by defining a threshold as:

$$Threshold = \frac{g_{\max}}{g_{\min}}. \tag{2.3.11}$$

where $g_{\max}$, and $g_{\min}$ are the maximum and minimum gray level values in the moving window respectively. The gray-values in the window, which are greater than the *Threshold* in (2.3.11) are selected, and the central pixel in the window is replaced by their mean value. The speckle noise is modelled in this case with the $\chi^2$–PDF and can be approximated for N=1 images with the exponential PDF [3].

### *2.3.6 Homomorphic filtering (homo) and logarithmic point operation filtering (lslog)*

Homomorphic filtering is a method which converts multiplicative noise into additive noise by applying a low pass filter for additive noise reduction to reduce noise and has been used due to its easy and effective implementation [168], [325]. The idea is similar to the logarithmic point operations used in histogram improvement by de-emphasizing the dominant bright image pixels. The *homo* filter performs homomorphic filtering by calculating the FFT of the logarithmic compressed image, $g_{i,j}$, applying a denoising homomorphic filter function $H(.)$,

and then performing the inverse FFT of the image [229] to form the despeckled image $f_{i,j}$. The homomorphic filter function $H(.)$ maybe constructed either using a band-pass Butterworth or a high-boost Butterworth filter. In this study, a high-boost Butterworth filter was used for the homomorphic function $H(.)$ with [229]:

$$H(u,v) = \gamma_L + \frac{\gamma_H}{1+(D_0 / D(u,v))^2} \tag{2.3.12}$$

and

$$D(u,v) = \sqrt{(u-N/2)^2 + (v-N/2)^2} \tag{2.3.13}$$

where $D_0 = 1.8$ is the cut of frequency of the filter, $\gamma_L = 0.4$, $\gamma_H = 0.6$ are the gains for the low and high frequencies, $u$, $v$ are the spatial coordinates of the frequency transformed image, and N the dimensions of the image in the $u, v$, space respectively.

The homomorphic filtering is effective mainly on images with relatively low contrast [122], and there are researchers [196] that reported undesirable artefacts on MRI with this approach.

The *lslog* filter [324], assumes a multiplicative white noise model and transforms the multiplicative to additive noise by using the logarithm of the image. At the beginning, the logarithm of the noise image is calculated, the median filter for additive noise [285] is then applied on the image, and the resulting image is transformed exponentially back to its initial form. This type of filtering refers to a technique [37], [123] of pre-processing the observed image by transforming multiplicative noise into additive noise form, using some linear memory less operator.

### *2.3.7 Diffusion filtering*

Diffusion filters remove noise from an image by modifying the image via solving a partial differential equation (PDE). Despeckling is carried out depending on the image edges and their directions. Anisotropic diffusion is an efficient nonlinear technique for simultaneously performing contrast enhancement and noise reduction [37], [38], [324], [326], [344]-[347], without requiring any information from the image power spectrum. It may thus directly be applied to logarithmic compressed images. Consider applying the isotropic diffusion equation given by $dg_{i,j,t}/dt = div(cd\nabla g)$, using the original noisy image $g_{i,j,t=0}$, as the initial condition, where $g_{i,j,t=0}$, is an image in the continuous domain, $i, j$, specifies spatial position, $t$ is an artificial time parameter, $cd$, is the diffusion constant, and $\nabla g$, is the image gradient.

In the next Sections we present anisotropic diffusion (*ad*), speckle anisotropic diffusion (*adsr*), and coherent nonlinear anisotropic diffusion (*nldif*). Anisotropic diffusion filters usually require many iteration steps compared with the local statistic filters.

*2.3.7.1 Anisotropic diffusion filtering (ad)*

Perona and Malik [347] replaced the classical isotropic diffusion equation, as described above, by the introduction of a function, $cd_{i,j,t} = f(|\nabla g|)$, with:

$$\frac{dg_{i,j,t}}{dt} = div\left[cd_{i,j,t}\nabla g_{i,j,t}\right] = \left[\frac{d}{di}cd_{i,j,t}\frac{d}{di}g_{i,j,t}\right] + \left[\frac{d}{dj}cd_{i,j,t}\frac{d}{dj}g_{i,j,t}\right] \tag{2.3.14}$$

where $|\nabla g|$, is the gradient magnitude, and $cd(|\nabla g|)$, is an edge stopping function, which is chosen to satisfy $cd \to 0$, when $|\nabla g| \to \infty$, so that the diffusion is stopped across edges. This function, called the diffusion coefficient, $cd(|\nabla g|)$, which is a monotonically decreasing function of the gradient magnitude, $|\nabla g|$, yields intra-region smoothing not inter-region smoothing [167], [326], [344], [346], [347], by stopping diffusion at the image edges. It increases smoothing parallel to the edge and stops smoothing perpendicular to the edge, as the highest gradient values are perpendicular to the edge and dilated across edges. In anisotropic diffusion the diffusion coefficient is allowed to vary according to the local image gradient. The choice of $cd(|\nabla g|)$, can greatly affect the extent to which discontinuities are preserved. For example if, $cd(|\nabla g|)$, is constant at all locations, then smoothing progresses in an isotropic manner. If $cd(|\nabla g|)$, is allowed to vary according to the local image gradient, then we have anisotropic diffusion. A basic anisotropic PDE is given in (2.3.14). Two different diffusion coefficients were proposed in [347] and derived in [346] as follows:

$$cd(|\nabla g|) = \frac{1}{1+(|\nabla g_{i,j}|/K)^2}, \tag{2.3.15}$$

and

$$cd(|\nabla g|) = \frac{2|\nabla g_{i,j}|}{2+(|\nabla g_{i,j}|/K_1)^2} \tag{2.3.16}$$

where K in (2.3.15) is a positive gradient threshold parameter, known as diffusion or flow constant, and $K_1^2 = K^2/2$ for (2.3.16) [326], [346]. In this study the diffusion coefficient in (2.3.15) was used, which was found to perform better in the carotid artery ultrasound images.

A discrete formulation of the anisotropic diffusion in (2.3.14) is given by [38], [326], [346], [347]:

$$\frac{dg_{i,j}}{dt} = \frac{\lambda_d}{|\eta_s|}\left\{cd_{i+1,j,t}\left[g_{i+1,j} - g_{i,j}\right] + cd_{i-1,j,t}\left[g_{i-1,j} - g_{i,j}\right] + cd_{i,j+1,t}\left[g_{i,j+1} - g_{i,j}\right] + cd_{i,j-1,t}\left[g_{i,j-1} - g_{i,j}\right]\right\} \tag{2.3.17 a}$$

where the new pixel gray value, $f_{i,j}$, at location $i, j$ is:

$$f_{i,j} = g_{i,j} + \frac{1}{4}\frac{dg_{i,j}}{dt}, \tag{2.3.17 b}$$

where $cd_{i+1,j,t}, cd_{i-1,j,t}$, $cd_{i,j+1,t}$, and $cd_{i,j-1,t}$, are the diffusion coefficients for the west, east, north and south pixel directions, in a four pixel neighborhood, around the pixel $i,j$, where diffusion is computed respectively. The coefficient of variation leads to the largest diffusion where the nearest-neighbor difference is largest (strongest edge), while the smallest diffusion is calculated where the nearest-neighbor difference is smallest (the weakest edge). The constant $\lambda_d \in \Re^+$ is a scalar that determines the rate of diffusion, $\eta_s$ represents the spatial neighborhood of pixel $i,j$, and $|\eta_s|$ is the number of neighbors (usually four except at the image boundaries). Perona and Malik [347] linearly approximated the directional derivative in a particular direction as $\nabla g_{i,j} = g_{i+1,j} - g_{i,j}$ (for the west neighbor of the central pixel $i,j$). Modifying the image according to the above equation in (2.3.17), which is a linear isotropic diffusion equation, is equivalent to filtering the image with a Gaussian filter. The parameters for the anisotropic diffusion filter used in this study were, $\lambda_d = 0.25$, $\eta_s = 8$, and the parameter $K = 30$, which was used for the calculation of the diffusion coefficient $cd(|\nabla g|)$ in (2.3.15).

*2.3.7.2 Lee diffusion and speckle reducing anisotropic diffusion filtering (lsmedcd, adsr)*

By assigning slightly different weights to (2.3.17), the output of the filter *lsmedcd*, may be formed as [38]:

$$f_{i,j} = g_{i,j} + \frac{1}{\eta_s} div(1 - k_{i,j}\nabla g_{i,j}) \tag{2.3.18}$$

with the weighting factor, $k_{i,j}$, which can be calculated with (2.3.2a)-(2.3.2h). The *lsmedcd* filter as shown in (2.3.18) operates in 8 different directions within the moving window.

The essence of speckle reducing anisotropic diffusion is the replacement of the gradient based edge detector, $cd(|\nabla g|)$, in original anisotropic diffusion PDE with the instantaneous coefficient of variation suitable for speckle filtering, $c_{adsr}(|\nabla g|)$. The *adsr* speckle reducing anisotropic diffusion filter [38], uses two seemingly different methods, namely the Lee [22]-[26], [159] and the Frost diffusion filters [27], [28]. A more general updated function for the output image by extending the PDE versions of the despeckle filter is [38], [74]:

$$f_{i,j} = g_{i,j} + \frac{1}{\eta_s} div(c_{adsr}(|\nabla g|)\nabla g_{i,j}). \tag{2.3.19}$$

The diffusion coefficient for the speckle anisotropic diffusion, $c_{adsr}(|\nabla g|)$, is derived [38] as:

$$c_{adsr}^2(|\nabla g|) = \frac{\frac{1}{2}|\nabla g_{i,j}|^2 - \frac{1}{16}(\nabla^2 g_{i,j})^2}{(g_{i,j} + \frac{1}{4}\nabla^2 g_{i,j})^2}. \tag{2.3.20}$$

It is required that $c_{adsr}(|\nabla g|) \geq 0$. The above instantaneous coefficient of variation combines a normalized gradient magnitude operator and a normalized Laplacian operator to act like an edge detector for speckle images. High relative gradient magnitude and low relative Laplacian indicates an edge. The *adsr* filter utilizes speckle reducing anisotropic diffusion after (2.3.17) with the diffusion coefficient, $c_{adsr}(|\nabla g|)$ in (2.3.20) [38], [74].

*2.3.7.3 Exponential damp kernel filters utilizing diffusion (lsmedc)*

The *lsmedc* filter [28], [38] is an adaptive filtering algorithm that uses an exponentially damped convolution kernel, which adapts itself to regions and features containing edges by exploiting local statistics. The *lsmedc* differs from *lsmv* filter with respect that the scene reflectivity is estimated by convolving the observed image with the impulse response of the ultrasound system. The impulse response of the ultrasound system is obtained by minimizing the MSE between the observed and the scene reflectivity model, which is assumed to be an autoregressive model. The filter output is determined by [38]:

$$f_{i,j} = \sum_{i,j} g_{i,j} m_{i,j}, \tag{2.3.21}$$

with $m_{i,j} = \frac{e^{-K\sigma_n^2 d_{i,j}}}{\sum e^{-K\sigma_n^2 d_{i,j}}}$, and $d_{i,j} = \sqrt{(g_{i-1,j} - g_{i,j})^2 - (g_{i+1,j} - g_{i,j})^2}$

where K is the damping factor, $\sigma_n^2$ the noise variance of the image, and $i, j$ the pixel coordinates. The factor $K$ is chosen such that in homogeneous regions $K\sigma_n^2$, approaches zero, yielding the mean filter output. At edges, $K\sigma_n^2$, becomes so large that filtering is inhibited completely. The implementation of the filter consists of defining a circular symmetric filter with a set of weighting values $m_{i,j}$ for each pixel.

The relationship of *lsmedc* filter and anisotropic diffusion is given in [38] and the output image can be calculated as:

$$f_{i,j} = g_{i,j} + \frac{1}{\eta_s} div(m_{i,j} \nabla g_{i,j}) \tag{2.3.22}$$

where $m_{i,j}$, is calculated with (2.3.21), and $\eta_s$, represents the spatial neighbourhood of the pixel $i, j$. The *lsmedc* filter has been originally developed for SAR images to provide an alternative to homomorphic filtering because of its simple implementation.

*2.3.7.4 Coherent nonlinear anisotropic diffusion (nldif)*

The applicability of the *ad* filter (2.3.17) is restricted to smoothing with edge enhancement, where $|\nabla g|$ has higher magnitude at edges. In general, the function $cd(|\nabla g|)$, in (2.3.16) can be put into a tensor form that measures local coherence of structures such that the diffusion process becomes more directional in both the gradient and the contour directions, which represent the directions of maximum and minimum variations, respectively. Therefore, the *nldif* filter will take the form:

$$\frac{dg_{i,j,t}}{dt} = div[D\nabla g] \tag{2.3.23}$$

where $D \in \Re^{2x2}$, is a symmetric positive semi-definite diffusion tensor representing the required diffusion in both gradient and contour directions and, hence enhancing coherent structures as well as edges. The design of D as well as the derivation of the coherent nonlinear anisotropic diffusion model may be found in [345] and is given as:

$$D = (\omega_1 \;\; \omega_2) \begin{pmatrix} \lambda_1 & 0 \\ 0 & \lambda_2 \end{pmatrix} \begin{pmatrix} \omega_1^T \\ \omega_2^T \end{pmatrix} \text{ with} \tag{2.3.24a}$$

$$\lambda_1 = \begin{cases} \alpha\left(1 - \dfrac{(\mu_1 - \mu_2)^2}{s^2}\right) & if \;\; (\lambda_1 - \lambda_2)^2 \le s^2 \\ 0, & else \end{cases} \tag{2.3.24b}$$

$$\lambda_2 = \alpha.$$

where the eigenvectors $\omega_1$, $\omega_2$, and the eigenvalues $\lambda_1$, $\lambda_2$, correspond to the directions of maximum and minimum variations and the strength of these variations, respectively. The flow at each point is affected by the local coherence measured by $(\mu_1 - \mu_2)$ in (2.3.24 b).

The parameters used in this study for the *nldif* filter were $s^2 = 2$ and $\alpha = 0.9$ which were used for the calculation of the diffusion tensor $D$ and the parameter step size $m = 0.2$, which defined the number of diffusion steps performed. The local coherence is close to zero in very noisy regions and diffusion must become isotropic ($\mu_1 = \mu_2 = \alpha = 0.9$), whereas in regions with lower speckle noise the local coherence must correspond to $(\mu_1 - \mu_2)^2 > s^2$ [345].

### *2.3.8 Wavelet filter (waveltc)*

Wavelet filtering, as proposed by many researchers [88], [109], [142], [180], [228], [229], belongs to a different class of methods by exploiting the decomposition of the image into the wavelet basis and zeros-out wavelet coefficients in order to despeckle the image. Further, the WT is a linear transform, which implies that speckle noise will remain speckle noise in the wavelet domain.

A wavelet has its energy concentrated in time to give a tool for the analysis of transient, non-stationary or time-varying phenomena. Wavelets can be used to analyze signals in different spatial resolutions. Their advantage is in their ability to analyze a signal with accuracy in both the time and frequency domains [90]. This is not the case when applying traditional Fourier analysis, where there is significant accuracy in the frequency domain, or in the temporal domain, but less accuracy in the temporal domain. In other words, increasing accuracy in one domain implies a decrease in precision in the other domain. Wavelets are also known for their capacity to identify singularities, associated with fine variations of the signal to be evaluated [88], [90], [107], [180], [228]. For denoising, we need to identify the specific image scales where the most of the image energy lies.

The general basic approach of using wavelets is to:

a) Compute the 2D WT of the noisy image, (see 2.2.5b, $g_{i,j} = f_{i,j} + nl_{i,j}$), and express it as, $g_{i,j} = f_{iT_i+s_i,jT_j+s_j} + nl_{iT_i+s_i,jT_j+s_j}$, where $T_i$; $T_j$ are the sampling periods along horizontal and vertical directions, and $s_i$, $s_j$ are the sampling shifts [348].

b) Alter the WT computed in a), by modifying the wavelet coefficients, i.e pass the 2D WT through a threshold, $thr$. The set of computed coefficients are called the discrete wavelet transform (DWT) and we have:

$$W(g_{i,j}) = W(f_{i,j}) + W(nl_{i,j}) \tag{2.3.25}$$

In our case, it is desired to recover $W(f_{i,j})$, from a DWT $W(g_{i,j})$, by reducing $W(nl_{i,j})$ in the wavelet domain.

c) Compute the inverse WT using the modified coefficients computed in the point above, to emphasize or highlight the reconstructed image edges.

Speckle reduction filtering in the wavelet domain, presented in this work, uses the idea of soft-thresholding denoising first proposed by Donoho [350] and also investigated by [141], [152], [157], [323]. Wavelet shrinkage methods, such as hard- and Donoho's soft-thresholding, have been investigated for speckle reduction of images on a logarithmic scale. An advantage of

a soft threshold is that it smoothes, while hard thresholding preserves features [348]. Soft thresholding is a simple, non-linear technique, which operates on one wavelet coefficient at a time. In its most basic form, each coefficient is thresholded by comparing it with the threshold. This is accomplished by hard thresholding, which means setting to zero the elements whose absolute values are lower than the threshold, or by soft thresholding, which involves first setting to zero the elements whose absolute values are lower than the threshold and then scaling the nonzero coefficients toward zero. The *waveltc* filter, presented in this study, performs de-noising of an image using soft-thresholding as proposed in [350], by calculating the threshold as proposed in [180]. Its operation may be described as follows:

a) Estimate the variance of the speckle noise, $\sigma_n^2$, from the logarithmic transformed original image, with (2.2.2).

b) Choose Symmlet wavelets and two levels or scales, P, for the decomposition. Donoho's soft thresholding method, used in this work, was developed on orthonormal wavelet transform, primarily with Daubenchies's Symmlet 8 basis wavelet. The DWT is applied to the original image to separate the horizontal, vertical and diagonal details at different levels, thus transforming the corrupted image to a set of wavelet coefficients.

c) Set the initial threshold value at $thr = t_0$.

d) Soft threshold the wavelet coefficients with the threshold of point c), in order to obtain the noisy part of the image. Soft thresholding operation can be represented as [350]:

$$u = T(v,t) = sign(v)(|v| - t_0)_+ \tag{2.3.26}$$

where the threshold parameter $t_0$, is proportional to the noise level $\sigma_n$, and $u$, is the result of soft thresholding and has the same sign as $v$, if non zero. The expression $(|v| - t_0)_+$, is defined as:

$$(|v| - t_0)_+ = \begin{cases} |v| - t_0 & if \quad |v| \succ t_0 \\ 0, & otherwise. \end{cases} \tag{2.3.27}$$

The DWT coefficients are modified by:

$$W_j^d(g_{i,j}) = T\{W_j^d(f_{i,j}), t_j^d\} \tag{2.3.28}$$

where $d = 1,2, j = 1,...,k, k \le J$, $j$, is the decomposition level, and $t_j^d$, is a threshold related to the noise level, orientation, and scale, and can be computed through a linearly decreasing function as:

$$t_j^d = \begin{cases} (T_{\max} - \alpha(j-1))\sigma_j^d \; if & T_{\max} - \alpha(j-1) \succ T_{\min} \\ T_{\min}\sigma_j^d, & otherwise \end{cases} \tag{2.3.29}$$

where $\sigma_j^d$, is the standard deviation, $\alpha$, is a decreasing factor between two consecutive levels, $T_{\max}$, $T_{\min}$, are a maximum and a minimum factor for $\sigma_j^d$, with, $1 \le j \le J$, and $d \in \{1,2\}$. For the case of an unknown noise level, we use $\sigma_j^d$, to estimate the noise level of the image. The threshold $t_j^d$, is primarily calculated using, $\sigma_j^d$, and a decreasing factor, $T_{\max} - \alpha(j-1)$. Donoho [350] proposed a threshold for additive noise such as, $thr = \sigma_n\sqrt{2\log(N)}$, [90], [350], where $\sigma_n$, is the noise standard deviation in the image, and $N$ is the block size in the wavelet transform (i.e N=8). Hard threshold rule usually leads to small MSE where soft-threshold can maintain the smoothness of the original signal. The threshold is estimated by using denoising decomposition at two levels with symmetry wavelets [90], [350].

e) Perform the inverse WT.

f) Calculate the standard deviation of the noisy image.

g) Calculate the difference between the estimated deviation and the calculated deviation. If the difference is below the tolerance in step c), then got to i).

h) Renew the threshold $thr = thr + step_of_threshold * delta$. Go to d).

i) Subtract the noisy image from the original image to obtain the despeckled image.

# *Chapter 3*

# *IMT and Plaque Segmentation*

# CHAPTER 3: IMT AND PLAQUE SEGMENTATION

Outlining or segmenting organs and specifically the carotid artery or plaque is an important task in the treatment of the subject under investigation. However, manual outlining is tedious, time consuming and suffers from intra- and inter-observer variability. New techniques are therefore needed for accomplishing the above tasks.

In this Chapter an introduction to previous work on IMT and plaque segmentation on ultrasound imaging is addressed, and deformable models are briefly introduced. Furthermore, the theoretical concepts of the IMT and plaque snakes segmentation method in 2D ultrasound images of the carotid artery are explained. The IMT snakes segmentation method, utilizes normalization, despeckling, and an automatic contour initialization, for initially positioning the snake, which is then deformed to accurately fit the desired boundaries. The plaque snakes segmentation method uses the blood flow image first to detect the initial contour of the plaque, and then despeckle filtering and snakes to deform the initial contour for best fit of plaque boundaries. Finally, reference is given to some other snake methods, and the snake initialisation procedures for the IMT and plaque are presented.

## 3.1 Introduction

The aim of image segmentation is to partition an image into a number of non-overlapping regions that form a complete description of the image. A wide range of work has been undertaken to achieve this aim and segmentation has found diverse applications ranging from medical to military. It is still a subject of an on-going investigation and it cannot be conclusively stated that the segmentation problem has been solved. For the goal of delineating the IMT, and the plaque borders in the carotid artery, it is not necessary to obtain a complete segmentation of the image, but to obtain a partial segmentation so that discriminates between wall and blood and wall and plaque borders.

In this Chapter, we focus on the IMT and plaque segmentation from ultrasound images of the carotid artery by utilising despeckle filtering as explained in Chapter 2. The relation of despeckle filtering and segmentation may be explained as follows. Despeckling may be used as a pre-processing step for the segmentation. Most existing segmentation techniques like active contours and the watershed transform (WT), process gradient information in the image. Because of the relatively low SNR in ultrasound images, speckle noise degrades the performance of these techniques considerably [220], [238], [335], [338], so that active contours, and other segmentation techniques might get stuck in the speckle noise. By despeckle filtering the performance of the segmentation techniques might be enhanced.

Extracting the boundaries of objects in images is one of the most important problems in computer vision and image processing. A wide variety of mathematical and computational approaches have been proposed for solving segmentation problems. Surveys of segmentation methods concerning the most common algorithms have been undertaken by Haralick et al. [128], and most image processing texts generally provide a broad overview of the more common algorithms [1]-[9], [111].

Several other techniques have also been proposed in the literature to segment the cavities of the heart in ultrasound images [175], [190], [218] tumours in the liver [211], [354], and the prostate [80]. Furthermore, several classical segmentation techniques have been described under which, the most recent is the HT [150], [151], [201], [204], the WT [11], [135], [137], [140], [143], and active contours, or snakes [242]-[256]. Some more traditional segmentation techniques include, histogram analysis [211], region growing and spit-merge algorithms [3], [245], colour space analysis and segmentation [7]-[9], pixel classification for segmentation [3]-[9], gradient segmentation [148], [251], [258], edge and zero-crossing detectors such as Canny [128], and radial search and boundary following algorithms [7]-[9]. Instead of exploiting only pixel information as low-level edge-detection techniques do, active contours or snakes [243], also use information about the boundaries as part of an optimization procedure. Active contours are used extensively for segmentation, and a number of alternative approaches have been proposed such as, geometric deformable models, [60], [225], discrete dynamic contour [222], geometric active contours, [60], [95], [179], [225] and level sets [97], [111], [179], [221], [239]. When the exact shape of an object is unknown or is impossible to parameterize it, techniques that can evolve the target solution or adapt their result to the image are used. This implies the use of flexible shape formulations [155]. Another disadvantage of these methods is that spectrally similar but spatially disjoint regions are never associated together, thus complicating their identification. Also, it is often not clear at what point the region growing process should be terminated, resulting in under- and over-segmentation. In addition the region growing approach tends to be a very computationally intensive process. As it is shown in the literature, snakes get stuck because of the strong speckle noise [231], the HT [201], [218], and the WT [11] shows over or under segmentation. Furthermore, the HT and the WT methods are slow and pose problems with the initial contour initialisation [204].

In the next section we present previous work on carotid IMT and plaque segmentation. Also we introduce theoretical concepts on snakes, and explain why snakes have been chosen to segment the IMT and plaque from ultrasound images of the carotid artery.

## 3.2 Previous work on carotid IMT segmentation

Traditionally, the IMT is measured by manual delineation of the intima and the adventitia layers [41], [44], [55], [57], [99], [227], [254]-[256]. The manual tracing methods are not only tedious and time consuming, but also unreliable [100], [241], [245], [255]. In addition manual outlining of the lumen and the IMT by experts requires substantial experience, it is time consuming and varies according to the training, experience and the subjective judgment of the experts. The measurements suffer therefore from considerable inter- and intra-observer variability [79], [186], [253].

TABLE 3.1
AN OVERVIEW OF ULTRASOUND SEGMENTATION TECHNIQUES IN VASCULAR IMAGING.

| IMT Segmentation Technique | Year | Input | 2D/3D | AIC | UI | MC | $IMT_{mean}$ [mm] | N |
|---|---|---|---|---|---|---|---|---|
| Balloon snake [333] | 1991 | US | 2D | No | No | Yes | - | 3 |
| Dynamic programming [85] | 1997 | USC | 2D | No | No | No | - | 1 |
| Dynamic programming [253] with cost function optimization | 1997 | USC | 2D | No | No | No | 0.93 | 69 |
| Texture based [220] | 1997 | USC | 2D | - | Yes | No | 0.68 | 29 |
| Optimal graph searching [7] | 1998 | US | 2D | No | Yes | No | - | 1 |
| Star Kalman Filter [41] | 2000 | USC | 2D | No | No | No | - | - |
| Multiscale dynamic programming [178] | 2000 | USC | 2D | No | Yes | No | 0.92 | 50 |
| Discrete dynamic contour [64], [78] | 2000 | USC | 2D | No | Yes | No | - | 7 |
| Discrete dynamic contour [102], [103] | 2001 | USC | 3D | No | Yes | No | 0.75 | 4 |
| Deformable model [55] | 2001 | USC | 3D | Yes | Yes | Yes | - | 200 |
| Morphology operators [185] | 2002 | US | 2D | - | No | No | - | 2 |
| Snakes [82], [241] | 2002 | USC | 2D | Yes | Yes | Yes | 0.65 | 32 |

US: Ultrasound images, USC: Ultrasound carotid images, AIC: Automatic initial contour, UI: User interaction, MC: Manual correction possible, $IMT_{mean}$: Mean IMT in mm, N: Number of cases investigated.

Table 3.1 summarises various computerized methods that have been developed for vascular ultrasound image segmentation. Furthermore, in Table 3.1 the year of investigation (Year), the input image (Input), the image dimensions (2D/3D), the proposed automatic initial contour (AIC), possible user interaction (UI), possible manual correction (MC), the segmented mean IMT ($IMT_{mean}$) in millimeters as well as the number of images investigated (N) are presented respectively. Most of the techniques presented in Table 3.1 are computer-assisted border tracing procedures that require input from experts.

Cohen [333] proposed a Balloon snake model, in 2D ultrasound images of the heart and used the finite element method to calculate the function of continuity. Gustavson [85] implemented four different methods, namely maximum gradient, dynamic programming, mathematical models, and matched filter for segmenting the IMT and the lumen from one

longitudinal image of the carotid artery. The results showed that the dynamic programming algorithm performed better than the others in respect of speed and boundary continuity, although the detected boundaries could not be drawn correctly. Wendelhag et al. [253] developed a computerized analysis system to extract the boundaries of the IMT using dynamic programming with cost function optimization in longitudinal 2D images of the carotid artery. However, the system requires manual correction after automatic tracing, and three weighting factors must be tuned due to the varied characteristics of the ultrasound instrumentation.

In another study, Mojsilovic et al. [220] proposed a method for intra-vascular images of the carotid artery based on textural operators to separate different tissue regions and morphological processing to refine the extracted contours. Sonka et al. [7] proposed optimal graph searching for ultrasound images of the carotid artery, but the algorithm requires manual and empirical estimations to be made by the expert. Abolmaesumi [41] proposed a star algorithm to estimate the center of the artery in transversal carotid images and a Kalman filter approach to estimate the carotid artery boundary. The star algorithm was able to detect the center of the carotid by considering it as the center of gravity but the results were not very accurate.

Liang et al. [178] applied multiscale dynamic programming to detect the approximate boundaries of the carotid vessel walls in transversal 2D carotid artery images by reducing the inter-observer variability. A cost function was proposed, which is a weighted sum of terms, in fuzzy expression forms, representing image features and geometrical characteristics of the vessel interfaces. This cost function was then used to guide the detection of the boundaries in a fine scale image. The weights were adjusted by a training procedure, which was long and required human experts tracing. Therefore, this method is not appropriate to evaluate a large database of images, as strong human expert tracing and involvement is required.

In his research, Mao et al. [64], [78], proposed a deformable discrete dynamic contour model in 2D transversal images of the carotid artery, with only one seed point to guide the initialization of the deformable model for each lumen cross section. The snake initial contour was generated using the entropy map of the image and morphological operators. The method requires a large database of images and depends on the quality of the training database, which is used in the development of the optimization. Furthermore, manually outlined boundaries are also required.

Ladak [103] developed a discrete dynamic contour model for segmenting the inner arterial lumen and wall in longitudinal carotid ultrasound images, where the initial snake contour was supplied by the expert. The contour was then deformed to fit the inner boundary of the artery wall, dilated and then deformed to fit to the outer wall boundaries. The segmentation was performed on every 2D image where finally a 3D spline surface was reconstructed with finite element meshing from all the 2D segmented outlines [102]. The method was tested on blood

MRI images where the expert was able to edit the final snake contour. A similar deformable model for 3D carotid ultrasound images was developed by Jill [77], [79], where the mesh, generated from the finite element triangulation was used to extract the final 3D boundary. Zahalka et al. [55], proposed a geometrically deformable model for 3D transversal carotid images by providing a seed point in the lumen of the carotid artery. The snake required three input parameters and a contour variability was reported in the segmentation, which was due to the selection of the seed point. Xiao et al. [185] proposed segmentation of synthetic, breast and cardiac ultrasound images with intensity inhomogeneity correction using mathematical morphological operations by first filtering the image to remove noise. Cheng et al. [241] proposed a snakes segmentation system for detecting the IMT in 2D longitudinal images of the carotid artery based on a snake model, where the expert must indicate manually the staring and ending points of the snake contour. The proposed technique failed to detect the borders of the IMT when strong speckle noise was apparent in the ultrasound image and the analysis of the system was limited to a graphical comparison rather than a quantitative metrological evaluation.

There are a few known commercially available software-imaging systems in the last years from some research groups [7], [241], [253], as well as from the industry, such as from Phillips medical systems [330]. The HDI Lab and the QLAB quantification software for the IMT detection, from Philips medical systems are both software packages, which use a cineloop (multiple image frames of the same region) display for image quantification. Cineloops acquired by the ATL HDI-5000 scanner [330] (see Chapter 5.2), can be easily transferred to a personal computer running HDI Lab or QLAB. Both software tools allow the expert to quantify image characteristics within multiple regions-of-interest and make comparisons between several regions or images. They are especially useful for characterizing tissue images, and contrast-enhanced images, and are capable of measuring the IMT at the far or near wall of the carotid artery when cineloop images are available.

The problems that are associated with the computer assisted border tracing segmentation procedures are the following:

a) They do not take into consideration the speckle noise [44], [64], [78], [79], [82], [220], or the image normalization [205], [208], [322].

b) They are sensitive to the initial snake contour [220], [241], or to initial seed points, which should be placed manually [55], [61], [220], thus creating a contour variability. If the initial contour is placed far away from the boundary of interest then the snake will not be attracted [64], [80], [241].

c) They have difficulties of processing into concave boundary regions [116], [117], [124].

d) Some weighting factors that should be tuned due to the varied characteristics of the ultrasound instrumentation must be entered manually or empirically [55], [178], [185], [220]. Some other weights may be adjusted by a training procedure, which is long and requires experts tracing [64], [178].

e) The snake is implemented as a close contour [40], [55], [124], that might not be that suitable for the IMT segmentation.

f) They require manual correction after automatic tracing [64], [220], [241], [253].

g) In a number of cases there was no ground truth segmentation delineations from experts to be compared to the computer-assisted methods [82], [116], [117], [220], [241].

h) Different measurement procedures were used between the manual and the snakes segmentation methodologies (see Fig. 3.1) [64], [79], [103], [178], [241], [253], [333].

i) Different criteria were used for assessing the performance of the segmentation algorithms [7], [40], [44], [55], [82], [85].

j) They were evaluated on a limited number of images, where the intra-and inter-observer variability could not be assessed [33], [78], [103], [185].

In this work, we have used a number of evaluation metrics for boundary detection (see Chapter 4, Chapter 5.7, Chapter 5.8) such as statistical measures, the inter observer error, the coefficient of variation, the Wilcoxon rank sum test, a variation of the Hausdorff distance, the Pearson correlation test, the MSE, the correlation coefficient, histograms of the mean IMT, and the manual measurements performed by two experts. The Williams&Shah snakes segmentation algorithm was investigated on a large database consisting of 100 ultrasound images.

### *3.2.1 On the difference between manual and automated IMT measurements*

Figure 3.1a presents a longitudinal ultrasound image of the carotid artery where the echoes in the region of interest can be schematically grouped into seven echo zones Z1-Z7. The upper side of Z3, Z5, Z7 is the leading edge denoted as I3, I5 and I7, and can be mapped to the near-wall intima lumen-interface, the far-wall lumen-intima interface and, the far-wall media-adventitia interface respectively. Consequently the distance between I5 and I7 is the far-wall IMT. With this understanding, the determination of the IMT at the far wall of the artery becomes equivalent to accurately detecting the echo boundaries I5 and I7, which may be mapped at the far wall intensity diagram in Fig. 3.1b marked with points A. Figure 3.1b shows a schematic diagram of the lumen-intima and media-adventitia intensity interface of the far wall of the carotid artery, which is preferred for IMT measurements.

When measurements are performed manually, the point of the maximum gradient (A) is mostly marked, but sometimes the threshold for visibility of the echo interface for the human

eye, is above this point in the weaker echo. In those cases the expert tends to mark more closely at the top of the intensity curve for the lumen-intima interface. This will result in a thinner IMT compared with the automated measurements [178], [253]. At the media-adventitia interface, the automated detection matches the manual detection well. However, for the lumen-intima interface, due to the weak echo, the visibility threshold can be well above the point of the maximal gradient (A). In this case, the expert tends to set the interface point closer to the top of the echo. However, this difference is clinically acceptable as long as the proposed segmentation method performs consistently.

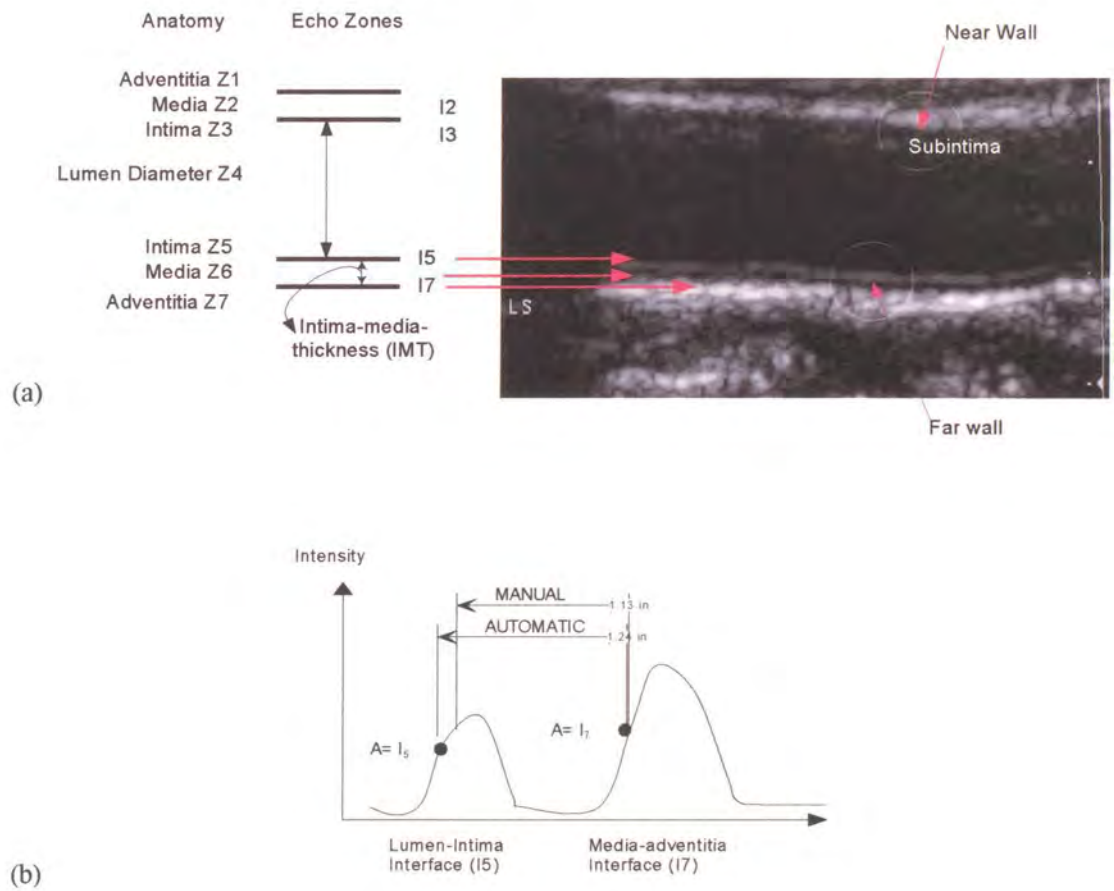


**Fig. 3.1**: (a) Illustration of the intima-media (IM). IM contains the area between the intima and adventitia. The sub-intima region may cause problems in searching the adventitia layer due to speckle noise and due to its interference caused from the adventitia layer. (b) Intensity schematic illustration of a lumen-intima and media-adventitia interface at the far wall of the carotid artery. Modified from [253].

## 3.3 Previous work on carotid plaque segmentation

Table 3.2 summarises various computerized methods that have been developed for vascular segmentation of the plaque in carotid artery images. Furthermore, in Table 3.2 the year of investigation (Year), the input image (Input), the image dimensions (2D/3D), the proposed

automatic initial contour (AIC), possible user interaction (UI), possible manual correction (MC), as well as the number of images investigated (N) are presented respectively. All techniques presented in Table 3.2 require input from experts.

TABLE 3.2
AN OVERVIEW OF PLAQUE SEGMENTATION TECHNIQUES IN VASCULAR IMAGING.

| Plaque Segmentation Technique | Year | Input | 2D/3D | AIC | UI | MC | N |
|---|---|---|---|---|---|---|---|
| Ultrasound Images | | | | | | | |
| Discrete dynamic contour [64] | 2000 | USC | 2D | No | Yes | No | 7 |
| Kalman Filters [41] | 2000 | USC | 2D | No | No | No | 1 |
| Balloon [100] | 2000 | USC | 3D | No | No | No | 2 |
| Canny edge detection [47] | 2004 | USC | 2D | No | No | No | - |
| Morphological based [46] | 2004 | USC | 2D | No | No | No | - |
| IVUS Images | | | | | | | |
| Optimal graph searching [72] | 1998 | USC | 2D | No | Yes | No | 20 |
| MRI | | | | | | | |
| Mean shift [61] | 2001 | MRI | 2D | Yes | No | No | 22 |
| Active contour, GVF [191] | 2002 | MRI | 2D | No | No | No | 20 |
| Dynamic programming [321] | 2003 | MRI | 2D | Yes | No | No | 62 |

USC: Ultrasound carotid images, AIC: Automatic initial contour, UI: User interaction, MC: Manual correction possible, N: Number of cases investigated.

Mao et al. [64], proposed a discrete dynamic contour model for extracting the carotid artery lumen in 2D transversal ultrasound images. The method generated the initial contour using the entropy map of the original ultrasound image and required an initial seed point, which was specified by the expert. A major drawback of this method was that a large database of images was necessary for generating the initial contour, which was dependent on the quality of the training database used for the development of the optimization. Furthermore, manually outlined boundaries were also required.

Abolmaesumi et al. [41] introduced an algorithm for extracting the carotid artery boundaries from transversal carotid ultrasound images. The proposed algorithm was based on the use of both temporal and spatial Kalman filters in order to track the center and the walls of the artery. The star algorithm detected the center of the carotid by considering it as the center of gravity but the results were not very accurate. Manual correction of the final borders and user interaction was not possible. Jill [100] proposed a semi-automatic method for tracking the progression of atherosclerotic plaque in 3D images of the carotid artery, by using the Balloon model [333], represented by a triangular mesh. The mesh was manually placed within the interior of the carotid artery and it was then driven outward until it reached the vessel wall by applying an inflation force to the mesh. The method was applied to two 3D artificial carotid images acquired from two different vessel phantoms. Results showed that segmentation was not very accurate, it was very time consuming, and borders were not reliably drawn. Manual correction as well as user interaction was not possible. Hamou et al. [47], proposed a method, which was based on

the canny edge detector to detect the plaque regions in carotid artery ultrasound images. However, in the proposed method the expert had to specify three threshold parameters. Furthermore, the proposed algorithm was not user friendly, and the accuracy of the results depended to a large extent, on the appropriate selection of these threshold parameters.

Finally, a morphological based approach for the carotid contour extraction was proposed in [46] for longitudinal ultrasound images of carotid artery, and this incorporated four different stages. These were despeckle filtering, contour quantisation, morphological contour detection, and a contour enhancement stage. The disadvantage of the method was that the expert had no interaction with the system as all segmentation steps, which were made through morphological processing, were predefined. Furthermore, the final plaque segmentation produced many small-connected contours, showing all the edges of the carotid ultrasound image, instead of generating a single closed loop contour indicating the plaque borders.

Other researchers used a graph-searching approach to detect the wall and plaque borders from IVUS images of the carotid artery [72], [184]. The method was used to identify globally optimal plaque borders, where initial information about the wall thickness, plaque location and initial plaque borders was both required, and specified by the expert. The use of IVUS, poses a certain risk to the patients, as discussed in Chapter 1, due to the insertion of a catheter in the patient's artery. Moreover, the system proposed in [72] required a sequence of IVUS images to be provided. In addition, the method proposed in [72], and [184] was tested on 20 transversal IVUS images of the carotid artery. In another study, Xu [61] applied a mean shift density estimation algorithm to segment 22 multiple transversal MRI of the carotid artery. In this case, the initial contour was estimated by finding the center of the gravity in the lumen area and extending radial rays to the lumen border of the carotid artery. Results showed that the segmentation was very time consuming, reliable borders were not drawn, and the segmentation results were not compared with the hand outlined boundaries of experts. Other researchers have attempted to segment the carotid plaque from vascular MRI, by using active contours based on the GVF field, in order to detect the artery, lumen, and plaque borders [191], where the initial contour was placed manually by the expert. The method was tested on 20 MRI images and the results were compared with the manual delineations of one expert. Furthermore, the coefficient of variation was also used in order to compare the manual with the GVF snakes segmented boundaries. Yang [321] proposed a dynamic programming approach, to detect the plaque borders in each MRI frame. The method was tested on 62 transversal MRI of the carotid artery from six vessel specimens, and it was compared with the manual delineations of an expert. For the estimation of the initial plaque contour, the expert was required to specify four seed points.

There are currently no other methods reported in the literature for accurately and efficiently segmenting the plaque borders in ultrasound longitudinal images of the carotid artery.

## 3.4 Active contours (snakes)

There has been a tremendous surge of interest in deformable templates in the context of medical image analysis, where deformable models were used to segment anatomic structures [352]. One of the earlier approaches to deformable template analysis [105], [332], was aimed to find facial features for the purpose of recognition. Deformable templates evolve a shape to match the image data. Earlier approaches were the HT [201], [204], and the WT [11], but they require too many parameters, they have a high computational load, and generate over and under segmentation results.

Active contours are curves that deform within digital images to recover object shapes [124], [179], [243], [244], [259], [333]. They are classified as either parametric active contours (PACs) or geometric active contours (GACs), according to their presentation and implementation. PACs are represented explicitly as parameterized curves in a Lagrangian formulation [101], [179], [240]. GACs are represented implicitly as level-sets of 2D distance functions, which evolve according to an Eulerian formulation [60], [223]. They are based on the theory of curve evolution implemented via level-set techniques [179], [239]. Current level-set techniques have difficulties in representing open curves, as in our application for the segmentation of the IMT in the carotid artery, while snakes are well suited for applications where open curves are required [97], [111].

In 1988 Kass [243] introduced a new approach for locating features of interest in images, called active contours or snakes, which was defined by an energy functional and a solution was found using techniques of variational calculus and the finite difference methods [259]. The user interactively specified the initial position of the snake [97]. Cohen [333] improved the above method of Kass by using finite element methods, whereas C.-M. Chen [231], proposed a new snake model with three important features, namely a modified-trimmed filter for noise reduction, adaptive weighting parameters for weighting the third snake-energy term (see 3.4.2), and edge enhancement by integration to capture the slowly varying edges. Williams&Shah [124], improved the model proposed by Kass in [243], by incorporating a new energy continuity term in (3.4.2), so that contour points were more evenly spaced, thus making the estimation of the curvature more accurate. Amini [334] pointed out some of the problems of Kass's approach [243], including numerical instability and tendency for points to bunch up on strong portions of an edge contour, by proposing dynamic programming. This approach was more stable and allowed the inclusion of hard constraints inherent in the formulation of the functional however it

was slow having high complexity. Chang [205] proposed a 3D snake for malignant breast tumor excision, where the image was first despeckled by anisotropic diffusion, and then estimated an initial close snake contour for the tumor, using morphology operators. In all of the above mentioned snakes segmentation approaches, snake requires that a close contour must be detected. Snakes have been successfully employed in many other applications such as motion tracking [7], [106], [240], [251], in medical images [7], [241], in facial image gesture [250], in edge detection [243], shape modelling [216], segmentation [39], [44], [187], and in border detection in artificial images [124], [116], [185].

Many modifications of the snake model have been proposed [7], [55], [64], [82], [253]. Recently Wang [260] proposed a modification of the ziplock snake [250], where multiple contour features in artificial images were detected more accurately. Valvrede [108] applied deformable models on nine mammogram images for vessel segmentation by defining a new energy function associated with the image noise and avoiding the tendency of snake contour points to bunch up. Other researchers proposed a pressure force [333], to solve the concave problem, however, the details in determining the amplitude of force were not mentioned. Yuen [252], combined the split and merge algorithm with the snake problem to overcome the problem of the snakes initialization. Good results were obtained but this method was computationally very expensive.

A snake is a parametric contour that deforms over a series of iterations. Each element $v(s,t)$, along the snake contour depends on two parameters: namely $s$, which is the space (curve) parameter, and the $t$, which is the time (iteration) parameter, and may be described as [7]:

$$v(s,t)=\begin{cases} s & space \quad (curve) \quad parameter \\ t & time \quad (itteration) \quad parameter \end{cases}. \tag{3.4.1}$$

Internal forces, image forces, and external forces influence the snake contour, which evolves as a set of points (contour) to match the image data. This set of points aims at fitting the target feature to be extracted. A snake contour may be represented parametrically by $v(s)=[x(s),y(s)]$, where $(x,y)\in\Re^2$, denotes the spatial coordinates of an image and $s\in[0,1]$, represents the parametric domain (see also Fig. 3.2). The snake adapts itself by a dynamic process that minimizes an energy function defined as [82], [124], [231], [243], [336]:

$$E_{snake}(v(s)) = E_{\text{int}}(v(s)) + E_{image}(v(s)) + E_{ext}(v(s)) =$$

$$\int_s (\alpha(s)E_{cont} + \beta(s)E_{curv} + \gamma(s)E_{image} + E_{external})ds = \tag{3.4.2}$$

$$\int_s (\alpha(s)\left|\frac{dv(s)}{ds}\right|^2 + \beta(s)\left|\frac{d^2v(s)}{ds^2}\right|^2 + \gamma(s)E_{image} + E_{external})ds.$$

The aim of the snake is to evolve by minimizing (3.4.2), and we seek therefore points in $v(s)$, such that the first derivative of (3.4.2) is zero, as follows:

$$\frac{dE_{snake}}{dv} \equiv 0. \tag{3.4.3}$$

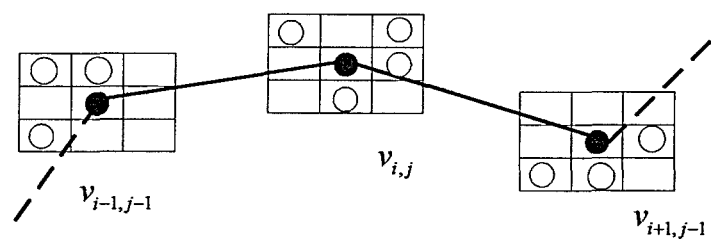


**Fig: 3.2.** Illustration of the snake contour deformation. Open circles represent snake points that are candidates to replace the original (solid) point.

By minimizing the snake energy in (3.4.2), we are trying to locate the curve at the points of maximum gradient $|\nabla g|$, which act as an edge detector. The classical snake model of Kass [243], involves an edge detector, which depends on the gradient of the image to stop the evolving curve at the boundary of the object. At each iteration step, the energy function in (3.4.2) is evaluated for the current point $v_{i,j}(s)$ (see Fig. 3.2, $v_{i-1,j-1}, v_{i,j}, v_{i+1,j-1}$), and for the points in its *mxn* neighborhood (3x3 neighborhood in Fig. 3.2 but also larger neighborhoods may be chosen (5x5, 7x7) [231]), along the *arc* length, $s$, of the contour. Subsequently the point $v_{i,j}(s)$, is moved to the position in the neighborhood attaining the minimum energy (open circle points in Fig. 3.2). The term $E_{\text{int}}(v)$ in (3.4.2) denotes the internal energy derived from the physical characteristics of the snake, it keeps the contour smooth, and is given by the continuity $E_{cont}(v)$, and the curvature energy term, $E_{curv}(v)$, as:

$$E_{\text{int}} = E_{cont}(v(s)) + E_{curv}(v(s)) = \alpha(s)\left|\frac{dv(s)}{ds}\right|^2 + \beta(s)\left|\frac{d^2v(s)}{ds^2}\right|^2. \tag{3.4.4}$$

### *3.4.1 Approximation of the first order differential*

The continuity energy, $E_{cont}(v)$, which is formed from the first order differential, $\frac{dv(s)}{ds}$, in (3.4.4), measures the energy due to stretching (elastic energy). It gives us the rate of change for the length of the contour, which is the longitudinal contraction of the curve. It may be formulated in discrete form, by calculating the average spacing between all the contour points, which is the Euclidean distance, and then subtracting the distance between the current point and the point before it as [124], [155] (see Fig. 3.2):

$$E_{cont} = \left|\frac{dv(s)}{ds}\right|^2 \approx d - \left|v_{i,j} - v_{i-1,j-1}\right|^2 = d - (x_{i,j} - x_{i-1,j-1})^2 + (y_{i,j} - y_{i-1,j-1})^2, \qquad (3.4.5)$$

where $d$, is the average distance between snake points, $v_{i,j}$, $v_{i-1,j-1}$, are the current and the precedent contour snake points, and $x_{i,j}$, $x_{i-1,j-1}$, $y_{i,j}$, and $y_{i-1,j-1}$, are the $x, y$ coordinates of the contour snake points respectively. The term, $\left|v_{i,j} - v_{i-1,j-1}\right|$, is the distance between the two snake contour points. Square values are used to avoid the square rooting thus speeding up the calculations, and the continuity term is thus normalized to be in the range of [0, 1]. Points with a distance between them, which is near the average distance between all contour points, will have small values for $E_{cont}(v)$. The average distance, $d$, between points is calculated for every iteration.

### *3.4.2 Approximation of the second order differential*

The curvature term, $E_{curv}(v)$, is formed from the second order differential, $\frac{d^2v(s)}{ds^2}$, in (3.4.4), and controls the contribution of the curvature energy due to point variation. It gives us the convexity of the curve, and may be formulated in discrete form as [124], [155] (see Fig. 3.2):

$$E_{curv} = \left|\frac{d^2v(s)}{ds^2}\right|^2 \approx \left|v_{i-1,j-1} - 2v_{i,j} + v_{i+1,j-1}\right|^2 = \\ (x_{i-1,j-1} - 2x_{i,j} + x_{i+1,j-1})^2 + (y_{i-1,j-1} - 2y_{i,j} + y_{i+1,j-1})^2, \qquad (3.4.6)$$

where $v_{i-1,j-1}$, $v_{i,j}$, $v_{i+1,j-1}$, are the precedent, current, and next snake contour points, and $x_{i-1,j-1}$, $x_{i,j}$, $x_{i+1,j-1}$, $y_{i-1,j-1}$, $y_{i,j}$, $y_{i+1,j-1}$, are the $x, y$ coordinates of the contour snake points respectively. Small values of (3.4.6) encourage the reduction of curvature, which forces the contour to both maintain its shape and prevent the formation of corners. If corners or other

shape features are desired in the final result, $\beta(s)$, which controls the natural behaviour of the snake, can be adjusted accordingly to raise or lower the influence of curvature in the function minimization. The internal energy in (3.4.2) contains a first-order term controlled by $\alpha(s)$, and a second order term controlled by $\beta(s)$. The first order derivative discourages stretching and makes the model behave like an elastic string by introducing tension. The second order derivative discourages bending and makes the model behave like a rigid rod by producing stiffness. The weighting parameters $\alpha(s)$, and $\beta(s)$, may be used to control the strength of the model's tension, and stiffness (rigidity), respectively. Low values of $\alpha(s)$ imply that the points can change in spacing greatly. The weighting parameter $\alpha(s)$ controls how evenly spaced the points in the contour will be, because $E_{\text{int}}$ is high for segments that are much shorter than or much longer than the mean distance between points. Larger $\alpha(s)$ implies larger stretching, i.e. the snake resists more in stretching. If $\alpha(s)$ is large, the snake tends to shrink (reduce length). Also the smoothness of the snake increases. When $\alpha(s) = 0$, then the points in the contour are unevenly spaced, and eventually maybe placed on top of each other. The introduction of $\alpha(s)$ allows smaller or larger contractions and therefore makes the snake act like an elastic string [155], [243].

The term $\beta(s)$ controls the curvature of the contour. Large values of $\beta(s)$ may keep the contour smooth except at corners, whereas low values imply that the curvature is not minimized and the contour may form corners. It regulates the rate of change of the curve in the direction normal to its boundary, and therefore it may be compared as a rigid string. High values predispose the snake to smooth contours. If $\beta(s) \neq 0$ then the snake may better resist to bending. The term $\beta(s)$ is progressively decreased around a corner until reaching a null value at the exact corner location. If $\beta(s) = 0$ then it may develop corners.

Finally the term $\gamma(s)$, in (3.4.2) is a constant, and controls the influence of image gradients on energy by balancing the image energy term, $E_{image}$ [231]. A large value of $\gamma(s)$ is useful in making the curve converge faster.

The snakes segmentation algorithm determines first the energy for each snake point according to (3.4.2), which are stored as the points with the minimum energy. This ensures that if any other points are found to have equally or smaller energy, then the contour points will remain the same. Then the local 3x3 neighbourhood, around each snake point, is searched to determine whether any other point has a lower energy than the current contour point. If it does, then that point is returned as the new contour point.

For the design of the snake model for extracting the intima and adventitia layer, the factors $\alpha(s)$, and $\beta(s)$, are assumed to be dependent of position. For the calculation of $\alpha(s)$, and $\beta(s)$, it is necessary to take into consideration the irregular spacing between the contour points of the snake. This can be considered in the model by calculating the parameters $\alpha(s)$, and $\beta(s)$, as follows [124], [246]:

$$\alpha_i = \frac{\alpha}{h_i^2},\ \beta_i = \frac{\beta}{h_i^4}, \tag{3.4.7}$$

where $h_i$, is the distance between the snake points $v_{i,j}$, and $v_{i-1,j-1}$. To control the mechanical properties of the snake, the expert may also tune these parameters interactively. Both parameters are determined by the demand of the application and the characteristics of objects. Note that increasing both weighting factors may enhance the effect of the physical properties of the model, and thereby diminish the influence of the external forces.

Some other researchers proposed different formulations for the snake energy in (3.4.2), where some other additional forces for characterizing the image features such as the Balloon active model [333], the dual active contour model [242], the energy function in various applications [249], and training on the-fly of the contour models by observing boundaries accepted by the expert [226]. In [252] the internal energy of the snake, which was applied as a close contour on artificial images, was modified by minimizing the area inside the snake instead of minimizing the length of the snake contour.

### *3.4.3 Approximation of the image energy term*

The $E_{image}(v)$ term in (3.4.2), represents the image energy due to some relevant features such as the gradient of edges, lines, regions [241], and texture [124], and some other forces given by the user or based on the application. It attracts the snake to low-level features such as brightness and edge data. The term, $E_{image}(v)$, is [116], [117], [179], [258]:

$$E_{image}(v(s)) = \int_0^1 P(v(s))ds, \tag{3.4.8}$$

where $P(v(s))$, denotes a scalar potential function defined on the image plane. Another feature of the image energy is the local gray level ratio between the outside and the inside of the contour. Thus, the image force is chosen to be the gradient difference between the inside and the outside of the contour, but it is set to zero during the contour deformation when the gray level ratio between the outside and the inside of the contour is above a threshold. The gradient acts as a driving force while the local gray level ratio plays a role as a stopping criterion to find the

location of inflation of the gray level profile. To apply snakes to images, image potentials are designed whose local minima coincide with intensity extrema, edges and other image features of interest. For example the contour will be better attracted to intensity edges in an image, $g_{i,j}$, by choosing a potential [241], [243], such that we convolve the image with a Gaussian function:

$$P_{i,j} = -c\left|\nabla(G\sigma_{i,j} * g_{i,j})\right|, \tag{3.4.9}$$

where $c$, controls the magnitude of the potential, $\nabla$, is the gradient operator, and $G\sigma_{i,j} * g_{i,j}$, denotes the image convolved with a 2D Gaussian smoothing filter, $G\sigma_{i,j}$, whose characteristic width, $\sigma$, controls the spatial extent of the local minima of $P$. Thus the image force may be calculated by firstly normalizing the gradient magnitude in the range [0, 255]. The maximum and the minimum gradient magnitude in the neighborhood of each snake point, $v_{i,j}$, are then evaluated as $\nabla g_{\max}$, and $\nabla g_{\min}$, respectively. If the dynamic range in the neighborhood is too small (say smaller than 5) then the minimum is modified to be $\nabla g_{\min} = \nabla g_{\max} - 5$. The image force for each neighborhood term may be then calculated as the re-normalized gradient [124]:

$$E_{image} = \frac{(\nabla g_{\min} - \nabla g_{i,j})}{(\nabla g_{\max} - \nabla g_{\min})}, \tag{3.4.10}$$

where $\nabla g_{\min}$, $\nabla g_{\max}$, are the minimum and maximum gradient values in the pixel snake contour point neighborhood, and $\nabla g_{i,j}$, is the gradient value at the current location of the observed snake contour point. The image energy term, $E_{image}$, is in the range of [-1, 0] and is more negative for large gradient values, so that contour points will be attracted to edges with strong energy.

Equations (3.4.6) and (3.4.10) are normalized in the range of zero to one using the maximum gradient value in the pixel neighborhood. The energy image term, $E_{image}$, is already normalized to this range as shown in (3.4.10). All terms constituting (3.4.2), are each multiplied with their respective factors and then added together, as shown in (3.4.2), to form the energy calculation for a specific contour location.

Some other implementations of the image energy, which depend on the application, were reported in [116], where a new external force is introduced, called gradient vector flow (GVF), which is computed as the diffusion of the gradient vector of the gray level or binary image derived from the image. Xu [116], [117], applied the GVF method in one MRI and three artificial images where the initialization was made manually and this posed a problem especially when the snake is initialized far away from the boundary of interest. In addition this method had

difficulties, forcing a snake into long, and thin boundary indentations that was realized as a close contour. A generalized formulation of the GVF (GGVF) was given in [258] concerning the external force of the GVF snake, with an improvement in the convergence of the active contour into long thin boundaries, but the snake was still implemented as a close contour. Recently, an improvement of the GVF snake [116], [258], was reported for image video sequences using multiscale GVF flow snakes [206] for vessel boundary tracking. Hamarneh [119]-[121], developed an improved graphical user interface for segmenting images using the active contour model. The method was applied on real world and medical ultrasound images but the problem was still the placement of the initial snake contour, which had to be placed manually by the expert. A new force in the energy functional (3.4.2) was additionally introduced, where a number of parameters have to be set manually thus making the deformation process very difficult.

### *3.4.4 Approximation of the external energy term*

Finally the external snake energy term, $E_{external}(v)$, in (3.4.2), is user defined and optional where many options are available [252]. In our application two external forces were used, namely the line and the edge force described as:

$$E_{external}(v) = \omega_{line} E_{line} + \omega_{edge} E_{edge}. \tag{3.4.11}$$

The line functional, $E_{line}(v)$, in (3.4.11), generates forces that move the snake towards bright or dark lines depending on the sign of $\omega_{line}$, whereas in our implementation a negative value was chosen in order to seek for a light line, which represents the bright echoes produced by the adventitia layer. The term $E_{line}(v)$ is expressed by, $E_{line}(v) = g_{i,j}$, which is the grayscale value at the current snake contour point. Finally, the edge functional, $E_{edge}(v)$, tries to lock the snake within regions with large gradient values and is given by the negative of the squared magnitude of the current contour point, $g_{i,j}$, as:

$$E_{edge}(v) = -\left|\nabla g_{i,j}\right|^2. \tag{3.4.12}$$

## 3.5 Other snakes approaches

Most of the researchers have only investigated close snake contours [59], [60], [61], [225], [226]. There are also open snake contours presented in the literature [241], [242], [250], [253], [270], as also presented in this dissertation. These require a slightly different formulation from the Kass [243], and the Williams&Shah [124] snake, and only minor modifications for implementation. Snakes utilizing open contours use the same algorithm as snakes utilizing

closed contours, except that the starting and the ending points of the snake contour, may be anchored as explained in Appendix IV.

One difficulty with the snakes segmentation algorithm is its sensitivity to noise due to its local neighborhood action [108], [176]. Also, the snake algorithm can end up in an oscillatory position where the final contour simply jumps between two equally attractive energy minima [250], [304], [306]. One solution in resolving this difficulty is by increasing the size of the snake neighborhood, but this incurs much greater complexity [248]. Another solution is to despeckle the area, where the snake is applied, as proposed in [221], [231], [259], and in our recent studies [154], [238], [335], [338]. In order to allow snakes to expand, a normal force can be included which inflates the snake and pushes it over unattractive features [333]. The force can be implemented by the addition of a normal force as:

$$F_{normal} = \rho n(s), \tag{3.5.1}$$

which is added to the snakes energy functional (3.4.2), where $n(s)$, is the normal force, and $\rho$ weights its effect. If the magnitude of the normal force is too large, it may force the contour to pass over features of interest. Another way to allow expansion is to modify the elasticity constraints so that the internal energy in (3.4.2) becomes [237]:

$$E_{\text{int}} = \alpha(s)\left(\left|\frac{dv(s)}{ds}\right|^2 - (L+\varepsilon)\right)^2 + \beta(s)\left|\frac{d^2v(s)}{ds^2}\right|^2, \tag{3.5.2}$$

where the length adjustment $\varepsilon$, when positive, $\varepsilon > 0$, and added to the contour length, $L$, causes the contour to expand. When negative, $\varepsilon < 0$, this causes the contour length, $L$, to shrink and so the contour contracts.

Some snake approaches have included factors that attract contours to regions using statistical models [244], or texture [245], to complement operators that combine edge detection with region growing. Also the snake model can be generalized to higher dimensions and there are 3D snake surfaces [246]. Finally an approach has introduced snakes for moving objects, by including velocity [247].

### *3.5.1 Balloon snake*

Cohen [333] introduced the Balloon snake model, whose internal energy causes it to expand from inside of the boundary until it reaches it. He improved the original snake model by adding a normalization force field term to the energy functional in (3.4.2), which may then be rewritten by substituting the external field force as:

$$F_{image} = -\frac{k\nabla E_{image}}{\left\|\nabla E_{image}\right\|} = k_1 n(s) - k\frac{\nabla E_{image}}{\left\|\nabla E_{image}\right\|}, \tag{3.5.3}$$

where $n(s)$, is a normal unity vector normal to the snake curve at point $v(s)$, and $k_1$, is the amplitude of this force. Cohen proposed, the addition of the term, $k_1 n(s)$, in (3.5.3), to the force field, $F_{image}$, which makes the contour have a more dynamic behavior, because he observed that due to noise, some isolated points are gradient maxima and can stop the curve when it passes by. The curve may be considered as a Balloon that is inflated. By changing the sign of, $k_1$, in (3.5.3), the curve will deflate instead of inflate. Now as the curve expands, it will be attracted and stopped by edges as before, but since there is now a pressure force, if the edge is too weak the curve may pass through without stopping at this point. If the curve runs into an isolated point, it tends to create a tangent discontinuity at this point. The smoothing effect with the help of the inflation force, removes the discontinuity and the curve may pass through the edge.

### *3.5.2 Lai&Chin snake*

Snakes have been formulated not only to include local shape, phrased in terms of regularization [248], where a single parameter controls snake evolution, emphasizing a snakes natural compromise between its own forces and the image forces. Regularization involves using a single parameter to control the balance between the external and the internal forces. Given a regularization parameter, $\lambda_\pi$, the snake energy in (3.4.2) can be given as:

$$E_{snake}(v(s)) = \int_{s=0}^{1} \{\lambda_\pi E_{\text{int}}(v(s)) + (1-\lambda_\pi)E_{image}(v(s))\}ds. \tag{3.5.4}$$

If, the regularization parameter, $\lambda_\pi = 1$, the snake will use only the internal energy, whereas if $\lambda_\pi = 0$, the snake will be attracted only to the selected image function. Usually, regularization concerns selecting a value between zero and one. The regularization parameter, which is calculated at each contour, is given in as [248]:

$$0 < \lambda_{\pi_i} = \frac{\sigma_n^2}{\sigma_i^2 + \sigma_n^2} < 1, \tag{3.5.5}$$

where $\sigma_i^2$, and $\sigma_n^2$, are the variance, and the noise variance at a snake point $i$ respectively, and are bounded as [248]:

$$\frac{1}{\sigma_i^2} + \frac{1}{\sigma_n^2} = 1. \tag{3.5.6}$$

### *3.5.3 Gradient vector flow (GVF) snake*

The GVF snake was originally introduced by Xu and Prince [116], [117], in order to improve some poor properties, of the force field generated by the gradient operator, such as its sensitivity to initialization, and its ability to move into concave boundaries where the following conditions were enforced:

a) The gradient of an edge map, $\nabla(-E_{ext}(i,j))$, has vectors pointing towards the edges, which are normal to the edges at their location.

b) The vectors generally have large magnitude only in the immediate vicinity of the edges.

c) In homogeneous regions where the image is nearly constant, the gradient of the edge map, $\nabla(-E_{ext}(i,j))$, is nearly zero.

The overall approach is to use the force balance equation and introduce a new external force field, $F_{ext} = v(i,j)$, which is called GVF. The idea is based on the Helmholtz theorem [219], which states that the most general static field can be decomposed into two components, namely an irrotational (curl-free) and a solenoidal (divergence-free) component. In the classic case the static field is irrotational, since it is the gradient of a potential function. A more general static field may be obtained by allowing the possibility that it comprises both an irrotational and a solenoidal component.

The external energy term, in the energy functional in (3.4.2) may be chosen differently, in order to lead the snake toward step edges [117], [243] as:

$$E^1_{external}(v) = -\left|\nabla g_{i,j})\right|^2, \tag{3.5.7a}$$

$$E^2_{external}(v) = -\left|\nabla(G\sigma_{i,j} * g_{i,j})\right|^2, \tag{3.5.7b}$$

where $G\sigma_{i,j}$, is a 2D Gaussian function with standard deviation, $\sigma$. If the image is a line drawing (black on white), then the appropriate external forces include [333]:

$$E^3_{external}(v) = g_{i,j}, \tag{3.5.7c}$$

$$E^4_{external}(v) = G\sigma_{i,j} * g_{i,j}. \tag{3.5.7d}$$

Variational calculus techniques are employed to minimize the energy functional in (3.4.2) leading to the following Euler equations:

$$\alpha i_{ss} - \beta i_{sss} - \frac{dE_{external}}{di} = 0, \qquad \alpha j_{ss} - \beta j_{sss} - \frac{dE_{external}}{dj} = 0. \tag{3.5.8a}$$

This can be viewed as a force balance equation:

$$F_{internal} + F^{P}_{external} = 0, \tag{3.5.8b}$$

where $F_{internal} = ai_{ss} - bi_{ss}$ and $F^{P}_{external} = -\nabla E_{external}$.

The overall approach is to use (3.5.8b) as a starting point for designing the snake. Replacing the external forces $(-dE_{external}/di,\ -dE_{external}/dj,)$ in (3.5.8a) in the $i, j$ directions respectively, with a vector field, $(u, v)$, which is called GVF, we have [117]:

$$\alpha i_{ss} - \beta i_{sss} + u(i(s), j(s)) = 0, \quad \alpha j_{ss} - \beta j_{sss} + v(i(s), j(s)) = 0. \tag{3.5.9}$$

The $(u, v)$ terms at a given position, $(i, j)$, are determined by descending the following energy functional [116], [117], [258]:

$$E_{GVF}(u,v) = \iint \mu(|\nabla f|)(u_i^2 + u_j^2 + v_i^2 + v_j^2)didj + \iint (1 - g(|\nabla f|))((u - f_i)^2 + (u - f_j)^2)didj.$$

$$\text{with } f_{i,j} = \left|\nabla G\sigma_{i,j} * g_{i,j}\right|, \text{ and } g|\nabla f| = \exp(-\frac{\nabla f}{L_{GVF}}), \tag{3.5.10}$$

where $L_{GVF}$, is a positive constant, which is used to control the smoothness of the resulting vector field. The vector field guides the snake to the major boundaries. The parameter, $\mu$, is a regularization parameter governing the tradeoff between the first term and the second term in the integrand. This parameter should be set according to the amount of noise present in the image, where stronger noise implies an increased value of $\mu$.

The solution to (3.5.8) can be obtained explicitly by the following iteration equations [117]:

$$x_t(s,t) = \alpha i_{ss} - \beta i_{sss} + u(i(s,t), y(s,t)) = 0$$

$$y_t(s,t) = \alpha j_{ss} - \beta j_{sss} + v(i(s,t), j(s,t)) = 0 \tag{3.5.11}$$

where in these equations the active contour, $v(s) = [x(s), y(s)]$, is treated as a function of time, $t$, as well as, $s$, such as, $v(s,t) = [x(s,t), y(s,t)]$. In digital image processing the discrete versions of (3.5.11) are used. For a complete discrete implementation of the GVF algorithm, see [117].

## 3.6 Snake initialization

In this section, the initialization procedure for the IMT and plaque snake initial contour estimation is described.

### *3.6.1 IMT contour initialization*

It is important to place the initial snake contour as close as possible to the area of interest otherwise the snake may be trapped in local minima or false edges, and converge to a wrong location. The initial snake contour selection and the convergence are two of the main limitations of the snake models proposed in the literature [55], [64], [124], [178], [185], [241], [243], [253]. Traditionally, most of the researchers used to place the initial contour by hand using the experience of medical experts. This procedure was very cumbersome, tedious, expert dependent and highly time consuming especially if a large database of images were to be segmented [93].

Various researchers proposed snake initialization methods in the past. Zahalka et al. [55] proposed a method where an initial point was chosen in the middle of the lumen of a transversal ultrasound image of the carotid artery. Radial rays $5^0$ apart, were then calculated, which were extended radialy outward from the initial point. Wendelhag et al. [253], proposed a dynamic programming method with an initial estimation of the approximate positions of intima and adventitia in longitudinal ultrasound images of the carotid artery. The initial boundaries were then refined by a cost function containing image feature terms. Mojsilovic et al. [220] used a fraction of image in runs measure (FOIIR) obtained with the gray-level run length method in longitudinal ultrasound images. For the separation of the plaque and adventitia region the mean gray level (MGL) was used. Liang et al. [178] performed fuzzy set theory for the initial snake contour estimation where the approximate vessel wall positions were first estimated in a coarse-scale image, which then guided the detection of the boundaries in a fine-scale image. Mao et al. [64] estimated an initial contour for transversal ultrasound images to match the lumen of the carotid artery initially with a circular contour.

Cheng et al. [241] located the adventitia border by placing manually on the gradient image the starting and ending points of the initial contour. The procedure was performed for longitudinal ultrasound images and the point selection had to be made above the intima in the lumen area. Some other researchers [124], [185], [243], [336], estimated the initial snake contour by hand or by placing the initial contour 10-20 pixels away from the desired boundary [231]. Neuenschwander et al. [250] proposed the ziplock snake, which was an open contour implementation, and it was initialized, by specifying a few points through which, the contour must pass, thus minimizing the expert's effort. The ziplock snake suffered from problems like the initialization procedure, computational efficiency, and the location of concave and convex parts of the object were not well detected. An initialization for the ziplock snake was proposed recently [260], but still more than two points through which the contour passes must be specified.

In another study, Yuen et al. [252] located the initial snake contour in artificial images, by using the center of gravity of the object and extented radial vertical lines from center to the

perimeter searching for the points with the maximum gradient. Some other researchers used the GHT [203] for the snake initialisation but it was shown not to be very accurate and was very time consuming [248].

Still other researchers [242], tried to solve some of the problems connected with the snake initialization by using a dual contour approach. In this approach, the two contours were deformed in such a way, so that they could not be attracted together, and so that they enclosed the target shape with an inner and an outer contour. The disadvantage of this approach was that the shape of interest could not be located accurately, as the snake contours were deformed in predefined directions.

All the above methods involved expert dependence, some of them required parameter initialization which had to be chosen empirically, some were applied to artificial images and only a few were proposed for ultrasound images.

The IMT snakes initialization method proposed in this dissertation, (see Chapter 5.7.2), requires minimum expert interaction, is not expert dependent and is an open snake contour implementation.

### *3.6.2 Plaque contour initialization*

In the literature, very few approaches have been proposed for segmenting the atherosclerotic carotid plaque from ultrasound images, where the initial contour was placed manually by the user [46], [47], [53], [100], [192]. A method for segmenting the arterial walls and plaque from transversal MRI images based on dynamic programming was proposed in [321], where the initial contour was found by manually placing four points on the artery walls. There are no other studies reported in the literature, where an initialisation procedure was proposed for extracting the borders of the carotid atherosclerotic plaque in longitudinal ultrasound images.

In this work we propose an initialisation procedure for detecting the initial plaque borders in the carotid artery, which is described in Chapter 5.8.2.

# *Chapter 4*

# *Image Quality, Texture Analysis, and ROC Analysis*

# CHAPTER 4: IMAGE QUALITY, TEXTURE ANALYSIS, AND ROC ANALYSIS

Image quality plays an important role in various image-processing applications. A great deal of effort has been made in recent years to develop objective image quality and segmentation measures that correlate well with perceived quality measurements. However, only limited progress has been made. In this Chapter, we define various image quality, texture measures and receiver operating characteristics (ROC) measures, which may be used to evaluate the despeckle filtering and segmentation techniques, presented in Chapter 2 and Chapter 3 respectively.

## 4.1 Image quality

When is an image good or bad? A straightforward definition of image quality is based on the question: How well does an image communicate information required by an expert? This is called the intelligibility of the image or the diagnostic image quality [273]. A more technical definition of image quality relates to the question: How much does an image deviate from an ideal image or scene? This is called the fidelity of an image or technical image quality. Both aspects may be determined by comparing the processed images with the ground truth.

Ultrasound is subject to a number of artefacts that degrade image quality and compromise diagnostic confidence [128], [160]. For medical images, quality can be objectively defined in terms of performance in clinically relevant tasks such as lesion detection and classification [329]. For applications in which images are ultimately to be viewed by human experts, the only correct method of quantifying visual image quality is through objective evaluation. In practice, however, objective evaluation is usually too inconvenient, time consuming and expensive. The goal of research in image quality is to define and develop quantitative measures that can automatically predict perceived image quality.

Traditionally the ROC analysis was the dominant technique for evaluating image quality, where a subjective image quality index can be evaluated from the area under the ROC curves [363]. To construct a typical ROC study a large number of images are required to be evaluated in order to obtain a statistically significant result [300]. Usually in ROC studies, experts are asked to review the images before and after processing in order to provide a yes or no decision.

The wide spread of mobile and portable telemedicine ultrasound scanning instruments also necessitates the need for better image processing techniques, in order to offer a clearer image to the medical practitioner, and transfer the image with the minimum loss of quality. This makes the use of efficient image quality evaluation criteria an important task [174].

An objective image quality metric can play an important role in a broad range of applications. First, it may be used to dynamically monitor and adjust image quality. Second it may be used to optimise algorithms and parameter settings of image processing systems [278]. For instance, a quality metric can assist in the optimal design of a despeckle filter. Objective image quality measures can be classified according to the availability of an original image (noise image), with which the despeckled image is to be compared. Most existing approaches are known as full-reference, meaning that a complete reference image is available. In some practical applications, however, the reference image is not available, and a no-reference or blind quality assessment approach is desirable. In a third type of method the reference image is only partially available in the form of a set of extracted features made available as side information to help evaluate the quality of the despeckled image. In our case of the ultrasound longitudinal images of the carotid artery are readily available. The despeckling process will help the expert to perform a more accurate and error free diagnosis. Therefore we will focus in this work on full-reference image quality assessment measurements.

A lot of researchers have tried in the past to develop quality assessment methods that utilise the known characteristics of the human visual system (HVS). It is generally easy for the HVS to assess the quality of two similar images and decide on which one looks better. In [361] image quality metrics are separated into the three categories:

a) Human perception: In this category a selected group of viewers evaluate a range of images according to their subjective criteria. It involves measuring the performance of a display device by measuring the ability of the expert to perform a task using that device. The advantage is that it may be applied even in the absence of any reliable model. The major disadvantages are, cost of data collection, it is very time consuming, and the large amount of cases needed for the evaluation.

b) Objective measures based on theoretical models: In this category mathematically based theoretical models are used to take advantage of the fact that images can be represented as a matrix of numerical values. One may then apply some transformations to these matrices. These measures are still very attractive because they are easy to calculate, have usually low complexity, and they are independent of viewing conditions and individual experts.

c) Subjective measures based on mathematically defined models of the HVS: The functional components of the HVS are very difficult to be implemented, so the measures belonging to this category are the most difficult to implement.

In this study human perception evaluation was carried and objective measures were extracted for evaluating the results of depeckle filtering and segmentation techniques.

## 4.2 Optical perception testing procedures

In order to be able to design accurate and reliable quality metrics, it is necessary to understand what quality means to the expert. An expert's satisfaction when watching an image depends on many parameters, such as: viewing distance, display size, resolution, brightness, contrast, sharpness, colourfulness, naturalness, and other factors [284], [285], [291].

It is also important to note that there is often a difference between fidelity (the accurate reproduction of the original on the display), and perceived quality. Sharp images with high contrast are usually more appealing to the average expert. Likewise, subjects prefer slightly more colourful and saturated images despite realizing that they look somewhat unnatural [292]. For studying visual quality some of the definitions above should be related to the HVS. For instance, it is very popular between medical image experts to specify viewing distance in terms of display size, i.e. in multiples of screen height. The ratio of the preferred viewing distance to screen height is usually constant [293]. However, recent experiments with larger displays showed that this might not be the case. While the preferred viewing distance is indeed around 6 to 7 screen heights for smaller displays, it approaches 3 to 4 screen heights with increasing display size [293].

Unfortunately, subjective quality may not be described by an exact figure, due to its inherent subjectivity, it can only be described statistically. Even in psychological threshold experiments, where the task of the expert is to give a yes or no answer, there exists a significant variation between experts, contrast sensitivity functions, and other critical low-level visual parameters [287]-[293]. When speckle noise is apparent in the image, the expert's differing experiences with noise are bound to lead to different weightings of the artifact [286]. Researchers showed that experts and non-experts (with respect to image quality) examine different critical image characteristics to form their final opinion [286], [291]. In light of these difficulties, testing procedures for subjective quality assessment are discussed in detail in Appendix II.

The visual perception evaluation, in this study, was carried out according to the ITU-R recommendations similar with the Double Stimulus Continuous Quality Scale (DSCQS) procedure [316] (see also Appendix II). The presentation sequence for a DSCQS trial is shown in Fig. 4.1a. Experts are shown multiple sequence pairs consisting of a reference (Ref.) and a test sequence (Test), which are rather short (typically 10 seconds). The reference and test sequence are presented twice in alternating fashion, with the order of the two chosen randomly for each trial. Experts are not informed which is the reference and which is the test sequence. They rate each of the two separately on a continuous quality scale ranging from bad to excellent as shown in Fig. 4.1b. Analysis is based on the difference in rating for each pair, which is calculated from an equivalent numerical scale from 1 to 100. This differencing removes a lot of the subjectivity with respect to scene content and experience. It is noted that in this study the

observation time was not limited to 10 seconds, as in the DSCQS method, but we have allowed the experts to observe the image for as long as they wanted, and were also able to go back and forth to observe the images.

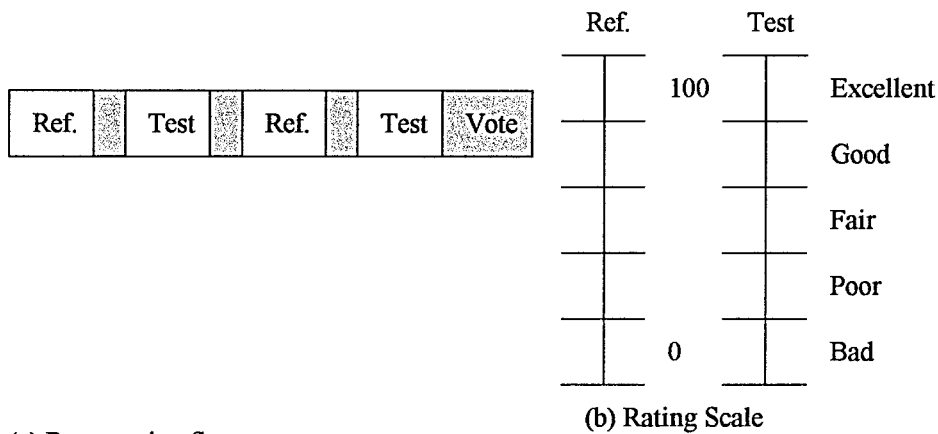


(a) Presentation Sequence

(b) Rating Scale

**Fig. 4.1**: DSCQS method: (a) the reference and the test sequence are presented twice in alternated fashion, (b) the order of the two is chosen randomly for each trial, and experts are not informed which is which. They rate each of the two separately on a continuous quality scale ranging from bad to excellent (Modified from [7] pp. 572, Fig. 10.1).

## 4.3 Image quality metrics

In this section we propose a number of image quality metrics, that can be used for objectively evaluating the despeckle filters proposed in Chapter 2. Differences between images were evaluated using the following image quality evaluation metrics, which were used as statistical measures, between the original noisy image, $g_{i,j}$, and the despeckled, $f_{i,j}$, image.

a) The normalised mean square error MSE:

$$MSE = \frac{1}{MN}\sum_{i=1}^{M}\sum_{j=1}^{N}\left(\frac{g_{i,j} - f_{i,j}}{lpg_{i,j}}\right)^2 \tag{4.1}$$

which measures the quality change between the original, $f_{i,j}$, and the despeckled image, $g_{i,j}$, in an $MxN$ window [300]. The $lpg_{i,j}$, is the low pass filtered of the original image, $g_{i,j}$. In case that, $lpg_{i,j}$, is equal zero, its value is replaced with the smallest gray level value in the image. The $MSE$, has been widely used to quantify image quality and when is used alone, it does not correlate strongly enough with perceptual quality. It should be used therefore together with other quality metrics and visual perception [294], [300].

b) The normalised root mean square error, RMSE, which is the square root of the squared error averaged over the $MxN$ array [3]:

$$RMSE = \sqrt{\frac{1}{MN}\sum_{i=1}^{M}\sum_{j=1}^{N}(\frac{g_{i,j}-f_{i,j}}{lpg_{i,j}})^2}\ . \tag{4.2}$$

The popularity of $RMSE$ arises mostly from the fact that is in general the best approximation of the standard error.

c) The normalised error summation in the form of the Minkowski metric, which is the norm of the dissimilarity between two images, as follows [272], [278], [287], [300]:

$$Err = \left(\frac{1}{MN}\sum_{i=1}^{M}\sum_{j=1}^{N}\left|\frac{g_{i,j}-f_{i,j}}{lpg_{i,j}}\right|^{\beta}\right)^{1/\beta} \tag{4.3}$$

with $1<\beta_{err}<4$. For $\beta_{err} = 2$, one obtains the RMSE expression in (4.2), whereas for $\beta_{err} = 1$, the absolute difference, and for $\beta_{err} = \infty$, the maximum difference measure.

d) The normalised geometric average error, $GAE$, is a measure, which shows if the despeckled image is very bad [316], and it is used to replace or complete the $RMSE$. It is positive only if every pixel value is different between the original and the despeckled image. The $GAE$, is zero, if there is a very good transformation between the original and the despeckled image, and high if the transformation with the original is extremely bad. This measure is also used for tele-ultrasound, when transmitting ultrasound images and is defined as:

$$GAE = (\prod_{i=1}^{N}\prod_{j=1}^{M}\sqrt{\frac{g_{i,j}-f_{i,j}}{lpg_{i,j}}})^{1/NM}\ . \tag{4.4}$$

The $GAE$ may be used to replace the $RMSE$, which is dominated by its large individual terms and is calculated for an image with dimensions $NXM$. This amounts to a severe error in $RMSE$ when large individual terms are present. For this reason the $RMSE$ is often replaced by the GAE.

e) While signal sensitivity and image noise properties are important by themselves, it is really the ratio of them that carries the most significance. The normalised SNR [133] pp. 169-170, [331] is defined as:

$$SNR = 10\log_{10}\frac{\sum_{i=1}^{M}\sum_{j=1}^{N}(\frac{g_{i,j}^2+f_{i,j}^2}{lpg_{i,j}})}{\sum_{i=1}^{M}\sum_{j=1}^{N}(\frac{g_{i,j}-f_{i,j}}{lpg_{i,j}})^2}\ . \tag{4.5}$$

It is calculated over an image area with dimensions $NXM$. The $SNR$, $RMSE$, and $Err$, prove to be very sensitive tests for image degradation, but there are completely

non-specific. Any small change, in image noise, despeckling, and transmitting preferences would cause an increase of the above measures.

f) The normalised peak signal to noise ratio, PSNR, is defined as [331]:

$$PSNR = -10\log_{10}\frac{MSE}{s_{\max}^{2}} \tag{4.6}$$

where $s_{\max}$, is the maximum pixel value in the image. The $PSNR$, is higher for a better-despeckled image and lower for a poorly despeckled image. It measures image fidelity that is how closely an image (despeckle) resembles usually the corrupted original.

g) The mathematically defined universal quality index, Q, [272] models any distortion as a combination of three different factors, which are, loss of correlation, luminance distortion, and contrast distortion. The Q is defined as:

$$Q = \frac{\sigma_{gf}}{\sigma_f \sigma_g}\frac{2\bar{f}\bar{g}}{(\bar{f})^2+(\bar{g})^2}\frac{2\sigma_f\sigma_g}{\sigma_f^2+\sigma_g^2}, \quad -1 < Q < 1 \tag{4.7}$$

where $\bar{g}$, and $\bar{f}$, represent the mean of the original and despeckled image values, with their standard deviations, $\sigma_g$, and $\sigma_f$, of the analysis window, and $\sigma_{gf}$, represents the covariance between the original and transformed images. $Q$ is computed for a sliding window of size 8x8 without overlapping. Its highest value is 1 and is achieved when both images are identical ($g_{i,j} = f_{i,j}$), while its lowest value is –1 for $f_{i,j} = 2\bar{g} - g_{i,j}$.

h) The structural similarity index, SSIN, between two images [278], is a generalization of (4.7) and is defined as:

$$SSIN = \frac{(2\bar{g}\bar{f} + c_{ssin_1})(2\sigma_{gf} + c_{ssin_2})}{(\bar{g}^2 + \bar{f}^2 + c_{ssin_1})(\sigma_g^2 + \sigma_f^2 + c_{ssin_2})}, \quad -1 < Q < 1 \tag{4.8}$$

where $c_{ssin_1}$, $c_{ssin_2}$, are constants. The Q, defined in g), corresponds to the special case that in (4.8), $c_{ssin_1} = c_{ssin_2} = 0$, which produces unstable results when either $(\bar{g}^2 + \bar{f}^2)$ or $(\sigma_g^2 + \sigma_f^2)$, is very close to zero. The range of values for the $SSIN$ lies between –1, for a bad and 1, for a good similarity between the original and the despeckled images respectively. It is computed, similarly to the $Q$ measure, for a sliding window of size 8x8 without overlapping.

i) The speckle index, C, [131] for log-compressed ultrasound images is defined as:

$$C = \frac{1}{MN} \sum_{i=1}^{M} \sum_{j=1}^{N} \frac{\sigma^2_{i,j}}{\mu_{i,j}} \tag{4.9}$$

and is an average measure of the amount of speckle presented in the image area with size $MxN$, as a whole (over the whole image). It is used in most adaptive filters to adjust the weighting function $k_{i,j}$, in (2.3.1), described in section 2, because it reflects the changes in contrast of the image in the presence of speckle noise. It does not depend on the intensity of the local mean but on the variance, $\sigma^2$, and the mean, $\mu$, of the whole image. The larger C is, the more likely that the observed neighbourhood belongs to an edge, thus C may be used also as an edge detector.

j) Lesions detectability can be quantified using the contrast-to-speckle ratio, *CSR* [199]. It is calculated by defining two regions of interest (i.e. the original image and the despeckled), and using the mean pixel value, and the variance, to quantify the contrast, $(\mu_1 - \mu_2)/\mu_1$, and the speckle index noise, $\sqrt{(\sigma_1^2 + \sigma_2^2)/\mu_1}$. The ratio of these two quantities is termed as *CSR* and is defined as:

$$CSR = ((\mu_1 - \mu_2)\mu_1)/\sqrt{(\sigma_1^2 + \sigma_2^2)} \tag{4.10}$$

where $\mu_1$, $\mu_2$, $\sigma_1$, $\sigma_2$, are the mean and standard deviations of the original and despeckle images respectively. The *CSR*, provides a quantitative measure of the detectability of low contrast lesions, when one region is completely inside the lesion and the second is the background media.

The quality measures proposed above, do not necessarily correspond to all aspects of the expert's visual perception of the errors, nor do they correctly reflect structural coding artefacts [283], but if they are all combined together, and with the subjective tests, may offer a more accurate evaluation result. Subjective tests are tedious, time consuming and expensive, and the results depend on the expert's background, motivation, and other factors [272], [273], [284]. However, all these measures cover the visual quality just partly. The visual quality of an image is difficult to define with mathematical precision, since it is dependent on the properties of our visual system. We know, for example, that our visual system is more tolerant to a certain amount of noise than to a reduced sharpness. On the other hand it is very sensitive to certain specific artefacts, like blips and bumps [294].

## 4.4 Texture analysis

Following the despeckling, texture features may be extracted from the original and the despeckled images in order to be used for texture analysis. Texture analysis is one of the most

important features used in image processing and pattern recognition. It can provide information about the arrangement and spatial properties of fundamental image elements. Many methods have been proposed to extract texture features, e.g. the co-occurrence matrix [262], and the texture spectrum in the achromatic component of the image [263].

### *4.4.1 Texture measures*

Some of the most common texture feature algorithms that have been used for ultrasound texture analysis are: simple statistical features (SF), spatial gray level dependence matrices (SGLDM) [128], gray level difference statistics (GLDS) [129], neighbourhood gray tone difference matrix (NGTDM) [214], statistical feature matrix (SFM) [213], laws texture energy measures (TEM) [211], [212], fractal dimension texture analysis (FDTA) [210], [211], and Fourier power spectrum (FPS) [129]. These texture features are usually computed on a region of interest, for example the region prescribed by the plaque contour that is automatically or manually drawn.

The SF includes the $\mu$, median, $\sigma^2$, $\sigma^3$, and $\sigma^4$ values. The SGLDM, texture features as proposed by Haralick et al. [128], are the most frequently used texture features. These are based on the estimation of the second-order joint conditional probability density functions that two pixel pairs, ($k$, $l$) and ($m$, $n$), with distance, $d$, in direction specified by the angle, $\theta$, have intensities of gray level, $g$, and gray level, $f$. Based on the probability density functions, the following texture measures, and their variants [128] are computed: angular second moment (ASM), contrast, correlation, inverse difference moment (IDM), sum average, variance (sum and difference), and entropy (sum and difference). For a chosen distance, $d$, that is usually one pixel and for angles, $\theta = 0^0, 45^0, 90^0$ and $135^0$, four values for each of the above texture measures are computed. The mean and range of these four values are usually computed for each feature, and they are used as two different feature sets. The GLDS algorithm [129], uses first order statistics of local property values based on absolute differences between pairs of gray levels or of average gray levels in order to extract the following texture measures: contrast, ASM, entropy, and mean. Amadasun and King [214] proposed the NGTDM, in order to extract textural features, which correspond to visual properties of texture. The following features are extracted: coarseness, contrast, busyness, complexity, and strength. The FDTA is based on the work of Mandelbrot [210], who developed the fractional Brownian motion model in order to describe the roughness of natural surfaces. The Hurst coefficients ($H^{(k)}$) [211], are computed for different image resolutions, where a smooth texture-surface is described by a large value of the parameter, $H^{(k)}$, whereas the reverse applies for a rough texture-surface. The FPS, computes the radial and angular sum of the sample FPS, where coarse texture has high values

concentrated near the origin, and in fine texture the values are more spread out. The 56 different texture measures used in this study are further described in the Appendix III.

### *4.4.2 Feature selection*

In order to identify the most discriminant features for the classification task (features that have the highest discriminatory power), the distance between asymptomatic and symptomatic images was calculated for the set of all ultrasound images, before and after despeckle filtering for each feature as follows [10], [131]:

$$dis_{i,c} = |m_{i1} - m_{i2}| / \sqrt{(\sigma^2_{i1} + \sigma^2_{i2})} \tag{4.11}$$

where $i$, is the feature index, $c$, if $o$, indicates the original image set and if $f$, indicates the despeckled image set, $m_{i1}$, and $m_{i2}$, are the mean values and $\sigma_{i1}$, and $\sigma_{i2}$, are the standard deviations of the asymptomatic and symptomatic classes respectively. The most discriminant features are the ones with the greatest distance values [10]. If the distance after despeckle filtering is increased i.e.:

$$dis_{if} > dis_{io} \tag{4.12}$$

then it can be derived that the classes may be better separated.
For each feature, a percentage distance was computed as:

$$feat_dis_i = (dis_{if} - dis_{io})100. \tag{4.13}$$

For each feature set, a score distance was computed as:

$$Score_Dis = (1/N_{feat}) \sum_{i=1}^{N_{feat}} (dis_{if} - dis_{io})100 \tag{4.14}$$

where $N_{feat}$, is the number of features in the feature set. It should be noted that for all features a larger feature value shows improvement.

The Wilcoxon rank sum test was also used in order to identify if for each texture feature a significant (S) difference or not (NS) exists between the original and the despeckled images at $p<0.05$.

### *4.4.3 kNN Classifier*

The statistical pattern recognition k-nearest-neighbour (kNN) classifier with $k = 7$, was used to classify a plaque as asymptomatic or symptomatic [10], [132]. The kNN classifier was chosen because it is simple to implement and computationally very efficient. This is highly desired due to the many feature sets and filters tested [211].

In the kNN algorithm in order to classify a new pattern, its k-nearest-neighbours from the training set, are identified. The new pattern is classified to the most frequent class among its neighbours based on a similarity measure that is usually the Euclidean distance. In this work the kNN carotid plaque classification system was implemented for values of $k = 1, 3, 5, 7$ and 9 using for input the eight texture feature sets and morphology features described above.

The leave-one-out method was used for evaluating the performance of the classifier, where each case is evaluated in relation to the rest of the cases, characterized by no bias concerning the possible training and evaluation bootstrap sets. This method calculates the error or the classifications score by using $n-1$ samples in the training set and testing or evaluating the performance of the classifier on the remaining sample. It is known that for large $n$, this method is computationally expensive. However, it is approximately unbiased, at the expense of an increase in the variance of the estimator [144].

## 4.5 ROC analysis

In this section we focus on the problem of measuring the performance of medical image segmentation techniques by taking into consideration the ROC analysis, which describes the subjective performance of an expert. Our aim is to be able to make meaningful statements of the form-"Algorithm A performs better than algorithm B at detecting the IMT or plaque boundaries" or "Algorithm A performs better than the medical expert does". Performance metrics of this type are of course very complex than those for abnormality detection problems. In the following sections, performance metrics for measurement problems and for image segmentation are defined.

### *4.5.1 Performance metrics for detection problems*

When the goal is to estimate the value of some scalar or vector quantity, it is natural to focus on the difference between the calculated result (automatic segmentation), and some independent measure of the true value (manual segmentation). Because the absolute value of the difference typically varies with the size of the true value, it is typical to focus on a mean relative error [7], [363]:

$$mean_relative_error = \frac{(automatic_segmentation) - (manual_segmentation)}{manual_segmentation}, \quad (4.15)$$

where automatic, and manual segmentation represent the snakes segmented, and manually segmented boundaries respectively.

The metrics presented in this section, include the relative frequency of correct and incorrect decisions. In the context of detecting the presence of an abnormality in an image, the terms true positive (TP), false positive (FP), true negative (TN), and false negative (FN), are commonly

used [7], [363]. The above definitions are explained below and summarized in Fig. 4.2 as follows:

| | | **Algorithm Decision** | |
|---|---|---|---|
| | | Abnormality present | Abnormality not present |
| **Truth of clinical Situation** | Abnormality present | TP | FN |
| | Abnormality not present | FP | TN |

**Fig. 4.2**: Definition of TP, FN, FP, and TN.

TP: The abnormality is actually present and the expert as well as the segmentation algorithm, correctly identifies as so.

TN: The abnormality is absent and the expert as well as the segmentation algorithm, decides that an abnormality is absent.

FP: The abnormality is not actually present according to the expert, and the segmentation algorithm, incorrectly decides that it is.

FN: The abnormality is present according the expert, and the segmentation algorithm, incorrectly decides that it is absent.

Several additional performance metrics are derived from the TP, FN, FP, and TN. The sensitivity of a detection algorithm refers to how frequently the algorithm report that an abnormality exists in the instances where one actually does exist. Sensitivity can be stated as a fraction between 0 and 1, or as a percentage between 0 and 100.

The definition of sensitivity (or recall) [39] can be stated in terms of the number of TP and FN. By definition, the sum of the TP and FN is the set of all instances where an abnormality exists. Thus, the sensitivity, $R$, is given as [7]:

$$R = \frac{TP}{(TP + FN)} = TPF,\ 0 \le R \le 1. \tag{4.16}$$

The $R$, can range from a low of 0, indicating that none of the abnormalities are detected, to a high of 1 (or 100 percent), indicating that all of the abnormalities are detected. The true positive fraction, TPF is the same as the sensitivity, $R$.

The specificity, $Sp$, of a detection algorithm refers to how frequently it correctly reports normal when no abnormality exists. As with $R$, $Sp$, is also stated as a fraction between 0 and 1, or as a percentage between 0 and 100. The definition of $Sp$, can be stated in terms of the numbers of TN and FP. By definition, the sum of the TN and the FP is the set of all normal instances. Thus, $Sp$ is given as:

$$Sp = \frac{TN}{(TN + FP)} = 1 - FPF \,,\; 0 \le Sp \le 1 \,. \tag{4.17}$$

An $Sp$, of 1 would indicate that every normal instance is reported as normal. The false positive fraction, FPF, is the same as, $1 - Sp$ which is the fraction of the normal cases that is falsely reported as abnormal.

The ideal detection algorithm would have both, an $R$, and $Sp$, of 1 (or 100 percent). This would imply finding the abnormality in every instancé where one existed, and never falsely saying that an abnormality existed. Of course, one generally cannot expect to achieve such perfection in practice.

Precision, $P$, [39] measures the proportion of the nominated positive examples that are correct as:

$$P = \frac{TPF}{(TPF + FPF)} \,,\; 0 \le P \le 1 \tag{4.18}$$

Stating only one of the $R$, and $Sp$, for an algorithm is generally meaningless. A perfect $R$, is easily achieved by a detection algorithm, which always decides that an abnormality exists. A perfect $Sp$, is easily achieved by a detection algorithm that never decides that an abnormality exists. In the typical situation, greater $R$, can be gained by accepting lower $Sp$, and vice versa. To determine if one technique outperforms another, it is useful to combine the above measures into a single measure of goodness, which is the effectiveness measure, $E$, [39], which is proposed as:

$$E = 1 - \frac{PR}{(1-\alpha)P + \alpha R} \,,\; 0 \le E \le 1 \tag{4.19}$$

where $\alpha = 1/(\beta^2 + 1)$, and $E$, is $\beta$ times more heavily weighted towards $R$, than $P$. In this work, $P$, and $R$, are equally weighted ($\beta = 1$). Since $E$, is an inverse measure of goodness, we will generally quote segmentation performance in terms of $F = 1 - E$, in what follows.

Ideally, the snakes segmentation method should have a 100% score for all above statistics. A 100% score for the $R$, indicates that the method detects all plaque pixels. A 100% score for the $Sp$, would indicate that it never detects a plaque pixels in a non-plaque zone.

### *4.5.2 Evaluation of the plaque segmentation*

To evaluate the performance of the plaque snakes segmentation method, we compare the manually segmented borders defined by an expert with the snakes segmented borders detected from the segmentation algorithm. The intra- and inter-observer variability caused by the same and by multiple experts, as explained in Chapter 4.2, was also taken into account, and results are presented in Chapter 6.

Let $GT$, denote the manually segmented area representing ground truth, $\overline{GT}$, its complement, and $AS$, the segmented area obtained by the snakes segmentation method. ROC analysis is used to assess the $R$, and $Sp$, of the method by the fraction of $TP$, and $FP$, detected [363] respectively. The $TPF$, is calculated when the snakes segmentation method detects a plaque (plaque is present) and the expert identifies it as so. The $FPF$, is calculated when the snakes segmentation method detects no plaque and the expert incorrectly decides that there is plaque present. The $TNF$, is calculated when the snakes segmentation method identifies no plaque and the expert identifies it as so (absent). The $FNF$, is calculated when the snakes segmentation method identifies plaque presence and the expert incorrectly identifies plaque absence. Ratios of overlapping areas were also assessed by applying the similarity kappa index, $KI$, [364] and the overlap [365] index. These indices were computed as follows:

$$\begin{aligned} TPF &= \frac{AS \cap GT}{GT}, & TNF &= \frac{AS \cap GT}{AS}, \\ FPF &= \frac{|AS - GT|}{\overline{GT}}, & FNF &= \frac{|AS - GT|}{AS}, \\ KI &= 2\frac{GT \cap AS}{GT + AS}, & overlap &= \frac{GT \cap AS}{GT \cup AS}, \end{aligned} \tag{4.20}$$

where $\cap$ denotes the intersection and $\cup$ the union of the two areas.

The intersection of two variables ($AS$, $GT$) is the probability that both $AS$ and $GT$ occurs ($P(AS \cap GT)$) (see Fig. 4.3a). The union of the two variables may be described as the probability, $P(AS \cup GT) = P(AS) + P(GT) - P(AS \cdot GT)$, that either $AS$ or $GT$ occurs (see Fig. 4.3b).

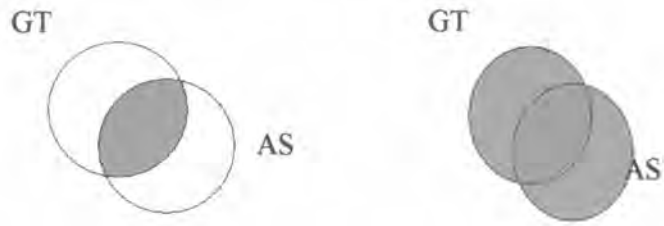


(a) (b)

**Fig. 4.3:** (a) Intersection, and (b) union of two variables, $AS$ and GT.

# *Chapter 5*

# *Methodology*

# CHAPTER 5: METHODOLOGY

In this Chapter, we present the methodology of our work, where the material used, the ultrasound scanners for acquiring the ultrasound images, the process of recording the ultrasound images, image normalisation, generation of an artificial carotid image, despeckle filtering, the procedure followed by the two experts for the visual perception evaluation, texture analysis, and image quality evaluation metrics, are presented respectively. Furthermore, the manual segmentation procedure for the IMT, visual perception evaluation for the snakes segmentation, the snakes segmentation procedure for the IMT, univariate statistical analysis and correlation analysis are presented respectively. In Chapter 5.8 the protocol for the manual segmentation procedure for the plaque, visual perception evaluation, the snakes segmentation for plaque with four different snake algorithms, and the evaluation of the plaque segmentation methods are presented respectively.

## 5.1 Material

Four imaging datasets were used in this study. The first imaging dataset was used for evaluating the image quality of two ultrasound scanners, the second for evaluating despeckle filtering, the third for segmenting the IMT, and the fourth for plaque segmentation.

The first image dataset was collected at the Cyprus Institute of Neurology and Genetics, using an ATL (model HDI-3000 Advanced Technology Laboratories, Seattle, USA) and an ATL (model HDI-5000 Advanced Technology Laboratories, Seattle, USA) duplex scanners [330]. For the image quality evaluation, 80 B-mode longitudinal ultrasound images of the CCA were collected from both scanners.

The second image dataset was collected at the Irvine Laboratory for Cardiovascular Investigation and Research, in Saint Mary's Hospital, Imperial College of Science Technology and Medicine, UK, using an ATL HDI-3000 duplex scanner. For despeckle filtering, a total of 440 (220 asymptomatic and 220 symptomatic) B-mode, and blood flow (PW Doppler), longitudinal ultrasound images of the CCA were collected. This dataset represents a range of atherosclerotic disease with irregular geometry typically found in this vessel.

The third image dataset consists of a total of 100 B-mode longitudinal ultrasound images of the CCA used for IMT segmentation. They were acquired using the ATL HDI-3000 ultrasound scanner, from the Cyprus Institute of Neurology and Genetics.

The fourth image dataset consists of 80 B-mode and blood flow longitudinal ultrasound images, used for segmenting the atherosclerotic carotid plaque. These images were selected representing atherosclerotic plaque types II, III and IV, (see Chapter 5.8), with irregular geometry typically found in this blood vessel. The images were captured using an ATL HDI-

3000 ultrasound scanner in Saint Mary's Hospital, Imperial College of Medicine, Science and Technology, UK, from asymptomatic and symptomatic real patient cases.

For all the above cases, asymptomatic images were recorded from patients at risk of atherosclerosis in the absence of clinical symptoms, whereas symptomatic images were recorded from patients at risk of atherosclerosis, which have already developed clinical symptoms, such as a stroke episode.

## 5.2 Acquisition

In this work the ATL HDI-3000 and the ATL HDI-5000 ultrasound scanners [330] (see Fig. 1.3) were used for capturing the ultrasound images. The images were logarithmically compressed and were recorded digitally on a magneto optical drive with a resolution of 768x576 pixels with 256 gray levels. Longitudinal scans were performed using duplex scanning and colour flow imaging [149]. The images were captured with the ultrasound probe positioned at right angles to the adventitia and the image was magnified, or the depth was adjusted so that the plaque would fill a substantial area of the image giving approximately a resolution of 16.66 pixels/mm. B-mode scan settings were adjusted so that the maximum dynamic range was used with a linear post-processing curve. The position of the probe was adjusted so that the ultrasonic beam was vertical to the artery wall. The time gain compensation, TGC, curve was adjusted, (gently sloping), to produce uniform intensity of echoes on the screen, but it was vertical in the lumen of the artery where attenuation in blood was minimal, so that echogenicity of the far wall was the same as that of the near wall. The overall gain was set so that, the appearance of the plaque was assessed to be optimal, and slight noise appeared within the lumen. It was then decreased so that at least some areas in the lumen appeared to be free of noise (black).

The ATL HDI-3000 ultrasound scanner is equipped with a 64-element fine pitch high-resolution 38 mm broadband array, a multi element ultrasound scan head with an operating frequency range of 4-7 MHz, an acoustic aperture of 10x8 mm, and a transmission focal range of 0.8-11 cm [330].

The ATL HDI-5000 ultrasound scanner is equipped with a 256-element fine pitch high-resolution 50 mm linear array, a multi element ultrasound scan head with an extended operating frequency range of 5-12 MHz, and real spatial compound imaging. The scanner increases the image clarity using SonoCT™ (real-time compound imaging) by enhancing the resolution and borders. Several tests made by the manufacturer [330] showed that the ATL HDI-5000 scanner was overall superior to conventional 2D imaging, primarily because of the reduction of speckle, contrast resolution, tissue differentiation, and higher visual quality images.

As discussed in Chapter 2, ultrasound images are often considered as being corrupted by multiplicative noise with Rayleigh distribution, known as speckle. However, commercial

ultrasound equipment also perform a non-linear image compression, which reduces the dynamic range of the ultrasound signal, for visualization purposes. This non-linear compression, also known as logarithmic compression, distorts the probability distribution of the observed data. In order to overcome this difficulty some authors prefer to work with the backscatter echo (RF-signal), i.e. the sensor output before being compressed [351]. This avoids the problem of dealing with the nonlinear compression performed by the ultrasound system, which is usually unknown. However, this approach is not always easy to implement since the RF output is not available in most ultrasound equipment. The effect of non-linear processing, however, has been considered by some researchers [271], [351], for noise reduction with median and adaptive filtering [351]. In most of the cases the compression law is unknown and it has to be estimated from the observed signal. As described in section 2.2 with equation (2.2.1), it is considered that the backscattered signal (noisy signal on the ultrasound display), is modified by a non-linear transformation as follows:

$$g_{i,j} = \alpha_{comp} \log(z_{i,j}) + \beta_{comp} \tag{5.1}$$

where $g_{i,j}$, and $z_{i,j}$, are the logarithmic compressed recorded signal and the original ultrasound signal respectively in a pixel location $i, j$. The parameters $\alpha_{comp}$, and $\beta_{comp}$, usually take the values of $\alpha_{comp} = \beta_{comp} = 20$ [351].

In this study we applied all image processing algorithms on the logarithmically compressed images, as given in (5.1).

## 5.3 Image normalization

The need for image normalisation (standardisation), or post-processing was suggested [128], and some kind of normalisation using only blood echogenicity as a reference was applied in ultrasound images of carotid artery [93], [235]. In this study, brightness adjustments of ultrasound images were carried out based on the method introduced in [322]. It was shown that this method improves image compatibility by reducing the variability introduced by different gain settings, different operators, different equipment, and facilitates ultrasound tissue comparability [337], [358].

The method illustrated in Fig. 5.1, was implemented in MATLAB (6.1.0.450 version, release 12.1, May 2001, by The Mathworks, Inc.), which was used for the implementation of the normalisation procedure as well as for all other methods employed in this study. Algebraic (linear) scaling of the image was performed by linearly adjusting the image so that the median gray level value of the blood was 0-5, and the median gray level of the adventitia (artery wall) was 180-190. The scale of the gray level of the images ranged from 0-255. Thus the brightness of all pixels in the image including those of the plaque, were readjusted according to the linear

scale defined by the two reference regions. This results in a significant improvement in the comparability of the ultrasound tissue characteristics. It is noted that a key point to maintaining a high reproducibility was to ensure that the ultrasound beam was at right angles to the adventitia, adventitia was visible adjacent to the plaque and that for image normalization a standard sample consisting of 2/4ths of the width of the brightest area of adventitia was obtained.

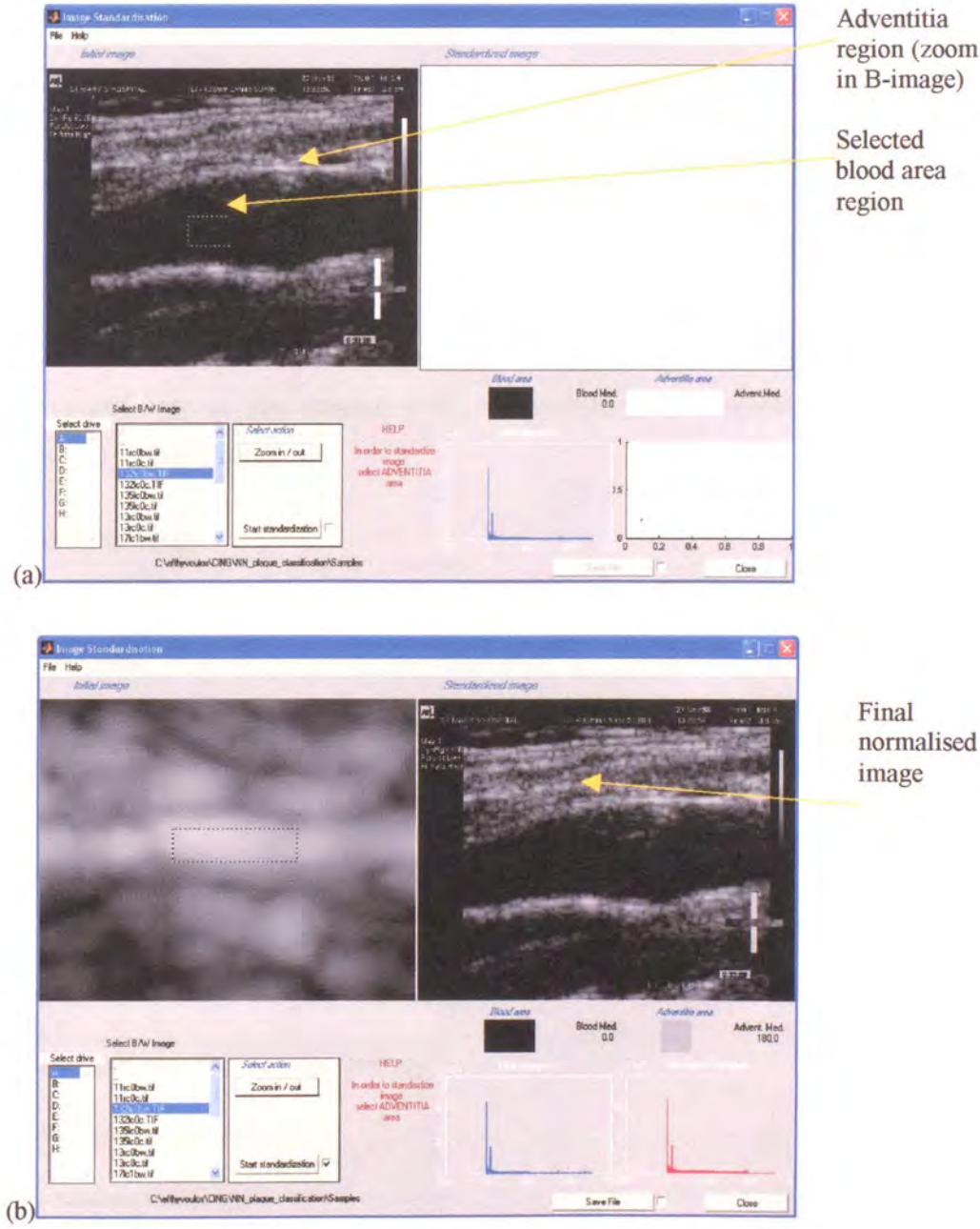


**Fig. 5.1**: Normalization of a carotid ultrasound image: two reference points are selected in order to normalize the image: (a) blood area is selected and, (b) adventitia area located over the plaque is selected.

## 5.4 Generation of an artificial carotid image

In order to evaluate despeckle filtering, an artificial carotid image was generated. Despeckle filtering was evaluated visually by two experts (cardiovascular surgeon, neurovascular specialist), on the artificial carotid image corrupted by speckle noise. The artificial image (shown in Fig. 6.3a), has a resolution of 150x150 pixels, and was generated with gray level values of the bottom, strip, middle and upper segments of 182, 250, 102, and 158 respectively. This image was corrupted by speckle noise, which was generated using the equation, $g_{i,j} = f_{i,j} + n_{i,j} f_{i,j}$, where $g_{i,j}$, and $f_{i,j}$, are the noisy and the original images respectively, and $n_{i,j}$, a uniformly distributed random noise with mean 0 and a variance $\sigma_n^2 = 0.07$.

## 5.5 Image quality of two ultrasound scanners

For evaluating the image quality of the two ultrasound scanners used in this work (ATL HDI-3000, and ATL HDI-5000), visual perception evaluation (see Chapter 5.6.1), image quality evaluation metrics (see Chapter 4.3) and texture measures (see Chapter 4.4) were used. The evaluation was carried out on the original (NF), normalized (N), despeckled (DS), and normalized despeckled (NDS) images.

## 5.6 Despeckle filtering

In order to accurately locate structure boundaries, quantify morphology, and better visualize the position of structures, it is necessary to pre-process the ultrasound images in a way that suppresses the speckle noise while retaining the salient tissue boundaries in the image. Many researchers refer to speckle as the major difficulty in analyzing and segmenting ultrasound images [345], [348], [351].

In this work, we investigated the following despeckle filters which were presented in Chapter 2:

- First order statistics filters- *lsmv*, and *wiener*
- Homogeneous mask areas filter-*lsminsc*
- Median filtering-*median*
- Linear scaling filtering-*ls*
- Maximum homogeneity filter- *homog*
- Geometric filtering-*gf4d*
- Homomorphic filtering-*homo*

- Anisotropic diffusion-*ad*
- Coherence linear anisotropic diffusion-*nldif*
- Wavelet filtering-*waveltc*

In the following subsections, the visual perception evaluation, texture analysis and image quality evaluation metrics used for evaluating the performance of despeckle filtering are presented.

### *5.6.1 Visual perception evaluation*

As explained in Chapter 4, visual evaluation can be broadly categorized as the ability of a person to extract information from within an ultrasound image and to provide anatomical information. The visual evaluation varies of course from expert to expert and is subject to the expert's variability [329], which may be described by the ROC curves [329], [363]. The visual perception evaluation, in our study, was carried out according to the ITU-R recommendations, with the DSCQS procedure [316], explained in Chapter 4.2 of this dissertation. We will introduce in this section the procedure followed by the experts to evaluate despeckle filtering.

For the visual evaluation of the despeckle filters presented in Chapter 2, a total of 100 ultrasound images of the carotid artery, taken from 100 different patients (50 asymptomatic and 50 symptomatic) were evaluated visually by two vascular experts (a cardiovascular surgeon, and a neurovascular expert) before and after despeckle filtering in order to assess the performance of the filters. These 100 images were selected from the 440 image dataset using visual perception as a criteria. A graphical user interface was developed in MATLAB as shown in Fig. 5.2 and was used by the two experts for the visual perception evaluation. For each case, the original and the despeckled images (despeckled with filters *lsmv, lsminsc, median, wiener, ls, homog, gf4d, homo, ad, nldif,* and *waveltc*), were presented without labelling at random to the two experts.

The two experts evaluated the area around the distal common carotid, between 2-3 cm before the bifurcation and the bifurcation. Furthermore, the experts were examining the image in the lumen area, in order to identify the existence of a plaque or not, which significantly reduces blood flow, and if the borders and the texture of the plaque were better visible after despeckle filtering. They were examining initially the adventitial layer at the near wall of the carotid artery, by trying to locate visually the vessel walls with the surrounding tissues. They were then examining the far wall of the carotid artery in order to locate and visually measure the IMT of the carotid artery, which may serve as an indicator of cardiovascular disease. To further assess the intra-observer variability, the two experts, evaluated the same set of images, approximately one year after the initial evaluation, as explained in Chapter 4.2.

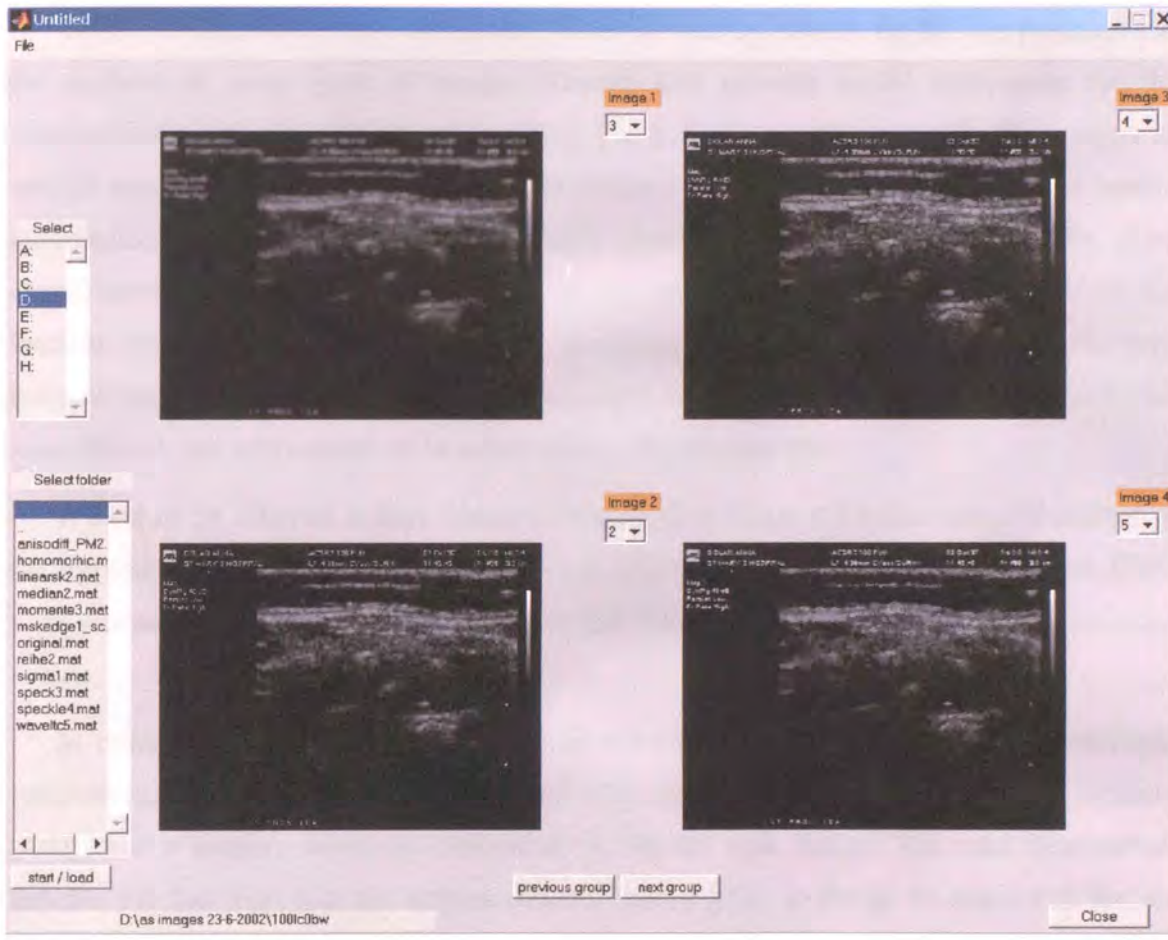


**Fig. 5.2**: The graphical user interface for the visual image evaluation carried out by the experts. The screen illustrates four different despeckled images and their corresponding scores.

For each image, an individual expert is asked to assign a score in the one to five scale, corresponding to low and high subjective visual perception criteria. Five was given to an image with the best visual perception. Therefore the maximum score for a despeckle filter is 500, if the expert assigned the score of five for all the 100 images. For each image, the score was divided by five to be expressed in a percentage format. The experts were allowed to give equal scores to more than one image in each case. For each class and for each image the average score was computed.

All the visual evaluation experiments were carried out at the same workstation under indirect fluorescent lighting typical of an office environment. The two vascular experts were allowed to position themselves comfortably with respect to the viewing monitor, where a typical distance of about 50 cm was kept. Experts in real-life applications employ a variety of conscious and unconscious strategies for image evaluation, and it was our intent to create an environment as close as possible to the real one.

### *5.6.2 Texture analysis*

Texture contains important information, which is used by humans for the interpretation and the analysis of many types of images. Texture also provides useful information for the characterization of atherosclerotic plaque [10], [127]. It is especially useful for the analysis of natural scenes since they mostly consist of textured surfaces. Texture refers to the spatial interrelationships and arrangement of the basic elements of an image [214]. Visually, these spatial interrelationships and arrangements of the image pixels are seen as variations in the intensity patterns or gray tones. Therefore, texture features have to be derived from the gray tones of the image. Although it is easy for humans to recognize texture, it is quite a difficult task to be defined, and subsequently to be interpreted by digital computers.

A total of 55 different texture features, introduced in Chapter 4.4 and further described in the Appendix III, plus the speckle index (4.9), C, and the contrast-to-speckle ratio (4.10), CSR, were extracted from the 220 asymptomatic and 220 symptomatic, original and despeckled images.

In order to identify the most discriminant texture features, separating asymptomatic and symptomatic ultrasound images, before and after despeckle filtering, the distance measure (4.11), and a distance score were computed (4.14), for each feature. The most discriminant features are the ones with the highest distance values [10]. It should be noted that for the statistical features, second, and fourth moment, a decreasing distance shows improvement, whereas for all other features a larger feature distance shows improvement.

The Wilcoxon matched-pairs signed rank sum test, described in Chapter 4.4.2, was used in order to detect if for each texture feature, a significant (S) difference or not (NS), exists between the original and the despeckled images at $p<0.05$. The test was applied on all the 220 asymptomatic and 220 symptomatic, original and despeckled images of the carotid artery.

The statistical k-nearest-neighbour (kNN) classifier using the Euclidean distance with k=7, as described in Chapter 4.4.3, was also used to classify a plaque, before and after despeckle filtering, as asymptomatic or symptomatic [10]. The leave-one-out method was used for evaluating the performance of the classifier, where each case is evaluated in relation to the rest of the cases. This procedure is characterized by no bias concerning the possible training and evaluation bootstrap sets. The kNN classifier was chosen because it is simple to implement and computationally very efficient. This is highly desired due to the many feature sets and filters tested [211].

### *5.6.3 Image quality evaluation metrics*

In order to evaluate differences between the original and the despeckled images, the image quality evaluation metrics proposed in Chapter 4.3 were also used. These quality evaluation

metrics MSE, RMSE, M3, M4, GAE, SNR, PSNR, Q, and SSIN, were computed for the 220 asymptomatic and 220 symptomatic ultrasound images of the carotid artery. It is noted that for this evaluation, the image quality evaluation metrics were not divided by the low pass filtered image $lpg_{i,j}$ (see Chapter 4.3).

## 5.7 IMT segmentation

In this section IMT manual and snakes segmentation based measurements are presented.

The IMT snakes segmentation measurements were performed in the CCA (see Fig. 1.5). Measurements on the near wall typically suffer from lower image quality caused by overlap of echo pulses, they are less accurate, and therefore less reproducible than those taken from the far wall [313], [322]. This is because the adventitia is more echogenic than the blood and bright echoes produced by the adventitia of the near wall can "spill" into the adjacent blood. Thus, echoes from the blood are lost. This effect is far less apparent on the far wall where the media and media-adventitia interface are closer to the probe than the adventitia. Therefore a far wall measurement is utilized most frequently. The IMT was defined as the distance between the leading edge of the lumen-intima interface and the leading edge of the medial-adventitia interface (see Fig. 3.1, interfaces Z5-Z7).

### *5.7.1 Manual measurements and visual perception evaluation*

Using a system developed in MATLAB, the two experts manually outlined the IMT according to a specific protocol which will be described below. Figure 5.3 demonstrates the manual IMT segmentation software. The software provided an easy to use user interface for segmenting the vessel wall and the lumen directly from the acquired ultrasound images.

Although the power Doppler (blood flow image) was found to be useful for locating the lumen, only the B-mode image was used when delineating the wall and the lumen boundaries in order to eliminate errors due to color artifacts and reverberations occurring from the blood flow image [208], [238], [322]. For the purpose of this study the vessel wall and lumen are defined as follows:

a) The lumen is the boundary enclosing the interior region of the vessel through which blood flows (see Fig. 3.1, interface Z4).

b) The lumen appears as a dark region in a B-mode ultrasound image (see Fig. 3.1, region between interfaces Z3-Z5).

c) The vessel wall is the boundary separating the intima-blood interface (see Fig. 3.1 interface Z5).

d) The intima media interface is frequently visible except in cases where artifacts may obscure visualization of this boundary (see Fig. 3.1, interfaces Z5-Z7).

e) On longitudinal ultrasound images, the IMT and the vessel wall are always defined as a pair of two open contours, which may be represented by a cubic spline.

The two vascular experts delineated the IMT on 100 longitudinal ultrasound images of the carotid artery before and after image normalization (see section 5.3), and despeckle filtering with the *lsmv* filter (see section 2.3.1.1), by selecting 20-40 consecutive points for the adventitia and the intima layers at the far wall of the CCA. The points on the adventitia and the intima were then linearly interpolated. The measurements were performed between 2-3 cm proximal to the bifurcation of the CCA on the far wall. The bifurcation of the CCA was used as a guide and all measurements made from that region (see Fig. 1.5). The IMT was then calculated as the average of all measurements. The measuring points and delineations were saved for comparison with the snakes segmentation method.

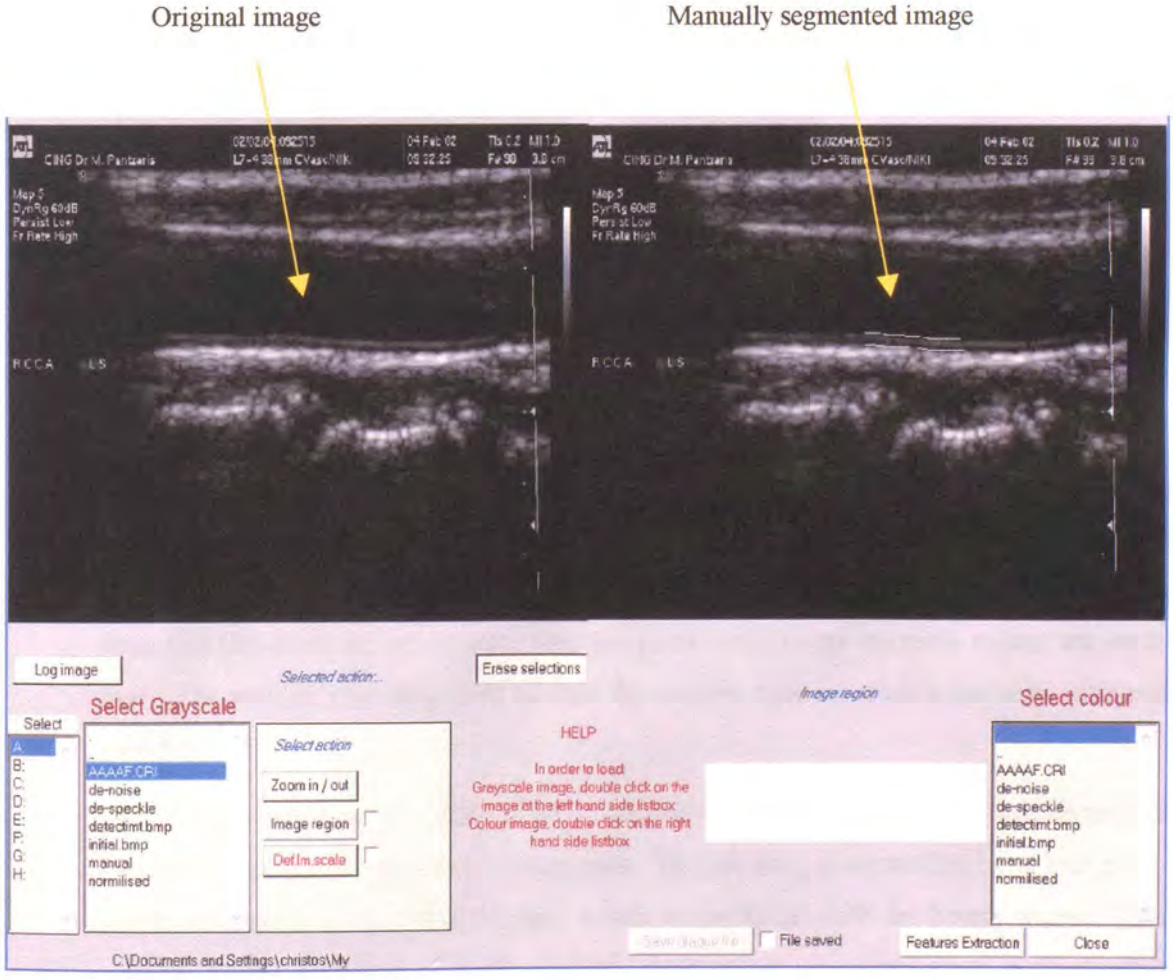


**Fig. 5.3**: Demonstration of the manual IMT segmentation module.

The protocol for the IMT manual delineation described above may be applied on ultrasound images, if a plaque is not present in the CCA. When there is a plaque present, then measurements of the IMT may not be made according to the above protocol, as the IMT may not be measured at the position of the plaque. Measurements in this case, must be made before or after the plaque formation, where the artery walls are entirely free from plaque formation.

Furthermore, the two experts evaluated visually the results of the IMT snakes segmentation algorithm, on all 100 longitudinal ultrasound images of the carotid artery. Their primary interest was the area around the IMT borders of the carotid artery, and whether they can differentiate blood from carotid wall, and IMT, when compared with the manual delineation results.

The intra-observer variability of the manual segmentation measurements was also investigated, and therefore all 100 ultrasound carotid images were again delineated from both vascular experts at time 12 months.

### *5.7.2 IMT initialisation*

Before running the IMT snakes segmentation algorithm, an IMT initialization procedure was carried out. The objective of this procedure was to place the IMT initial snake contour as close as possible to the area of interest, because of the problems discussed in Chapter 3.6.1. The procedure is described as follows (see Fig. 5.4):

a) Load the initial B-mode image, and select using the mouse the area of interest on the image, where the IMT will be detected. The area may be drawn around the IMT borders (see Fig. 5.4a). The selected cropped area is shown in Fig. 5.4b.

b) Despeckle the selected area by applying the *lsmv* despeckle filter presented in Chapter 2 (see Fig. 5.4c).

c) Convert the area to binary by image thresholding, in order to extract edges more easily. A threshold is calculated from the despeckled grayscale image according to [15], which is then applied to all the pixels in the image. Pixels that have smaller intensity values than this threshold are set to zero, whereas pixels with larger intensity values are set to one. The area is thus simplified so that the borders may be more accurately extracted (see Fig. 5.4d).

d) Dilate the binary image (from point c above) by applying a dilation morphological operation that grows the binary image area. The growing is controlled by a 3x3 pixel-structuring element consisting of ones, which is multiplied with the binary image. This morphological operation is performed to close small gaps and form a continuous boundary (see Fig. 5.4e).

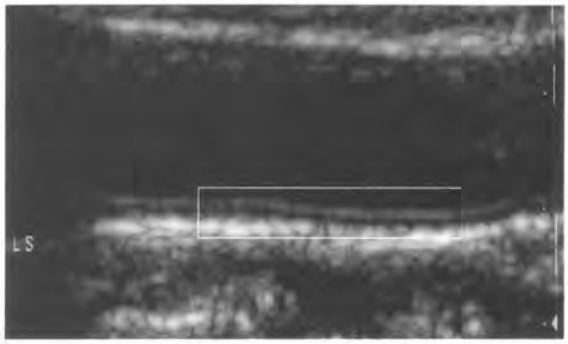

(a) Ultrasound image with selected area.

(b) Cropped area.

(c) Despeckled area.

(d) Binary cropped area.

(e) Dilated cropped binary area.

(f) Remove erroneous edges.

(g) Interpolating B-spline.

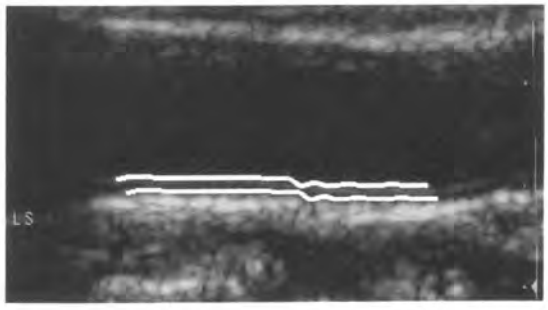

(h) Initial snake contours.

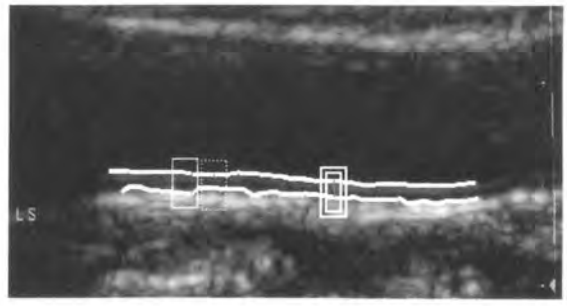

(i) Final snake contours.

**Fig. 5.4**: IMT contour initialization procedure and final snakes contours: (a) Original ultrasound image with selected area, (b) cropped area, (c) despeckled area, (d) binary cropped area, (e) dilated cropped area, (f) dilated area after removal of small edges, (g) construction of the interpolating B-spline, (h) detected initial contours for the adventitia and the intima layers, and (i) final contours after the snake deformation. The $IMT_{mean}$, is shown with double line box, the $IMT_{\max}$, with a full line box and the $IMT_{\min}$, with dashed line box.

e) On the dilated area erroneous small edges that might trap the snake have to be removed. This is carried out by labeling connecting components in the image where the number of connecting components was chosen to be eight. Small segments that are smaller than 20 pixels, and do not belong in the boundary are therefore removed (see Fig. 5.4f).

f) Extract the contour matrix of the above area by locating points and their coordinates on the adventitia (contour) and construct an interpolating B-spline (see Fig. 5.4g).

g) Sample the interpolating B-spline in 30 equal segments, in order to define 30 snake elements on the contour.

h) Map the detected contour points from g), on the B-mode image of Fig. 5a) to form the initial snake contour for the adventitia (see Fig. 5h).

i) Displace the contour for the adventitia, upwards for up to 17 pixels (1.02mm) to detect the intima layer. This displacement is based on the observation that the IMT lies between 0.6 mm and 1.4 mm (0.6 mm < IMT< 1.4 mm), with a mean IMT of 1.0 mm [7]. By taking in consideration that the spatial resolution (distance between two pixels) is 0.06 mm, then the IMT is lying within the range of 10 < IMT <24 pixels, with a mean of 17 pixels. Therefore the displacement of the contour, in order to estimate the intima should be in average 17 pixels (1.02 mm) upwards. Figure 5.4h shows the initial contour estimation for the adventitia and the intima layers as they have been detected by the initialization technique.

### *5.7.3 IMT segmentation*

Figure 5.5 shows the edge map of the original artificial carotid image, of Fig. 6.3a, and the initial snake contour estimation. This was detected by the procedure described in 5.7.2 at the far wall of the edge map. It is shown that the proposed method detects the initial IMT contours accurately, thus positioning the snake as close as possible to the borders of interest, and offering the possibility of using the method in real time applications.

Using the snakes segmentation method, first proposed by Kass [243], and later enhanced by Williams&Shah [124], as described in Chapter 3.4, the final IMT contours for the image in Fig. 5.4a were detected, measured and are shown in Fig. 5.4i. The snake iterations are repeated until the number of snake points moved to new locations is less than a specified threshold or the user-defined maximum number of iterations has been reached. After tests made with the Williams&Shah snakes segmentation method, we have chosen three as the maximum number of points moved to new locations, and 50 for the maximum number of iterations. A small number of points moved and a large number of iterations ensures that the energy functional in (3.4.2), will reach always its minimum in the observed area of points. We have chosen in our study the initial values, $\alpha(s)=0.6$, $\beta(s)=0.4$, and $\gamma(s)=2$ (see equation 3.4.2) to start the snake

deformation which is consistent with other studies [241], [252], [260]. Figure 5.6 shows the module developed using the MATLAB software for the IMT segmentation in ultrasound images of the carotid artery.

After both final snake contours have been extracted (see Fig. 5.4i), the distance lumen-intima interface to the media-adventitia interface is measured between pixel pairs. This distance is calculated at all points along the arterial segment of interest and then averaged to obtain the mean IMT ($IMT_{mean}$). Also the maximum ($IMT_{\max}$), minimum ($IMT_{\min}$), and median ($IMT_{median}$) IMT values, are calculated, displayed, and plotted on the B-mode image. Figure 5.4i shows the detected $IMT_{mean}$, $IMT_{\max}$, and $IMT_{\min}$ values with a double line box, full line box, and a dashed line box respectively.

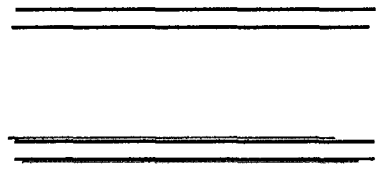

**Fig. 5.5**: Edge map of an artificial carotid image of the original image in Fig. 6.3a, and the detected initial contours for the IMT.

When segmenting the IMT, the user has to decide first, which layer, intima or adventitia, is better to detect based on the images available taking into consideration the following:

a) Is there a lot of noise in the lumen near the intima?

b) Which layer, intima or adventitia, has a stronger contrast?

c) Are the edges on the image better displayed at the intima or at the adventitia layer?

Relying on our experience after experiments carried out, and based on a number of unpublished observations, there is a strong noise component in the lumen near the intima. On the other hand, it seems that the adventitia has a stronger contrast. Therefore, it is better if the IMT detection starts first from the adventitia. Prior to the segmentation, the image, or the selected area of interest, which is the area around the IMT, is enhanced by applying the despeckle filter *lsmv* (see Chapter 2.3.1.1). We can also apply normalisation to the selected area as proposed in Chapter 5.3, by enhancing the gray level change from black to white [322].

As discussed earlier, it is importnat to place the initial snake contour as close as possible to the area of interest otherwise the snake may be trapped into local minima or false edges, and converge in a wrong location. The snake is threfore initialised with the proposed IMT initialisation procedure as described in Chapter 3.6.1 and Chapter 5.7.2.

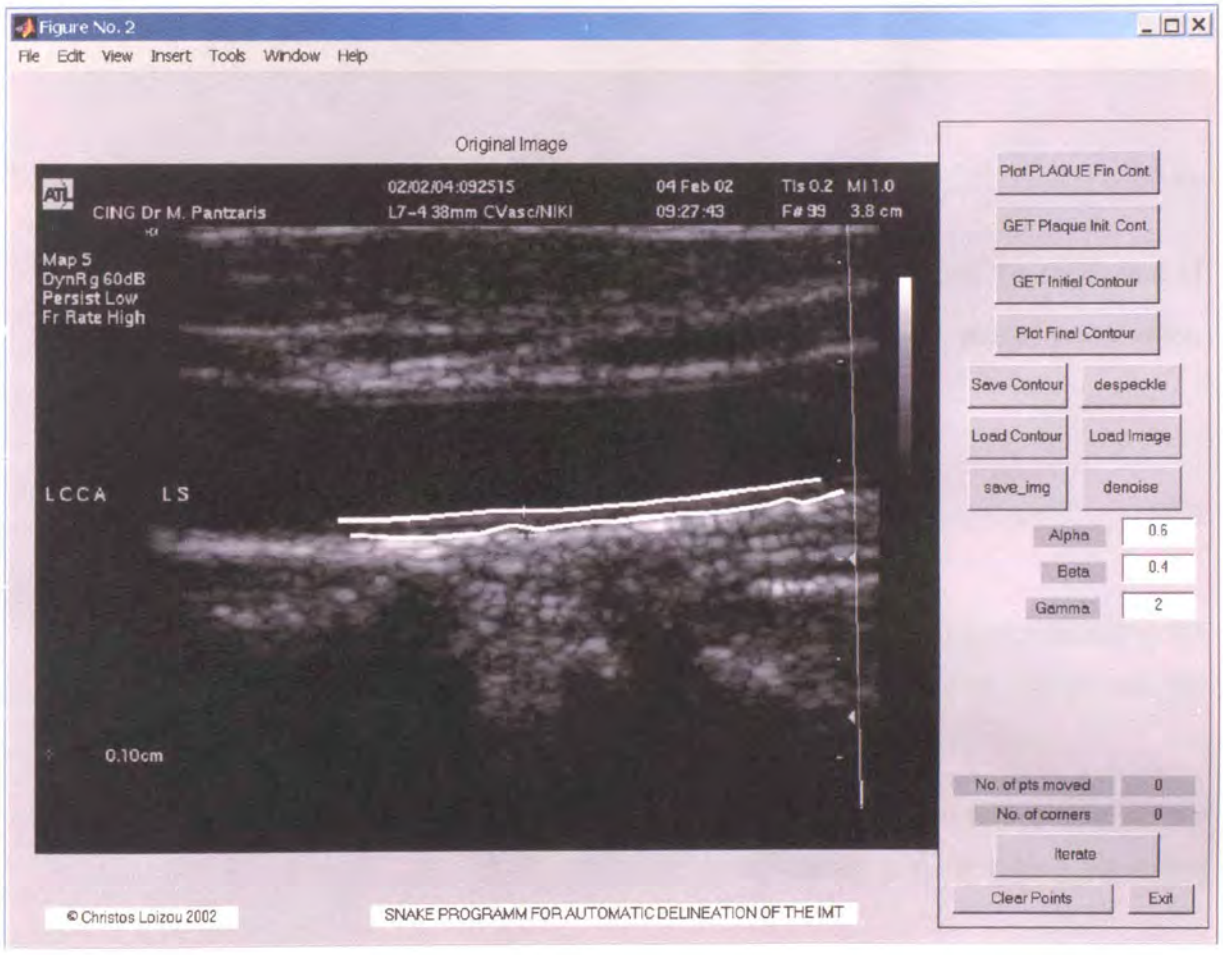


**Fig. 5.6**: Demonstration of the IMT segmentation module.

According to our experience it is much better to perform the IMT measurements on longitudinal images of the carotid artery, than in the transversal images. This is because the visualization is much better and more accurate in longitudinal images, whereas in transversal images the visualization is poor and many images of the same position are required in order to construct the whole carotid bulb. Additionally, in longitudinal images the whole length of the artery may be more easily inspected and thus the IMT and plaque are better visualized and detected.

### *5.7.4 Univariate statistical analysis*

The Williams&Shah IMT snakes segmentation method was applied on 100 longitudinal ultrasound images of the carotid artery. In order to investigate how the results of the snakes segmentation method, differs from the manual delineation results, we used the following evaluation metrics.

We computed the parameters, $IMT_{mean}$, $IMT_{\min}$, $IMT_{\max}$ and $IMT_{median}$, as well as the inter-observer error [265]:

$$se = \sigma_{IMT} / \sqrt{2} . \tag{5.2}$$

where $\sigma_{IMT}$ is the variance of all IMT measurements. We also calculated the coefficient of variation, $CV\%$, which describes the difference as a percentage of the pooled mean value, $IMT_{mean}$ [131], [265]:

$$CV\% = \frac{se}{IMT_{mean}} 100 . \tag{5.3}$$

The Wilcoxon matched-pairs signed rank sum test was also used in order to identify if for each measurement a significant (S) difference or not (NS) exists between the snakes and the manual segmented boundaries, at $p < 0.05$.

Further a variation of the Hausdorff distance, $HD$, [265], between two curves was calculated. It reflects the maximum mismatch between the manual and the snakes segmented areas, and is calculated as:

$$HD = \left| Manual - Snake_Segmented \right| . \tag{5.4}$$

where small values for the $HD$ are favourable.

Also the Pearson correlation test was used, at a significance level of 0.05, which returns the Pearson product moment correlation coefficient, $r_{pearson}$, that ranges from –1.0 to 1.0 inclusive and reflects the extent of a linear relationship between two data sets [265].

The $MSE$, between the snakes segmented and the manually segmented boundaries was also calculated, which estimates the minimum average distance squared [131], between the two curves. Therefore small values for $MSE$ are required.

The strength of the relationship between the snakes segmented and the manually segmented methods is indicated by the correlation:

$$c_{m,a} = \frac{Cov_{m,a}}{\sigma_m \sigma_a}, \tag{5.5}$$

where $Cov_{m,a}$, is the covariance between the snakes (a) and the manual (m) measurements and, $\sigma_m$, $\sigma_a$, are the standard deviations of the two measurements respectively [269]. Further, the correlation coefficient, $\rho_{corel}$, was investigated to determine the relationship between the measurements at a significance level of 0.05 (i.e. for 100 subjects correlation values above 0.1654 are significant).

These statistical metrics have been computed for the Williams&Shah snakes segmentation measurements for the cases, no filtering (NF), despeckled (DS), normalized (N), normalized despeckled (NDS), and for the manual segmentation measurements, for the cases, manual (M), and manual normalized (MN) from both experts, respectively. Additionally, in order to assess the intra-observer variability between the two experts, the manual measurements on original (M), and normalized (MN) images were repeated from both experts, one year after the first measurements.

In order to assess the normality of the distributions, histograms for all the $IMT_{mean}$ values were computed. Specifically, the histograms for the 100-ultrasound images of the carotid artery were plotted, for the snakes segmentation cases NF, DS, N, NDS, and for the manual segmentation cases M, and MN, from both experts. If the histogram of a distribution is skewed or has very long tails, then the assumption of normality may not be valid [264].

Furthermore, box plots (Whisker diagrams) were computed for the snakes segmentation cases NF, DS, N, NDS, and the manual segmentation cases M, and MN from both experts. The box plots, demonstrate the dispersion or spread of the distribution for the $IMT_{mean}$ values, for all the 100-ultrasound images of the carotid artery. A box plot diagram provides a simple graphical summary of the set of data. It shows a measure of central location (the median), two measures of dispersion (the range and inter-quartile range), the skewness (from the orientation of the median relative to the quartiles) and potential outliers (marked individually). Box plots are especially useful when comparing two or more sets of data and can be used to indicate the degree of symmetry in a distribution.

Bland-Altman plots [264] were also used to further evaluate the agreement between the Williams&Shah snakes segmentation and the manual segmentation method. The plots were investigated for the snakes segmentation cases, NF, DS, N, NDS, and for the manual segmentation cases M, and MN, from both experts. By using Bland-Altman plots, the distributions of the differences between all different cases were computed.

### *5.7.5 Correlation analysis*

Linear regression analysis (correlation plots), was also used, using the least squares method, at a confidence interval of 95% ($p<0.05$), in order to validate the Williams&Shah snakes segmentation method, and to assess the inter-observer variability of the two experts. Correlation coefficients, slope and intercept, were therefore calculated, between the cases M-NF, MN-NF, MN-DS, MN-N, MN-DS, M-DS, M-N, and M-NDS, in order to compare the snakes segmented IMT borders, with the manually segmented IMT borders, and with each other.

## 5.8 Plaque segmentation

Four different snakes segmentation methods were used for plaque segmentation. These methods were the Williams&Shah, Balloon, Lai&Chin, and the GVF snake, presented in Chapter 3.5. An initialisation procedure for detecting the initial plaque borders in longitudinal ultrasound images of the carotid artery was developed for all snakes segmentation methods. The initialisation procedure uses, the outline of the blood flow image to detect the initial snake placement. For the evaluation of the plaque snakes segmentation method the evaluation metrics proposed in Chapter 4.5 were used.

### *5.8.1 Manual measurements and visual perception evaluation*

Before the detection of the plaque borders, by the snakes segmentation method manual delineation from the experts is required for comparison purposes. The plaque identification and segmentation tasks are quite difficult, and must be performed by experts. In this work one neurovascular expert, manually segmented the images. The expert delineated the plaque borders, between plaque and artery wall, and those borders between plaque and blood, on 80 longitudinal B-mode ultrasound images of the carotid artery, before and after image normalization, using MATLAB software developed by other researchers from our group (see Fig. 5.8). The procedure for carrying out the manual delineation process was established by a team of experts and was documented in the ACSRS project protocol [208]. The correctness of the work carried out by the single expert was monitored and verified by at least another expert.

Usually the plaques are classified into the following types [208], [238], [322], [335] (see Fig. 5.7):

- Type I: Uniformly echolucent (black) plaques, where bright areas occupy less than 15% of the plaque area (see Fig. 5.7b). If the fibrous cup is not visible, the plaque can be detected as a black filling defect only by using color blood flow, (see Fig. 5.7a), or power Doppler.
- Type II: Mainly echolucent plaques, where bright echoes occupy 15-50% of the plaque area (see Fig. 5.7c).

- Type III: Mainly echolucent plaques, where bright echoes occupy 50-85% of the plaque area (see Fig. 5.7d).
- Type IV: Uniformly echogenic (white) plaques, where bright echoes occupy more than 85% of the plaque area (see Fig. 5.7e).
- Type V: Calcified cup with acoustic shadow so that the rest of the plaque cannot be visualized (see Fig. 5.7f).

In this work, only plaques of type II, III and IV, were delineated by the expert, as for these types of plaques, the fibrous cup, which is the border between blood and plaque, may be more easily identified and thus the expert may perform the manual delineation more reliably. For the type I plaques, borders are not visible well. Plaques of type V produce acoustic shadowing and the plaque is also not visible well. Plaques of type I, and V, were therefore not delineated in this study.

Figure 5.8 demonstrates the manual outlining procedure, where an ultrasound image with the outline of the carotid plaque at the near wall, and the corresponding colour blood flow image are illustrated (see Fig. 5.8a). The expert applied a log transformation on the greyscale B-mode image and then prescribed the outline of the plaque by marking 20 to 40 consecutive points of the plaque border on the B-mode ultrasound image (see Fig. 5.8b). The expert was guided by the blood flow image, which indicate the plaque-blood borders, in order to delineate the plaque on the B-mode image. The manually segmented plaque was saved in order to be compared with the snakes segmentation results (Fig. 5.8c), or used for texture analysis.

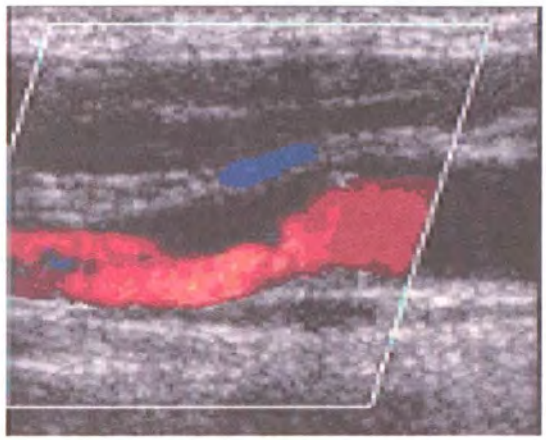

(a) Blood flow image for type I plaque.

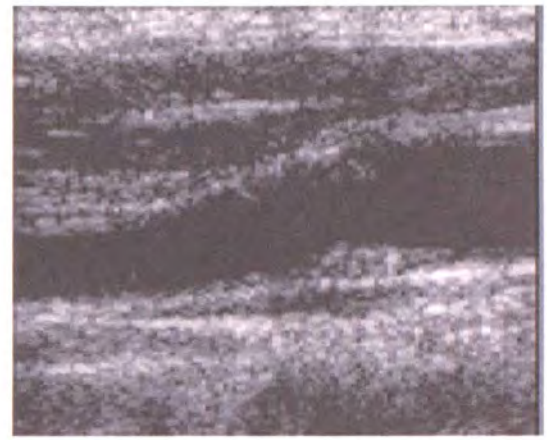

(b) Type I plaque.

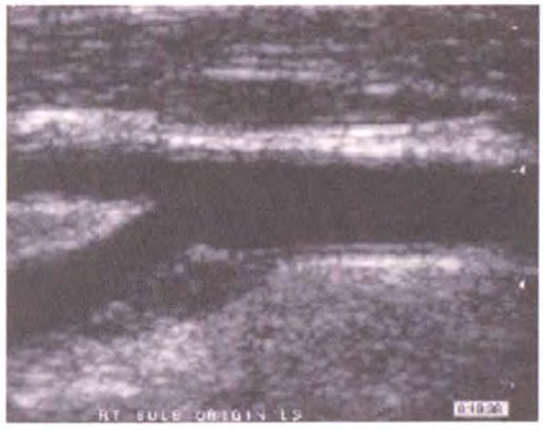

(c) Type II plaque.

(d) Type III plaque.

(e) Type IV plaque.

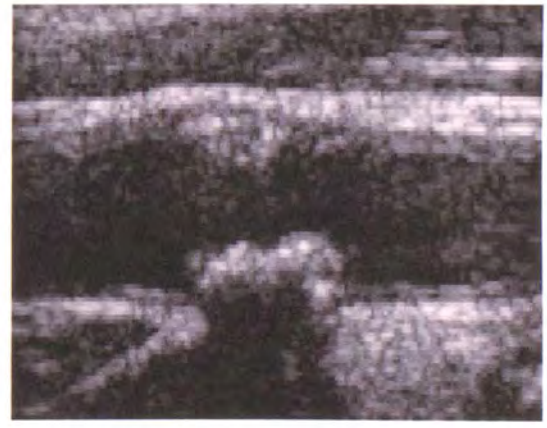

(f) Type V plaque.

**Fig. 5.7**: Types of plaque: (a) blood flow image for the type I plaque, (b) type I plaque: the plaque is not visible, (c) type II plaque: bright echoes occupy < 50% of plaque, (d) type III: bright echoes occupy 50%-80% of plaque, (e) type IV: bright echoes occupy 80%-100% of plaque, (f) type V plaque: calcified plaque where borders cannot be visualized well.

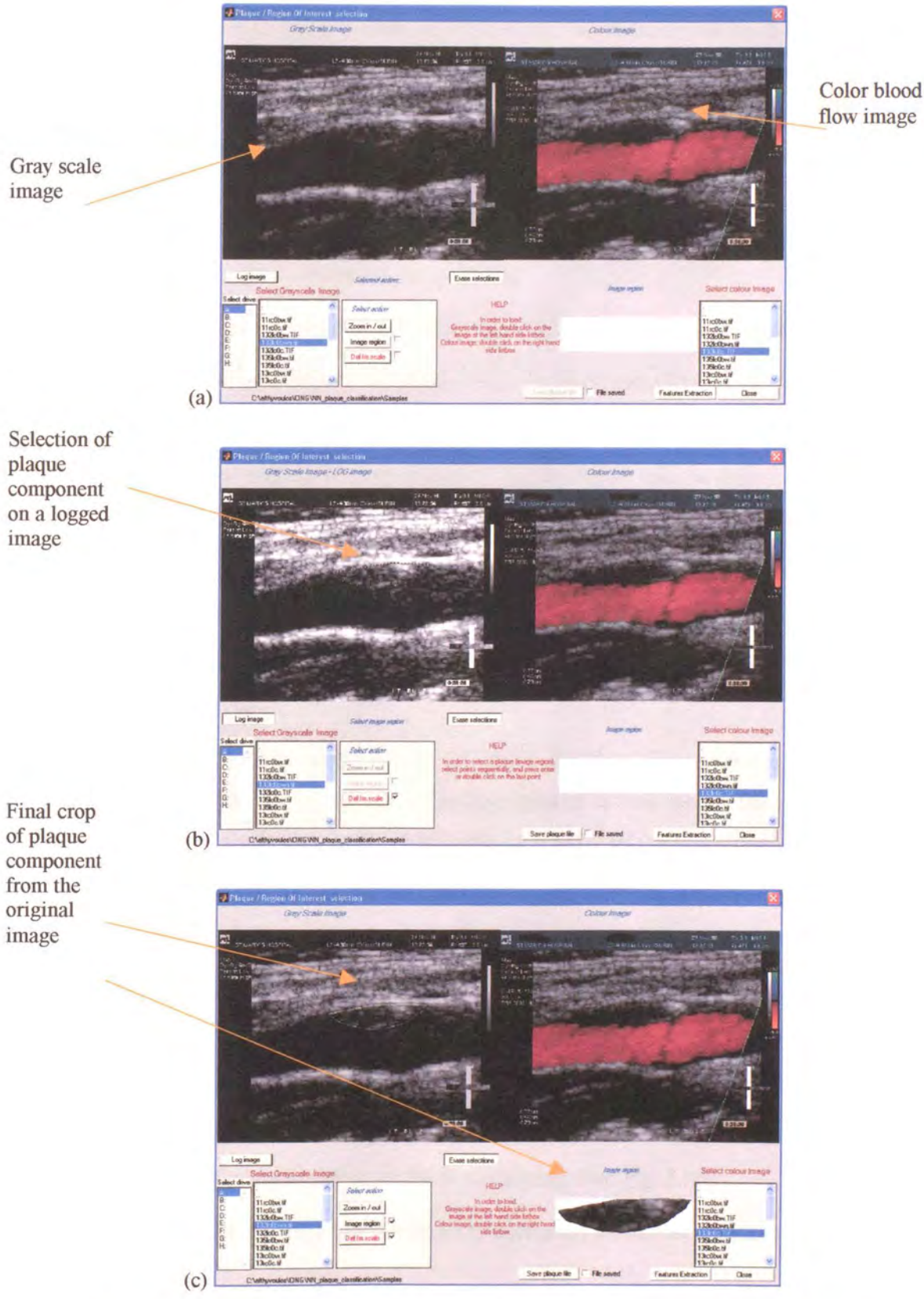


**Fig. 5.8**: Selection of a plaque: (a) The gray scale image and the blood flow colour image are loaded, (b) expert has selected a log transform on the gray scale image for better visualising the plaque, and (c) the final selected plaque is saved.

### *5.8.2 Plaque initialisation using the blood flow image*

In most of the cases a plaque is visualised in a B-mode longitudinal ultrasound image and its size confirmed in transverse section. However, uniformly echolucent plaques are not obvious on B-mode, and colour flow imaging is needed. These echolucent plaques, are seen as black filling deffects. PW Doppler is used to measure velocity in order to grade the degree of stenosis. In this work we have used the blood flow image, in order to extract the initial snake contour estimation for the plaque borders in the carotid artery. The limitations of this approach, i.e. using the blood flow image to locate the blood borders are the following:

a) The colour flow sometimes overlaps with areas of the tissue wall or a plaque, and

b) The colour does not always fill up places where the blood has a low speed.

In this subsection we describe the plaque snake contour initialsation procedure, carried out using both the blood flow and the B-mode images. This procedure may be described as follows (see Fig. 5.9):

a) Cross correlate the B-mode image (Fig. 5.9a) with the blood flow image (Fig. 5.9b) and extract the borders of the blood flow area.

b) Dilate the extracted blood flow edge image, to eliminate small gaps and remove small undesired regions.

c) From the dilated edge blood flow image, detect the blood flow edge contour (see Fig. 5.9c). Mark a region of interest on the edge contour (a task carried out by the expert, illustrated by a rectangle in Fig. 5.9c) where the lower or upper boundary of plaque is covered. This is used as an initial snake contour.

d) Sample the initial snake contour at 20 to 40 consecutive points to construct an interpolating B-spline.

e) Connect the first and the last snake points on the initial contour to form a close contour.

f) Despeckle the B-mode image by the *lsmv* filter described in Chapter 2.3.1.1.

g) Map the initial plaque contour on the B-mode image (see Fig. 5.9d).

h) Deform the initial contour by the snake to accurately locate the plaque-blood borders, and

i) Save the final plaque contour and display it on the B-mode image (see Fig. 5.9e).

(a) Original B-mode image.

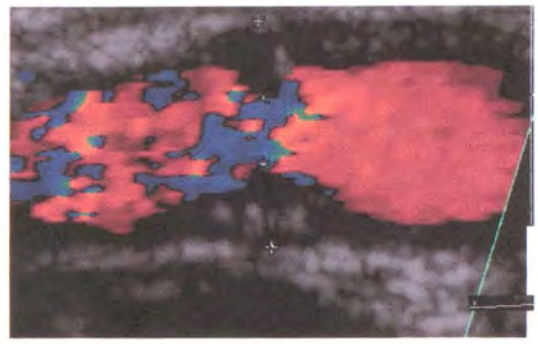

(b) Blood flow image.

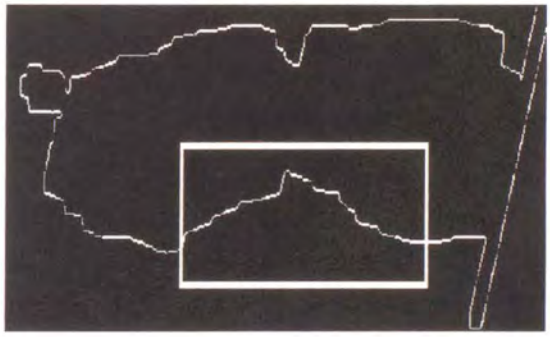

(c) Initial blood flow edge contour.

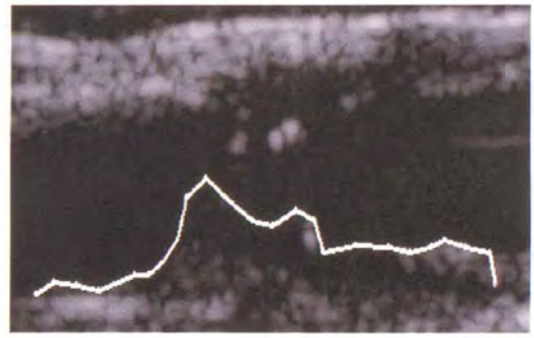

(d) Sampled initial snake contour.

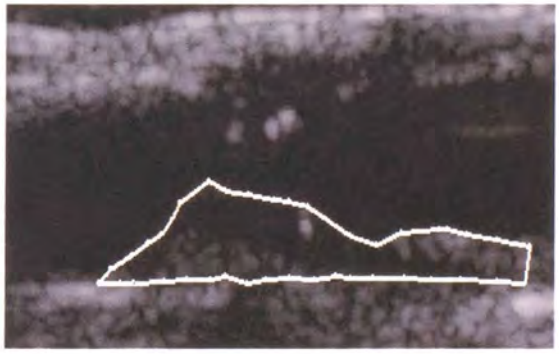

(e) Snakes segmentation results.

(f) Manual segmentation results.

**Fig. 5.9**: Plaque initialization using the blood flow image procedure: (a) Original ultrasound B-mode image of a carotid artery with plaque at the far wall, (b) blood flow image, (c) initial blood flow edge contour with the area for the initial contour selected by the expert, (d) sampled initial snake contour, (e) snakes segmentation of plaque, and (f) manual segmentation of plaque.

### *5.8.3 Plaque segmentation*

Four different snakes segmentation methods were used for the plaque segmentation. The methods were the Williams&Shah, Balloon, Lai&Chin, and the GVF snake, presented in Chapter 3.5. Figure 5.10 shows the module developed using MATLAB software for the Williams&Shah plaque snakes segmentation method. An example of an ultrasound longitudinal image with a plaque at the near wall of the carotid artery is illustrated. The final plaque contour, is succesfully deliniated by the Williams&Shah snakes segmenattion algorithm, where the initial plaque contour was estimated using the blood flow image, as described in section 5.8.2.

**Fig. 5.10**: Demonstration of the plaque segmentation module.

It is important to position the initial plaque snakes contour as close as possible to the area of interest, otherwise the snake may be trapped into local minima or false edges, and converge in a wrong location. The initial snake contour, is therfore positioned using the initialisation procedure proposed in section 5.8.2.

To verify the plaque segmentation results the expert evaluated visually the results of the plaque snakes segmentation method on 80 longitudinal ultrasound images of the carotid artery.

The primary interest of the expert was to check if the plaque borders and the outline of the plaque were detected correctly by the snakes segmentation methods.

The four different snakes segmentation methods implemented were, the Balloon snake [333], the snake of Lai&Chin [248], and the GVF snake [116], as presented in Chapters 3.5.1-3.5.3, which were compared with the Williams&Shah (see Chapter 3.4) snakes segmentation method.

All four different plaque snakes segmentation methods were evaluated on 80 symptomatic B-mode and blood flow (PW Doppler) longitudinal ultrasound images of the CCA, representing different types of atherosclerotic plaque formation with irregular geometry typically found in this blood vessel.

The parameter values for the four different snakes segmentation methods, were the same in all experiments, and they were chosen for the Williams&Shah snake to be equal to $\alpha = 0.6$, $\beta = 0.4$, $\gamma = 2$, the regularisation parameter, $\lambda_\pi$, for the Lai&Chin snake, was variable and was calculated according to (3.5.5), and (3.5.6), and the elasticity, rigidity and the regularisation parameters for the GVF snake was, $\alpha_{GVF} = 0.05$, $\beta_{GVF} = 0$, $\mu_{GVF} = 0.2$, which are consistent with other studies [53], [241], [252], [260].

The four different plaque snakes segmentation methods were evaluated in three longitudinal ultrasound plaque images of the carotid artery bifurcation by calculating the number of the snake iterations, and the computational time needed for the snake to converge in its final position. The computational efficiency of the algorithms was tested by direct comparisons of iterations and computational time between the four different plaque snakes segmentation algorithms.

To furthermore demonstrate the working principle of the four plaque snakes segmentation methods, the total snake energy (3.4.2), $E_{snake}(v)$, the continuity energy, $E_{cont}(v)$, the curvature energy, $E_{curv}(v)$, and the image energy, $E_{image}(v)$, were plotted over the number of iterations. Furthermore, the snake parameters, $\alpha$, and $\beta$, (see 3.4.2) for the Lai&Chin snakes segmentation method were plotted over the number of iterations. The variability of these parameters over the time was thus investigated.

### *5.8.4 ROC analysis of plaque segmenattion methods*

In order to evaluate the performance of the four plaque snakes segmentation methods, we compared the manually segmented borders, delineated by an expert, with the snakes segmented borders on all 80 ultrasound images. The ROC analysis was used, with the true and false positives, and negative fractions, to assess the specificity, and sensitivity of the segmentation

method, by the true-positive fraction, $TPF$, and false-positive fraction, $FPF$, detected (see Chapter 4.5) [363]. Some additional performance metrics proposed in Chapter 4.5, such as the sensitivity, $R$ (4.16), the specificity, $Sp$ (4.17), the precision, $P$ (4.18), and $F$ (see 4.19), which is calculated from the effectiveness measure $E$, were also calculated for all four different snakes segmentation methods. Box plots of TPF, TNF, FPF, FNF, KI index, and overlap index, were plotted for all four different snakes segmentation methods.

Furthermore, ROC curves for all four different snakes segmentation methods were plotted and compared with each other. ROC curves [363] are used as a standard analysis tool to evaluate the sensitivity, $R$, (4.16), and specificity, $Sp$, (4.17), of diagnostic procedures. ROC analysis estimates a curve of the positive rate (sensitivity), versus the false positive rate (1-specificity), which describes the inherent tradeoff sensitivity and specificity of a diagnostic system.

# *Chapter 6*

# *Results*

# CHAPTER 6: RESULTS

In this Chapter we present the image quality evaluation results of two ultrasound scanners, the results of the despeckle filters presented in Chapter 2, the performance of the Williams&Shah snakes segmentation technique for the IMT, presented in Chapter 3.4, as well as the plaque segmentation results for the four different snakes segmentation techniques, presented in Chapter 3.5, namely the Williams&Shah, Balloon, Lai&Chin, and the GVF. Various criteria were used in order to compare the effectiveness of the despeckle filters such as: $\mu$, $\sigma^2$, $\sigma^3$, $\sigma^4$, SNR, C, CSR, and other image and texture metrics, as presented in Chapter 4.3 and Chapter 4.4. These metrics were applied on the original and despeckled images respectively. For evaluating the IMT and plaque segmentation methods, the evaluation metrics presented in Chapter 5.7.4, Chapter 5.7.5, and Chapter 4.5 were also used. Two experts evaluated visually the despeckle filtering results. Two experts manually delineated the IMT whereas one expert manually delineated the plaque contour.

## 6.1 Image quality evaluation of two ultrasound scanners

In this section, we evaluate image quality, based on MSE, RMSE, Err3, Err4, GAE, SNR, PSNR, quality index, Q, and structural similarity index, SSIN, in ultrasound imaging of the carotid artery. These criteria as well as statistical and texture features were computed on 80 ultrasound longitudinal images of the carotid artery bifurcation, recorded from two different ultrasound scanners, the ATL HDI-3000, and the ATL HDI-5000, before and after despeckle filtering, and after despeckle filtering and normalization. The image quality and texture measures were presented in Chapter 4.3, and Chapter 4.4, respectively (see also Chapter 5.5). The results of our study showed that image quality was improved after normalisation and normalization and despeckle filtering for both scanners. This finding is also in agreement with the visual perception evaluation carried out by the two vascular experts. Furthermore, the ultrasound images may be better visualised with the HDI ATL-5000 scanner, after normalisation and normalisation and despeckle filtering.

### *6.1.1 Visual perception*

Figure 6.1 illustrates the original before filtering, NF, despeckled, DS, normalised, N, and normalised despeckled, NDS, images for the two ultrasound image scanners. The images were depseckled with the filter *lsmv* (Chapter 2.3.1.1), which was applied for four times iteratively on the images using a 5x5 pixel window. It was shown that the images for the ATL HDI-3000 scanner have greater speckle noise compared to the ATL HDI-5000 images. Moreover the

lumen borders and the IMT were more easily identified with the ATL HDI-5000 on the N and NDS images.

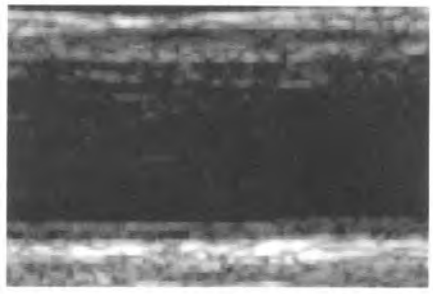

(a) Original (NF) 3000.

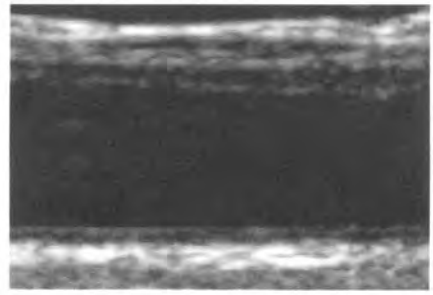

(b) Original (NF) 5000.

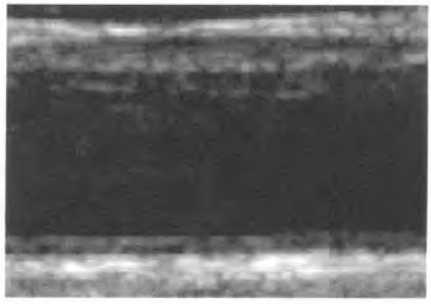

(c) Despeckled (DS) 3000.

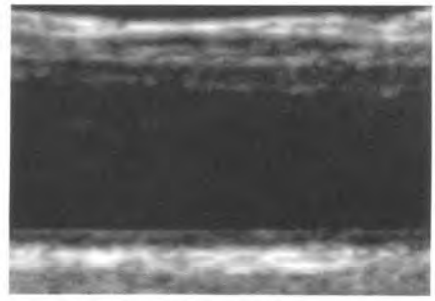

(d) Despeckled (DS) 5000.

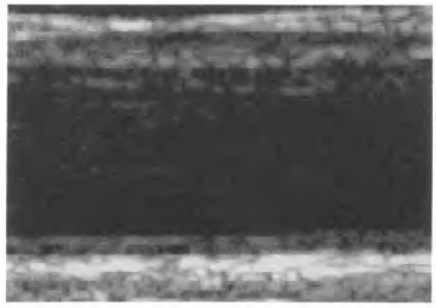

(e) Normalized (N) 3000.

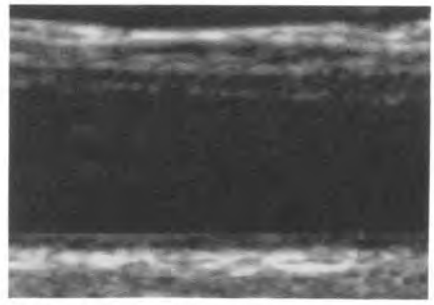

(f) Normalized (N) 5000.

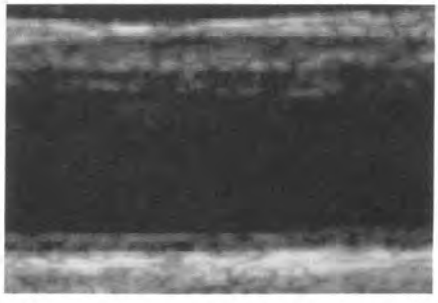

(g) Normalized despeckled (NDS) 3000.

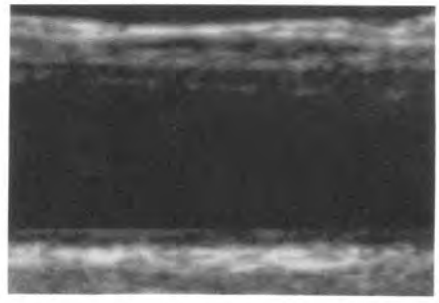

(g) Normalized despeckled (NDS) 5000.

**Fig. 6.1**: Ultrasound carotid artery images, taken from one patient at the Cyprus Institute of Neurology and Genetics, of the original (NF), despeckled (DS), normalized (N), and normalized despeckled (NDS) of the ATL HDI-3000, and ATL HDI-5000 shown in the left and right columns respectively.

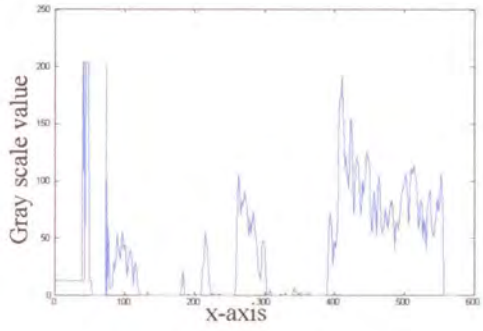


(a) Original (NF) 3000.

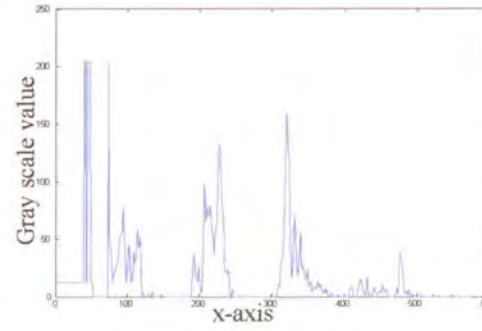


(b) Original (NF) 5000.

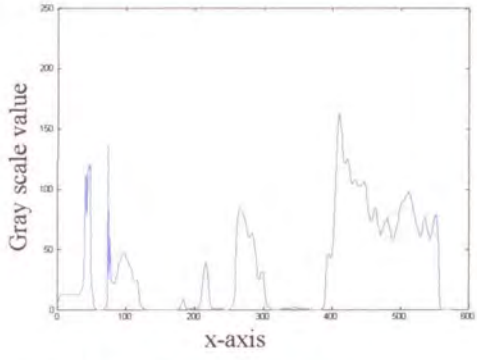


(c) Despeckled (DS) 3000.

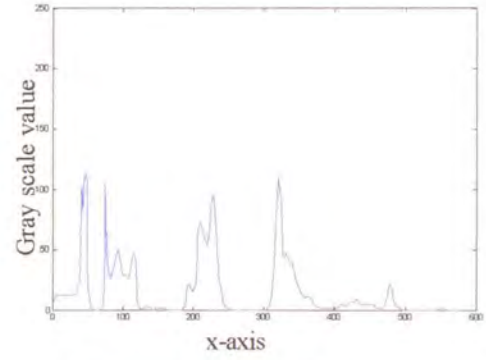


(d) Despeckled (DS) 5000.

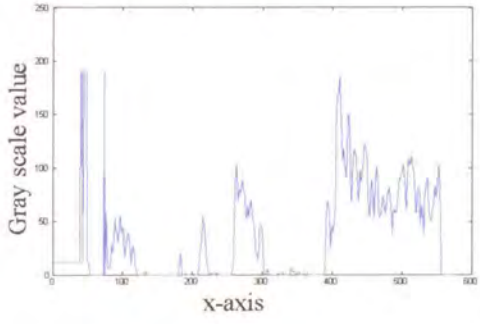


(e) Normalised (N) 3000.

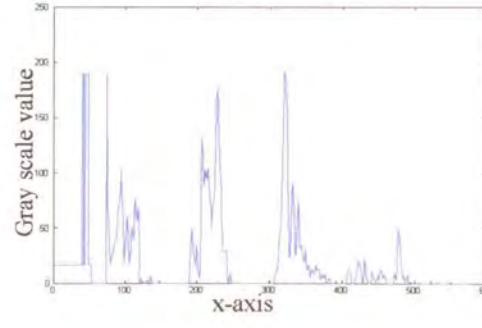


(f) Normalised (N) 5000.

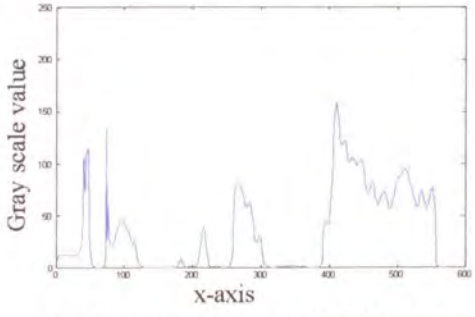


(g) Normalised despeckled (NDS) 3000.

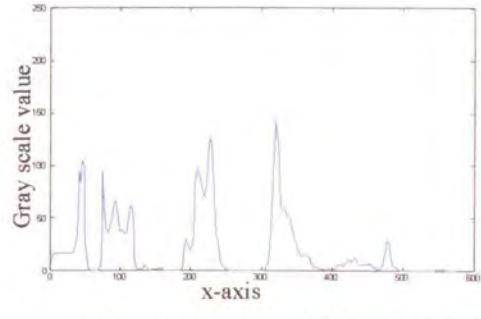


(h) Normalised despeckled (NDS) 5000.

**Fig. 6.2**: Line profiles for the NF, DS, N, and NDS images, for the ATL HDI-3000, and ATL HDI-5000 scanner, shown in the left and right columns respectively. The gray scale values, and the column 240, are shown in the y- and x-axis.

Figure 6.2 shows line profiles using a line, from the top to bottom of an ultrasound carotid image (see Fig. 6.3a) for the original, NF, despeckled, DS, normalised, N, and normalised despeckled, NDS, images for the ATL HDI-3000 and ATL HDI-5000 scanner. Figure 6.2 also shows, that despeckle filtering sharpens the edges. The contrast in the ATL HDI-3000 images was decreased after normalisation and despeckle filtering, whereas the contrast for the ATL HDI-5000 images, was increased after normalisation.

Table 6.1 presents the results, in percentage (%) format for the visual perception evaluation made by the two vascular experts on the two scanners. It is clearly shown that the highest scores were obtained for the normalized despeckled images, NDS, followed by the normalised images, N, for both scanners from both experts. The visual perception evaluation in Table 6.1 showed that the NDS images were rated higher, than the NF, DS, and N, images by both experts, for both scanners. Furthermore, the N images were rated higher than the DS and NF images.

TABLE 6.1
VISUAL PERCEPTION EVALUATION FOR THE IMAGE QUALITY ON 80 IMAGES PROCESSED FROM EACH SCANNER FOR THE ORIGINAL (NF), DESPECKLED (DS), NORMALIZED (N), AND NORMALIZED DESPECKLED (NDS). SCORES ARE EXPRESSED IN PERCENTAGE FORMAT.

| Scanner Images | ATL HDI-3000 | | | | ATL HDI-5000 | | | |
|---|---|---|---|---|---|---|---|---|
| | *NF* | *DS* | *N* | *NDS* | *NF* | *DS* | *N* | *NDS* |
| Angiologist | 30 | 43 | 69 | 72 | 26 | 42 | 59 | 70 |
| Neurovascular Specialist | 41 | 56 | 54 | 71 | 49 | 53 | 59 | 72 |
| Average | 36 | 50 | 62 | 72 | 38 | 48 | 59 | 71 |

NF: No filtering, DS: Despeckle, N: Normalised, NDS: Normalized despeckled.

### *6.1.2 Statistical and texture features*

Table 6.2 presents the results of the statistical and texture features, as presented in Chapter 4.4, for the 80 images recorded from each image scanner. As shown in the first part of Table 6.2, the effect of despeckle filtering for both scanners was similar, that is the mean and the median were preserved, the standard deviation was reduced, the skewness and the kurtosis were reduced, thus making the image histogram more symmetric and less flattened, and the speckle index was reduced. The statistical measures, presented in Table 6.2, were generally better after normalization, N, and normalization and despeckle filtering, NDS. Some measures such as the skewness, kurtosis, speckle index, and contrast, are better than the original, NF, and despeckled, DS, after normalization, N, for both scanners, and are even better after despeckle filtering and normalization, NDS. It is therefore shown that when normalization is performed on the images, the statistical features in the first part of Table 6.2 are better, than after despeckle filtering.

In the second part of Table 6.2, it was shown that the entropy was increased and the contrast

was reduced. The ASM was reduced for the despeckled, DS, images for both scanners and for the normalized despeckled, NDS, images for the ATL HDI-5000 scanner. No statistically significant difference was found for all features in Table 6.2 when performing the non-parametric Wilcoxon rank sum test at $p < 0.05$, between the original, NF, and despeckled, DS, the original, NF, and normalized, N, and the original, NF, and normalized despeckled, NDS, features for both scanners. Furthermore, Table 6.2 showed that, the entropy that is a measure of the information content of the image was higher for the ATL HDI-5000 in all the cases. The $ASM$, that is a measure of the inhomogeneity of the image was lower for the ATL HDI-5000 in the cases of the DS and NDS images. Furthermore, the entropy and the $ASM$ were more influenced from despeckling than normalization as they were reaching their best values after despeckling. Despeckle filtering reduced in both scanners the speckle index, the mean and the median were preserved, the skewness and the kurtosis were reduced, thus making the image histogram more symmetric and less flattened. When images are normalized after despeckle filtering, NDS, the above discussed measures, showed additionally a better performance. Some measures such as the skewness, kurtosis, and speckle index, are better only after normalization, N, for both scanners, and becoming even better after despeckle filtering and normalization, NDS. It was therefore shown that the normalization performs better than despeckle filtering on these images.

TABLE 6.2

STATISTICAL AND TEXTURE FEATURES (MEAN VALUES FOR 80 IMAGES PROCESSED FROM EACH SCANNER) FOR THE ORIGINAL (NF), DESPECKLED (DS), NORMALIZED (N) AND NORMALIZED DESPECKLED (NDS) IMAGES.

| Scanner | ATL HDI-3000 | | | | ATL HDI-5000 | | | |
|---|---|---|---|---|---|---|---|---|
| Images | *NF* | *DS* | *N* | *NDS* | *NF* | *DS* | *N* | *NDS* |
| Statistical Features (SF) | | | | | | | | |
| Mean ($\mu$) | 22.13 | 21.78 | 26.81 | 26.46 | 22.72 | 22.35 | 27.81 | 27.46 |
| Median | 3.07 | 4.53 | 3.56 | 5.07 | 3.73 | 5.23 | 4.59 | 6.07 |
| Stand. Deviation | 40.67 | 36.2 | 45.15 | 41.48 | 41.22 | 36.7 | 45.9 | 42.31 |
| Skewness ($\sigma^3$) | 2.88 | 2.49 | 2.23 | 2.00 | 2.84 | 2.45 | 2.17 | 1.94 |
| Kurtosis ($\sigma^4$) | 12.43 | 10.05 | 7.94 | 6.73 | 12.13 | 9.82 | 7.56 | 6.43 |
| Speckle Index (C) | 0.29 | 0.27 | 0.25 | 0.24 | 0.28 | 0.27 | 0.24 | 0.23 |
| SGLDM-Range Values | | | | | | | | |
| Entropy | 0.24 | 0.34 | 0.25 | 0.34 | 0.40 | 0.48 | 0.41 | 0.48 |
| Contrast | 667 | 309 | 664 | 303 | 618 | 302 | 595 | 287 |
| ASM | 0.36 | 0.35 | 0.38 | 0.37 | 0.37 | 0.33 | 0.39 | 0.35 |

NF: No filtering, DS: Despeckle, N: Normalised, NDS: Normalized despeckled.

### *6.1.3 Quality evaluation metrics*

Table 6.3 illustrates the image quality evaluation metrics, presented in Chapter 4.3, for the 80-ultrasound images recorded from each image scanner, between the NF-DS, NF-N, NF-NDS, and N-NDS images. Best values were obtained for the NF-N with lower RMSE, Err3, and Err4, higher SNR, and PSNR for both scanners. The GAE was 0.00 for all cases, and this can be attributed to the fact that the information between the original and the processed images remains unchanged. Best values for Q and SSIN were obtained for the NF-N images for both scanners, whereas best values for SNR were obtained for the ATL HDI-3000 scanner on the NF-N images.

It was shown from Table 6.3, that the effect of despeckle filtering was more obvious on the ATL HDI-3000 scanner, which showed that the ATL HDI-5000 scanner produces images with lower noise and distortion. Moreover, it was obvious that all quality metrics presented here were equally important for image quality evaluation. Specifically for the most of the quality metrics, better measures were obtained between the NF-N, followed by the NF-NDS, and N-NDS images for both scanners. It is furthermore important to note that a higher PSNR (or equivalently, a lower RMSE) does not necessarily imply a higher subjective image quality, although they do provide some measure of relative quality. Table 6.1 showed that the NDS images were rated visually better from both experts, followed by the N images, although the quality metrics in Table 6.2, and Table 6.3 were rated better for the N images. For example the best SNR value, Table 6.3, for the HDI ATL-3000 scanner was given for the NF-N and N-NDS images but the optical perception was not equally the best for these images, where the NDS images were rated better followed by the N images. Noise measures may be therefore misused when evaluate image quality and when the image is corrupted by a degradation other than additive noise.

TABLE 6.3
IMAGE QUALITY EVALUATION METRICS BETWEEN THE ORIGINAL-DESPECKLED (NF-DS), THE ORIGINAL-NORMALIZED (NF-N), THE ORIGINAL-NORMALIZED DESPECKLED (NF-NDS) AND THE NORMALIZED-NORMALIZED DESPECKLED (N-NDS) IMAGES.

| Evaluation Metrics | ATL HDI-3000 | | | | ATL HDI-5000 | | | |
|---|---|---|---|---|---|---|---|---|
| | *NF-DS* | *NF-N* | *NF-NDS* | *N-NDS* | *NF-DS* | *NF-N* | *NF-NDS* | N-NDS |
| MSE | 1.4 | 1.3 | 2.0 | 1.3 | 1.2 | 1.3 | 1.9 | 1.3 |
| RMSE | 1.2 | 0.4 | 1.4 | 1.1 | 1.1 | 0.5 | 1.3 | 1.1 |
| Err 3 | 3.8 | 0.8 | 3.9 | 3.5 | 3.7 | 0.8 | 3.8 | 3.5 |
| Err 4 | 8.2 | 1.2 | 8.0 | 7.52 | 8.1 | 1.3 | 7.8 | 7.5 |
| GAE | 0 | 0 | 0 | 0 | 0 | 0 | 0 | 0 |
| SNR | 5.0 | 16.5 | 4.8 | 5.4 | 5.3 | 15.9 | 5.1 | 5.4 |
| PSNR | 48.0 | 59 | 45.6 | 44.6 | 47.4 | 58.5 | 46 | 44.6 |
| Q | 0.7 | 0.93 | 0.73 | 0.69 | 0.72 | 0.93 | 0.72 | 0.71 |
| SSIN | 0.9 | 0.95 | 0.92 | 0.83 | 0.94 | 0.95 | 0.91 | 0.83 |

NF: No filtering, DS: Despeckle, N: Normalised, NDS: Normalized despeckled.

The two experts evaluated furthermore visually, 10 B-mode ultrasound images with different types of plaque (type I-type V) [238], as shown in Fig. 5.7. In order to be able to identify the type of plaque, they have inspected the blood flow image (Fig. 5.7a). The visual evaluation results showed that the plaques recorded by the ATL HDI-5000 scanner were more easily identified. The visual perception evaluation of the 10 B-mode ultrasound plaque images, showed that the plaque may be better identified on the ATL HDI-5000 scanner after normalization and despeckle filtering, NDS, where the borders of the plaque and the surrounding tissue may be better visualized, compared with the ATL HDI-3000 scanner. Specifically when inspecting dangerous plaques, with more that 70% of stenosis, with the ATL HDI-5000 scanner, the vascular experts were able to identify them better, and thus sparing patients from an unnecessary operation. The experts stated that, the risk of stroke might be better identified when using the ATL HDI-5000 scanner, or when using despeckling on the ATL HDI-3000 scanner. Furthermore, type I, and type V, plaques, which are usually excluded from different studies, were rated visually better on the ATL HDI-5000 scanner.

## 6.2 Despeckle filtering

In this Section we present the results of the despeckle filters described in Chapter 2, and evaluate their performance on 220 asymptomatic and 220 symptomatic longitudinal ultrasound images of the carotid artery. A total of 56 texture features, as presented in Chapter 4.4, were computed from each image before and after despeckle filtering, from which only the most discriminant ones, are presented. Furthermore, following the methodology presented in Chapter 5.6, the performance of these filters was investigated using the visual perception evaluation performed by two vascular experts (section 5.6.1), texture analysis, the Wilcoxon rank sum test, the statistical kNN classifier (section 5.6.2), and nine different image quality evaluation metrics (section 5.6.3).

### *6.2.1 Despeckle filtering on an artificial and a real carotid image*

Despeckle filtering was evaluated on an artificial carotid artery image (see Fig. 6.3a), corrupted by speckle noise as described in section 5.4.

Figure 6.3 shows the original noisy image of the artificial carotid artery, degraded by speckle noise, together with the despeckled images. Figure 6.4 shows line profiles (intensity), for the line marked in Fig. 6.3a for all despeckle filters. The profile results show that most of the filters (*median*, *wiener*, *lsmv*, *waveltc*, *lsminsc*, and *gf4d*), preserved the edge boundaries preserving the locality and minimally affecting the reference values in each region (as documented in Chapter 5.6). Best results were given for the filters *median, wiener, lsmv, lsminsc*, and *gf4d*. The filters *ad, nldif, ls, waveltc, homog*, and *homo* do not preserve the edges, moving the line profiles to darker grayscale values. Moreover, it is shown from Fig. 6.4i, that the filter *homo* is very noisy.

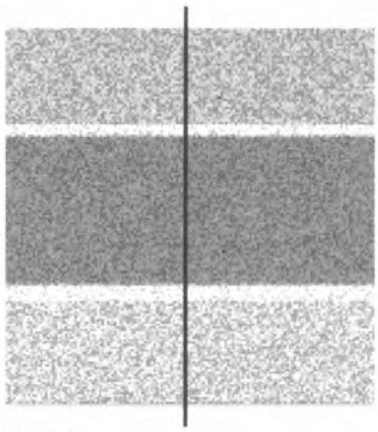

(a) original noisy image.

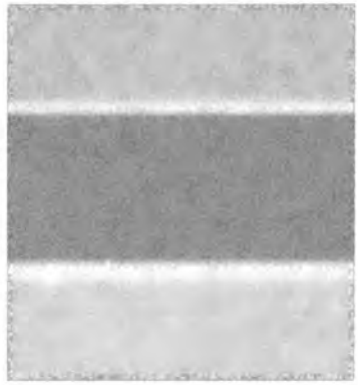

(b) *lsmv.*

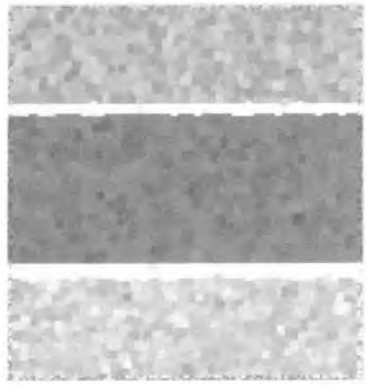

(c) *lsminsc.*

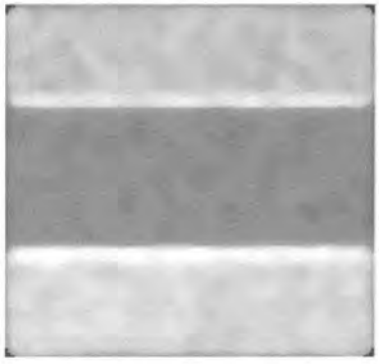

(d) *median.*

(e) *wiener.*

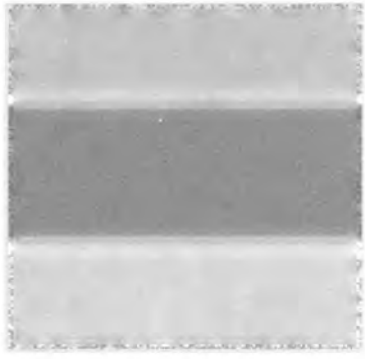

(f) *ls.*

(g) *homog.*

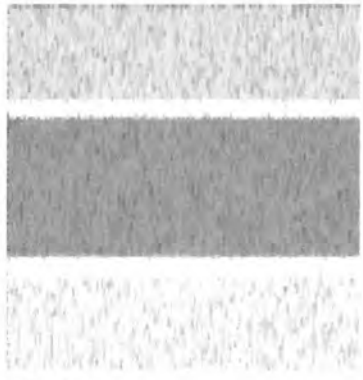

(h) *gf4d.*

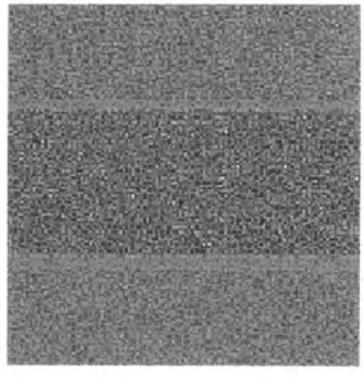

(i) *homo.*

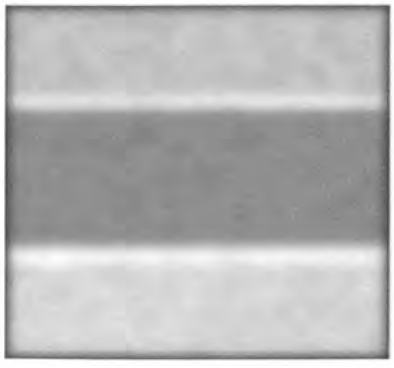

(j) *ad.*

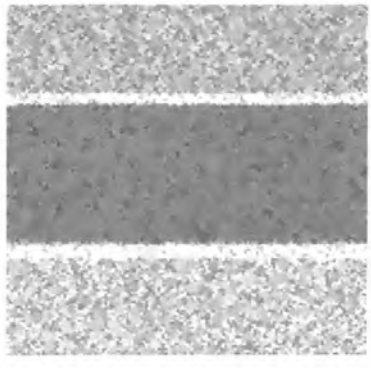

(k) *nldif.*

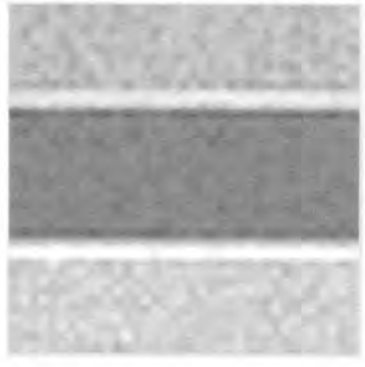

(l) *waveltc.*

**Fig. 6.3:** Original noisy image of an artificial carotid artery given in (a), and the application of the 11 despeckle filters given in (b)-(l). (Vertical line given in (a) defines the position of the line intensity profiles plotted in Fig. 6.4).

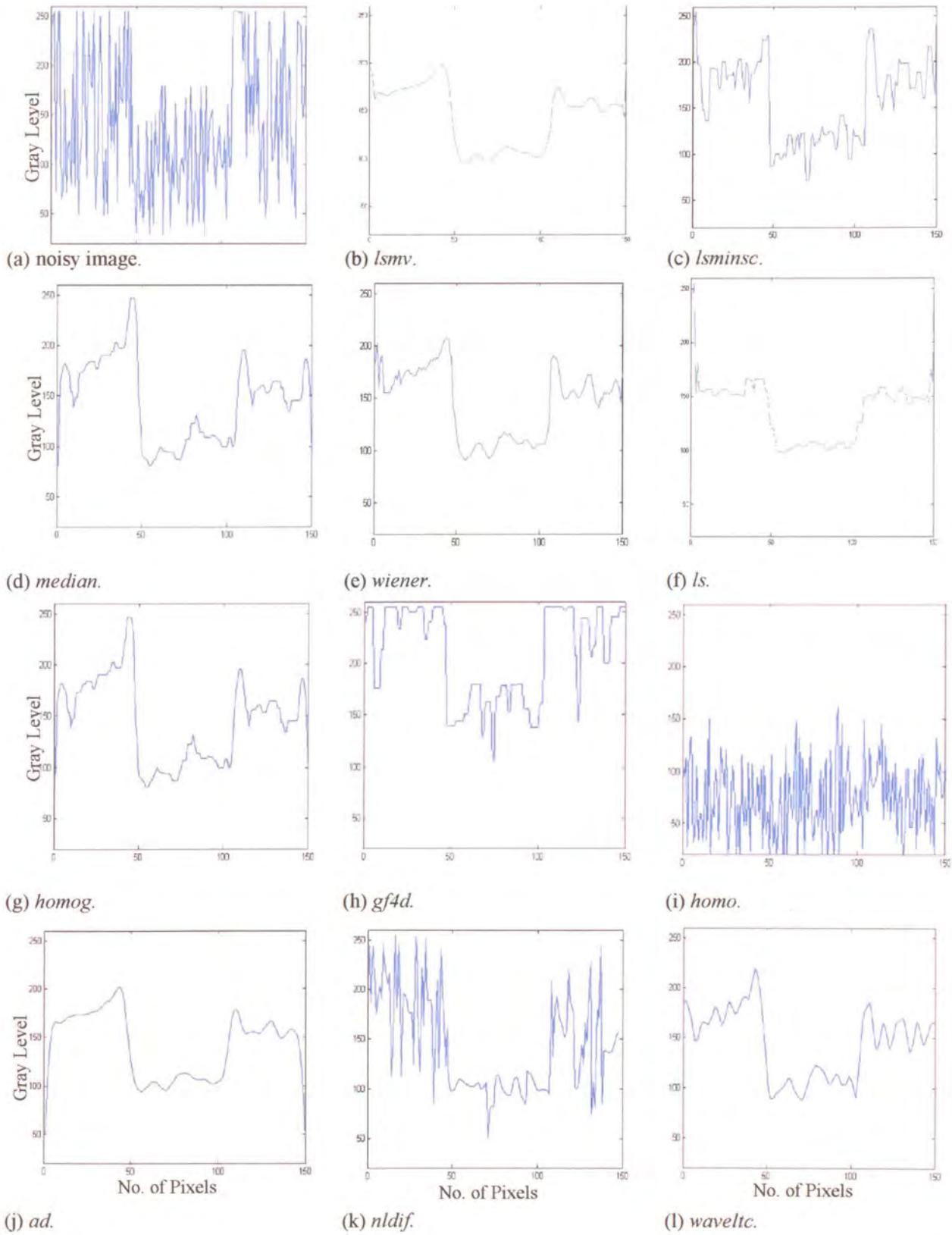


**Fig. 6.4**: Line profiles of the line illustrated in Fig. 6.3a for the original noisy image (a), and the 11 despeckled images given in (b)-(l).

Table 6.4 tabulates the statistical features, $\mu$, median, $\sigma^2$, $\sigma^3$, $\sigma^4$, the NGTDM contrast, the speckle index, C, and the contrast-speckle-radio, CSR (4.10), for the artificial image and the 11 filters illustrated in Fig. 6.3. The filters are categorized in local statistics, linear scaling (LS), maximum homogeneity (HF), geometric (GF), homomorphic (HM), diffusion and wavelet filters, as introduced in Chapter 2. Also the number of iterations (Nr. of It.), for each despeckle filter is given, which was selected based on the speckle index, C, and on the visual perception of the two vascular experts. When C was minimally changing then the filtering process was stopped. As shown in Table 6.4, all filters reduced the C with the exception of the *homo* filter, which exhibited the worst performance as it moves the mean of the image, $\mu$, to a darker gray level value, thus making the image darker. The CSR is better for the *homo, gf4d, lsminsc, waveltc, wiener, median,* and *lsmv*. Filters that reduced the variance, $\sigma^2$, while preserving the mean, $\mu$, and the median compared to the original image, were: *homo, ls, wiener, waveltc, ad, homog, median,* and *lsmv*. The contrast, of the image is increased by the filters *gf4d* (enormously), *homo, lsminsc, ls, median,* and *homog* and it is decreased by the filters *ad, wiener, waveltc,* and *lsmv*. It is noted that filters *gf4d, lsmv* and *lsminsc* reduced C, increased CSR, *lsmv* reduced the contrast, whereas *lsminsc* increased the contrast.

TABLE 6.4
SELECTED STATISTICAL FEATURES FOR FIG. 6.3A BEFORE AND AFTER DESPECKLE FILTERING. BOLDED VALUES SHOW IMPROVEMENT AFTER DESPECKLE FILTERING.

| | *original* | Local Statistics | | | | LS | HF | GF | HM | Diffusion | | Wavelet |
|---|---|---|---|---|---|---|---|---|---|---|---|---|
| Feature | *image* | *lsmv* | *lsminsc* | *median* | *wiener* | *ls* | *homog* | *gf4d* | *homo* | *ad* | *nldif* | *waveltc* |
| Nr. of It. | | 4 | 1 | 2 | 2 | 3 | 3 | 3 | 2 | 20 | 5 | 5 |
| $\mu$ | 138 | 145 | 157 | 145 | 145 | 143 | 145 | 176 | 55 | 139 | 143 | 146 |
| Median | 132 | 151 | 162 | 152 | 157 | 157 | 156 | 157 | 55 | 152 | 132 | 156 |
| $\sigma^2$ | 53 | 41 | 46 | 40 | 37 | 33 | 40 | 46 | 24 | 39 | 51 | 38 |
| $\sigma^3$ | 0.85 | -0.1 | 0.09 | 0.07 | -0.2 | -0.2 | 0.02 | 0.07 | 0.36 | -0.35 | 0.44 | -0.09 |
| $\sigma^4$ | 2 | 2 | 1.8 | 2 | 1.6 | 1.8 | 1.8 | 1.8 | 4 | 2 | 2 | 1.6 |
| Contrast | 124 | 68 | **239** | **141** | 27 | **201** | **132** | **1072** | **340** | 26 | 60 | 50 |
| $C = (\sigma^2/\mu)100$ | 38 | **28** | **29** | **28** | **26** | **23** | **28** | **26** | 44 | **28** | **36** | **26** |
| CSR | | **99** | **263** | **100** | **101** | **74** | **100** | **527** | **1305** | **14** | **68** | **115** |

LS: Linear scaling, HF: Homogeneity, GF: Geometric, HM: Homomorphic.

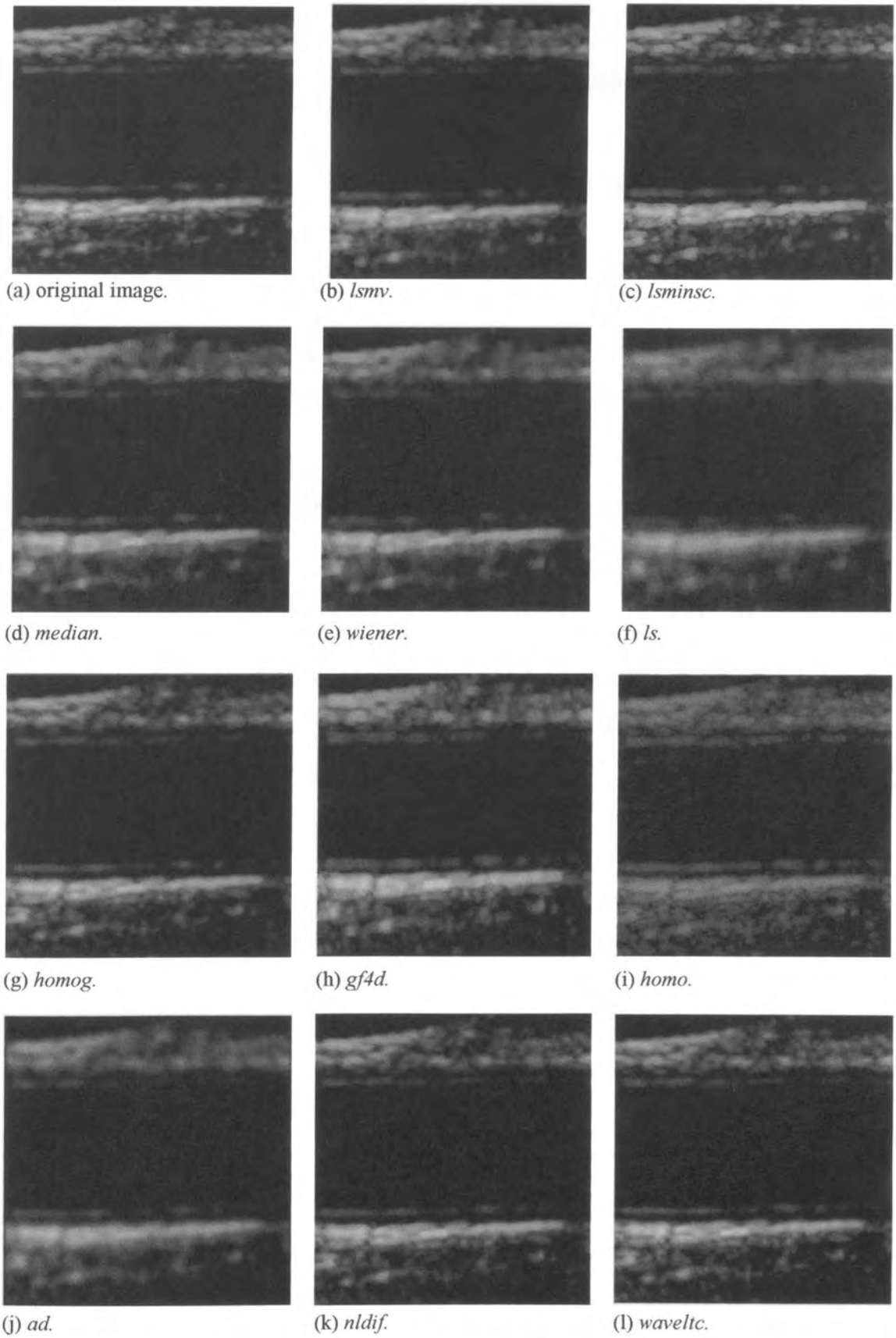

(a) original image. (b) *lsmv.* (c) *lsminsc.*

(d) *median.* (e) *wiener.* (f) *ls.*

(g) *homog.* (h) *gf4d.* (i) *homo.*

(j) *ad.* (k) *nldif.* (l) *waveltc.*

**Fig. 6.5**: Original ultrasound image of the carotid artery (2-3 cm proximal to bifurcation) given in (a), and the despeckled images given in (b)-(l).

The despeckled images of Fig. 6.3 were also assessed by the two experts. Filters that showed an improved smoothing after filtering, as assessed visually by the two experts, using visual perception criteria, are presented in the following order: *waveltc, lsmv, nldif, ad, gf4d* and *median*. Filters that showed a blurring effect especially on the edges were: *ls, lsminsc, homog, homo* and *wiener*.

Figure 6.5 shows an original longitudinal ultrasound image of a symptomatic carotid artery together with the despeckled images. The best visual results as assessed by the two vascular experts were obtained by the filters *lsminsc,* and *lsmv* whereas the filters *gf4d, ad,* and *nldif* also show good visual results but, smooth the image considerably and thus edges and subtle details may be lost. Filters that showed a blurring effect are *median, wiener, ls, homog, and waveltc.* Filters *wiener, homog,* and *waveltc* showed poorer visual results.

### *6.2.2 Texture analysis*

Despeckle filtering, and texture analysis, were carried out on 440 carotid plaque ultrasound images (220 asymptomatic, 220 symptomatic). Table 6.5 tabulates the results of feature distance, $feat_dis_i$, (4.13), and score distance, $Score_Dis$, (4.14), for SF, SGLDM range of values and NGTDM feature sets. The results of these feature sets are presented only, since these sets were the ones with the best performance. The values in bold represent the values that showed an improvement after despeckle filtering when compared to the original. The last row in each sub-table shows the $Score_Dis$ for all features, as given in (4.14), where the highest value indicates the best filter in the sub-table. Additionally a total score distance $Score_Dis_T$ was calculated for all feature sets and it is shown in the last row of Table 6.5. Some of the despeckle filters, shown in Table 6.5, are changing a number of texture features, by increasing the distance between the two classes, (asymptomatic and symptomatic), and therefore making the identification and separation of asymptomatic, and symptomatic plaques more feasible. The positive values in Table 6.5 shows an increase between the two classes whereas the negative a deterioration.

In the first part of the Table 6.5 the results of the statistical features, SF, are presented, where the best $Score_Dis$ was given by the *homo* filter followed by the *lsminsc, lsmv, homog, nldif, waveltc, ls, median,* and *wiener,* with the worst $Score_Dis$ given by *gf4d.* All filters reduced the speckle index, C. Almost all filters reduced the kurtosis, $\sigma^3$, and the asymmetry, $\sigma^4$, of the histogram, as it may be seen from the bolded values in the first part of Table 6.5.

In the second part of the Table 6.5 the results of the SGLDM range of values features set are tabulated. The filters with the highest $Score_Dis$ in the SGLDM range of values features set, are *homo, lsminsc, median,* and *ad* whereas the filters *nldif* and *gf4d* are presenting a low

*Score_Dis*. Texture features, which were improved in most of the filters, are the contrast, correlation, sum of squares variance, SOSV, sum average, SAV, and sum variance, $\sum Var$.

In the third part of Table 6.5, for the NGTDM feature set, almost all filters showed an improvement in *Score_Dis*. Best filters in the NGTDM features category were, the *homo, lsminsc* and *lsmv*. Texture features that improved the most were the completion, coarseness and contrast. The completion of the image was increased by all filters.

TABLE 6.5
FEATURE DISTANCE (4.13) AND SCORE_DIS (4.14) FOR SF, SGLDM RANGE OF VALUES, AND NGTDM TEXTURE FEATURE SETS BETWEEN ASYMPTOMATIC AND SYMPTOMATIC CAROTID PLAQUE ULTRASOUND IMAGES. BOLDED VALUES SHOW IMPROVEMENT AFTER DESPECKLE FILTERING.

| | Local Statistics | | | | LS | HF | GF | HM | Diffusion | | Wavelet |
|---|---|---|---|---|---|---|---|---|---|---|---|
| Feature | *lsmv* | *lsminsc* | *median* | *wiener* | *ls* | *homog* | *gf4d* | *homo* | *ad* | *nldif* | *waveltc* |
| Nr. of It. | 4 | 1 | 2 | 2 | 3 | 3 | 3 | 2 | 20 | 5 | 5 |
| SF-Statistical Features | | | | | | | | | | | |
| Mean | **14** | **22** | **4** | **19** | **24** | **11** | **3** | **164** | **18** | **5** | **15** |
| Median | -5 | -17 | -5 | -26 | -30 | -5 | -15 | **110** | -29 | -6 | -15 |
| $\sigma^2$ | 18 | 38 | 7 | 18 | 21 | 13 | **-2** | 140 | 9 | 7 | 18 |
| $\sigma^3$ | **12** | **16** | **9** | **5** | **5** | **7** | -0.1 | **149** | **17** | **7** | **8** |
| $\sigma^4$ | **-12** | **-14** | **-6** | **-7** | **-9** | **-4** | **-3** | 117 | **-21** | 6 | **-9** |
| C | 0.4 | 0.3 | 0.4 | 0.3 | 0.4 | 0.3 | 0.4 | 0.08 | 0.3 | 0.4 | 0.3 |
| *Score_Dis* | 27 | 45 | 9 | 9 | 11 | 22 | -17 | 680 | -6 | 19 | 17 |
| SGLDM Range of Values–Spatial Gray Level Dependence Matrix | | | | | | | | | | | |
| ASM | -21 | -0.5 | **2** | -29 | -47 | -4 | -8 | -47 | -25 | -17 | -20 |
| Contrast | **47** | **107** | **64** | **14** | **45** | **32** | -3 | **165** | **104** | **13** | **22** |
| Correlation | **12** | **59** | **24** | **15** | **8** | -5 | **2** | **10** | **54** | -4 | -4 |
| SOSV | **9** | **40** | **10** | **18** | **16** | **16** | -2 | **101** | **9** | **8** | **20** |
| IDM | -50 | -11 | **2** | -48 | -36 | -29 | -8 | **94** | -54 | -34 | -43 |
| SAV | **17** | **24** | **7** | **23** | **20** | **15** | **3** | **169** | **22** | **6** | **18** |
| $\sum Var$ | **19** | **38** | **9** | **18** | **12** | **15** | -2 | **90** | **9** | **8** | **20** |
| $\sum Entr$ | -34 | -14 | **3** | -49 | -41 | -19 | -4 | -11 | -47 | -30 | -36 |
| *Score_Dis* | -1 | 243 | 121 | -38 | -23 | 21 | -22 | 571 | 72 | -50 | -23 |
| NGTDM–Neighbourhood Gray Tone Difference Matrix | | | | | | | | | | | |
| Coarseness | **30** | **87** | **9** | **4** | -30 | -16 | -7 | **72** | -36 | -37 | -33 |
| Contrast | **7** | -0.3 | **8** | -9 | -16 | **0.4** | -4 | **105** | **5** | -27 | -15 |
| Busyness | **17** | **26** | **8** | -30 | -36 | **1** | -4 | **48** | -14 | -39 | **8** |
| Completion | **64** | **151** | **53** | **21** | **96** | **80** | **2** | **150** | **63** | **18** | **27** |
| *Score_Dis* | 118 | 264 | 78 | -14 | 14 | 66 | -13 | 375 | 18 | -85 | -13 |
| *Score_Dis_T* | 144 | 551 | 208 | -43 | 2 | 108 | -52 | 1626 | 84 | -116 | -19 |

ASM: Angular 2nd moment, SOSV: Sum of squares variance, IDM: Inverse difference moment, SAV: Sum average, $\sum Var$: Sum Variance. LS: Linear Scaling, HF: Homogeneity, GF: Geometric, HM: Homomorphic.

Finally, in the last row of Table 6.5, the total score distance, $Score_Dis_T$, for all feature sets is shown, where best values were obtained by the filters *homo*, *lsminsc*, *lsmv*, *median*, *homog*, and *ad*.

Table 6.6 shows the results of the rank sum test, which was performed on the SGLDM range of values features set of Table 6.5, for all the 11 despeckle filters. The test was performed to check if significant differences exist between the features computed on the 440 original and the 440 despeckled images (220 asymptomatic, 220 symptomatic). Filters that resulted with the most significant number of features after despeckle filtering as shown with the score row of Table 6.6 were the following: *lsmv* (7), *gf4d* (6), *lsminsc* (5) and *nldif* (4). The rest of the filters gave a lower number of significantly different features.

TABLE 6.6
WILCOXON RANK SUM TEST FOR THE SGLDM RANGE OF VALUES TEXTURE FEATURES APPLIED ON THE 440 ULTRASOUND IMAGES OF CAROTID PLAQUE BEFORE AND AFTER DESPECKLE FILTERING. THE TEST SHOWS WITH S SIGNIFICANT DIFFERENCE AFTER FILTERING AT $p<0.05$ AND NS NO SIGNIFICANT DIFFERENCE AFTER FILTERING AT $p>=0.05$. THE P VALUE IS ALSO GIVEN IN PARENTHESIS.

| | Local Statistics | | | | LS | HF | GF | HM | Diffusion | | Wavelet | Score |
|---|---|---|---|---|---|---|---|---|---|---|---|---|
| Feature | *lsmv* | *lsminsc* | *median* | *wiener* | *ls* | *homog* | *gf4d* | *homo* | *Ad* | *nldif* | *waveltc* | |
| ASM | S (0.00) | S (0.00) | NS (0.07) | NS (0.06) | NS (0.07) | S (0.00) | S (0.02) | NS (0.41) | S (0.00) | S (0.01) | S (0.00) | 7 |
| Contrast | S (0.00) | NS (0.08) | NS (0.06) | NS (0.07) | NS (0.08) | NS (0.25) | S (0.03) | NS (0.17) | NS (0.07) | S (0.03) | NS (0.57) | 3 |
| Correlation | S (0.00) | S (0.00) | NS (0.17) | NS (0.06) | NS (0.09) | NS (0.67) | S (0.01) | NS (0.09) | NS (0.06) | NS (0.26) | NS (0.1) | 3 |
| SOSV | S (0.01) | NS (0.22) | NS (0.19) | NS (0.31) | NS (0.76) | NS (0.56) | S (0.05) | NS (0.2) | NS (0.43) | NS (0.5) | NS (0.19) | 2 |
| IDM | S (0.00) | S (0.00) | S (0.00) | NS (0.09) | NS (0.31) | S (0.00) | S (0.04) | S (0.00) | NS (0.51) | S (0.04) | S (0.00) | 8 |
| SAV | NS (0.85) | NS (0.16) | NS (0.29) | NS (0.11) | NS (0.06) | NS (0.5) | NS (0.6) | NS (0.07) | NS (0.17) | NS (0.66) | NS (0.12) | 0 |
| $\sum Var$ | S (0.02) | S (0.01) | NS (0.24) | NS (0.29) | NS (0.9) | NS (0.47) | NS (0.51) | NS (0.6) | NS (0.59) | NS (0.55) | NS (0.09) | 2 |
| $\sum Entr$ | S (0.04) | S (0.03) | NS (0.3) | NS (0.06) | NS (0.08) | NS (0.08) | S (0.04) | NS (0.73) | NS (0.09) | S (0.01) | S (0.02) | 5 |
| Score | 7 | 5 | 1 | 0 | 0 | 2 | 6 | 1 | 1 | 4 | 3 | |

ASM: Angular 2nd moment, SOSV: Sum of squares variance, IDM: Inverse difference moment, SAV: Sum average, $\sum Var$: Sum Variance. LS: Linear Scaling, HF: Homogeneity, GF: Geometric, HM: Homomorphic, Score: illustrates the number of S.

Some texture measures, shown in Table 6.6, were more influenced after despeckle filtering than others. Specifically, features that showed a significant difference after despeckle filtering (see Score column in Table 6.6), were the inverse difference moment, IDM (8), angular second moment, ASM (7), sum of entropy (5), contrast (3), correlation (3), sum of squares variance, SOSV (2), and sum variance, $\sum Var$ (2). These features were mostly affected after despeckle

filtering and they were significantly different. The high score number of the significantly different features for a despeckle filter, allows a better distinction between two classes (original and despeckle or asymptomatic and symptomatic).

Table 6.7 shows the percentage of correct classifications score for the kNN classifier with k=7 for classifying a subject as asymptomatic or symptomatic. The classifier was evaluated using the leave one out method [211], on 220 asymptomatic, and 220 symptomatic images on the original, and despeckled images. The percentage of correct classifications score is given for the following feature sets: Statistical Features, SF, Spatial Gray Level Dependence Matrix Mean Values, SGLDMm, Spatial Gray Level Dependence Matrix Range of Values, SGLDMr, Gray Level Difference Statistics, GLDS, Neighborhood Gray Tone Difference Matrix, NGTDM, Statistical Feature Matrix, SFM, Laws Texture Energy Measures, TEM, Fractal Dimension Texture Analysis, FDTA, and Fourier Power Spectrum, FPS. The average classification success score for each despeckle filter, is shown in the last row of Table 6.7. Filters that showed an improvement in classifications success score compared to that of the original image set, were in average (last row of Table 6.7) the filter *homo* (3 %), *gf4d* (1%), and *lsminsc* (1%).

TABLE 6.7
PERCENTAGE OF CORRECT CLASSIFICATIONS SCORE FOR THE KNN CLASSIFIER WITH K=7 FOR THE ORIGINAL AND THE DESPECKLED IMAGE SETS. BOLDED VALUES INDICATE IMPROVEMENT AFTER DESPECKLING.

| Feature set | No of Feat. | *original* | Local Statistics | | | | LS | HF | GF | HM | Diffusion | | Wavelet | Score |
|---|---|---|---|---|---|---|---|---|---|---|---|---|---|---|
| | | | *lsmv* | *lsminsc* | *wiener* | *median* | *ls* | *homog* | *gf4d* | *homo* | *ad* | *nldif* | *waveltc* | |
| SF | 5 | 59 | **62** | **61** | **61** | 57 | 57 | **63** | 59 | **65** | **60** | 52 | **61** | 7 |
| SGLDMm | 13 | 65 | 63 | 64 | 62 | 63 | 61 | **69** | **67** | **68** | 61 | **66** | 63 | 4 |
| SGLDMr | 13 | 70 | 66 | **72** | 64 | 66 | 64 | 65 | 70 | 69 | 64 | 65 | 65 | 1 |
| GLDS | 4 | 64 | 63 | **66** | 61 | **69** | 59 | 64 | **66** | **72** | 59 | 58 | 62 | 4 |
| NGTDM | 5 | 64 | 63 | **68** | 60 | **69** | **66** | 63 | **65** | 57 | 60 | 61 | 62 | 4 |
| SFM | 4 | 62 | 62 | 60 | 62 | 58 | 56 | 55 | **65** | **68** | 59 | 56 | 55 | 2 |
| TEM | 6 | 59 | **68** | 52 | **60** | 59 | 55 | **66** | **60** | **65** | 53 | **60** | **60** | 7 |
| FDTA | 4 | 64 | 63 | **66** | 53 | **68** | 51 | 53 | 62 | **73** | 55 | 54 | 62 | 3 |
| FPS | 2 | 59 | 54 | **64** | 59 | 58 | 55 | 59 | 59 | 59 | 52 | 48 | 55 | 1 |
| Average | | 63 | 63 | **64** | 60 | 63 | 58 | 62 | **64** | **66** | 58 | 58 | 61 | |

SF: Statistical Features, SGLDMm: Spatial Gray Level Dependence Matrix Mean Values, SGLDMr: Spatial Gray Level Dependence Matrix Range of Values, GLDS: Gray Level Difference Statistics, NGTDM: Neighborhood Gray Tone Difference Matrix, SFM: Statistical Feature Matrix, TEM: Laws Texture Energy Measures, FDTA: Fractal Dimension Texture Analysis, FPS: Fourier Power Spectrum.
LS: Linear Scaling, HF: Homogeneity, GF: Geometric, HM: Homomorphic.

Feature sets, which benefited mostly by despeckle filtering were (last column in Table 6.7) the SF (7), TEM (7), SGLDMm (4), GLDS (4), and NGTDM (4), when counting the number of despeckle filters, in which the correct classifications score was improved. Less improvement was observed, for the feature sets FDTA, SFM, FPS and SGLDMr. For the feature set SGLDMr better results were given for the *lsminsc* filter with an improvement of 2%. This is the only filter

that showed an improvement for this class of features. For the feature set TEM the filter *lsmv* shows the best improvement with 9%, whereas for the FPS feature set the filter *lsminsc* gave the best improvement with 5%. The filter *lsminsc* showed significant improvement in the GLDS and NGTDM feature sets, whereas the filter *lsmv* showed significant improvement for the feature sets SF and TEM.

### *6.2.3 Image quality evaluation metrics*

Table 6.8 tabulates the image quality evaluation metrics presented in Chapter 4.3, for the 220 asymptomatic and 220 symptomatic ultrasound images between the original and the despeckled images respectively. Best values were obtained for the *nldif*, *lsmv* and *waveltc* with lower MSE, RMSE, Err3, and Err4 and higher SNR and PSNR for both the asymptomatic and symptomatic ultrasound images sets. The GAE was 0.00 for all cases, and this can be attributed to the fact that the information between the original and the despeckled images remains unchanged. Best values, for both asymptomatic and symptomatic images sets, for the universal quality index, Q, and the structural similarity index, SSIN were obtained for the filters *lsmv* and *nldif*.

TABLE 6.8
IMAGE QUALITY EVALUATION METRICS COMPUTED FOR THE 220 ASYMPTOMATIC AND 220 SYMPTOMATIC IMAGES.

| | Local Statistics | | | | LS | HF | GF | HM | Diffusion | | Wavelet |
|---|---|---|---|---|---|---|---|---|---|---|---|
| Feature set | *lsmv* | *lsminsc* | *wiener* | *median* | *ls* | *homog* | *gf4d* | *homo* | *ad* | *nldif* | *waveltc* |
| Asymptomatic Images | | | | | | | | | | | |
| MSE | 13 | 86 | 19 | 131 | 131 | 42 | 182 | 758 | 132 | 8 | 11 |
| RMSE | 3 | 9 | 4 | 10 | 10 | 6 | 13 | 27 | 11 | 2 | 3 |
| M3 | 7 | 17 | 5 | 25 | 25 | 14 | 25 | 38 | 21 | 5 | 4 |
| M4 | 11 | 26 | 7 | 41 | 41 | 24 | 40 | 49 | 32 | 10 | 5 |
| GAE | 0 | 0 | 0 | 0 | 0 | 0 | 0 | 0 | 0 | 0 | 0 |
| SNR | 25 | 17 | 23 | 16 | 16 | 21 | 14 | 5 | 14 | 28 | 25 |
| PSNR | 39 | 29 | 36 | 29 | 29 | 34 | 27 | 20 | 28 | 41 | 39 |
| Q | 0.83 | 0.78 | 0.74 | 0.84 | 0.84 | 0.92 | 0.77 | 0.28 | 0.68 | 0.93 | 0.65 |
| SSIN | 0.97 | 0.88 | 0.92 | 0.94 | 0.94 | 0.97 | 0.88 | 0.43 | 0.87 | 0.97 | 0.90 |
| Symptomatic Images | | | | | | | | | | | |
| MSE | 33 | 374 | 44 | 169 | 169 | 110 | 557 | 1452 | 374 | 8 | 23 |
| RMSE | 5 | 19 | 6 | 13 | 13 | 10 | 23 | 37 | 19 | 3 | 5 |
| M3 | 10 | 33 | 9 | 25 | 25 | 20 | 43 | 51 | 31 | 5 | 6 |
| M4 | 16 | 47 | 11 | 38 | 39 | 30 | 63 | 64 | 43 | 7 | 8 |
| GAE | 0 | 0 | 0 | 0 | 0 | 0 | 0 | 0 | 0 | 0 | 0 |
| SNR | 24 | 13 | 22 | 16 | 16 | 17 | 12 | 5 | 12 | 29 | 25 |
| PSNR | 34 | 23 | 33 | 26 | 26 | 28 | 21 | 17 | 23 | 39 | 36 |
| Q | 0.82 | 0.77 | 0.70 | 0.79 | 0.79 | 0.87 | 0.75 | 0.24 | 0.63 | 0.87 | 0.49 |
| SSIN | 0.97 | 0.85 | 0.89 | 0.81 | 0.91 | 0.94 | 0.85 | 0.28 | 0.81 | 0.97 | 0.87 |

MSE: Mean square error, RMSE: Randomised mean square error, M3, M4: Minowski metrics, GAE: Geometric average error, SNR: Signal to noise radio, PSNR: Peak signal to noise radio, Q: Universal quality index, SSIN: Structural similarity index.
LS: Linear Scaling, HF: Homogeneity, GF: Geometric, HM: Homomorphic.

### *6.2.4 Visual perception by experts*

Table 6.9.1 shows the results of the visual perception evaluation of the original and despeckled images made by the two experts, a cardiovascular surgeon and a neurovascular expert. They evaluated 100 ultrasound images before and after despeckle filtering (50 asymptomatic (A) and 50 symptomatic (S)). For each case a total of 10 images were evaluated (one original and nine filtered). For each case, for each image, the experts assigned a score in the one to five scale based on subjective criteria. Therefore the maximum score for a filter is 500, if the expert assigned the score of five for all the 100 images. For each filter, the score was divided by five to be expressed in percentage format. The last row of Table 6.9.1 presents the overall average percentage (%) score assigned by both vascular experts for each filter.

For the cardiovascular surgeon, in Table 6.9.1, the average score, showed that the best despeckle filter is the *lsmv* with a score of 62%, followed by *gf4d, ls, median, homog* and *original* with scores of 52%, 51%, 50%, 45% and 41% respectively. For the neurovascular expert, the average score showed that the best filter is the *gf4d* with a score of 72%, followed by *lsmv, original, lsminsc* and *median* with scores of 71%, 68%, 68% and 66% respectively. The overall average % score shows that the highest score was given to the filter *lsmv* (67%), followed by *gf4d* (62%), *median* (58%), *ls* (55%) and *original* (54%). It should be emphasized that the despeckle filter *lsmv* is the only filter that was graded with a higher score than the original by both vascular experts for the asymptomatic and symptomatic image sets.

TABLE 6.9.1
PERCENTAGE SCORING OF VISUAL EVALUATION OF THE ORIGINAL AND DESPECKLED IMAGES (50 ASYMPTOMATIC (A) AND 50 SYMPTOMATIC (S)) BY THE EXPERTS.

| Experts | A/S | *original* | Local Statistics | | | LS | HF | GF | HM | Diffusion | Wavelet |
|---|---|---|---|---|---|---|---|---|---|---|---|
| | | | *lsmv* | *lsminsc* | *median* | *ls* | *homog* | *gf4d* | *homo* | *nldif* | *waveltc* |
| Cardiovascular | A | 33 | 75 | 33 | 43 | 57 | 47 | 61 | 19 | 43 | 32 |
| Surgeon | S | 48 | 49 | 18 | 57 | 45 | 43 | 42 | 20 | 33 | 22 |
| Average % | | 41 | 62 | 26 | 50 | 51 | 45 | 52 | 19 | 38 | 27 |
| Neurovascular | A | 70 | 76 | 73 | 74 | 64 | 63 | 79 | 23 | 52 | 29 |
| Expert | S | 66 | 67 | 63 | 58 | 52 | 45 | 65 | 55 | 41 | 28 |
| Average % | | 68 | 71 | 68 | 66 | 58 | 54 | 72 | 39 | 47 | 28 |
| Overall Average % | | 54 | 67 | 47 | 58 | 55 | 50 | 62 | 29 | 43 | 28 |

LS: Linear Scaling, HF: Homogeneity, GF: Geometric, HM: Homomorphic.

We may observe from Table 6.9.1, a difference in the ratings between the two vascular experts and this is because, the cardiovascular surgeon is primarily interested in the plaque composition and texture evaluation whereas the neurovascular expert is interested to evaluate the degree of stenosis and the lumen diameter in order to identify the plaque contour. Filters *lsmv,* and *gf4d,* were identified as the best despeckle filters, by both experts, as they improved visual perception with overall average scores of 67% and 62% respectively. The filters *waveltc*

and *homo* were scored by both experts with the lowest overall average scores of 28% and 29% respectively.

TABLE 6.9.2
PERCENTAGE SCORING OF VISUAL EVALUATION OF THE ORIGINAL AND DESPECKLED IMAGES (50 ASYMPTOMATIC (A) AND 50 SYMPTOMATIC (S)) BY THE EXPERTS ONE YEAR AFTER THE FIRST VISUAL EVALUATION.

| Experts | A/S | *original* | Local Statistics | | | LS | HF | GF | HM | Diffusion | Wavelet |
|---|---|---|---|---|---|---|---|---|---|---|---|
| | | | *lsmv* | *lsminsc* | *median* | *ls* | *homog* | *gf4d* | *homo* | *nldif* | *waveltc* |
| Cardiovascular | A | 28 | 57 | 43 | 62 | 49 | 41 | 53 | 16 | 39 | 31 |
| Surgeon | S | 44 | 65 | 24 | 57 | 49 | 39 | 51 | 23 | 37 | 21 |
| Average % | | 36 | 61 | 34 | 60 | 49 | 40 | 52 | 20 | 38 | 26 |
| Neurovascular | A | 62 | 65 | 64 | 69 | 67 | 51 | 65 | 19 | 49 | 24 |
| Expert | S | 64 | 62 | 71 | 53 | 51 | 49 | 69 | 49 | 44 | 26 |
| Average % | | 63 | 64 | 68 | 61 | 59 | 50 | 67 | 34 | 47 | 25 |
| Overall Average % | | 50 | 63 | 51 | 61 | 54 | 45 | 60 | 27 | 43 | 26 |

LS: Linear Scaling, HF: Homogeneity, GF: Geometric, HM: Homomorphic.

Table 6.9.2 shows the results of the visual perception evaluation made by the same experts, one year after the first visual evaluation. The visual perception evaluation was repeated in order to assess the intra-observer variability between the same expert and was performed under the same conditions as the first visual evaluation

For the cardiovascular surgeon, the average score, showed that the best despeckle filter is again the *lsmv* with a score of 61%, followed by *median, gf4d, ls, homog* and *original* with scores of 60%, 52%, 49%, 40% and 36% respectively. For the neurovascular expert, the average score showed that the best filter is the *lsminsc* with a score of 68%, followed by *gf4d, lsmv, original,* and *median* with scores of 67%, 64%, 63% and 61% respectively. The overall average% score shows that the highest score was given to the filter *lsmv* (63%), followed by *median* (61%), *gf4d* (60%), *ls* (54%) and *original* (50%). The intra-observer variability results in Table 6.9.2 shows a consistency in almost all results, with only very small differences between filters. The despeckle filter *lsmv* is again, the only filter that was graded with a higher score than the original by both vascular experts for the asymptomatic and symptomatic images.

### *6.2.5 Additional comments by experts*

The two experts have made additional comments for each despeckle filter when they evaluated the images visually. These comments are presented in Table 6.10. The images were evaluated according to the protocol described in Chapter 5.6.1.

Both experts were in agreement that the best despeckle filters for visual perception, are the *lsmv*, *lsminsc*, *gf4d*, and *median*, whereas the worst filters were the *waveltc* followed by the *homo* and *nldif* (see also Table 6.9.1, Table 6.9.2, and Table 6.10). Furthermore, both experts

agreed that almost all despeckle filters reduced the noise substantially and images may be better visualized after despeckle filtering.

By examining all the visual results of Fig. 6.3-Fig. 6.5, the statistical results of Table 6.4-Table 6.8, the visual evaluation of Tables 6.9.1 and Table 6.9.2, and the additional comments made by the experts in Table 6.10, we can conclude that the best filters are the *lsmv* and the *gf4d*, which may be used for both plaque composition enhancement and plaque texture analysis, whereas the filters *lsmv, gf4d* and *lsminsc* are more suitable to identify the degree of stenosis and therefore may be used when the primary interest is to outline the plaque borders.

TABLE 6.10
ADDITIONAL COMMENTS ON DESPECKLE FILTERING MADE BY THE EXPERTS.

| Filter name | Comments made by the vascular experts on ultrasound images of the carotid artery |
|---|---|
| *original* | The plaque, and or IMT borders may not be easily visualized between posterior and anterior tissue. Therefore the adventitia, at the far wall may not be easily located. |
| *lsmv* | It helps to visualize the borders between blood and wall but not very good to visualize the borders between the wall and the surrounding tissue. It does not blur edges, and it helps visualizing the plaque borders. |
| *lsminsc* | Not very suitable for the far wall and IMT segmentation, but it is one of the best filters, providing information about the plaque, as the borders of the plaque may be better distinguished after filtering. |
| *median* | Not good for the far wall IMT detection. It blurs, gives double edges and smoothes the image too much. Helps to locate the boundaries of plaque, but *lsminsc* is better for plaque visualization. |
| *wiener* | It is not bad between blood and wall boundaries but the noise still remains on edges after filtering. It is, therefore not helpful either for IMT or plaque segmentation. |
| *ls* | Although not bad for visual perception, it is not suitable for the IMT and plaque segmentation, as it blurs homogeneous areas and edges. In some images produces double edges. It is not very helpful for visualizing the IMT, either in near or far wall of the carotid artery. |
| *homog* | Breaks the edges between blood and wall causing blurring between wall and surrounding tissue. It may help sometimes to locate the boundaries of the far wall (adventitia). |
| *gf4d* | It sharpens the edges. It helps to locate the boundaries of the far wall (adventitia) and the plaque may be better visualized. Borders between blood and plaque may be well separated. |
| *homo* | Very bad for border detection and visualization, as the image becomes darker after filtering. It is therefore not recommended. |
| *ad* | Although not very good visually, it may be used in some images to visualize the borders between wall and blood. It is in general not well suited as a pre-processing step prior to segmentation of the IMT and plaque borders. |
| *nldif* | Although good visually, the IMT and plaque borders may be not well distinguished. It is not very helpful to locate either adventitia, nor intima, nor plaque. |
| *waveltc* | The visualization after despeckle filtering, is better between blood and vessel and between vessel and tissue. Also the walls appear continuous but their contrast is very low. It may be good for boundary detection between vessel and the surrounding tissue at the near wall. |

## 6.3 IMT segmentation

In this Section we present the results of the Williams&Shah IMT snakes segmentation technique, where the segmentation algorithm and methodology were described in section 3.4 and section 5.7 respectively. The snake parameters used in this study, were chosen as proposed in section 5.7.3, with $\alpha = 0.6$, $\beta = 0.4$, and $\gamma = 2$, where the mean number of iterations needed for the snake to converge to its final position was 14. We have tested and validated the Williams&Shah IMT snakes segmentation technique on 100 longitudinal ultrasound images of the carotid artery bifurcation using the visual interpretation results, the manual measurements by two vascular experts, image normalisation, despeckling, univariate statistical analysis, and correlation analysis as presented in Chapter 5.7. Our results on IMT segmentation showed that no significant difference was found between the IMT manual and the IMT Williams&Shah snakes segmentation measurements. Better segmentation results were obtained for the normalised despeckled images.

### *6.3.1 An example of IMT segmentation*

Figure 6.6a shows a longitudinal ultrasound image of the carotid artery, with the manual delineations (M) from the two experts (Fig. 6.6b, Fig. 6.6c), the automatic initial snake contour estimation (Fig. 6.6d), and the Williams&Shah snakes segmentation results for the cases of no filtering (NF) (Fig. 6.6e), despeckled (DS) (Fig. 6.6f), normalized (N) (Fig. 6.6g), and normalized despeckled (NDS) (Fig. 6.6h).

TABLE 6.11
COMPARISON BETWEEN THE MANUAL AND THE SNAKES SEGMENTATION MEASUREMENTS FOR THE CASES B-H IN FIG. 6.6. MEASUREMENTS ARE IN MILLIMETERS (MM).

| | Manual Measurements | | | | Snakes Segmentation Measurements | | | |
|---|---|---|---|---|---|---|---|---|
| | Expert 1 | | Expert 2 | | | | | |
| | M | MN | M | MN | NF | DS | N | NDS |
| $IMT_{mean}$ ($sd$) | 0.74 (0.14) | 0.92 (0.11) | 0.82 (0.12) | 0.98 (0.15) | 0.82 (0.22) | 0.81 (0.21) | 0.82 (0.19) | 0.82 (0.18) |
| $IMT_{min}$ | 0.38 | 0.76 | 0.71 | 0.72 | 0.61 | 0.60 | 0.60 | 0.60 |
| $IMT_{max}$ | 0.95 | 1.05 | 0.94 | 1.10 | 1.09 | 1.08 | 1.08 | 1.08 |
| $IMT_{median}$ | 0.66 | 0.90 | 0.85 | 0.95 | 0.79 | 0.78 | 0.78 | 0.78 |

M: Manual, MN: Manual normalised, NF: No filtering, DS: Despeckle, N: Normalised, NDS: Normalized despeckled, $sd$ : Standard deviation.

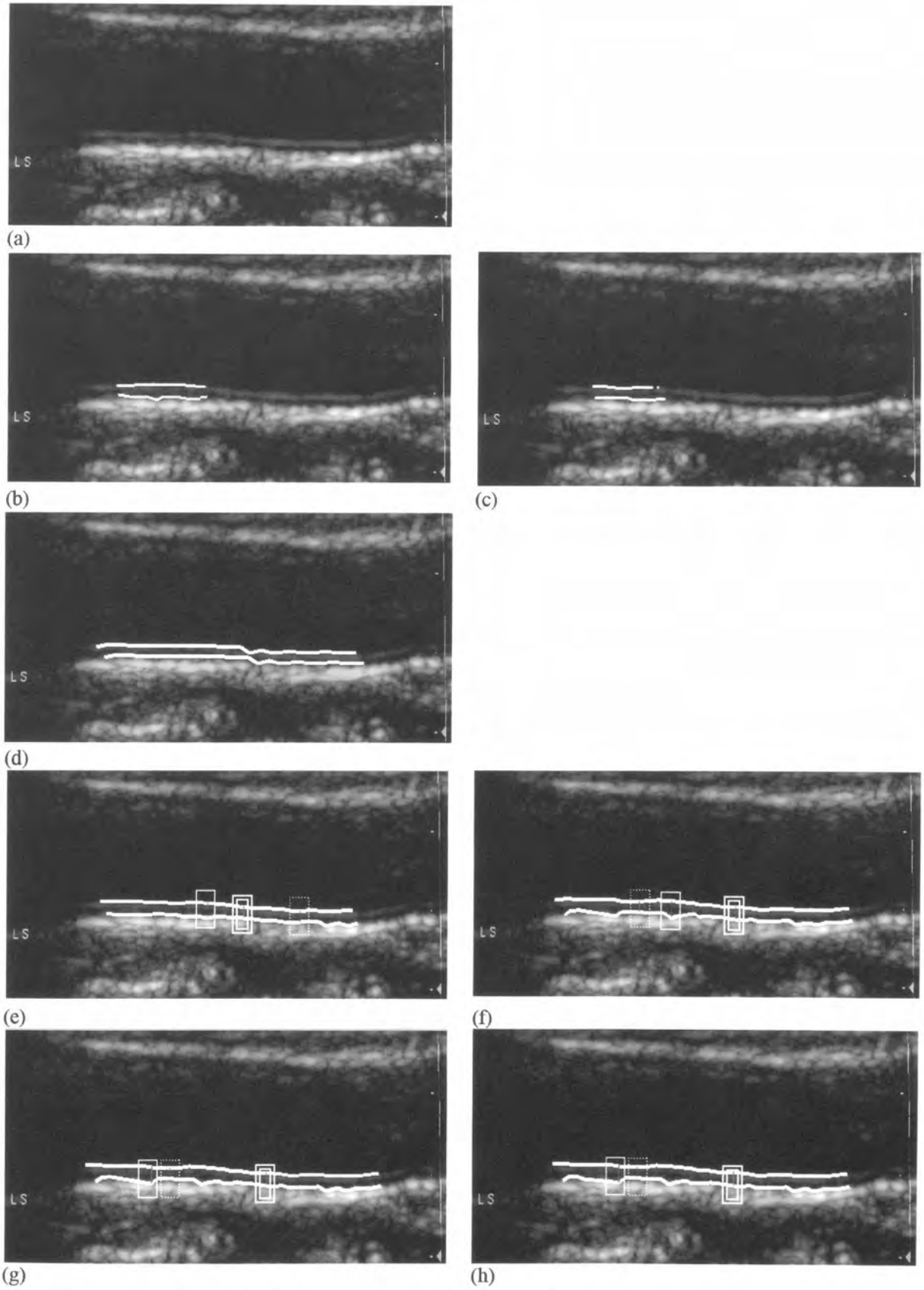


**Fig. 6.6**: (a) Original longitudinal ultrasound image of the carotid artery, (b) manual delineation from the first expert, (c) manual delineation from the second expert, (d) initial contour estimation, and the segmentation results of the IMT for (e) no filtering (NF), (f) despeckled (DS), (g) normalized (N), and (h) normalized despeckled (NDS) images. The detected $IMT_{mean}$, $IMT_{\max}$, and $IMT_{\min}$ are shown with a double, single, and dashed line boxes respectively.

The detected $IMT_{mean}$, $IMT_{\max}$, and $IMT_{\min}$ values, are shown with a double, full, and dashed line boxes respectively.

The $IMT_{mean}$, $IMT_{\min}$, $IMT_{\max}$, and $IMT_{median}$, measurements for Fig. 6.6 are presented in Table 6.11. The manual measurements are given for each expert, in cases when manual measurements were carried out, without normalization (M) and with normalization (MN). The Williams&Shah snakes segmentation measurements are given for the NF, DS, N and NDS cases, and were in the most of the cases, higher than the manual measurements, except in the MN case for both experts. The higher snakes segmentation results can be explained with Fig. 3.1b. The observed standard deviation, $sd$, values for the $IMT_{mean}$, was for the first expert, M (0.14), MN (0.11), for the second expert, M (0.12), MN (0.15), and for the snakes segmentation, NF (0.22), DS (0.21), N (0.19), and NDS (0.18) respectively. The results in Fig. 6.6 and Table 6.11 show, that the IMT was detected well in all snakes segmentation measurements but with variations between experts and methods. The best visual results as assessed by the two vascular experts were obtained on the NDS, followed by N and DS images.

### *6.3.2 Univariate statistical analysis*

Table 6.12.1 tabulates the manual and the Williams&Shah snakes segmentation results for 100 longitudinal ultrasound images of the carotid artery, for the $IMT_{mean}$, $IMT_{\min}$, $IMT_{\max}$ and $IMT_{median}$, with their standard deviations, $sd$, inter-observer error, $se$, and coefficient of variation, $CV\%$. The $IMT_{mean}$ $\pm$ standard deviation results for the first expert were, $0.67 \pm 0.16$ mm, $0.68 \pm 0.17$ mm, and for the second expert were, $0.65 \pm 0.18$ mm, $0.61 \pm 0.17$ mm on the original and normalized images respectively. The $IMT_{mean}$ $\pm$ standard deviation snakes segmentation results were $0.7 \pm 0.14$ mm, $0.69 \pm 0.13$ mm, $0.67 \pm 0.13$ mm, $0.68 \pm 0.12$ mm, for the NF, DS, N, and NDS images respectively. It is noted that both the $IMT_{mean}$, and $IMT_{median}$ measurements are very close.

Best segmentation results are shown with bolded values and were obtained for the NDS images, with a standard deviation of the $IMT_{mean}$, $sd = 0.12$ mm, an inter-observer error of the $IMT_{mean}$, $se = 0.08$ and a coefficient of variation, $CV\% = 12.5\%$ respectively.

Table 6.12.2 presents the manual measurements for 100 images of the carotid artery made by the two experts one year after the first measurements were made (see Table 6.12.1). This was carried out by both experts in order to assess the intra-observer variability. It is shown that the measurements of the second expert, are generally smaller giving a thinner IMT.

TABLE 6.12.1
COMPARISON BETWEEN MANUAL AND SNAKES SEGMENTATION MEASUREMENTS FOR THE 100 ULTRASOUND IMAGES OF THE CAROTID ARTERY. MEASUREMENTS ARE IN MILLIMETERS (MM). BOLDED VALUES SHOW BEST PERFORMANCE.

| | First Set of Manual Measurements at Time 0 | | | | Snakes Segmentation Measurements | | | |
|---|---|---|---|---|---|---|---|---|
| | Expert 1 | | Expert 2 | | | | | |
| | M1F | MN1F | M2F | MN2F | NF | DS | N | NDS |
| $IMT_{mean}$ | 0.67 | 0.68 | 0.65 | 0.61 | 0.70 | 0.69 | 0.67 | 0.68 |
| $(sd)$ | (0.16) | (0.17) | (0.18) | (0.17) | (0.14) | (0.13) | (0.13) | **(0.12)** |
| $IMT_{min}$ | 0.53 | 0.52 | 0.57 | 0.54 | 0.51 | 0.51 | 0.51 | 0.49 |
| $(sd)$ | (0.14) | (0.15) | (0.16) | (0.14) | (0.13) | (0.13) | (0.14) | **(0.11)** |
| $IMT_{max}$ | 0.82 | 0.85 | 0.75 | 0.70 | 0.90 | 0.88 | 0.86 | 0.87 |
| $(sd)$ | (0.22) | (0.21) | (0.19) | (0.20) | (0.20) | (0.19) | (0.17) | **(0.15)** |
| $IMT_{median}$ | 0.66 | 0.66 | 0.67 | 0.61 | 0.69 | 0.69 | 0.66 | 0.64 |
| $(sd)$ | (0.16) | (0.18) | (0.18) | (0.17) | (0.14) | (0.13) | (0.12) | **(0.12)** |
| $se$ | 0.11 | 0.12 | 0.13 | 0.11 | 0.10 | 0.09 | 0.09 | **0.08** |
| $CV\%$ | 16.7 | 17.1 | 19.1 | 17.2 | 13.8 | 13.4 | 13.2 | **12.5** |

M1F, M2F: Manual first set of measurements from expert 1, and 2, MN1F, MN2F: Manual normalised first set of measurements from expert 1, and 2, NF: No filtering, DS: Despeckle, N: Normalised, NDS: Normalized despeckled, $sd$ : Standard deviation, $se$ : Inter-observer error for mean values, $CV\%$ : Coefficient of variation.

TABLE 6.12.2
IMT MANUAL MEASUREMENTS (IN MM) FOR THE 100 ULTRASOUND IMAGES OF THE CAROTID ARTERY PERFORMED BY THE TWO VASCULAR EXPERTS.

| | Second Set of Manual Measurements at Time 12 months | | | |
|---|---|---|---|---|
| | Expert 1 | | Expert 2 | |
| | M1S | MN1S | M2S | MN2S |
| $IMT_{mean}$ | 0.74 | 0.71 | 0.55 | 0.57 |
| $(sd)$ | (0.17) | (0.17) | (0.11) | (0.13) |
| $IMT_{min}$ | 0.62 | 0.59 | 0.45 | 0.47 |
| $(sd)$ | (0.16) | (0.15) | (0.11) | (0.14) |
| $IMT_{max}$ | 0.87 | 0.85 | 0.64 | 0.66 |
| $(sd)$ | (0.23) | (0.21) | (0.13) | (0.14) |
| $IMT_{median}$ | 0.74 | 0.72 | 0.62 | 0.61 |
| $(sd)$ | (0.19) | (0.18) | (0.16) | (0.14) |
| $se$ | 0.12 | 0.11 | 0.08 | 0.1 |
| $CV\%$ | 16.2 | 16.8 | 14.0 | 16.8 |

M1S, M2S: Second set of manual measurements performed from expert 1 and 2 one year later, MN1S, MN2S: Manual normalised second set of measurements performed from expert 1 and 2 one year later, $sd$ : Standard deviation, $se$ : Inter observer error for mean values, $CV\%$ : Coefficient of variation.

TABLE 6.12.3
WILCOXON RANKSUM TEST FOR THE IMT MANUAL SEGMENTATION MEASUREMENTS. THE TEST SHOWS WITH S SIGNIFICANT DIFFERENCE AFTER FILTERING AT P<0.05 AND NS NO SIGNIFICANT DIFFERENCE AFTER FILTERING AT P>=0.05. THE P VALUE IS ALSO SHOWN IN PARENTHESIS.

| | | | First Set of Manual Measurements at Time 0 | | | | Second Set of Measurements at Time 12 months | | | |
|---|---|---|---|---|---|---|---|---|---|---|
| | | | Expert 1 | | Expert 2 | | Expert 1 | | Expert 2 | |
| | | | M1F | MN1F | M2F | MN2F | M1S | MN1S | M2S | MN2S |
| First Set of Manual Measurements at Time 0 | Expert 1 | M1F | | NS (0.45) | NS (0.07) | S (0.01) | S (0.01) | NS (0.2) | S (0.00) | S (0.00) |
| | | MN1F | NS (0.74) | | S (0.00) | S (0.00) | S (0.00) | NS (0.47) | S (0.00) | S (0.00) |
| | Expert 2 | M2F | NS (0.07) | S (0.00) | | S (0.04) | NS (0.45) | S (0.01) | S (0.00) | S (0.01) |
| | | MN2F | S (0.01) | S (0.00) | NS (0.45) | | NS (0.87) | S (0.00) | S (0.01) | S (0.03) |
| Second Set of Manual Measurements at Time 12 months | Expert 1 | M1S | S (0.01) | S (0.01) | NS (0.45) | NS (0.89) | | S (0.00) | NS (0.06) | S (0.03) |
| | | MN1S | NS (0.2) | NS (0.47) | S (0.01) | S (0.00) | S (0.00) | | S (0.00) | S (0.00) |
| | Expert 2 | M2S | S (0.00) | S (0.00) | S (0.00) | S (0.01) | S (0.01) | S (0.01) | | NS (0.54) |
| | | MN2S | S (0.00) | S (0.00) | S (0.01) | S (0.03) | S (0.03) | S (0.00) | NS (0.55) | |

M1F, M2F: Manual first set of measurements from expert 1, and 2, MN1F, MN2F: Manual normalised first set of measurements from expert 1, and 2, M1S, M2S: Manual second set of measurements from expert 1, MN1S, MN2S: Manual normalised second set of measurements from expert1, and 2.

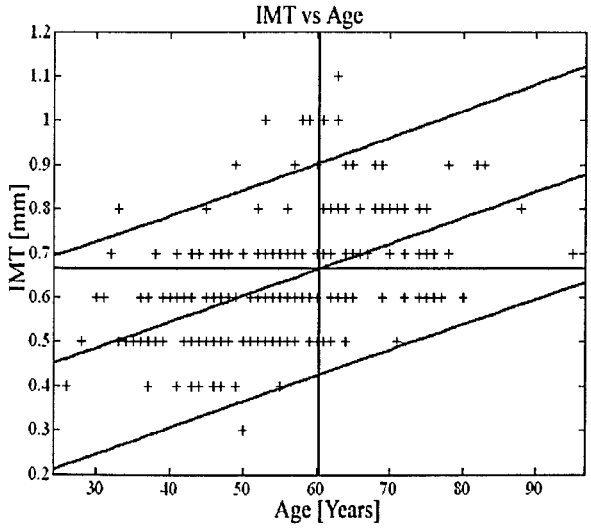


(a) $y = 0.67 \pm 0.24$, $x = 60.5$.

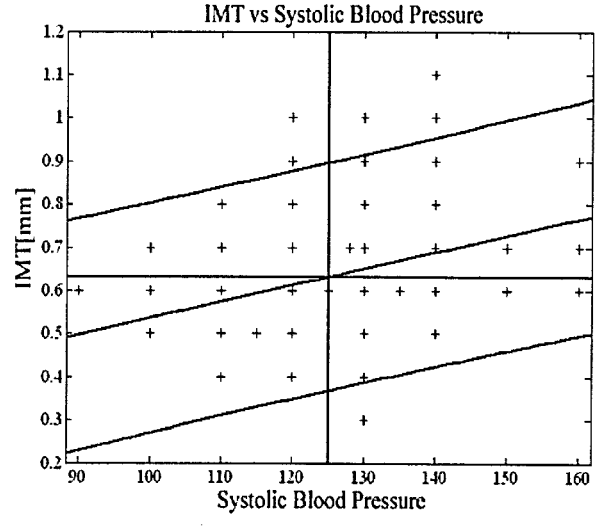


(b) $y = 0.63 \pm 0.26$, $x = 125$.

**Fig. 6.7**: Increase of $IMT_{mean}$ with: (a) age and (b) systolic blood pressure.

Furthermore, the standard deviation, $sd$, the inter-observer error, $se$, and the coefficient of variation, $CV\%$, for the measurements made by the second expert are also smaller.

Table 6.12.3 presents the results for the Wilcoxon rank sum test for all manual segmentation, measurements. It is shown that the measurements made by the two experts are mostly significantly different (S), showing high intra and inter observer variabilities.

Figure 6.7 presents the results of the $IMT_{mean}$ values versus age (see Fig. 6.7a), and systolic blood pressure (see Fig. 6.7b) respectively using regression analysis. It is shown that the $IMT_{mean}$ increases almost linearly with increasing age and systolic blood pressure. Furthermore, it is shown, from Fig. 6.7a, that the $IMT_{mean}$, at the age of 60.5 is 0.67 mm, whereas Fig. 6.7b shows, that the blood pressure for an $IMT_{mean}$ of 0.63 mm, is 125. Figure 6.7 also shows the confidence interval limits for the $IMT_{mean}$, with $\pm 0.24$ mm, and $\pm 0.26$ mm for age (seeFig.6.7a), and systolic blood pressure (see Fig. 6.7b) respectively.

Table 6.13.1 shows the results of the Wilcoxon rank sum test, a variation of the Hausdorff distance (HD), the covariance, and the $MSE$ between the first expert and the snakes segmentation measurements. The Wilcoxon rank sum test, which is displayed in the upper triangle of the left column of Table 6.13.1, showed that no-significant (NS) difference exists between the Williams&Shah snakes segmentation measurements and the manual measurements from the first expert. The NS difference between the two methods showed that the manual measurements may be replaced by the snakes segmentation measurements without confidence. The HD, which is displayed in the left column lower triangle of Table 6.13.1, showed that minimum mismatches were obtained between the N-M1F (3.4), NDS-MN1F (4.7), NDS-N (5.2), DS-NF (5.2), NDS-M1F and DS-MN1F (8.6) respectively.

The covariance is displayed in the upper triangle of the right column of Table 6.13.1. Higher covariance values were obtained for the cases M1F-MN1F (21.7), NF-DS (16.3), NF-N (14.4), DS-N (14.4), DS-NDS (13.1), N-NDS (12.9) and NF-NDS (12.8) respectively. MSE results were shown in the lower triangle of the right column. Low MSE values were observed for N-M1F (0.01), NDS-MN1F (0.02), NDS-N (0.03) and DS-NF (0.03) respectively.

Table 6.13.2 shows the results of the Wilcoxon rank sum test, a variation of the Hausdorff distance (HD), the covariance, and the $MSE$ between the second expert and the snakes segmentation measurements. The Wilcoxon rank sum test, which is displayed in the upper triangle of the left column of Table 6.13.2, showed that a significant difference (S) between the manual (M2F) and the manual normalised (MN2F) measurements of the second expert exists.

TABLE 6.13.1

TESTS AND MEASURES COMPUTED ON 100 ULTRASOUND IMAGES OF THE CAROTID ARTERY FROM THE FIRST EXPERT. LEFT COLUMN UPPER TRIANGLE: WILCOXON RANK SUM TEST (S=SIGNIFICANTLY DIFFERENT AFTER FILTERING AT P<0.05, NS=NOT SIGNIFICANTLY DIFFERENT AFTER FILTERING AT P>=0.05). THE P VALUES ARE ALSO SHOWN IN PARENTHESIS. LEFT COLUMN LOWER TRIANGLE: VARIATION OF THE HAUSDORFF DISTANCE (*$10^{-3}$). RIGHT COLUMN UPPER TRIANGLE: COVARIANCE, $c_{m,a}$. RIGHT COLUMN LOWER TRIANGLE: MEAN-SQUARE ERROR (*$10^{-3}$). BOLDED VALUES SHOW BEST PERFORMANCE.

| | Wilcoxon Ranksum Test and HD | | | | | | Covariance and MSE | | | | | |
|---|---|---|---|---|---|---|---|---|---|---|---|---|
| | M1F | MN1F | NF | DS | N | NDS | M1F | MN1F | NF | DS | N | NDS |
| M1F | - | NS (0.45) | NS (0.56) | NS (0.64) | NS (0.9) | NS (0.88) | - | **21.7** | 10.7 | 10.4 | 9.8 | 9.1 |
| MN1F | 13.3 | - | NS (0.90) | NS (0.79) | NS (0.30) | NS (0.55) | 0.20 | - | 11.5 | 11.1 | 10.4 | 9.5 |
| NF | 27.1 | 13.8 | - | NS (0.87) | NS (0.33) | NS (0.53) | 0.70 | 0.20 | - | **16.3** | **14.4** | **12.8** |
| DS | 21.9 | **8.6** | **5.2** | - | NS (0.41) | NS (0.69) | 0.50 | 0.07 | **0.03** | - | **14.4** | **13.1** |
| N | **3.4** | 9.9 | 23.7 | 18.5 | - | NS | **0.01** | 0.09 | 0.60 | 0.40 | - | **12.9** |
| NDS | **8.6** | **4.7** | 18.5 | 13.3 | **5.2** | - | 0.07 | **0.02** | 0.40 | 0.20 | **0.03** | - |

M1F: Manual first set of measurements from first expert, MN1F: Manual normalised first set of measurements from first expert, NF: No filtering, DS: Despeckle, N: Normalised, NDS: Normalized despeckled.

TABLE 6.13.2

TESTS AND MEASURES COMPUTED ON 100 ULTRASOUND IMAGES OF THE CAROTID ARTERY FROM THE SECOND EXPERT. LEFT COLUMN UPPER TRIANGLE: WILCOXON RANK SUM TEST (S=SIGNIFICANTLY DIFFERENT AFTER FILTERING AT P<0.05, NS=NOT SIGNIFICANTLY DIFFERENT AFTER FILTERING AT P>=0.05). THE P VALUES ARE ALSO SHOWN IN PARENTHESIS. LEFT COLUMN LOWER TRIANGLE: VARIATION OF THE HAUSDORFF DISTANCE (*$10^{-3}$). RIGHT COLUMN UPPER TRIANGLE: COVARIANCE, $c_{m,a}$. RIGHT COLUMN LOWER TRIANGLE: MEAN-SQUARE ERROR (*$10^{-3}$). BOLDED VALUES SHOW BEST PERFORMANCE.

| | Wilcoxon Ranksum Test and HD | | | | | | Covariance and MSE | | | | | |
|---|---|---|---|---|---|---|---|---|---|---|---|---|
| | M2F | MN2F | NF | DS | N | NDS | M2F | MN2F | NF | DS | N | NDS |
| M2F | - | S (0.04) | NS (0.06) | NS (0.10) | NS (0.07) | NS (0.09) | - | 17.4 | **24.3** | **25.8** | **24.6** | **26.5** |
| MN2F | 40.0 | - | NS (0.08) | NS (0.07) | NS (0.1) | NS (0.16) | 1.6 | - | 17.2 | 18.4 | 16.0 | 17.9 |
| NF | 46.2 | 86.2 | - | NS (0.87) | NS (0.33) | NS (0.53) | 2.1 | 7.4 | - | 16.3 | 14.4 | 12.8 |
| DS | 41.0 | 81 | **5.2** | - | NS (0.41) | NS (0.55) | 1.7 | 6.6 | **0.03** | - | 14.4 | 13.1 |
| N | 22.5 | 62.5 | 23.7 | 18.5 | - | NS (0.69) | 0.5 | 3.9 | 0.60 | 0.40 | - | 12.9 |
| NDS | 27.7 | 67.7 | 18.5 | 13.3 | **5.2** | - | 0.7 | 4.5 | 0.40 | 0.20 | **0.03** | - |

M2F: Manual first set of measurements from second expert, MN2F: Manual normalised first set of measurements from second expert, NF: No filtering, DS: Despeckle, N: Normalised, NDS: Normalized despeckled.

All other measurements showed that a no-significant (NS) difference exists between the Williams&Shah snakes segmentation measurements and the manual measurements from the first expert. The HD in Table 6.13.2 showed that minimum mismatches were obtained between the DS-NF (5.2), and NDS-N (5.2) respectively.

Higher covariance values, in Table 6.13.2, were obtained for the cases M2F-NDS (26.5), M2F-DS (25.8), M2F-N (24.6), and M2F-NF (24.3) respectively. Low MSE values were observed for DS-NF (0.03) and NDS-N (0.03) respectively.

Figure 6.8 presents the histogram distributions for the $IMT_{mean}$ values for the 100 ultrasound images of the carotid artery for the cases, M1F, MN1F, M2F, MN2F, NF, DS, N, and NDS respectively. All the histograms clearly illustrate that the $IMT_{mean}$ distribution is not Gaussian. The histograms for the snakes segmentation measurements show a higher concentration around the $IMT_{mean}$. The histogram for the DS images (see Fig. 6.8f), showed a clear peak at 0.7 mm whereas, the histogram for the NDS images in Fig. 6.8h, showed a maximum around 0.6 mm. Both DS and NDS histogram distributions were more robust than the rest showing a more concentrated IMT measurement than the others. The distributions of the NF and N in Fig. 6.8e and Fig. 6.8g, were also well concentrated, whereas the distributions of the M1F, MN1F, M2F and MN2F in Fig. 6.8a-Fig. 6.8d were not well distributed. The manual measurements from the two experts showed a high variability of the IMT measurements. Furthermore, it was shown that the values of the IMT in a normal carotid artery may vary between 0.4 mm and 1.2 mm, depending on age, and this is consistent with other studies [227].

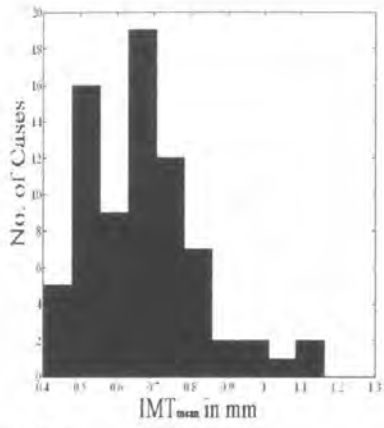


(a) M1F.

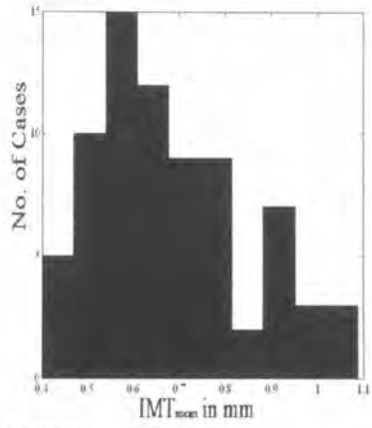


(b) MN1F.

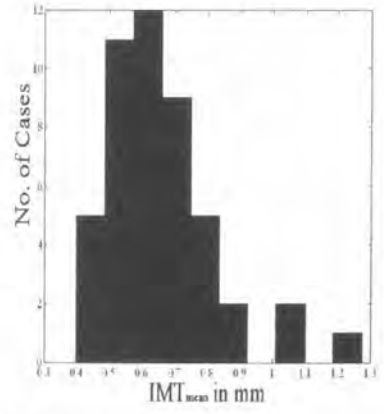


(c) M2F.

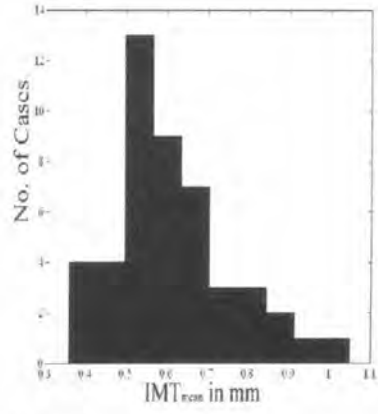


(d) MN2F.

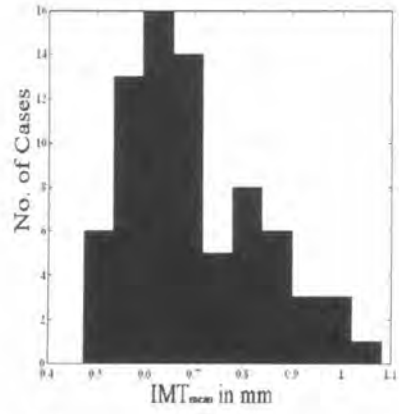


(e) NF.

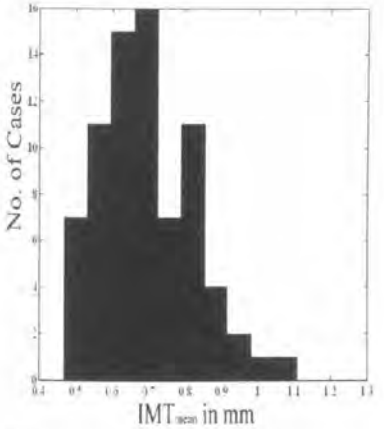


(f) DS.

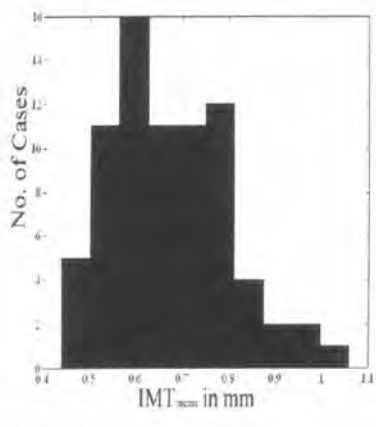


(g) N.

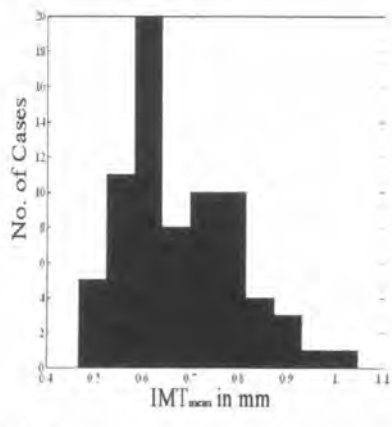


(h) NDS.

**Fig. 6.8**: Histograms of the $IMT_{mean}$ values for the: (a) manual first set of measurements from first expert (M1F), (b) manual normalized first set of measurements from first expert (MN1F), (c) manual first set of measurements from second expert (M2F), (d) manual normalised first set of measurements from second expert (MN2F), (e) no filtering (NF), (f) despeckle (DS), (g) normalised (N), and (h) normalized despeckled (NDS), images.

Figure 6.9 presents box plots to demonstrate the spread of the distributions for the $IMT_{mean}$ values for the 100 ultrasound images of the carotid artery for the manual segmentation cases MF, and MNF from expert one (M1F, MN1F) and expert two (M2F, MN2F), and the Williams&Shah snakes segmentation cases, NF, DS, N, and NDS, respectively. The best box-plot in Fig. 6.9a was obtained from the manual measurements made by the second expert, MN2F, after image normalisation. The distribution of measurements within this box was very small showing a better outlining consistency, with the upper and lower range of data being shorter than the other distributions. The skewness of this distribution was also low, as the median value is almost in the middle of the box. Fig. 6.9a also showed that the IMT measurements made from the second expert (M2F, MN2F) were more concentrated than the first expert (M1F, MN1F). Furthermore, it was shown that the second expert tended to delineate the IMT with smaller values than the first expert, as the $IMT_{mean}$ values for the second expert were smaller in both the M2F and MN2F cases. In addition, the second expert delineated some values, which lie out of the range of the box plot and these are shown as outliers above the distributions M2F, and MN2F. All box-plots for the IMT snakes segmentation method, shown in Fig. 6.9b, exhibited a positive skew distribution, as the median value was nearest to the lower quartile, and the lower whisker was shorter. The shortest box was the NDS, followed by the N distribution, which showed that the $IMT_{mean}$ values were less distributed than the other distributions. There were no outliers recorded in all four Williams&Shah snakes segmentation cases (NF, DS, N, NDS) for the IMT delineation.

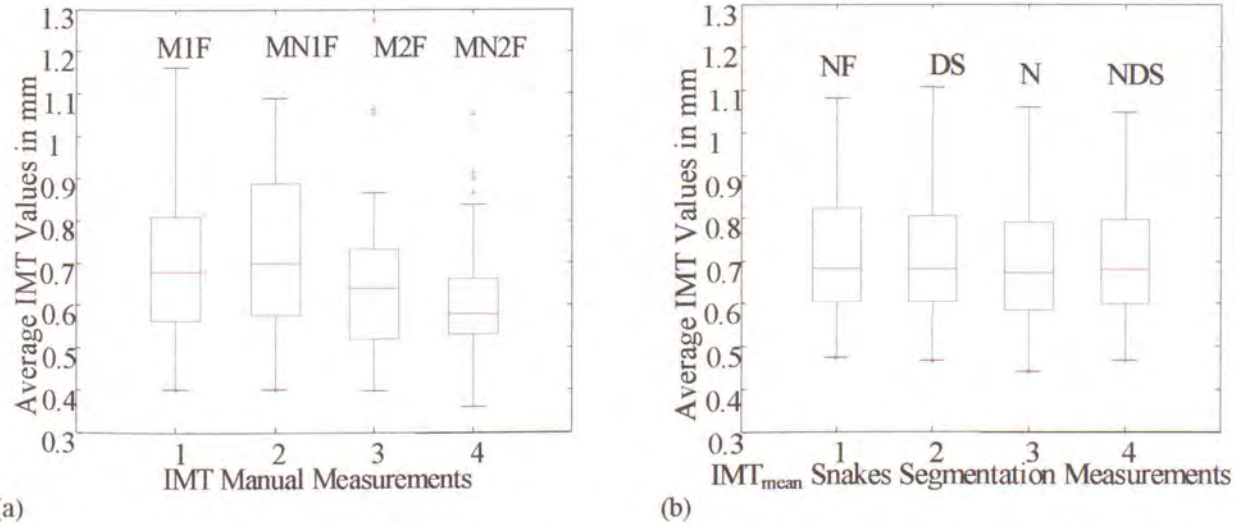


(a) (b)

**Fig. 6.9**: Box plots for the $IMT_{mean}$ values in mm: (a) for the manual and manual normalised first set of measurements, from expert one (M1F, MN1F) and expert two (M2F, MN2F), and (b) for the Williams&Shah snakes segmentation cases NF, DS, N, and NDS respectively.

### *6.3.3 Regression and correlation analysis*

The manual and the snakes segmented IMT borders were also compared using regression and correlation analysis.

In order to further assess the inter-observer variability between the two experts, we have plotted the manual segmentation results between the first and second expert, for the original (M1F), and the normalized images (MN1F), on a regression plot with a least squares regression line, as explained in section 5.7.4. Figure 6.10 shows scatter plots of the 100 measurements of the $IMT_{mean}$ measured by the two experts. In Fig. 6.10a the manual delineation results, M, between the two experts on the original images are shown (M1F, M2F), whereas Fig. 6.10b shows the manual delineation results, between the two experts, on the normalized images, (MN1F, MN2F). It is shown from Fig. 6.10a that the first expert (Expert1), tended to give larger measurements than the second expert (Expert 2). The manual measurements made by the two experts on the original images (see Fig. 6.10a) resulted in a confidence interval limit of ±0.32 mm. However, when image normalization was used, the results of the two experts as shown in Fig. 6.10b, were closer with a confidence interval limit of ±0.26 mm. Furthermore, the plotted points in Fig. 6.10b were closer to the ideal regression line, and more evenly distributed on both sides of it.

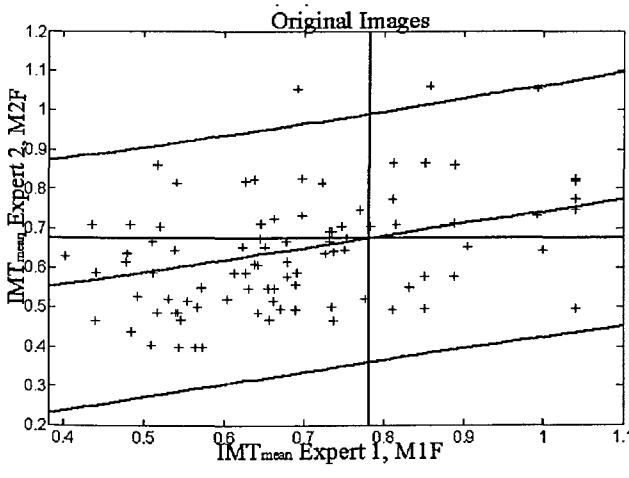


(a) $y = 0.68 \pm 0.32$, $x = 0.79$.

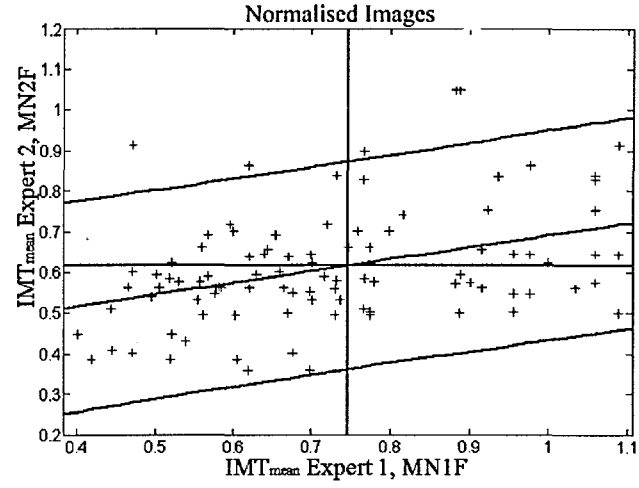


(b) $y = 0.62 \pm 0.26$, $x = 0.76$.

**Fig. 6.10**: A scatter plot with least squares regression line for the inter-observer variability of the manual IMT delineation between the two experts for 100 ultrasound images of the carotid artery, on: (a) the original (M), and (b) the normalised (MN) images.

Table 6.14 presents the results of the Pearson correlation and the correlation coefficient between the different snakes segmentation methods. Higher Pearson correlation values, illustrating stronger linear relationships, were observed for the NF-DS (0.98), NF-N (0.95), DS-

N (0.95), DS-NDS (0.92), and N-NDS (0.91) images respectively. Low Pearson correlation values were observed between the M1F-NDS (0.63), MN1F-NDS (0.66), M1F-NF (0.67), M1F-DS (0.70), MN1F-NF (0.71), M1F-N (0.71), MN1F-DS (0.73) and MN1F-N (0.75) respectively. In the right column of Table 6.14 higher values for the correlation coefficient were obtained for the cases NF-DS (0.97), NF-N (0.93), DS-N (0.93), DS-NDS (0.92), N-NDS (0.91) and NF-NDS (0.90) respectively.

TABLE 6.14
PEARSON CORRELATION TEST AND CORRELATION COEFFICIENT FOR THE 100 ULTRASOUND IMAGES OF THE CAROTID ARTERY. VALUES ABOVE 0.1654 SHOW SIGNIFICANT CORRELATION AT $p<0.05$. BOLDED VALUES SHOW BEST PERFORMANCE.

| | Pearson Correlation | | | | | Correlation Coefficient | | | | |
|---|---|---|---|---|---|---|---|---|---|---|
| | MN1F | NF | DS | N | NDS | MN1F | NF | DS | N | NDS |
| M1F | 0.90 | 0.67 | 0.70 | 0.71 | 0.63 | 0.88 | 0.59 | 0.62 | 0.63 | 0.63 |
| MN1F | | 0.71 | 0.73 | 0.75 | 0.66 | | 0.63 | 0.66 | 0.66 | 0.66 |
| NF | | | **0.98** | **0.95** | 0.90 | | | **0.97** | **0.93** | **0.90** |
| DS | | | | **0.95** | **0.92** | | | | **0.93** | **0.92** |
| N | | | | | **0.91** | | | | | **0.91** |

M1F: Manual first set of measurements from first expert, MN1F: Manual normalised first set of measurements from first expert, NF: No filtering, DS: Despeckle, N: Normalised, NDS: Normalized despeckled.

Figure 6.11 presents the regression lines for the correlations between (a) the NF-M1F, (b) NF-MN1F, (c) DS-MN1F, (d) N-MN1F, (e) NDS-MN1F, (f) DS-M1F, (g) N-M1F, and (h) NDS-M1F IMT segmentation results. The best regression line plot was obtained for the N-MN1F segmentation, as shown in Fig.6.11d, followed by the DS-MN1F in Fig. 6.11c, and the N-M1F in Fig. 6.11g. The best correlation coefficient was obtained for the N-MN1F, in Fig. 6.11d, with a correlation coefficient of $\rho = 0.75$, a slope of 0.89 and an intercept of 0.10, which differ significantly from one and zero respectively. The second best regression line was given by the DS-MN1F segmentation, in Fig. 6.11c, with a correlation coefficient, $\rho = 0.73$, a slope of 0.86 and an intercept of 0.11, whereas the third best regression plot was given for the N-M1F, shown in Fig.6.11g, and the NF-MN1F shown in Fig. 6.11b, which exhibited a correlation coefficient, $\rho = 0.71$, a slope of 0.84 and an intercept of 0.12, and $\rho = 0.71$, a slope of 0.80 and an intercept of 0.15, respectively.

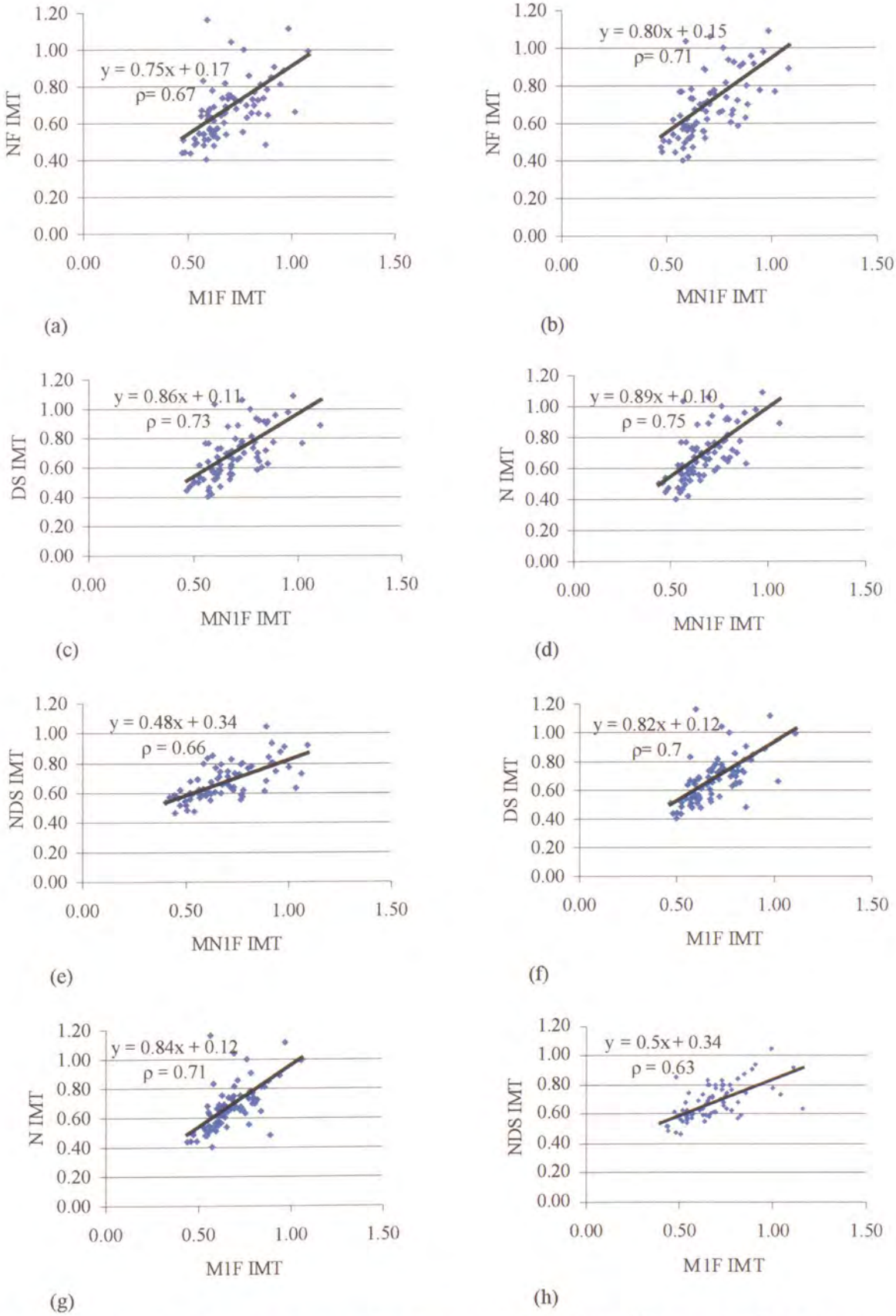


**Fig. 6.11**: Comparison of manually and snakes segmented IMT borders with regression lines, showing the correlations between: (a) the NF-M1F, (b) NF-MN1F, (c) DS-MN1F, (d) N-MN1F, (e) NDS-MN1F, (f) DS-M1F, (g) N-M1F, and (h) NDS-M1F detected IMT boundaries.

More useful information about the IMT segmentation accuracy, than the correlation plots, can be obtained by plotting a Bland-Altman plot, described in Chapter 5.7.4, of the manual versus the Williams&Shah snakes segmentation results. The Bland-Altman test may also be used when assessing reproducibility. Figure 6.12 illustrates the Bland-Altman plots for different combinations of the manual and snakes segmentation methods investigated. For both experts the best plots were obtained for the NDS images (see Fig. 6.12m, n, o, p), where the difference with the segmentation method for the manual measurements ± the standard deviation of the first expert, M1F, is 0.02±0.25 (see Fig. 6.12m), and for the manual measurements of the second expert, M2F, is −0.01±0.33 (see Fig. 6.12o).

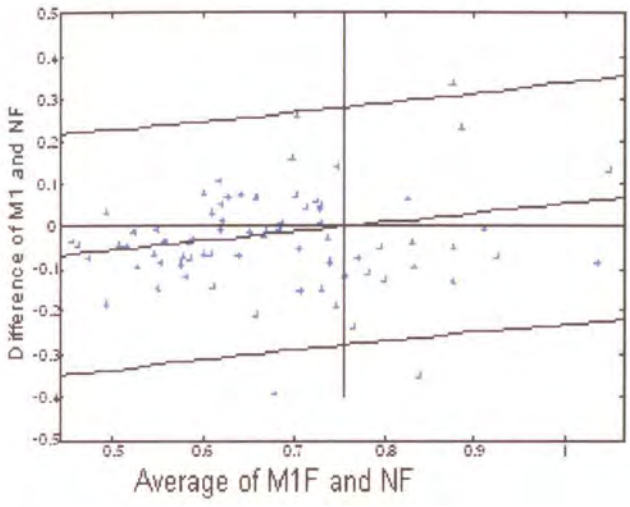


(a) $y = -0.00 \pm 0.28$, $x = 0.75$.

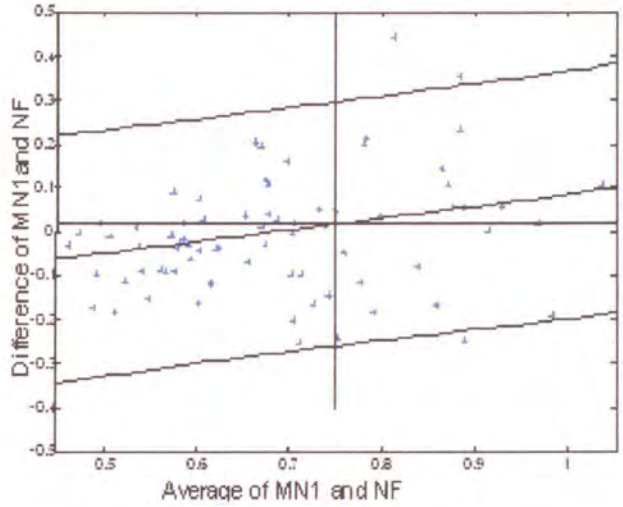


(b) $y = 0.02 \pm 0.28$, $x = 0.75$.

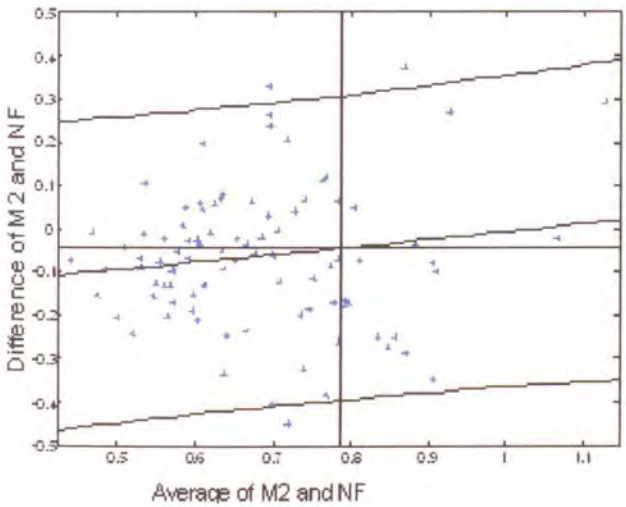


(c) $y = -0.04 \pm 0.35$, $x = 0.79$.

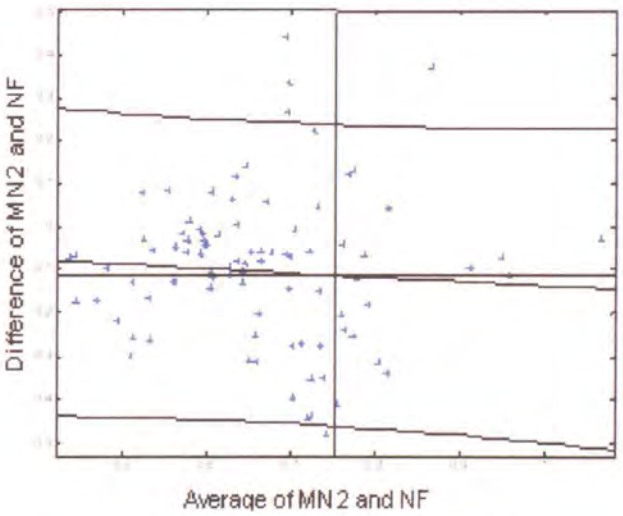


(d) $y = -0.11 \pm 0.35$, $x = 0.75$.

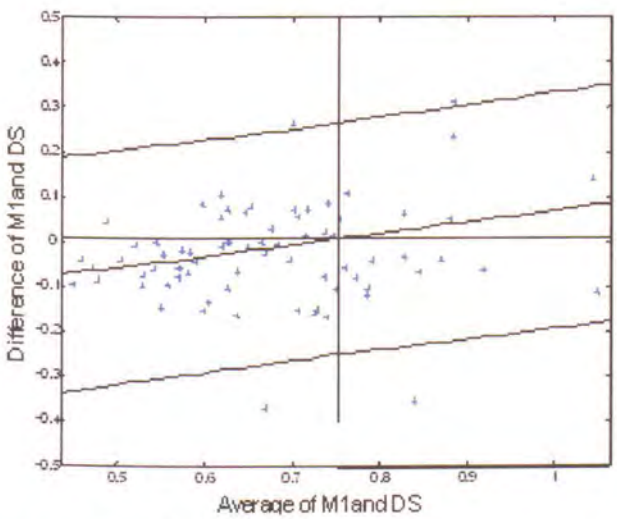


(e) $y = 0.01 \pm 0.26$, $x = 0.75$.

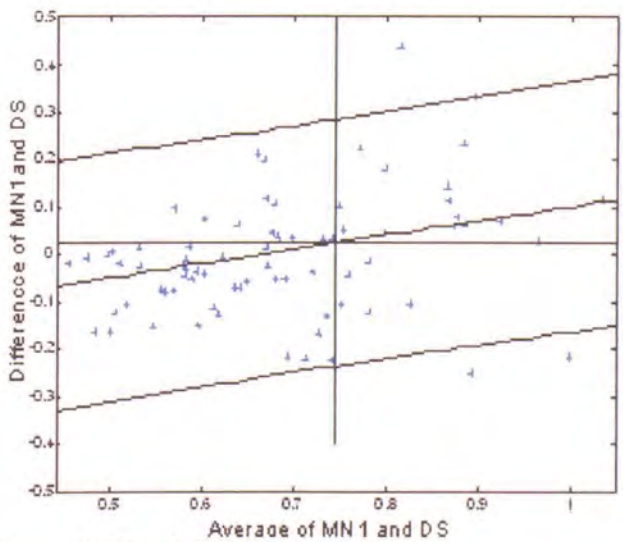


(f) $y = 0.02 \pm 0.26$, $x = 0.75$.

.../Fig. 6.12 cont'd

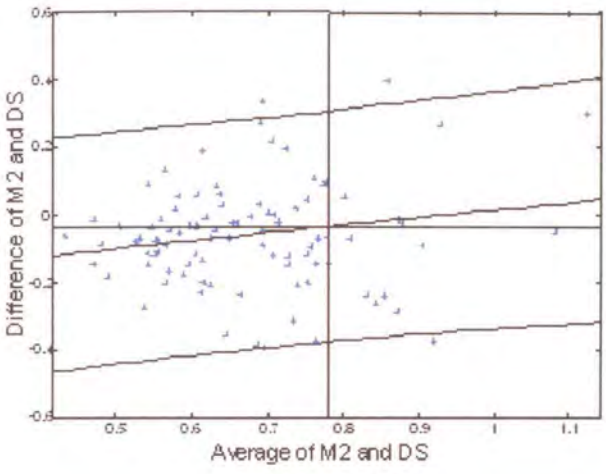


(g) $y = -0.04 \pm 0.34$, $x = 0.78$.

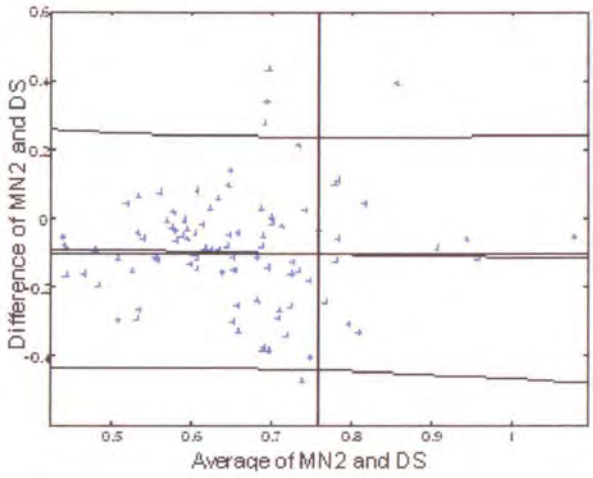


(h) $y = -0.10 \pm 0.34$, $x = 0.76$.

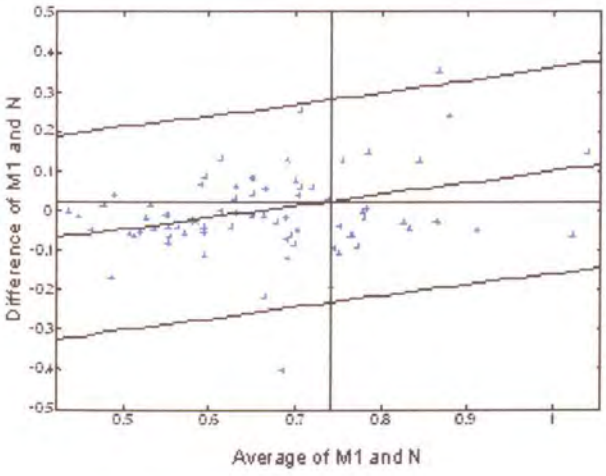


(i) $y = 0.02 \pm 0.25$, $x = 0.74$.

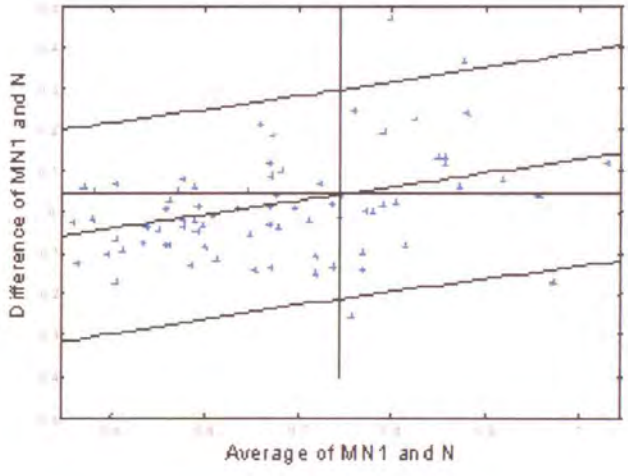


(j) $y = 0.04 \pm 0.26$, $x = 0.75$.

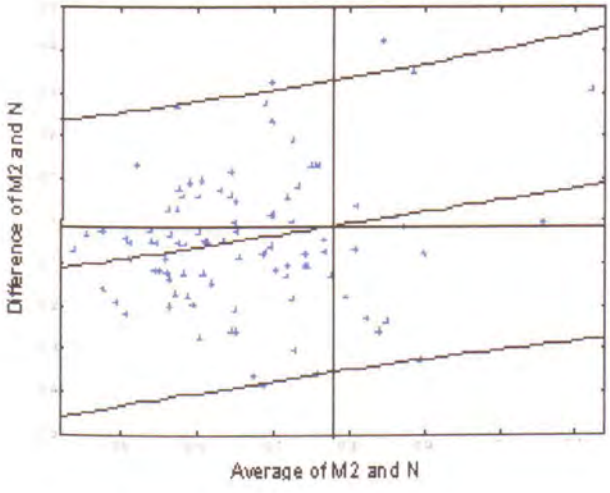


(k) $y = -0.01 \pm 0.34$, $x = 0.78029$.

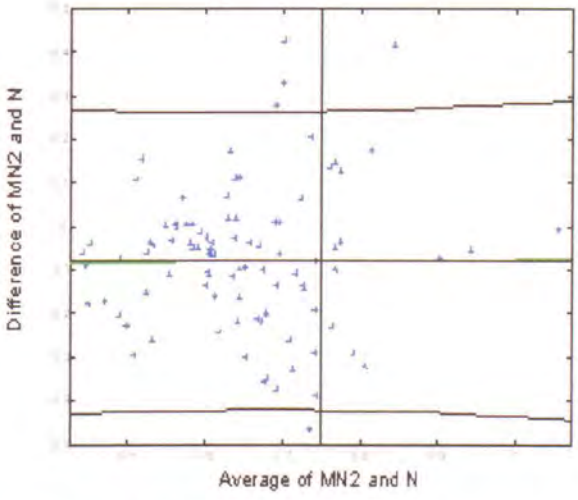


(l) $y = -0.08 \pm 0.34$, $x = 0.75$.

.../Fig. 6.12 cont'd

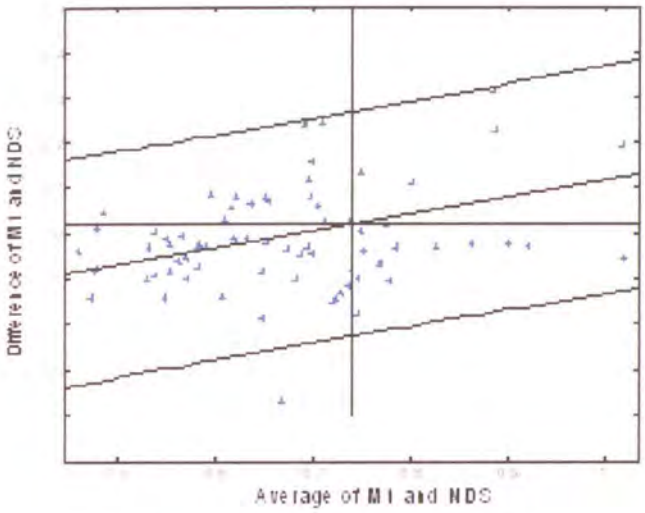


(m) $y = 0.02 \pm 0.25$, $x = 0.74$.

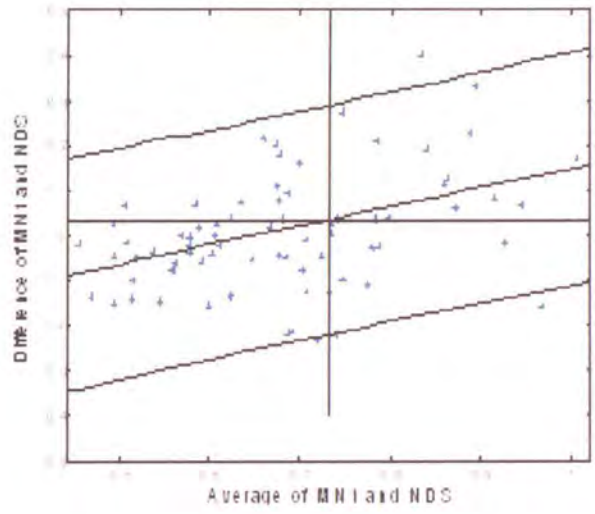


(n) $y = 0.03 \pm 0.25$, $x = 0.73$.

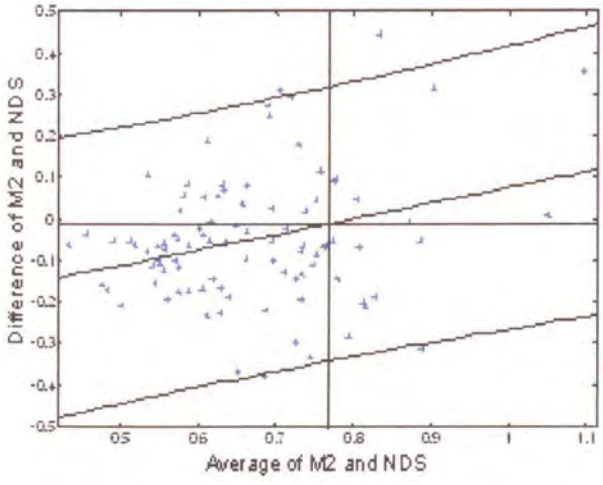


(o) $y = -0.01 \pm 0.33$, $x = 0.77$.

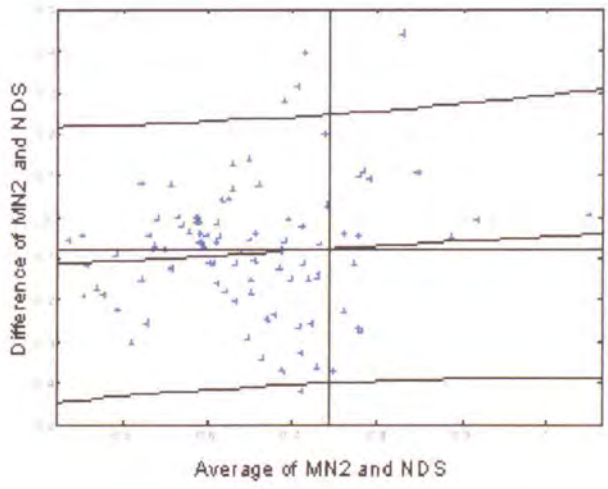


(p) $y = -0.08 \pm 0.32$, $x = 0.74$.

**Fig. 6.12**: Regression lines (Bland-Altman plots) of manual versus Williams&Shah snakes segmentation method for the $IMT_{mean}$ for the first set of measurements for both experts. The middle line represents the mean difference, and the upper and lower two outside lines represent the limits of agreement between the two methods, which are the mean of the data $\pm 2sd$ for the estimated difference between the two methods.

## 6.4 Plaque segmentation

In this Section we present the results of the four snakes segmentation methods, namely the Williams&Shah, Balloon, Lai&Chin, and GVF presented in Chapter 3 (sections 3.4, 3.5.1-3.5.3) for segmenting the athrerosclerotic carotid plaque from longitudinal ultrasound images. The four segmentation methods, use the blood flow image first to detect the initial contour of the plaque (see section 5.8.2), despeckle filtering using filter *lsmv* to filter the multiplicative noise from the image (see section 2.3.1.1), and then snakes to deform the initial contour for estimating the plaque boundaries. The accuracy and reproducibility of these methods was tested on 80 plaque longitudinal ultrasound images of the carotid artery, and the results were compared with the manual delineations of an expert. The four snakes segmentation methods were evaluated using visual perception made by an expert, and the snakes segmentation parameters. The four snakes segmentation methods were furthermore evaluated based on ROC analysis. Results showed that the Lai&Chin snakes segmentation method gives satisfactory results with no manual correction needed in most of the cases.

### *6.4.1 Examples of plaque segmentation*

Figure 6.13 illustrates the original longitudinal ultrasound B-mode image of a carotid plaque with a manual delineation made by the expert in (a), and the results of the William&Shah snakes segmentation in (b), the Balloon segmentation in (c), the Lai&Chin segmentation in (d), and the GVF segmentation in (e). Figure 6.13f shows the segmentation contours computed in Fig. 6.13b-6.13e superimposed on the same image. As shown, the manual and the snakes segmentation results are visually very similar suggesting that all four snakes segmentation methods can be interchangeable. Furthermore, when superimposing all segmentation results (see Fig. 6.13f) it was shown that the differences between all four snakes segmentation methods are very small.

Figure 6.14 illustrates the manual (Fig. 6.14a), versus the snakes segmentation results (Fig. 6.14b-Fig. 6.14e), for a different longitudinal B-mode ultrasound image of the carotid plaque, for the William&Shah snakes segmentation method (red line), Balloon (blue line), Lai&Chin (yellow line), and GVF (green line). Fig. 6.14f shows the segmentation contours computed in Fig. 6.14b-Fig. 6.14e superimposed on the same image. The best segmentation results were obtained by the Lai&Chin method (yellow line), which was closer to the manual segmentation results, followed by the William&Shah snake (red line). Balloon and GVF snakes, yielded similar contours of the plaque. The Balloon snake inflates and moves far away from the actual object in many cases. The Balloon model may identify smooth regions, especially when the initial snake contour is very close to the actual object of interest.

(a) Manual delineation.

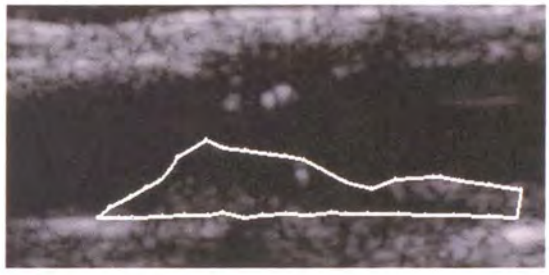

(b) Williams&Shah.

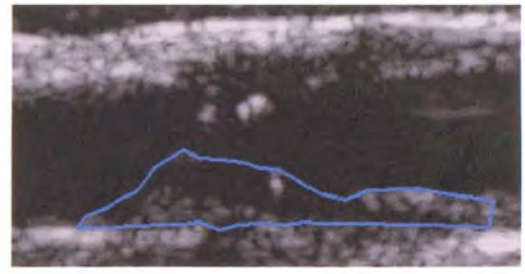

(c) Balloon.

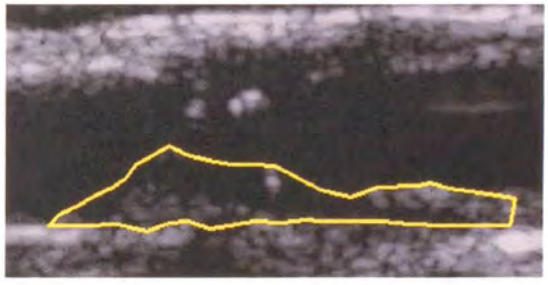

(d) Lai&Chin.

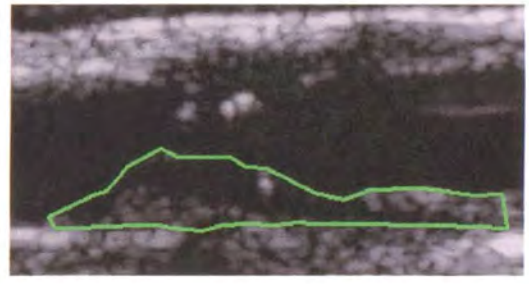

(e) GVF.

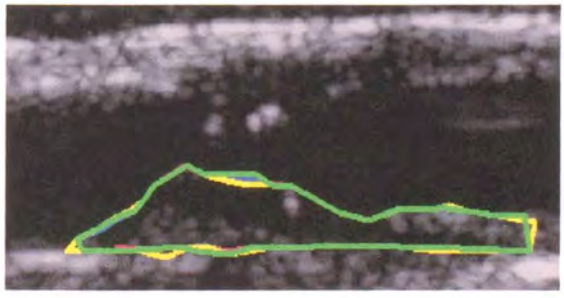

(f) Segmentation contours computed in (b)-(e) superimposed.

**Fig. 6.13**: Segmentation results on a longitudinal ultrasound B-mode image of the carotid artery with plaque, with: (a) manual segmentation, (b) Williams&Shah, (c) Balloon, (d), Lai&Chin, (e) GVF snake, and (f) segmentation contours computed in (b)-(e) superimposed.

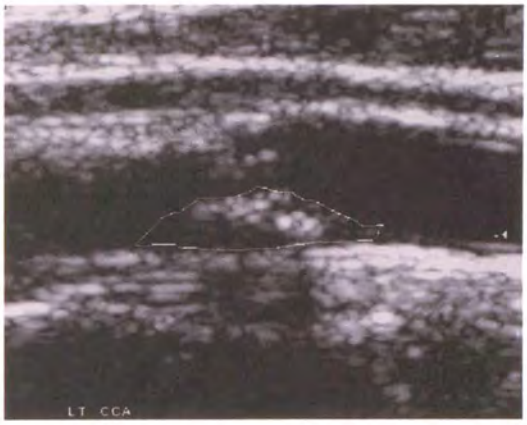


(a) Manual delineation.

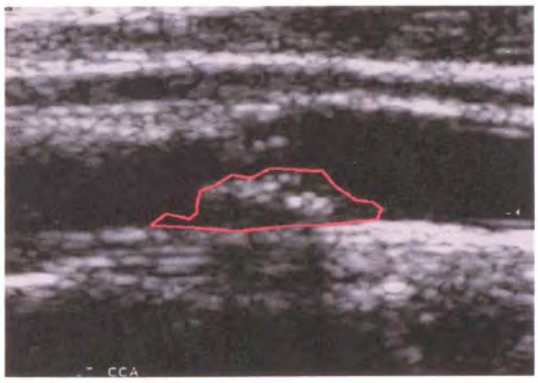

(b) Williams&Shah.

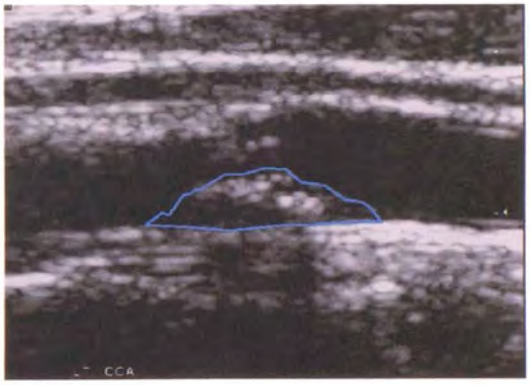

(c) Balloon.

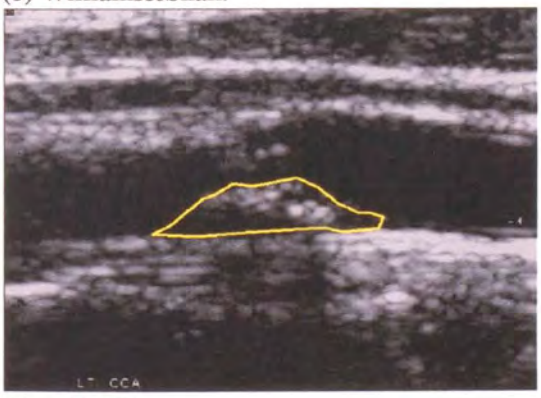

(d) Lai&Chin.

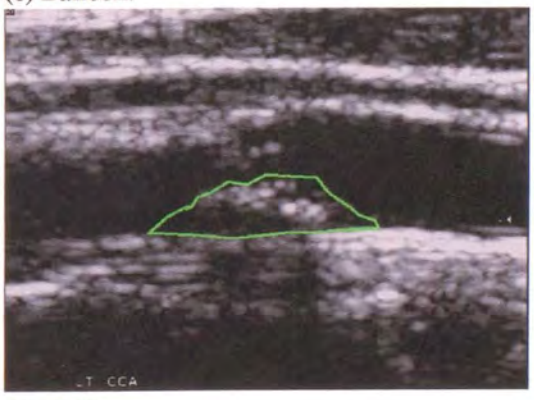

(e) GVF.

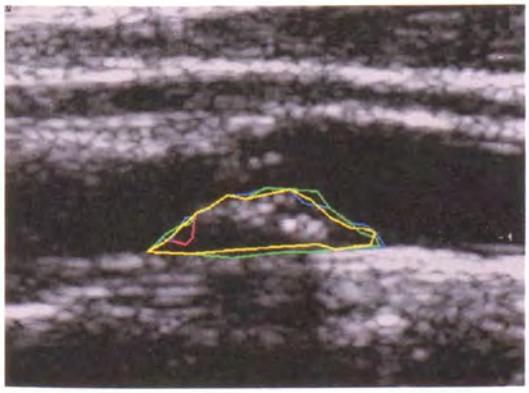

(f) Segmentation contours computed in (b)-(e) superimposed.

**Fig. 6.14**: Segmentation results on a longitudinal ultrasound B-mode image of the carotid artery with plaque, with: (a) manual segmentation, (b) Williams&Shah, (c) Balloon, (d), Lai&Chin, (e) GVF snake, and (f) all segmentation contours computed in (b)-(e) superimposed.

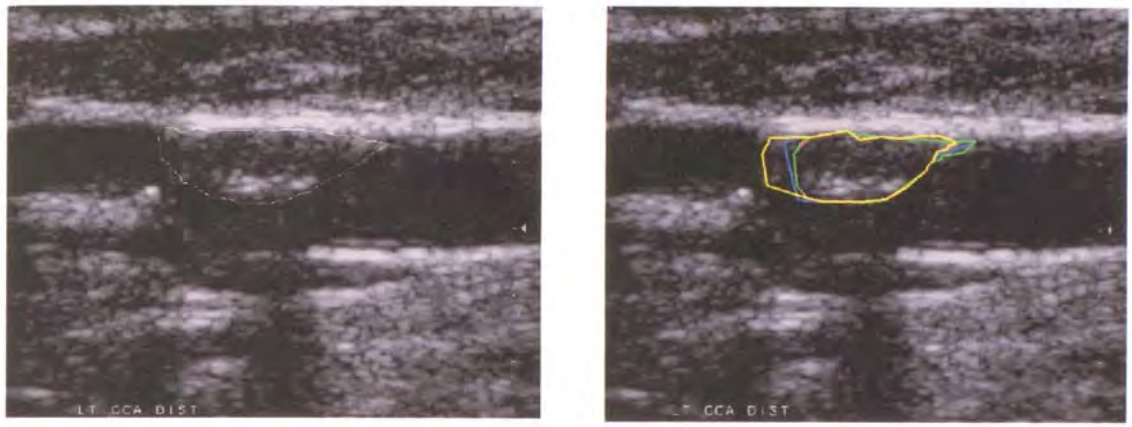


(a) (b)

**Fig. 6.15**: Segmentation results on a longitudinal ultrasound B-mode image of the carotid artery with plaque at the near wall, with: (a) manual segmentation, and (b) Williams&Shah (red line), Balloon (blue line), Lai&Chin (yellow line), and GVF (green line), snakes segmentation contours computed superimposed.

Finally Fig. 6.15 illustrates the manual (Fig. 6.15a), versus the snakes segmentation results (Fig. 6.15b) on a longitudinal ultrasound image with a plaque at the near wall superimposed, for the William&Shah snakes segmentation method (red line), Balloon (blue line), Lai&Chin (yellow line), and GVF (green line). The best snakes segmentation result was obtained by the Lai&Chin (yellow line) snakes segmentation method, which was closer to the manual segmentation.

Table 6.15 illustrates the number of iterations, and the computational time required, for the four plaque snakes segmentation methods, in one longitudinal ultrasound image of the carotid plaque illustrated in Fig. 6.14. The segmentation was performed on a Pentium III computer, with 512 Mb RAM, and 1.9 GHz processor speed. The initial snake contour was estimated, as described in section 5.8.2. The time required for the snake to converge in its final position, and the number of iterations, for all four different snakes segmentation methods were measured.

TABLE 6.15
NUMBER OF ITERATIONS AND COMPUTATIONAL TIME FOR THE FOUR DIFFERENT SNAKES SEGMENTATION METHODS.

| | Williams&Shah | Balloon | Lai&Chin | GVF |
|---|---|---|---|---|
| Iterations | 15 | 14 | 13 | 15 |
| Time (sec) | 13.03 | 12.31 | 11.71 | 12.73 |

The number of iterations for the Williams&Shah, Balloon, Lai&Chin, and GVF snakes segmentation methods, was 15, 14, 13, and 15, whereas the computational time was 13.03, 12.31, 11.71, and 12.73 seconds, respectively. The Lai&Chin snakes segmentation method,

exhibited the lower computational time (11.71 sec), and smaller number of iterations (13 iterations). The Balloon method, exhibited a larger number of iterations (14), and computational time (12.31 sec), the Williams&Shah run at 15 iterations and 13.03 sec and the GVF run at 15 iterations and 12.73 sec. Table 6.15 also showed that on average a relative small number of iterations and a low computational time was required for all four snakes segmentation methods, and this is due to the snake initialisation procedure, proposed in Chapter 5.8.2, with which the initial snake contour is placed close to the area of interest.

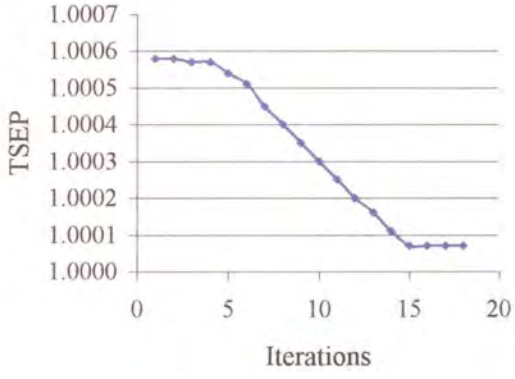


(a) Williams&Shah TSEP.

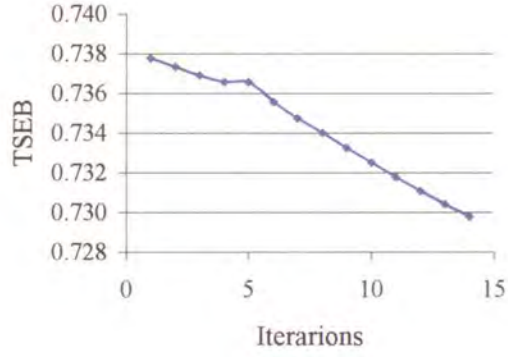


(b) Balloon TSEB.

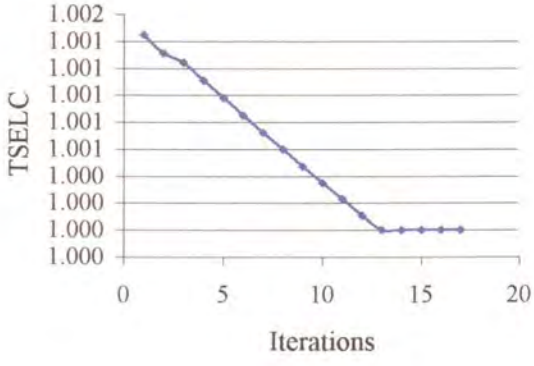


(c) Lai&Chin TSELC.

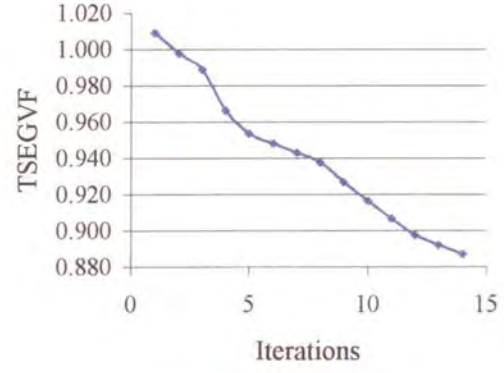


(d) GVF TSEGVF.

**Fig. 6.16**: Plots of the total snake energy for: (a) the Williams&Shah (TSEP), (b) Balloon (TSEB), (c) Lai&Chin (TSELC), and (d) GVF snake (TSEGVF) for the image in Fig. 6.14a.

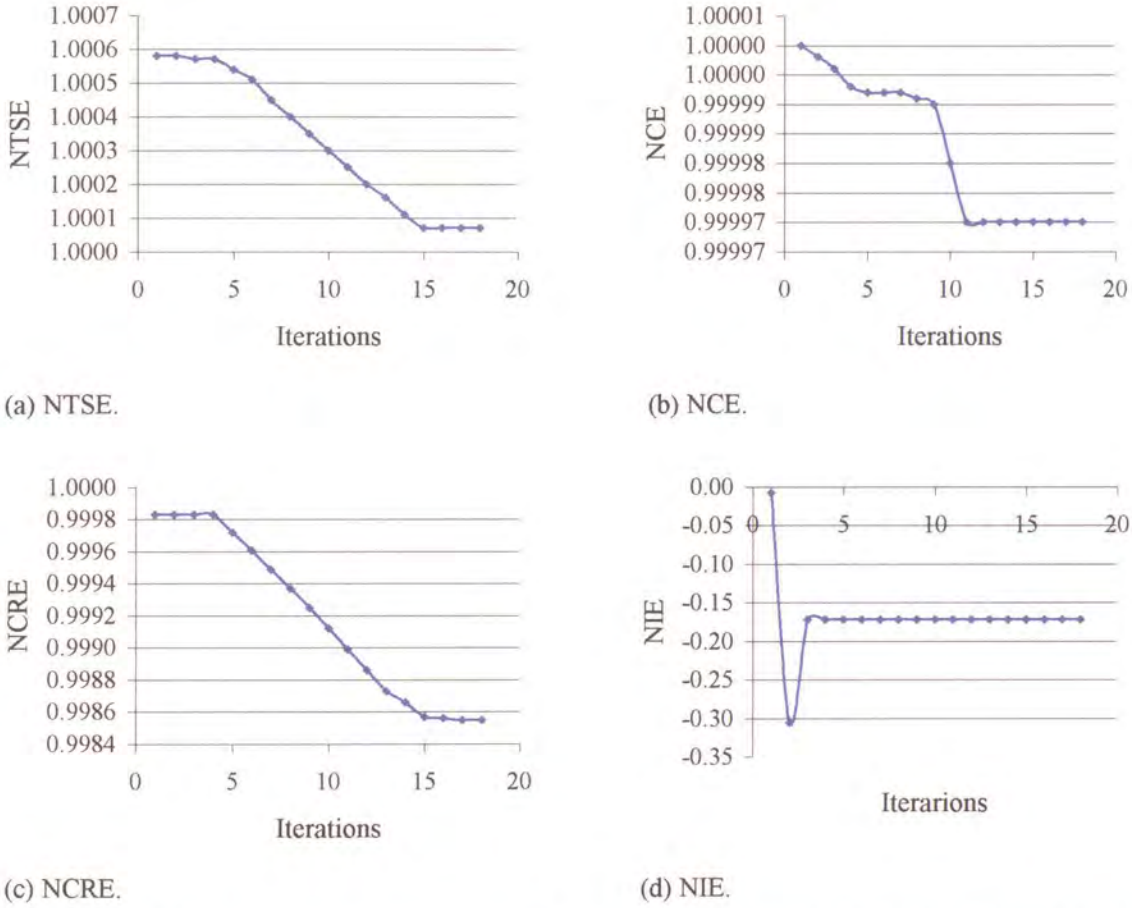


(a) NTSE. (b) NCE.

(c) NCRE. (d) NIE.

**Fig. 6.17**: Plots of the snake energy terms versus the number of iterations for the Williams&Shah snakes segmentation method for the image in Fig. 6.14, for: (a) normalized total snake energy (NTSE), (b) normalized continuity energy (NCE), (c) normalized curvature energy (NCRE), and (d) normalized image energy (NIE) terms respectively.

To illustrate the rate of convergence of the four snakes segmentation methods, the total snake energy (see (3.4.2)) for each iteration when processing the image in Fig. 6.14a, was recorded. Figure 6.16 shows the total snake energy for (a) the Williams&Shah snakes segmentation method (TSEP), (b) the Balloon (TSEB), (c) the Lai&Chin (TSELC), and (d) the GVF snake (TSEGVF) respectively. It can be seen that the TSEP, TSEB, TSELC, and TSEGVF converged at the $15^{th}$, $14^{th}$, $13^{th}$ and $14^{th}$ iterations respectively. The convergence for the TSELC is faster than the other three snakes segmentation methods.

To demonstrate the working principle of the Williams&Shah snakes segmentation method, and the rate of convergence for every energy term in (3.4.2), the snake energy terms were plotted versus the number of iterations, for the ultrasound image in Fig. 6.14a. They are shown in Fig. 6.17, with the normalised total snake energy, NTSE, (Fig. 6.17a), the normalised continuity energy term, NCE, (Fig. 6.17b), the normalised curvature energy term, NCRE, (Fig. 6.17c), and the normalised image energy term, NIE, (Fig. 6.17d) respectively. It was shown that

the fastest convergence was achieved by the NIE term after three iterations, followed by the NCE, NTSE, and NCRE terms with 11, 15, and 15 iterations respectively. The NCE term demonstrated a high drop out between the 8th and the 11th iteration, and then remained constant for the remaining iterations, whereas the NCRE and NTSE terms dropped linearly after the fourth iteration and then they remained constant after the 15th iteration. Figure 6.17 also showed that all energy terms except NIE require at least 15 iterations for the deformation process to settle.

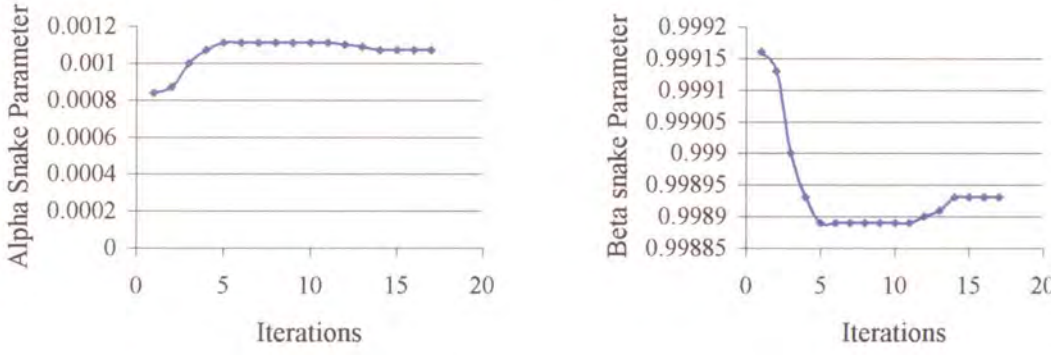


**Fig. 6.18**: Plots for the $\alpha$ and $\beta$ snake parameters for the Lai&Chin snakes segmentation method versus the number of iterations.

Figure 6.18 shows the variability of the $\alpha$ and $\beta$ snake parameters according to (3.5.5) and (3.5.6) versus the number of iterations for the Lai&Chin snakes segmentation method. It was shown that the $\alpha$ and $\beta$ parameters settled at their final values after the 15th iteration. The final values for these parameters were $\alpha = 0.0015$, and $\beta = 0.99893$.

### *6.4.2 Evaluation of plaque segmentation methods*

Table 6.16 presents a comparison of the four different plaque snakes segmentation methods (Williams&Shah, Balloon, Lai&Chin, and GVF) with the manual segmentation as performed by an expert on 80 longitudinal ultrasound images of the carotid plaque (as described in Chapter 5.8.4). Although all methods demonstrated similar performance, the best overall performance was demonstrated by the Lai&Chin snakes segmentation method. The results showed that the Lai&Chin snakes segmentation method, agrees with the expert in 80.89% of the cases, TNF, by correctly detecting no plaque, in 82.70% of the cases, TPF, by correctly detecting a plaque, disagrees with the expert in 15.59% of the cases, FNF, by detecting no plaque, and in 5.86% of the cases, FPF, by detecting a plaque. The similarity kappa index, KI, and the overlap index, for

the Lai&Chin snakes segmentation method were the highest, equal to 80.66% and 69.3% respectively.

The best FPF, and FNF, fractions were given by the Balloon snakes segmentation method, with 5.4% and 13.90% respectively. The GVF snakes segmentation method, showed for this experiment the worst results with the lowest similarity kappa index, KI, (77.25%), and the lowest overlap index (66.6%).

TABLE 6.16
ROC ANALYSIS FOR THE FOUR DIFFERENT PLAQUE SEGMENTATION METHODS AND THE MANUAL DELINEATIONS MADE BY AN EXPERT ON 80 ULTRASOUND IMAGES OF THE CAROTID ARTERY.

| Segmentation Method | System Detects | Expert Detects no plaque | Expert Detects plaque | KI | Overlap Index |
|---|---|---|---|---|---|
| Williams& Shah | No plaque | TNF=77.59% | FNF=19.64% | 78.86 % | 67.60 % |
| | Plaque | FPF=6.50% | TPF=81.76% | | |
| Balloon | No plaque | TNF=77.12% | **FNF=13.90%** | 77.87 % | 67.79 % |
| | Plaque | **FPF=5.40%** | TPF=80.35% | | |
| Lai&Chin | No plaque | **TNF=80.89%** | FNF=15.59% | **80.66 %** | **69.30 %** |
| | Plaque | FPF=5.86% | **TPF=82.70%** | | |
| GVF | No plaque | TNF=79.44% | FNF=14.90% | 77.25 % | 66.60 % |
| | Plaque | FPF=6.30% | TPF=79.57% | | |

Table 6.17 presents a comparison of the four different plaque snakes segmentation methods (Williams&Shah, Balloon, Lai&Chin, and GVF), on all 80 longitudinal ultrasound images of the carotid plaque, based on the sensitivity, R, specificity, Sp, precision, P, and the measure F, described in Chapter 4.5, and Chapter 5.8.4 (see also 4.16-4.19). Bolded values in Table 6.17 show best performance of the segmentation algorithms. The best sensitivity, R, was given by the Lai&Chin (0.827), followed by the Williams&Shah (0.8176), whereas the best specificity, Sp, was given by the Balloon (0.9460), followed by the Lai&Chin (0.9416) snakes segmentation method. The Lai&Chin gave the best precision, P, (0.9338), which is better than the rest of the segmentation methods, whereas the best F, was given by the Balloon (0.8882), followed by the Lai&Chin (0.8851) snakes segmentation method.

TABLE 6.17
ROC ANALYSIS FOR THE FOUR DIFFERENT PLAQUE SEGMENTATION METHODS AND THE MANUAL DELINEATIONS MADE BY AN EXPERT ON 80 ULTRASOUND IMAGES OF THE CAROTID ARTERY BASED ON THE SENSITIVITY, R, SPECIFICITY, SP, PRECISION, P, AND 1-EFFECTIVENESS MEASURE, 1-E.

| Segmentation Method | Sensitivity (R) | Specificity (Sp) | Precision (P) | F=1-E |
|---|---|---|---|---|
| Williams&Shah | 0.8176 | 0.9350 | 0.9263 | 0.8621 |
| Balloon | 0.8053 | **0.9460** | 0.9271 | **0.8882** |
| Lai&Chin | **0.8270** | 0.9416 | **0.9338** | 0.8851 |
| GVF | 0.7957 | 0.9370 | 0.9266 | 0.8824 |

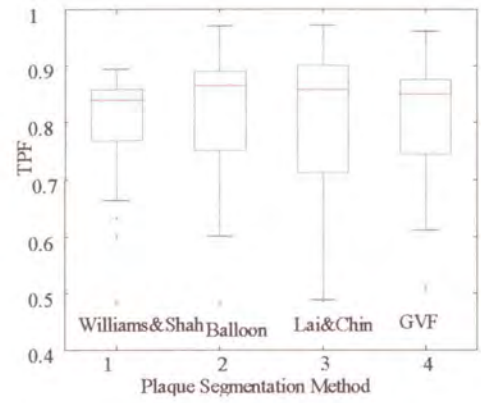


(a) TPF.

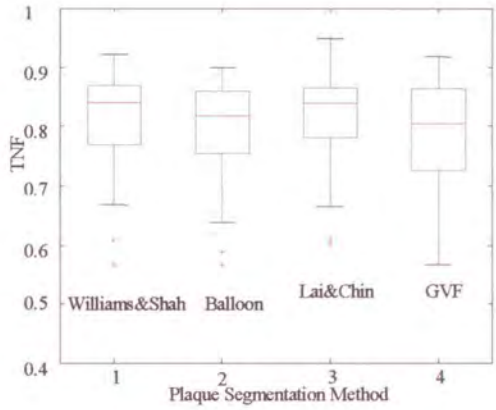


(b) TNF.

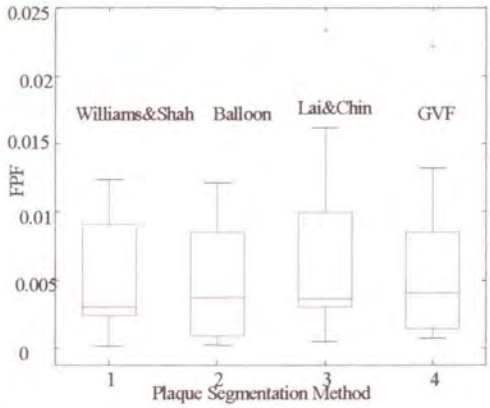


(c) FPF.

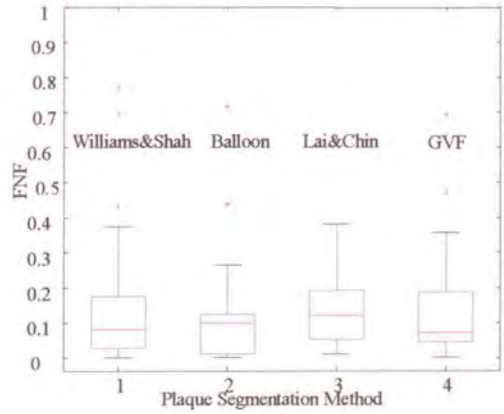


(d) FNF.

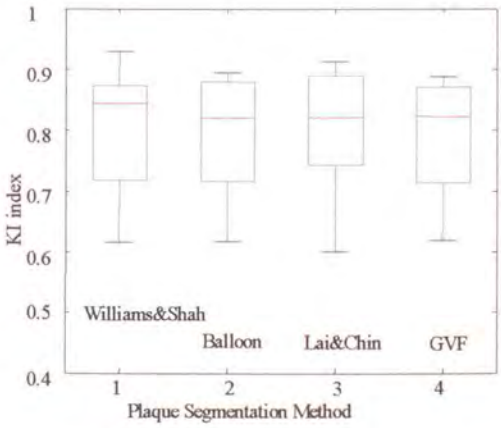


(e) KI index.

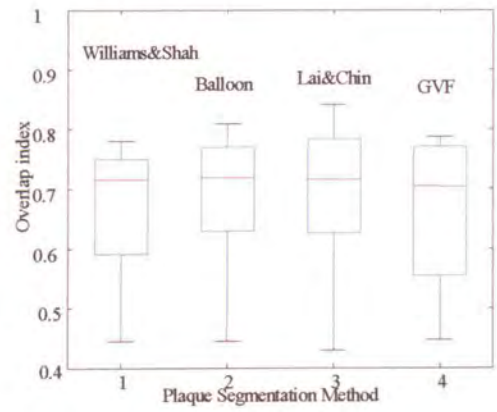


(f) Overlap index.

**Fig. 6.19**: Box plots for the four snakes segmentation methods (Williams&Shah, Balloon, Lai&Chin, and GVF) for: (a) TPF, (b) TNF, (c) FPF, (d) FNF, (e) Williams index, KI and (f) overlap index.

Figure 6.19 presents box plots to demonstrate the spread of the distributions for the TPF, TNF, FPF, FNF, the similarity kappa index, KI, and the overlap index for the four different plaque snakes segmentation methods. The box plots in Fig. 6.19, showed that the Williams& Shah exhibited the shortest box for the TPF (see Fig. 6.19a), with some outliers for the TPF, TNF and FNF. Balloon exhibited the shortest box for the FNF (see Fig. 6.19d), whereas the shortest box for the Lai&Chin was found for the TNF (see Fig. 6.19b), and the KI index (see Fig. 6.19e). Lai&Chin exhibited no outliers for the FNF (see Fig. 6.19d), and demonstrated a box with the smallest skewness for FNF, KI index, and the overlap index (see Fig. 6.19d, e, f).

Figure 6.20 shows the ROC curves, plotted as explained in Chapter 5.8.4, for the four snakes segmentation methods, based on the TPF and FPF fractions. The area below the ROC curve was 0.88, 0.85, 0.82, and 0.76 for the Lai&Chin, Balloon, GVF, and Williams&Shah snakes segmentation method respectively. It is clear, that the largest area under the ROC curve was obtained by the Lai&Chin snakes segmentation method.

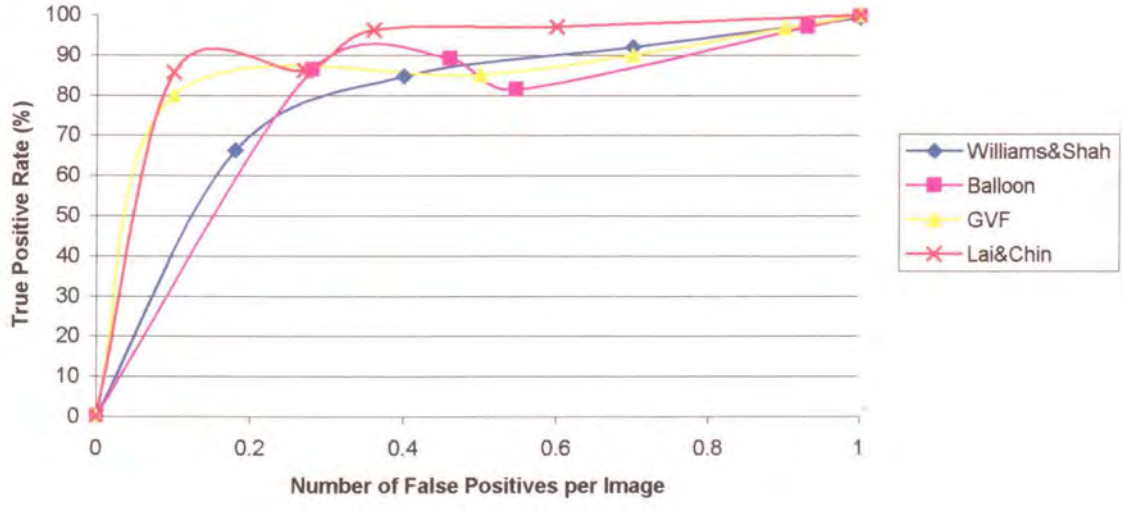


**Fig. 6.20**: ROC curve analysis based on the TPF and FPF fractions for the four snakes segmentation methods.

# *Chapter 7*

# *Discussion*

# CHAPTER 7: DISCUSSION

In this work, we have presented a review for despeckling and segmentation techniques for carotid ultrasound artery images. As a first task we have investigated the image quality of two different ultrasound scanner models based on statistical and evaluation metrics. Furthermore we have proposed despeckle filters that are more suitable for the despeckling of ultrasound images of the carotid artery. Additionally, a snakes segmentation technique was proposed for segmenting the IMT and the atherosclerotic carotid plaque from longitudinal ultrasound images. A system was developed that is capable of despeckling and segmenting the IMT and plaque borders in carotid artery ultrasound images, with better accuracy, and consistency compared with the manual delineations from the experts. The system can delineate the borders consistently, and thus enabling the expert to better and more accurately evaluate the risk of stroke. The aim of the system is not to entirely replace the manual delineations but to complement the experts manual evaluation.

## 7.1 Image quality evaluation of two ultrasound scanners

Image quality is very important in the assessment of atherosclerosis and the evaluation of the risk of stroke in ultrasound imaging. We have therefore, evaluated two different ultrasound scanners (ATL HDI-3000, and ATL HDI-5000) on 80 longitudinal ultrasound images of the carotid artery bifurcation, before and after despeckle filtering, after normalization, and after despeckle filtering and normalization. The evaluation was based on visual evaluation by two experts, despeckle filtering, statistical and texture features, as well as based on image quality evaluation metrics. It should be noted that there are no other studies found in the literature for comparing the performance of the two ultrasound scanners.

### *7.1.1 Visual perception*

It is clearly shown that the ATL HDI-5000 scanner produces images with higher quality. It was also shown that despeckle filtering and normalisation produces better images (see Fig. 6.1, Fig. 6.2, Table 6.1). Normalisation was also proposed in other studies using blood echogenicity as a reference and applied in carotid artery images [93], [235]. In [322], it was shown that normalisation improves the image compatibility by reducing the variability introduced by different gain settings, different operators, and different equipment.

### *7.1.2 Statistical and texture measures*

Some statistical measures, as shown in the first part of Table 6.2, were better after normalization, and some others, shown in the second part of Table 6.2, were better after despeckle filtering. Table 6.2 also showed that the contrast was higher for the NF and N images

on both scanners. All other measures presented in Table 6.2 are comparable showing that better values were obtained on the NDS images. Moreover it was shown that the entropy that is a measure of the information content of the image [128] was higher for both scanners in the cases of the NDS and DS images. Low entropy images have low contrast and large areas of pixels with same or similar gray level values. An image which is perfectly uniform will have a zero entropy. On the other hand, high entropy images have high contrast and thus higher entropy values [3]. The ATL HDI-5000 scanner produces therefore images with higher information content. The entropy was also used in other studies to classify the best liver ultrasound images [211], where it was shown that the experts rate images with higher entropy values better. In [10] entropy was used to classify between symptomatic and asymptomatic carotid plaques. Finally in [147] higher entropy values indicated a higher probability of a cloud to give rain.

### *7.1.3 Quality evaluation metrics*

Marginal differences were observed from Table 6.3 between the ATL HDI-3000 and the ATL HDI-5000 scanner. For example, the MSE and the RMSE remained almost the same for both scanners. It was documented in [272], [278], [279], [283], [289], that the MSE, RMSE, SNR and PSNR, are not objective measures for image quality evaluation nor do they correspond to all aspects of the visual perception. Furthermore, they do not correctly reflect artifacts [284], [289], [300]. While MSE and RMSE values were in the range of 0.4 to 2.0, for all cases, Err3, Err4, SNR, PSNR, Q, and SSIN were significantly better on the NF-N images for both scanners, showing that normalization increases the values of these measures. Using the recently proposed measures for objective image evaluation Q [272], and SSIN [278], the best performance for both scanners was given by the NF-N. The values for Q and SSIN for both scanners on the NF-N images were 0.95 and 0.95 respectively. These results were followed with Q=0.73, and SSIN=0.92 in the case of NF-NDS for the HDI ATL-3000 scanner, and Q=0.72, and SSIN=0.94 in the case of NF-DS for the HDI ATL-5000 scanner. It is noted that the findings of the image quality evaluation metrics showed that the best results were obtained on the NF-N and NF-NDS images, whereas the visual perception evaluation (see Table 6.1) showed that best results were obtained for the NDS and DS images.

The results of this study showed that normalization and despeckle filtering are an important procedure favouring image quality, and should be further investigated.

### *7.1.4 Summary findings on image quality evaluation*

Table 7.1 summarises the image quality evaluation results of this study, for the visual evaluation (Table 6.1), the statistical and texture analysis (Table 6.2), and the image quality evaluation metrics (Table 6.3), as presented in Chapter 6.1. A double plus sign in Table 7.1

indicates very good performance, while a single plus sign a good performance. Table 7.1 can be summarised as follows:

a) The NDS images were rated visually better on both scanners,

b) The NDS images showed better statistical and texture analysis results for both scanners, followed by the DS images,

c) The NF-N images on both scanners showed better image quality evaluation results, followed by the NF-DS on the ATL HDI-5000 scanner and the NF-NDS on the HDI-3000 scanner.

d) The ATL HDI-5000 scanner images have considerably higher entropy than the ATL HDI-3000 and thus more information content. However, based on the optical evaluation by the two experts, both scanners were rated similarly.

TABLE 7.1
SUMMARY FINDINGS OF IMAGE QUALITY EVALUATION IN ULTRASOUND IMAGING OF THE CAROTID ARTERY.

| Ultrasound Scanner | Visual Evaluation Table 6.1 | | | | Statistical and Texture Analysis Table 6.2 | | | | Image Quality Evaluation Table 6.3 | | | |
|---|---|---|---|---|---|---|---|---|---|---|---|---|
| | NF | DS | N | NDS | NF | DS | N | NDS | NF-DS | NF-N | NF-NDS | N-NDS |
| ATL HDI-3000 | | | | ++ | | + | | ++ | | ++ | + | |
| ATL HDI-5000 | | | | ++ | | + | | ++ | + | ++ | | |

++: Very good, +: Good.

The usefulness of the proposed quality evaluation metrics, in portable ultrasound systems and in wireless telemedicine systems still has to be investigated. It is also important to note that the methodology consists of a combination of subjective and objective measures that should be combined all together for a proper image quality evaluation result [316].

## 7.2 Despeckle filtering

Despeckle filtering is an important operation in the enhancement of ultrasound images of the carotid artery, both in the case of texture analysis, and in the case of image quality evaluation and visual evaluation by the experts. In this work a total of 11 despeckle filters were comparatively evaluated on 440 ultrasound images of the carotid artery and the validation results are summarised in Table 7.2. A sign (✓)indicates a good performance of a despeckle filter.

As given in Table 7.2, filters *lsmv, lsminsc,* and *homo,* improved the class separation between the asymptomatic and the symptomatic classes (see also Table 6.5). Filters *lsmv,*

*lsminsc*, and *gf4d* gave a high number of significantly different features (see Table 6.6). Filters *lsminsc*, *gf4d*, and *homo*, gave only a marginal improvement in the percentage of correct classifications success rate (see Table 6.7). Moreover, filters *lsmv*, *nldif*, and *waveltc*, gave better image quality evaluation results (see Table 6.8). Filters *lsmv*, and *gf4d*, improved the visual assessment carried out by the experts (see Table 6.91, Table 6.9.2)). It is clearly shown that filter *lsmv* gave the best performance, followed by filters *lsminsc*, and *gf4d* (see Table 7.2). Filter *lsmv* or *gf4d* can be used for despeckling asymptomatic images where the expert is interested mainly in the plaque composition and texture analysis. Filters *lsmv* or *gf4d* or *lsminsc* can be used for despeckling of symptomatic images where the expert is interested in identifying the degree of stenosis and the plaque borders. Filters *homo*, *nldif*, and *waveltc* gave poorer performance.

TABLE 7.2
SUMMARY FINDINGS OF DESPECKLE FILTERING IN ULTRASOUND IMAGING OF THE CAROTID ARTERY.

| Despeckle Filter | Statistical and Texture Features Table 6.5 | Statistical Analysis Table 6.6 | kNN Classifier Table 6.7 | Image Quality Evaluation Table 6.8 | Optical Perception Evaluation Table 6.9.1, Table 6.9.2 |
|---|---|---|---|---|---|
| Local Statistics | | | | | |
| *lsmv* | ✓ | ✓ | | ✓ | ✓ |
| *lsminsc* | ✓ | ✓ | ✓ | | |
| Geometric Filtering | | | | | |
| *gf4d* | | ✓ | ✓ | | ✓ |
| Homomorphic Filtering | | | | | |
| *homo* | ✓ | | ✓ | | |
| Diffusion Filtering | | | | | |
| *nldif* | | | | ✓ | |
| Wavelet Filtering | | | | | |
| *waveltc* | | | | ✓ | |

✓: Indicates good performance of a despeckle filter.

### *7.2.1 Despeckle filtering on an artificial and a real carotid image*

Figure 6.3 and Fig. 6.5 showed that good optical results were obtained by the despeckle filters *lsmv* (Fig. 6.3b, Fig. 6.5b), *lsminsc* (Fig. 6.3c, Fig. 6.5c), and *gf4d* (Fig. 6.3h, Fig. 6.5h). The *lsmv* removed the noise around the IMT, and thus the borders between IMT and blood were more easily identified. Moreover, it was shown from the line profile in Fig. 6.4b, that both the edge and the locality of boundaries were well preserved by the *lsmv* despeckle filter. The *lsminsc* shown in Fig. 6.3c, and Fig. 6.5c performed a textural orientation on the image, grouping the homogeneous areas together. This is good especially when applying the filter on plaque areas, as the plaque borders will be kept together. It was also shown from Fig. 6.4c, that

boundaries were well preserved for the filter *lsminsc* although some noise still remained after despeckle filtering. The images in Fig. 6.3h, and Fig. 6.5h, which were processed by the *gf4d*, were brighter after filtering, and the borders of the IMT were well recognized. Figure 6.4h showed that boundaries were also well preserved where some noise remained on edges. Finally the filter *nldif*, preserved the boundaries (Fig. 6.3k), but a lot of noise remained after filtering (Fig. 6.4k).

The rest of the images in Fig. 6.3 and Fig. 6.5, showed a blurring effect (Fig. 6.3d-g, i, j, l), edges were not well preserved (Fig. 6.3d-g, j, l), the image became darker after filtering (Fig. 6.3i), and homogeneous areas were blurred (Fig. 6.3d-g, i, j, l). The line profiles of the despeckle filters, *median*, *wiener*, *ls*, *homog*, *homo*, *ad*, *nldif*, and *waveltc*, in Fig. 6.4 showed that a substantial noise component remained after filtering (Fig. 6.4i,k), and that the locality of boundaries were not well preserved (Fig. 6.4d-g, i-l).

The results in Table 6.4, showed that the *gf4d*, increases enormously the contrast, followed by *homo*, and *lsminsc*, where the *lsmv*, *gf4d* and *lsminsc* reduces the speckle index, C, considerably. The contrast-to-speckle radio, CSR, was very good for the filter *homo*, followed by the *gf4d*, and *lsminsc*.

Despeckle filtering was investigated by other researchers and also in our study, on an artificial carotid image (Fig. 6.3), [38], on line profiles (Fig. 6.4) of different ultrasound images, [175], [326], [345], [349], and real longitudinal ultrasound images of the carotid artery (Fig. 6.5) [38]. There is only one study [38], where despeckle filtering was investigated on one real, and one artificial longitudinal ultrasound image of the carotid artery. Four different despeckle filters were applied in [38], namely the Lee [22], Frost [27], anisotropic diffusion [347], and a speckle reducing anisotropic diffusion filter [38]. The despeckle window used for the Lee, and Frost filters was 7x7 pixels. To evaluate the performance of these filters, the mean and the standard deviation were used, which were calculated in different regions of the carotid artery image, namely in lumen, tissue, and at the vascular wall. The mean gray level values of the original image for the lumen, tissue and wall regions were 1.03, 5.31, and 22.8, whereas the variance were 0.56, 2.69, and 10.61. The mean after despeckle filtering with the speckle anisotropic diffusion gave brighter values for the lumen and tissue. Specifically the mean for the lumen, tissue, and wall for the speckle reducing anisotropic diffusion was (1.19, 6.17, 18.9), Lee (1.11, 5.72, 21.75), Frost (1.12, 5.74, 21.83) and anisotropic diffusion (0.90, 4.64, 14.64). The standard deviation for the speckle anisotropic diffusion gave lower values (0.15, 0.7, 2.86) when compared with Lee (0.33, 1.42, 5.37), Frost (0.32, 1.40, 5.30), and anisotropic diffusion (0.20, 1.09, 3.52). It was thus shown that the speckle reducing anisotropic diffusion filter preserves the mean and reduces the variance. The number of images investigated in [38], was very small, visual perception evaluation by experts was not carried out, as well as only two statistical

measures were used to quantitatively evaluate despeckle filtering, namely the mean, and the variance before and after despeckle filtering as explained above. We believe that the mean and the variance used in [38] are not indicative and may not give a complete, and accurate evaluation result. Furthermore, despeckle filtering was investigated by other researchers on ultrasound images of, heart [345], pig heart [349], pig muscle [75], [76], kidney [141], liver [271], echocardiograms [348], CT lung scans [37], MRI images of brain [124], [228], [344], brain X-ray images [326], SAR images [38], [88], [91], [92], [98], [107], [229], and real world images [285].

Line plots, as used in our study (see Fig. 6.4), were also used in few other studies to quantify despeckle filtering performance. Specifically in [326], a line profile through the original and the despeckled ultrasound image of kidney was plotted, using adaptive Gaussian filtering. In [186] line profiles were plotted on four simulated and 15 ultrasound cardiac images of the left ventricle, in order to evaluate median filtering. In another study [345], line profiles through one phantom, one heart, one kidney, and one liver ultrasound image, were plotted where an adaptive shrinkage weighted median [271], [285], wavelet shrinkage [350], and wavelet shrinkage coherence enhancing [348] models were used and compared with a non linear coherent diffusion model [345]. Finally in [349], line plots were used in one artificial computer simulated image, and one ultrasound image of pig heart, where an adaptive shrinkage weighted median filter [271], a multiscale nonlinear thresholding without adaptive filter pre-processing [349], a wavelet shrinkage filtering method [350], and a proposed adaptive nonlinear thresholding with adaptive pre-processing method [349], were evaluated. In all above studies, visual perception evaluation by experts, statistical and texture analysis, on multiple images, as performed in our study, was not performed.

### *7.2.2 Texture analysis*

The results on texture analysis, presented in Chapter 6.2.2 (Table 6.5-Table 6.7), showed that the filters *lsmv*, *gf4d*, and *lsminsc* (Table 7.2), improved the class separation between the asymptomatic and the symptomatic classes (Table 6.5), by increasing the distance between them. These filters, *lsmv*, *gf4d*, and *lsminsc*, gave the highest number of significantly different features (Table 6.6), with 7, 6, and 5 respectively, and gave only a marginal improvement in the percentage of correct classification success rate (Table 6.7). The high number of significantly different features for these filters, showed that the two classes (asymptomatic, symptomatic), may be better separated after despeckle filtering with the filters *lsmv*, *gf4d*, and *lsminsc*. Table 6.5 showed that almost all despeckle filters increased the distance between the asymptomatic and the symptomatic images thus making the identification of a class more easily to identify. Table 6.5 also showed that most of the filters reduced the asymmetry, $\sigma^3$, and the skewness, $\sigma^4$, of the histogram. Table 6.6 showed, that despeckle filtering influenced more some

statistical features, such as the inverse difference moment, IDM, the angular second moment, ASM, and the sum entropy, $\sum Entr$, while other statistical features were less influenced by despeckle filtering. As a result, these features, which were more influenced, may be used in future research to evaluate despeckle filtering. The $Score_Dis_T$ in the last row of Table 6.5, showed that best feature distance was given by the filters *homo*, *lsminsc*, *median*, and *lsmv*. Table 6.7 showed that not all feature sets equally benefited from despeckle filtering. Specifically, the SF and TEM feature sets benefited from almost all despeckle filters (7), whereas the feature sets SGLDMm, GLDS, and NGTDM, benefited from four despeckle filters, FDTA three and SFM two. The features sets SGLDMr, and FPS, benefited from only one despeckle filter.

There were some results given in the recent literature based on texture analysis of ultrasound images for, the classification of atherosclerotic carotid plaque [10], [48], [127], [138], [139], liver ultrasound images [211], [236], electron microscopic muscle images [171], detection of breast masses [232], cloud images [147], SAR images [31], and some results given on artificial images from the pioneer researchers in texture analysis [128], [129]. There is no other study reported in the literature, where texture analysis (Table 6.5-Table 6.7) was used to the extent, that is used in our study, to evaluate despeckle filtering in ultrasound imaging. In studies [10], [48], [127], some of the texture measures used in our study (Table 6.5), were also used on a total of 230 ultrasound images of the carotid plaque (115 asymptomatic, 115 symptomatic), in order to characterise carotid plaques as safe or unsafe and identify patients at risk of stroke. Specifically in [10], and [148] all nine different features used in our study (see Table 6.7) were also used to classify a plaque as asymptomatic or symptomatic, where comparable values as in our study were obtained for all feature sets. Examples of the use of texture analysis were also provided in [232], for classifying malignant and benign tumours of breast, in [147] for classifying clouds and predicting weather, and finally in [129] to automatically classify terrain texture.

### *7.2.3 Image quality evaluation metrics*

The image quality evaluation results presented in Table 6.8 showed that the best values were obtained by the despeckle filters *nldif, lsmv,* and *waveltc*. It was shown from Table 6.8, that the effect of despeckle filtering was more obvious on the asymptomatic images, where generally better image quality evaluation results were obtained. Moreover, it is obvious that all quality evaluation metrics presented here were equally important for image quality evaluation. It is furthermore important to note that a higher PSNR (or equivalently, a lower RMSE) does not necessarily imply a higher subjective image quality, although they do provide some measure of relative quality. While some quality metrics for different images have been studied and

proposed in the literature, such as for MRI [273], natural and artificial images [272], [278], [286], to the best of our knowledge, no other comparative study exists that have investigated the application of the above metrics together with visual perception evaluation, on ultrasound images of the carotid artery. In previous studies [131], [160], [174], [181], [238], [272], [278], [286], [292], [294], [316], [329], [338], researchers evaluated image quality on real world images using either only the visual perception by experts or some of the evaluation metrics presented in Table 6.8. In all these studies, the comparison of the proposed method was made with another one, based on image quality evaluation metrics, such as the MSE [70], [88], [141], [285], [345], [349], PSNR [285], SNR [326], C [88], [141]; the mean, and the variance [38], [75], [229], [271], and line plots [75], [91], [125], [271], [345], [349] between the original and despeckled images. The usefulness of these measures was not investigated for the despeckling of ultrasound images. Furthermore, normalization and despeckling was not taken into consideration as in our study. In a recent study [160], we have investigated the image quality on ultrasound images of the carotid artery, where it was shown that despeckle filtering, increases the quality of these images.

Image quality metrics were also investigated for the evaluation of ultrasound spatial compound scanning [188], to compare the quality of JPEG images before and after compression using the PSNR, and SSIN [278], where values for the PSNR, and SSIN of 8.45, and 0.96, were measured respectively, while in our study, we have achieved values of 39, and 0.97, with the *lsmv* filter (see Table 6.8). In [300] real world images were evaluated based on their compression ratios, by using the MSE, and Q, where values of 30, and 0.92 were reported respectively. Furthermore real world images were also evaluated in [300], based on the MSE and Q, before and after, histogram equalization (1144.2, 0.74), median filtering (14.47, 0.78), wavelet compression (16.03, 0.68), and spatial displacement (141.2, 0.5).

In another study [285], where various median filtering techniques were investigated on real world images, the image quality measures, MSE, and PSNR, were used to compare, between the original and the filtered images. In [284] a number of quality metrics were reviewed to evaluate JPEG compression on still real world images, such as the MSE, SNR, PSNR, M3, and M4. In [345], where despeckle filtering was investigated on artificial and ultrasound images of heart, kidney and abdomen, the MSE values reported after despeckle filtering were 289, 271, 132, and 121, for four different despeckle filtering methods, namely the adaptive weighted median filtering [285], wavelet shrinkage enhanced [348], wavelet shrinkage [350], and non-linear coherence diffusion method [345]. Most of the researchers used the image quality measures such as the MSE [70], [88], [124], [141], [285], [345], [349], SNR [157], [161], [228], [340], and PSNR [285], in order to compare the original with the despeckled images.

In A. Achim's, et al. [88] research, values reported for the MSE were 133, 43, 49, 26, 22 for the original, and four despeckled SAR images respectively. In Achim's research four different despeckling methods were used, namely the Lee [22], gamma MAP filter [18], soft thresholding [350], and the WIN-SAR filter [88], which used a 7x7 pixel filtering window, and were applied on real world and SAR images.

In another study [141], MSE values reported were 26 for the original kidney ultrasound image, 13.7 after despeckling by median filtering [285], 13.8 after homomorphic Wiener filtering [229], 13.6 after soft thresholding [350], 13.5 after hard thresholding [350], and 12.74 after Bayesian denoising [141]. In our study the MSE values for the filter *lsmv*, *wiener*, *nldif*, and *waveltc*, (Table 6.8) were 13, 19, 8, 11, for the asymptomatic, and 33, 44, 8, 23, for the symptomatic images respectively, which are better or comparable with other studies reported above.

### *7.2.4 Visual perception and additional comments by experts*

The visual perception evaluation performed in Table 6.9.1 and Table 6.9.2, showed that the filters *lsmv*, *gf4d*, and *lsminsc* improved the visual assessment by experts. The intra-observer variability test (Table 6.9.2), which was repeated one year after the first visual evaluation (Table 6.9.1), showed that the differences between the visual evaluations made by the two experts were very low, and the results of the two tables were in agreement.

It was shown that the highest scores were obtained, for the filter *lsmv* for both tables. The differences, which are observed in the ratings between the two experts, were due to the fact that each expert was interested for a different tissue area in the ultrasound image of the carotid artery. Specifically the cardiovascular surgeon was primarily interested in the plaque composition and texture, whereas the neurovascular expert was interested in the degree of stenosis and the lumen diameter. The filter *lsminsc* was rated from the neurovascular expert with the highest score in Table 6.9.2. The expert found that this filter was very helpful when inspecting the degree of stenosis and the lumen diameter.

In Table 6.10 the two experts, evaluated the images before and after despeckle filtering, and gave some additional comments, which we think it is important to briefly discuss. It was shown that the primary interest of the experts were the borders between IMT, plaque, artery wall, and blood, in order to be able to exactly make a separation between them. Other important points taken into consideration from both experts during this examination were the texture of plaque, as the texture may give indication about the risk of stroke [10]. They have both commented the fact that the *lsmv* filter was good for visualising the borders between blood, plaque and wall but not between wall and surrounding tissue, the *lsminsc* helped specifically for the plaque visualisation as plaque borders were better after filtering, and that the *gf4d* sharpened the edges,

thus it may be used for plaque visualization and to separate the borders between blood and plaque.

To the best of our knowledge, no other studies were carried out on the visual evaluation of ultrasound images by using despeckle filtering and image normalisation with two experts. In a significant number of despeckle filtering studies, [38], [70], [75], [91], [92], [141], [228], [229], [271], [285], [326], [344], [345], [348], [349], visual evaluation was carried out by non-experts. There are very few results reported in the literature, where visual perception evaluation was carried out in ultrasound images. Specifically, despeckle filtering was evaluated visually by two experts in [348], where they manually delineated 60 echocardiographic images before and after despeckle filtering. Quantitative measurements were calculated in terms of the mean of absolute border difference and the mean of border area differences. The visual evaluation in [348], showed that the borders, which were manually defined by the experts were improved after despeckle filtering. In [98], the performance assessment of multi-temporal SAR image despeckling was evaluated from ten photo interpreters. The evaluation was made between the original and the three filtered results. The photo interpreters evaluated the accuracy of manual detection of geographical features, such as lines points and surfaces, by presenting the images in random order. The ten photo interpreters concluded that despeckle filtering improves the identification of the above criteria and that specific filters may be used to enhance points, lines or surfaces as required. In another study image quality was evaluated for compressed still images [110], where the images were presented to an unknown number of observers in random order. The observers were not experts, but they were untrained persons over 18 drawn from the university population.

### *7.2.5 Summary findings on despeckle filtering*

The results of our study showed, that observer variability, and sensitivity are important in image quality evaluation, and can only be compensated when assessments are made against a standard scale of quality, such as the image quality evaluation metrics proposed in this study. Observer variability may also be compensated by additional tests employing image quality and texture measures, as proposed in this study, for quantifying image quality.

The findings, from the despeckle filtering, in our study may be summarised as follows (see also Table 7.2): Filter *lsmv* or *gf4d* can be used for despeckling asymptomatic images where the expert is interested mainly in the plaque composition and texture analysis. Filters *lsmv* or *gf4d* or *lsminsc* can be used for despeckling of symptomatic images where the expert is interested in identifying the degree of stenosis and the plaque borders.

Filter *lsmv* gave very good performance with respect to:

a) Preserving the mean and the median, as well as decreasing the variance and the speckle index, C, of the image.

b) Increasing the distance of the texture features between the asymptomatic and the symptomatic classes.

c) Significantly changing the SGLDM range of values texture features after filtering based on the Wilcoxon rank sum test, where almost all feature sets with the exception of SAV, were significantly different.

d) Marginally improving the classification success rate of the kNN classifier for the classification of asymptomatic and symptomatic images in the case of SF, SMF and TEM feature sets, and

e) Improving the image quality of the image.

The *lsmv* filter, which is a simple filter, is based on local image statistics. It was first introduced in [22], [23], [159] by Jong-Sen Lee and co-workers, and it was tested visually on a few SAR images, with satisfactory results. It was also used for SAR imaging in [28] and [37], and image restoration in [29], [30], where the evaluation was made visually by the researchers, which they have concluded that the filter showed satisfactory results.

Filter *gf4d* gave very good performance with respect to:

a) Decreasing the variance and the speckle index, C, and increasing the contrast significantly of the image.

b) Marginally increasing the distance of the texture features between the asymptomatic and the symptomatic classes.

c) Significantly changing the SGLDM range of values texture features after filtering based on the Wilcoxon rank sum test, where almost all features sets with the exception of SAV, and $\sum Var$ were significantly different.

d) Improving the classification success rate of the kNN classifier for the classification of asymptomatic and symptomatic images in the cases of SGLDMm, GLDS, NGTDM, SFM and TEM feature sets.

The geometric filter *gf4d* was introduced by Grimmins [19], [162], and was tested visually on a few SAR images with satisfactory results.

Filter *lsminsc* gave the best performance with respect to:

a) Preserving the mean and the median, as well as decreasing the variance and the speckle index and increasing the contrast of the image.

b) Increasing the distance of the texture features between the asymptomatic and the symptomatic classes.

c) Significantly changing the SGLDM texture features after filtering based on the Wilcoxon rank sum test, where almost all features sets with the exception of the contrast, SOSV, and SAV were significantly different.

d) Improving the classification success rate of the kNN classifier for the classification of asymptomatic and symptomatic images in the case of SF, SGLDMr, GLDS, NGTDM, FDTA and FPS feature sets.

Filter *lsminsc* was originally introduced by Nagao in [165], and was tested on an artificial and an SAR image with satisfactory performance. In this study the filter was modified, by using the speckle index instead of the variance value for each sub window (as described in Chapter 2.3.1.3).

Filters used for despeckle filtering in ultrasound imaging by other investigators include: *median* [3], [8], [168], [285], *wiener* [27], [38], [87], [163], [164], [167], *homog* [2], [165], *homo* [122], [229], [324], [325], *adsr* [38], [74] and *waveltc* [70], [88], [109], [142], [180], [228], [229], [349]. However, these filters were evaluated on a small number of images, and their performance was tested based on the mean, median, standard deviation and speckle index of the image before and after despeckle filtering.

The *median* and the *wiener* filters were originally used by many researchers for suppressing the additive noise and later for despeckling different types of images [3], [8], [168], [285]. The results of this study showed that the *wiener* and *median* filters were not able to remove the speckle noise and produce blurred edges in the filtered image (see Fig. 6.3, 6.5). In our study the *median* filter performed poorer as shown in Table 6.4-Table 6.9.2.

The *homog* [2], [132], [165], and *homo* [168], [324], [325], filters, were recently used by some researchers for speckle reduction but our results in Table 6.4-Table 6.9.2 and the visual evaluation of the experts in Table 6.10, showed poor performance especially of the *homo* filter.

In a recent study [38], speckle reducing anisotropic diffusion was proposed as the most appropriate filter for ultrasound images of carotid artery. However, in this study, *ad*, as shown in Table 6.5-Table 6.8, performed poorer compared to *lsmv*, *gf4d*, and *lsminsc*.

Furthermore, wavelet filtering proposed by Donoho in [350], was investigated for despeckling SAR images [13], [88], [107], [152], [229], real world images [29], [90], [323], MRI [228], and ultrasound images [142], [146], [337], with favourable results. In this study, it was shown that the *waveltc* filter gave poorer performance in removing the speckle noise from the ultrasound images of the carotid artery (Table 6.4-Table 6.6).

All above investigators described their results as quite favourable with improvements in contrast enhancement, noise reduction and edge preservation after filtering, but we believe that these results were not well quantified. The reason is that researchers have used a small number of images, a limited number of texture descriptors to quantify the filtered images, and they have not included findings of experts such as our findings from the two vascular experts. On the other hand, the methods proposed in other studies, have not been evaluated and compared with other methods like in our study. For our filter evaluation, a large set of feature descriptors were employed which, when used with the statistical Wilcoxon test, the kNN-classifier, the visual assistance and the quantification of two experts offers a complete and more accurate result. In Table 6.6, the statistical test of significantly different features before and after despeckle filtering was presented, and it was shown that despeckle filters, *homo, waveltc, median* and *wiener,* proposed by other researchers, showed bad results as far as significant difference concerns, thus the classes (asymptomatic, symptomatic) could not be easily separated. The filters *lsmv, gf4d,* and *lsminsc* showed better results in this test.

Finally, Table 7.2 summarises the findings on despeckle filtering and proposes what despeckle filter should be used if the primary interest is the plaque texture and composition or the outline of the plaque together with the degree of stenosis and the lumen diameter. Specifically, Table 7.2 suggests what filter should be used for despeckle filtering if the expert is interested in computer aided diagnosis or visual perception evaluation. The final message is that depending on the purpose of the ultrasound scanning or the clinical diagnosis needed from the experts, one may have to use a different despeckle filter.

While in almost all studies where despeckle filtering was investigated, statistical and or texture analysis was used to evaluate despeckle filtering, the visual perception evaluation was used in few studies, where an original image was to be evaluated with a processed or a despeckled one. Also the number of the images used for the evaluation varied, and there is no other study reported where such a large number of images was used for evaluating despeckle filtering as in this study. It seems that visual evaluation is widely accepted in the medical community.

However, visual perception evaluation is associated with the problems presented in Chapter 4 (see also Appendix II). As it is well known, visual perception is very subjective and suffers from intra-and inter-observer variabilities. Furthermore, visual analysis is subjective to both systemic and random errors. A systemic error can be introduced when changing the screen settings or observed between different experts. Although appropriate training and method standardization should eliminate these potential problems visual perception evaluation still remains one of the biggest challenges in the automatic image analysis and evaluation. In order to overcome some of the difficulties of visual analysis, Haralick [128], suggested a

standardization, or normalization, procedure, as explained in Chapter 5.3, needs to be applied. This normalization has been also used in our study for the despeckling, segmentation, and image quality evaluation.

In conclusion, despeckle filtering is an important operation in the enhancement of ultrasonic imaging of the carotid artery. In this study it is shown that simple filters based on local statistics (*lsmv* and *lsminsc*), and geometric filtering (*gf4d*), can be used successfully for the processing of these images. In this context, despeckle filtering can be used as a pre-processing step for the automated segmentation of the IMT [338], and the carotid plaque [238], followed by the carotid plaque texture analysis, and classification. Initial findings show promising results, however, further work is required to evaluate the performance of the suggested despeckle filters at a larger scale as well as their impact in clinical practise. In addition, the usefulness of the proposed despeckle filters, in portable ultrasound systems and in wireless telemedicine systems still has to be investigated.

## 7.3 IMT segmentation

Ultrasound measurements of the human carotid artery walls were conventionally obtained by manually tracing interfaces between tissue layers. In this work, we have presented the Williams&Shah snakes segmentation technique for detecting the intima-media layer of the far wall of the CCA in longitudinal ultrasound images, after normalisation, despeckling, and despeckling and normalisation. An initialisation procedure for placing the snake in a close proximity to the area of interest was also presented.

We have tested and validated the Williams&Shah snakes segmentation technique on 100 longitudinal ultrasound images of the carotid artery using visual perception evaluation and the manual measurements made by two experts, a set of different evaluation criteria based on statistical measures, univariate statistical analysis, and error metrics as presented in Chapter 4.5, Chapter 5.7.4 and Chapter 5.7.5. The results of this study showed that no significant difference was found between the manual and the snakes segmentation measurements. This study also showed that the manual results were less dependent on the experts experience, the variability between experts was relatively low (see Table 6.12, and Fig. 6.10), and the IMT measurements were more reproducible on the NDS images (see Table 6.12-Table 6.14, Fig. 6.6-Fig. 6.12).

In the following sections we will discuss the results of the Williams&Shah IMT snakes segmentation method presented in Chapter 6.2.

### *7.3.1 IMT snakes segmentation*

Figure 6.6 showed that good snakes segmentation results were obtained on all images (NF, DS, N and NDS) when compared with the manual segmentation results (M, MN) from the two

experts (see also Table 6.11). A more careful examination of the images in Fig. 6.6 shows that the snakes segmentation results on the NDS and N images were closer to the manual segmentation results, than the segmentation results on the NF, and DS images.

Table 6.11 tabulates the results between the manual and the snakes segmentation measurements for the image shown in Fig. 6.6a. The $IMT_{mean}$ for the M and MN measurements for expert 1 was 0.74 mm, and 0.92 mm, and for the expert 2 was 0.82 mm, and 0.98 mm respectively. The standard deviation, $sd$, for the $IMT_{mean}$ on the NDS and N images was lower with 0.82±0.18 mm, and 0.82±0.19 mm respectively, whereas the $sd$, for the NF and DS images was larger with 0.82±0.22 mm and 0.81±0.21 mm respectively. Table 6.11 also shows that the manual IMT measurements have a larger range of values, ranging from 0.74-0.98 mm, whereas the snakes segmentation measurements are more concentrated for all cases NF, DS, N, NDS and range from 0.81-0.82 mm. The differences between all snakes segmentation measurements for the image in Fig. 6.6a, were very small and not easily identified by visual perception, thus a more detailed statistical examination was required.

The IMT snakes segmentation method in this study was performed on 100 longitudinal ultrasound images of the carotid artery bifurcation. In other studies reported in the literature the number of longitudinal ultrasound images of the carotid artery investigated were, 69 [253], 50 [178], 30 [86], [269], [270] and two [241]. The number of transversal images of the carotid artery were six [79], seven [64], and for the IVUS carotid images, 185 [73], 29 [220], and 20 [72], respectively. Finally, in [104] a discrete dynamic contour, which was initialized manually by the user, was used to segment 12 transversal MRI images of the carotid artery.

IMT segmentation was investigated by other researchers, on real longitudinal ultrasound images, [86], [178], [241], [253], [269], [270], transversal ultrasound images [64], [79], and IVUS [72], [73], [220], of the carotid artery. Specifically in [269] an active contour model improved by a multi resolution analysis was proposed using the Balloon snake [333] giving no details about the snake parameters used. In [104] a discrete dynamic contour snake model was proposed for transversal MRI of the carotid artery. An image energy term, the reciprocal of (3.5.7d), was added to the energy functional in (3.4.2). This snake, which was placed manually near to the area of interest, was applied on 12 MRI images with the snake parameters $\alpha = 1.0$, and $\beta = 0.5$. In [73] a snake model as proposed by Williams&Shah [124] was used to segment 185 IVUS images. The initial snake was placed manually and the snake parameters were chosen manually by the user. Furthermore, a discrete dynamic contour model was used in [64] on seven B-mode transversal images of the carotid artery. The snake functional was composed of internal and external forces as proposed in [333]. The initial snake contour was placed using an initial circle matching procedure, performed on the entropy image. The snake needed an average of 12 iterations to converge to its final position and the snake parameters were chosen manually by

the user. In [241] the Kass snake model [243] was used and applied on two longitudinal images of the carotid artery, with the snake parameters $\alpha = 0.6$, and $\beta = 0.4$. Finally in [253] dynamic programming was used to detect the boundaries in 69 longitudinal images of the carotid artery. In [178] multiscale dynamic programming with cost function optimization was used in 50 longitudinal ultrasound carotid images.

In other studies, where the task was to detect boundaries in the carotid artery, the segmented images were 185 transversal images of the carotid artery to detect the boundaries of the artery [73] based on active surface segmentation. In [79] a geometrically deformable model was applied to six transversal ultrasound carotid images to detect the lumen borders, where in [178], 50 longitudinal images of the carotid artery were used to detect the IMT based on multiscale dynamic programming. Two 3D ultrasound images of the carotid artery were used [55] to detect the blood borders based on a geometrically deformable model, and 69 longitudinal ultrasound images to detect the IMT based on snakes [253]. In [241] snakes were used on two longitudinal ultrasound images of the carotid artery, to detect the IMT borders, whereas in [220] texture analysis to detect the intima and adventitia layers in 29 IVUS images of the carotid artery was used. Finally 7 transversal images of the carotid artery were segmented in [222] based on a snake model to detect the lumen boundaries.

In different studies, where the task was to detect different image boundaries, the segmented images were, 44 ultrasound images of epicardial and endocardial as well as of a fetal skull and abdomen [265] segmented by many experts. In [231] snakes were used on 16 ultrasound images of the liver to detect tumor boundaries, and in [252] four real world images were employed to detect single and multiple objects using snakes. In [232] researchers used 56 mammographic images for detecting breast masses based on density slicing and texture flow analysis, whereas in [114] 33 3D CT images of the kidney were segmented using a deformable model to detect the kidney borders. In [185] one cardiac and one breast ultrasound image were segmented based on intensity inhomogeneity correction, whereas in [226] one ultrasound image of the gall bladder was segmented, based on an active contour model to detect the borders of the gall bladder. One MRI image of the heart was used in [116] to detect the borders of the left ventricle based on the GVF snake. In [189] a deformable model was proposed to segment six 3D cardiac ultrasound images of the left ventricle.

Although a lot of research work for the segmentation of IMT has been documented in the literature, there is currently no other study reported, where the IMT segmentation was estimated, on the original (NF), normalized (N), despeckled (DS), and normalized despeckled (NDS), longitudinal ultrasound images of the carotid artery bifurcation, as in our study. Furthermore, an accurate and effective snake initialization procedure for positioning the snake initial contour has not yet been proposed in the literature, and the initial contour estimation for the IMT, proposed

in this study, (see Chapter 5.7.2), maybe a further step towards the development of an accurate IMT snakes segmentation method for longitudinal ultrasound images of the carotid artery.

### *7.3.2 Univariate statistical analysis*

*Inter-observer variability*: The results from the univariate statistical analysis, performed in this study, were presented in Chapter 6.3.2 with Table 6.12.1 and Table 6.12.2. The smaller CV% (12.5%), as well as the smaller inter-observer error, *se* (0.08), in Table 6.12.1, for the NDS images, showed that the Williams&Shah snakes segmentation method, is more accurate, consistent, and reproducible when performed on the NDS images. Furthermore, the standard deviation, *sd*, for the $IMT_{mean}$, $IMT_{\min}$, $IMT_{\max}$, and $IMT_{median}$, was lower for the NDS images with 0.12 mm, 0.11 mm, 0.15 mm, and 0.12 mm respectively, whereas for the NF (0.14 mm, 0.13 mm, 0.2 mm, 0.14 mm), DS (0.13 mm, 0.13 mm, 0.19 mm, 0.13 mm), and N (0.13 mm, 0.14 mm, 0.17 mm, 0.12 mm) images was higher. The $IMT_{mean}$ snakes segmentation measurements performed on the NDS images (0.68 mm) were closer to all manual measurements (0.67 mm, 0.68 mm, 0.65 mm, 0.61 mm) made by the two experts, when compared with the segmentation results on the NF (0.70 mm), DS (0.69 mm), and N (0.67 mm), images respectively. The manual measurements reported in our study (0.67 mm, 0.68 mm, 0.65mm, 0.61mm for the first, M1F, MN1F and second expert M2F, MN2F) were smaller than the snakes segmented, and this finding was also reported in other studies. Specifically, the manual versus the snakes segmented IMT measurements reported in other studies were (0.88 mm vs 0.93 mm) [178], (0.88 mm vs 0.92 mm) [253], and (0.63 mm vs 0.72 mm) [269]. There is a large variation in the IMT measurements between the studies reported above and this study. This is due to the fact that the sample of images used in this study was mainly taken from asymptomatic patients. In other studies, images from symptomatic patients with larger IMT values were used. For both experts the Williams&Shah snakes segmentation method gave higher values for the IMT compared with the manual measurements as shown in Table 6.12.1. An explanation for this is given in Fig. 3.1b. The snakes segmentation procedure always marks the interface at the point of the maximal gradient, that is, the maximal change in echo intensity and this gives a larger IMT compared with the manual measurements.

Table 6.12.1 also showed that the standard deviation, *sd* for the $IMT_{mean}$, ($sd$ =0.16 mm, 0.17 mm, 0.18 mm, 0.17 mm for the manual segmentation cases M1F, MN1F, M2F, MN2F), was higher than in all snakes segmentation measurements ($sd$ =0.14 mm, 0.13 mm, 0.13 mm, 0.12 mm for the snakes segmentation cases NF, DS, N, and NDS). Furthermore it was shown that the coefficient of variation, $CV\%$, was also higher in the manual measurements ($CV\%$ =16.7, 17.1, 19.1, 17.2 for the manual segmentation cases M1F, MN1F, M2F, MN2F), than in all snakes segmentation measurements, ($CV\%$ =13.8, 13.4, 13.2, 12.5 for the snakes

segmentation cases NF, DS, N, NDS), showing consistent higher observer variability in manual IMT delineation. These findings were also reported in other studies [178], [253], [265], [270].

It was furthermore shown from Table 6.12.1, that the Williams&Shah snakes segmentation method yielded smaller inter-observer error, $se$, for all the snakes segmentation cases (NF 0.10, DS 0.09, N 0.09, NDS 0.08), compared to other studies, where higher values (0.176) were reported [178], [253]. The coefficient of variation, $CV\%$, of this study when compared to other studies [178], [265], [269], was higher for the manual measurements, but lower for the snakes segmentation measurements, which were performed on the NDS images. Specifically in [269], a $CV\% = 14\%$ was reported for the manual measurements made on 30 ultrasound longitudinal images of the carotid artery, whereas a $CV\% = 12.8\%$, was reported for the active contour snakes segmentation measurements improved by multi-resolution analysis. In [85], 30 longitudinal ultrasound images of the carotid artery were segmented using intensity diagrams by applying four different segmentation methods, namely dynamic programming, maximum gradient, model based, and matched filter, and the $CV\%$ was 2.24%, 2.85%, 9.93% and 6.34% respectively, whereas no results of the $CV\%$ for the manual measurements were given. In the studies reported above, i.e. [64], [85], [124], [178], [185], [265], [269], no despeckle filtering and image normalisation was carried out as performed in our study, whereas in [85] only the intensity diagrams for the artery lumen borders were plotted, and no visual results of the actual delineations of the IMT were given.

*Intra-observer variability*: In Table 6.12.2 the results of the intra observer variability performed by the two experts one year after the first visual examination are tabulated. The manual and manual normalised $IMT_{mean}$ measurements made by the first expert were 0.74 mm (M1S), 0.71 mm (MN1S) and by the second expert were 0.55 mm (M2S), and 0.57 mm (MN2S). The standard deviation $sd$ for the $IMT_{mean}$ were for the first expert 0.17 mm (on both the manual M1S, and manual normalised MN1S images), and for the second expert 0.11 mm, and 0.13 mm (M2S, MN2S). The coefficient of variation $CV\%$ for the first expert was 16.2% (M1S) and 16.8% (MN1S), and for the second expert was 14.0% (M2S) and 16.8% (MN2S). The inter-observer error, $se$, was for the first expert, 0.12 mm, and 0.11 mm, (on the original M1S and normalised MN1S images) whereas for the second expert were 0.08 mm, and 0.1 mm (on the original M2S and normalised MN2S images). It is shown from Table 6.12.2 that the first expert estimated the IMT with larger values while the second expert estimated the IMT with smaller values when compared with Table 6.12.1. The inter observer error, $se$, and the coefficient of variation, $CV\%$, in Table 6.12.2 were smaller in almost all cases when compared with Table 6.12.1. The results from Table 6.12.1 and Table 6.12.2 showed that high intra observer variabilities occur when manual measurements are made. It is documented in the literature that measurements of the inter-observer error, $se$, can be used as clinically useful

standard to measure the performance of image segmentation algorithms [265]. There are some results given in the literature for the intra observer variability for the IMT segmentation performed in carotid artery images. Specifically, in [44] the $IMT_{mean} \pm sd$ results of the first and second expert were 0.87±0.12 mm and 0.90±0.2 mm respectively. For the second set of measurements the results of the first and second expert were 0.85±0.11 mm and 0.85±0.17 mm respectively. It should be noted that direct comparisons between different studies, are difficult, due to the dependence on the measurement protocol, number and type of patients, tissue to be segmented and image quality.

In [184] a statistical approach for intra-coronary lumen segmentation was proposed and two experts delineated the lumen in 15 IVUS images for a second time. An inter-expert error was calculated for each expert indicating the difference in millimeters, between the first and the second set of delineations made by the same expert. The inter-expert error was 0.097 mm and 0.047 mm for the first and second expert respectively. The difference of the first expert was in our study 0.07 mm (0.74 mm-0.67 mm=0.07 mm) and 0.03 mm (0.71 mm-0.68 mm=0.03 mm) for the M and MN cases respectively. The difference of the second expert was 0.1 mm (0.65 mm-0.55 mm=0.1 mm) and 0.04 mm (0.61 mm-0.57 mm=0.04 mm) for the M and MN cases respectively. The difference for the same expert in this study was smaller on the normalized images, for both experts.

*Non-significantly different manual measurements*: Table 6.12.3 showed that the manual measurements made by the two experts were mostly significantly different showing high intra and inter observer variabilities.

*IMT versus age and blood pressure*: Figure 6.7 showed that a strong correlation between, the $IMT_{mean}$ and age, and the $IMT_{mean}$ and the systolic blood pressure, exists as reported in other studies [7], [99], [266], [318]. The IMT increases linearly for both men and women with increasing age and systolic blood pressure. The mean value for the $IMT_{mean}$, at the age of 60.5 was 0.66528±0.23831 mm (see Fig. 6.7a), whereas the mean IMT value, $IMT_{mean}$, in subjects with systolic blood pressure 125, was 0.63207±0.26377 mm (see Fig. 6.7b). The values presented in Fig. 6.7 were recorded from different subjects (with and without carotid disease) during a study made in a Cyprus village in 2004.

*Wilcoxon rank sum test, Hausdorff distance, covariance and MSE*: Table 6.13.1 and Table 6.13.2 showed that no significant differences (NS) between the manual and the Williams&Shah snakes segmentation method for all cases (M1F, MN1F, M2F, MN2F, NF, DS, N, NDS) were found using the Wilcoxon rank sum test. A significant difference was found only between the manual M2F and the manual normalised measurements MN2F of the second expert. The smallest Haussdorf distance, HD, was found between the N-M1F (3.4), NDS-N (5.2), DS-NF

(5.2), and NDS-N (5.2) images, which showed the minimum mismatch between these measurements. In [265] the HD value reported between the manual and the snakes segmented boundaries was 8.31 for transversal ultrasound images of the epicardial. The HD values reported in our study were better with N-M1F (3.4), NDS-MN1F (4.7), DS-NF (5.2), NDS-N (5.2) especially when despeckling and normalization was applied. Table 6.13.1 and Table 6.13.2, showed that higher covariance values, for the cases, M1F-MN1F (21.7), NF-DS (16.3), M2F-NDS (26.5), M2F-DS (25.8) and M2F-N (24.6) were obtained, showing that normalization and despeckling increased the covariance. The smallest MSE values in this study were obtained for the N-M1F (0.01) followed by the NDS-MN1F (0.02), showing that normalization and despeckle filtering achieves better results. The MSE between the manual and the snakes segmented boundaries, reported in other studies [185], [241], was 0.05 for longitudinal ultrasound images of the carotid artery. In [221] a GVF snake was evaluated on video sequences of rolling leukocytes where the MSE between the experts and the snakes segmented boundaries was 1.9. In [182] a cost function was proposed for differentiating between arterial wall and lumen in longitudinal ultrasound carotid artery images. The method was applied on five images of the carotid artery, recorded from patients at different ages, and the lowest MSE between the proposed method and the manually detected borders was 0.44 for a 40 year-old male population, and 0.89 for a 57 year-old male population. In [104] a discrete dynamic contour was proposed, which was initialized by the user, to segment transversal ultrasound images of the carotid artery, and the MSE was 0.958. The findings in this study showed that the manual segmentation method may be replaced by the Williams&Shah snakes segmentation method with the expert carrying out reliable snakes segmentation measurements.

*Histogram distributions*: Figure 6.8, where the histograms of the $IMT_{mean}$ values were presented, showed that the DS and the NDS distributions, in f), and h), respectively, were more robust than the rest of the distributions, showing more concentrated IMT snakes segmentation measurements. All the histograms illustrated that the $IMT_{mean}$ distribution was not Gaussian. The histograms for the snakes segmentation measurements showed a higher concentration around the $IMT_{mean}$ when compared with the manual segmentation measurements. The distributions of the NF, and N, in e), and g), were also well concentrated, whereas the distributions of the manual measurements M1F, MN1F, M2F, and MN2F in a)-d), were not well distributed. It is shown that a high variability between manual measurements is reported when inspecting the histogram distributions from the two experts. Histogram distributions were used in [227] in 27 longitudinal ultrasound carotid artery images of sheep. The IMT was recorded with two different methods namely by sonomicrometry and by a computerised device. The measurements from both methods were investigated by plotting the average diameter of the sheep's artery. It was found that the difference between methods followed a Gaussian distribution, and that the

computerised measurements were higher than those of the sonomicrometry. Furthermore it was shown that the new computerised device can be considered for clinical investigation.

*Box plots*: In Fig. 6.9, the manual segmentation measurements (M1F, MN1F, M2F, MN2F) from the two experts (Fig. 6.9a), and the Williams&Shah snakes segmentation measurements (NF, DS, N, NDS) (Fig. 6.9b) for the $IMT_{mean}$ were presented using box plots. The best box plot in Fig. 6.9a was recorded for the manual measurements made by the second expert, MN2F, on the manual normalized images. The range of values for this box was very small showing a better outlining consistency, the upper and lower range of data were shorter than the other distributions, and its skew was low, as the median value was almost in the middle of the box. Fig. 6.9a also showed that the IMT measurements made from the second expert (M2F, MN2F) were more concentrated than the first expert (M1F, MN1F). Furthermore, it was shown that the second expert tended to delineate the IMT with smaller values than the first expert, as the $IMT_{mean}$ values for the second expert were smaller in both the M2F and MN2F cases. In addition, the second expert delineated some values, which lay out of the range of the box plot (outliers) of the distributions M2F, and MN2F. All box plots for the Williams&Shah IMT snakes segmentation method, shown in Fig. 6.9b, exhibited a positive skew distribution, as the median value was nearest to the lower quartile, and the lower whisker was shorter. The shortest box was the NDS followed by the N distribution, which showed that the $IMT_{mean}$ values were less distributed for these images, than the other distributions. There were no outliers recorded for all four snakes segmentation cases (NF, DS, N, NDS), for the IMT delineation. The box plots presented in Fig. 6.9 showed, that the best distributions were given, for the manual normalised segmentation measurements, MN2F, and for the snakes segmentation measurements on the NDS images. In [265], box plots were used to compare the average boundary distances of three different segmentation algorithms with the manual delineated boundaries in cardiac images. It was shown that no significant difference between the performance of the three different segmentation algorithms exists. The average boundary distances between the epicardial and endocardial boundaries, of the three segmentation algorithms over 44 images were 3.87 mm, 4.58 mm, and 3.61 mm respectively. The authors proposed to use the third algorithm, as this was closer to the manual results performed by an expert. In [315] the $IMT_{mean}$ from 156 healthy volunteers was presented using box plots, between different ages using quartiles of age. It was shown that the $IMT_{mean}$, which ranged between 0.6 mm and 0.95 mm, increased linearly with age. Also box plots were plotted over the quartiles of a 10-year cardiovascular risk profile. It was shown that the $IMT_{mean}$ increases with systolic blood pressure. In [317] 24 longitudinal ultrasound images of the carotid artery from 11 young, and 13 old men were investigated. The $IMT_{mean}$ was plotted using box plots and it was 0.49 mm for

young men and 0.62 mm for old men. The IMT between old men with and without sympathetic nervous system activity was also compared. That comparison showed that the $IMT_{mean}$ for older men with sympathetic nervous system activity was higher (0.78 mm) than for those with no sympathetic nervous system activity (0.59 mm).

### *7.3.3 Regression and correlation analysis*

*Scatter plots*: In Fig. 6.10 scatter plots for the $IMT_{mean}$ values between the two experts on original and normalised images were presented. It was shown that the differences between experts were lower on the normalised images, as well as the manual measurements were better distributed, on the normalised images. Figure 6.10 also showed that the manual measurements for the $IMT_{mean}$ on the original images without normalisation (see Fig. 6.10a) tended to give higher values when compared with the measurements on the normalised images (see Fig. 6.10b). Specifically the manual measurements for the $IMT_{mean}$ for the first expert were 0.789 mm and 0.745 mm on the original and normalised images and for the second expert were 0.676 mm and 0.617 mm respectively. Figure 6.10 also showed that the confidence interval limits for the original images are larger (±0.315 mm) than the confidence interval limits of the normalised images (±0.256 mm). There are no other studies reported in the literature, where image normalisation, recently proposed in [322], was used prior to the delineation of the IMT.

*Pearson correlation, and correlation coefficient*: The Pearson correlation test presented in Table 6.14, showed that the strongest linear relation-ship exists between the NF-DS (0.98), DS-N (0.95), NF-N (0.95), DS-NDS (0.92), and N-NDS (0.91) images, whereas higher correlation coefficient values, $\rho$, were obtained for the cases NF-DS (0.97), DS-N (0.93), NF-N (0.93), and DS-NDS (0.92) respectively. The correlation coefficient, $\rho$, reported in other studies, was 0.98 [178] between the manual and a multiscale dynamic programming segmentation method for segmenting the lumen in longitudinal ultrasound images of the carotid artery. In [253] dynamic programming was used to segment the IMT in longitudinal ultrasound images of the carotid artery and the $\rho$, between the manual and the segmented boundaries, was 0.99. In [265] where cardiac ultrasound images were segmented, and compared with the manual measurements, the $\rho$, for the epicardial area was 0.95, and for the endocardial area was 0.91. In [269], an active contour model, with multi resolution analysis was proposed to segment the IMT in longitudinal ultrasound images of the carotid artery, and the $\rho$ between the manual and the segmented measurements was 0.90. Finally in [321], a dynamic programming approach was proposed to segment the wall and plaque from MRI transversal carotid artery images. The correlation coefficient $\rho$, between the manual and the segmented boundaries, was 0.92 for the detection of plaque thickness, and 0.96 for the detection of plaque area. Our results showed that

better correlation coefficient $\rho$, was obtained when normalization and despeckle filtering is applied, thus more accurate snakes segmentation results may be obtained.

*Regression lines*: Figure 6.11 showed that the best correlation coefficient was obtained between the MN1F-N (Fig. 6.11d), with $\rho = 0.75$, followed by the MN1F-DS (Fig. 6.11c), with $\rho = 0.73$, the M1F-N (Fig. 6.11g), and MN1F-NF (Fig. 6.11b), with $\rho = 0.71$, respectively. Furthermore, it was observed, that the correlation measurements for the NDS-MN1F (Fig. 6.11e), and NDS-M1F (Fig. 6.11h), were more concentrated around the regression line with almost no outliers, showing better delineation results on the NDS images. Correlation analysis was also used in other studies. For example, in [178], [253], correlation plots were used to assess the variability between the manual and a dynamic programming method for delineating the IMT in ultrasound longitudinal carotid images. The correlation coefficient found in both studies was 0.98, where only one observer was used to delineate the images. In [72] the correlation coefficient between the manual and snakes segmentation measurements for the segmentation of lumen and plaque area in carotid artery IVUS images was 0.94. In [256] correlation analysis was used to compare analogue and digital technologies for the IMT measurements. In [319] to compare the systolic diameter in carotid artery ultrasound images measured with conventional M-mode and SonoCT M-mode imaging where the correlation coefficient was 0.94. The correlation coefficient in [319] between IMT and age was 0.60. Finally in [317] the correlation coefficient between the IMT measurements and a muscle sympathetic nerve activity in 63 patients were compared and it was 0.82. There were no other studies reported in the literature where correlation analysis was used to compare an IMT segmentation method on N, DS and NDS ultrasound longitudinal images of the carotid artery.

*Bland-Altman plots*: As illustrated in Fig. 6.12, the Bland-Altman plots [264], [282], showed that while all but only a few of the data points lie within two sigma, $2\sigma$, of the mean, there was a large spread in the data points. Specifically, for both experts the best plots were obtained for the NDS images (see Fig. 6.12m, n, o, p), whereas the difference between the segmentation method and the manual measurements of the first expert, M1F, was 0.02 (see Fig. 6.12m), and for the manual measurements of the second expert, M2F, was 0.01 (see Fig. 6.12o). The standard deviation, for these cases, was 0.25 (see Fig. 6.12m), and 0.33 (see Fig. 6.12o) respectively. There was also a negative bias, estimated by the mean difference, which showed that on average the snakes segmentation algorithm overestimates the area relative to normal delineation. The Bland-Altman plots presented in Fig. 6.12 showed that, the best plot was obtained for the NDS images, with smaller differences between experts. Figure 6.12 also showed that the relative differences in IMT values remained constant in all cases, as the IMT increased from 0.4 mm, the lowest, to 0.9 mm, the highest value. Although there was some variability in the measurements of IMT with limits of agreement that ranged from –0.45 mm to

0.2 mm, with almost all points within these limits. The lower variability was observed for the M1F-NDS images and MN1F-NDS images from the first expert (Fig. 6.12m, n). The Bland-Altman test presented in Fig. 6.12 is a plot of the difference of two measurements against the average of the two measurements. It was also used in other clinical studies [175], [190], [202], [227], [240], [256], [257], [315]. The Bland-Altman test was also used in [175] to compare the results of manual and automated detection in myocardial borders, the segmentation results of the left and right ventricle in cardiac images [190], and the segmented border values between manual and automated detection in brachial ultrasound images [257]. There were no other studies reported in the literature, where this test was used to compare the manual and the snakes segmentation measurements of the IMT in carotid artery images.

### *7.3.4 Summary findings on IMT segmentation*

The most important findings of our study were the following:

a) There was no significant difference of the IMT measurements between the manual and the snakes segmentation measurements (see Table 6.13).

b) For the NDS images, better snakes segmentation results, with smaller inter-observer variability, $se$, smaller coefficient of variation, $CV\%$, (Table 6.12.1, Table 6.12.2), better histogram distributions (Fig. 6.8), better box plots (Fig. 6.8), better HD, covariance and MSE (Table 6.13), better correlation coefficient (Table 6.14, Fig. 6.11), and better Bland-Altman test (Fig. 6.12), were obtained.

Furthermore it is noted that better manual segmentation results were also obtained with lower standard deviation, $sd$, inter-observer error, $se$, coefficient of variation, $CV\%$, (Table 6.12.1, Table 6.12.2), better scatter plot (Fig. 6.10), good correlation coefficient (Fig. 6.11), and good Bland-Altman plot (Fig. 6.12), on the manual normalized (MN1F), images when compared with the manual segmentation results before image normalization (M1F).

The comparison of a new method against an established one has often been evaluated inappropriately through the use of the correlation coefficient, $\rho$, between the results of the two methods. Correlation coefficient, measures the strength of a relation between two variables, not the agreement between them. Moreover, correlation depends on the range of the variables measured, with wider ranges leading to better correlation [256], [280], [282]. More often, two methods measuring the same variable will be related, and thus the test of significance may be irrelevant regarding the question of agreement. Thus a high correlation coefficient between two methods may still incorporate sufficient disagreement to decide whether a method is better than another. The analytical approach of Bland Altman [264], [280], as used in this study, is more appropriate for the evaluation of the consistency of a new method of measurements compared with an established method. Through the use of this approach it was shown (see Fig. 6.12l-p)

that, between the MN1F and the NDS a small discrepancy, of around 0.05 mm was reported. On this basis the two methods (manual and snakes segmentation method), can be considered interchangeable. However, because the repeatability of the manual measurements, (intra- and inter-observer variability), was larger than this of the Williams&Shah snakes segmentation measurements, we conclude that the replacement of the manual with the snakes segmentation system is possible.

## 7.4 Plaque segmentation

Four different plaque snakes segmentation methods, for the segmentation of atherosclerotic carotid plaque in longitudinal ultrasound images were evaluated and the results were presented in Chapter 6.4. The four different snakes segmentation methods were the Williams&Shah (see Chapter 3.4), Balloon (see Chapter 3.5.1), Lai&Chin (see Chapter 3.5.2), and the GVF (see Chapter 3.5.3). The four different plaque snakes segmentation methods, use the blood flow image firstly to detect the initial contour of the plaque (see Chapter 5.8.2), despeckle filtering (despeckle with filter *lsmv*) to filter the multiplicative noise from the image (see Chapter 2.3.1.1), and then snakes to deform the initial contour for best fit of plaque boundaries. The accuracy and the reproducibility of the four plaque snakes segmentation methods was tested using 80 plaque longitudinal ultrasound images of the carotid artery, and the results were compared with the manual delineations of an expert. The comparison showed that the Lai&Chin snakes segmentation method gave better results with no manual correction needed in most of the cases. The TPF, and TNF, for the Lai&Chin snakes segmentation method, were 82.70%, and 80.89%, respectively. Better FNF, and FPF, were given by the Balloon with 13.90% and, 5.40% respectively. The Lai&Chin snakes segmentation method yielded better sensitivity, R, and precision, P, whereas better specificity, Sp, and effectiveness measure E, were given by the Balloon, followed by the Lai&Chin snakes segmentation method. The four snakes segmentation methods presented in this work represent the most widely used algorithms in computer image analysis in the recent years.

In the following sections we will discuss the results of the four plaque snakes segmentation methods, presented in Chapter 6.4.

### *7.4.1 Plaque snakes segmentation*

The snakes segmentation methods were investigated on real ultrasound images of the carotid plaque (Fig. 6.13, Fig. 6.14, Fig. 6.15). Figure 6.13 showed that the results of the manual segmentation method and the results of the four snakes segmentation methods were visually similar suggesting that all four segmentation methods may be used to complement the manual segmentation. Figure 6.13, Fig. 6.14 and Fig. 6.15 showed that the Lai&Chin snakes

segmentation method (yellow contour) was visually closer to the manual segmented boundaries delineated by the expert.

The research on plaque segmentation of carotid artery ultrasound images presented in the literature, is very limited. This is also shown from the small number of publications made in this area, which are mostly reported in conference proceedings. Specifically, in [46], [47] an unknown number of transversal ultrasound images of the carotid artery were used to detect the lumen borders of the carotid artery. The proposed method consisted of four stages, namely pre-processing, quantization, morphological contour detection, and contour enhancement. In the pre-processing step a histogram equalization was performed, and a median filter was applied for despeckling the image. The segmentation results were not that accurate. In [100] a dynamic balloon model [333] represented by a triangular mesh was applied for detecting the plaque borders on two 3D ultrasound carotid images where the initial contour was placed manually. The plaque borders were detected through reconstruction of the inner lumen borders. The result was a surface indicating the outline of the lumen.

Some other researchers applied their techniques on MRI images. Specifically a segmentation method for the arterial walls and plaque in transversal MRI images based on dynamic programming was proposed in [321]. The method was applied on 62 images and the plaque thickness mean absolute error between the manual and the segmented plaque borders were 0.3±0.1 mm and the correlation coefficient between the manual and the computer detected plaque area was 0.92. In [61], the plaque borders on 22 transversal MRI carotid images were segmented, based on the mean shift density estimation algorithm. A misdetection rate for the plaque area of 13.5% was reported verified with histology. In [191] an active contour segmentation method was applied on 20 MRI transversal carotid images to detect the lumen and the outer wall boundaries of the artery by using the GGVF force field [258]. The user placed the snake initial contour manually. The coefficient of variation $CV\%$, for the wall thickness was (9.54±8.81)%, which is considered to be rather large.

A number of artificial and real world images were segmented in [53] using snakes, where the snake initial contour was placed manually by an expert and some visual results were presented. Finally in [192], a segmentation framework was described for manually segmenting 24 transversal MRI images of the carotid artery.

There were no other studies reported in the literature, where snakes have been used to detect the plaque in longitudinal ultrasound images of the carotid artery. Thus the method, proposed in this dissertation presents the first snakes segmentation method for these images.

The four plaque snakes segmentation methods were further evaluated, on one longitudinal ultrasound image of the carotid artery, based on the number of iterations and the computational time (see Table 6.15). The performance of all four methods was very similar. The number of

iterations for the Lai&Chin, Balloon, GVF, and Williams&Shah snakes segmentation method were 13, 14, 15, and 15 iterations, and the corresponding convergence time was 11.71 sec, 12.31 sec, 12.73 sec, and 13.03 sec respectively. The Lai&Chin segmentation method gave the lowest computational time (11.71 sec), and the smallest number of iterations (13 iterations).

In the literature, the computational time was used to evaluate a weighted average segmentation method based on the time required for segmenting the carotid plaque in transversal MRI images. The time reported for the plaque segmentation method was 19 sec [192]. The number of iterations, and the computational time, were also used in other studies to evaluate the convergence of the Williams&Shah snakes segmentation algorithm on real world and artificial images [124], where the expert placed the initial contour manually. The times reported in [124], for the segmentation of a square, box, bottle, and a cup, were 0.25 sec, 1.87 sec, 1.22 sec, and 0.7 sec, where the number of iterations was 2, 15, 11, and 7 respectively: The lower computational time, and number of iterations reported in [124], compared to the results of this study was due to the fact that on real world images, borders are clearly defined and with a low noise component. This is the reason for the fast snakes convergence.

Figure 6.16 showed that the total snake energy term for the Lai&Chin snakes segmentation method, TSELC, required less iterations (13) to converge, while for the Balloon, GVF, and the Williams&Shah, the number of iterations were 14, 15, and 15, respectively.

The plots of the snake energy terms for the Williams&Shah snakes segmentation method, presented in Fig. 6.17, showed that almost all energy terms, (except the NIE), reached their minimum value, after 11 to 15 iterations, until the snake converged to its final position. The small number of iterations was achieved due to the snake initialisation procedure proposed in this study, which positioned the initial snake contour as close as possible to the actual plaque boundary. It was also shown, that the normalised image energy term, NIE, converged faster, (after 2 to 3 iterations), than the other snake energy terms.

The Lai&Chin plaque snakes segmentation method [248], which was based on variable snake parameters, $\alpha$, and $\beta$, gave the best segmentation result, as illustrated in Fig. 6.13, Fig. 6.14, and Fig. 6.15. Figure 6.18 showed that almost after six, and five iterations of the Lai&Chin snake, the final values of the parameters $\alpha$, and $\beta$, were reached respectively. The snake parameters, $\alpha$, and $\beta$, were calculated by taking into consideration the variance, $\sigma^2$, and the noise variance, $\sigma_n^2$, of the gray values around each snake point (see 3.5.5, 3.5.6).

The segmentation approach proposed by Lai&Chin also addressed initialisation, and showed how a Generalised Hough Transform (GHT) can be used to initialise a snake contour [155]. There are however limitations using the GHT for initialisation such as the huge memory storage required, prior knowledge of the object to be segmented, and an estimate of the number of

templates that should be enumerated [207] according to the variation of the desired shape of the object. Some researchers used other regularisation parameters to improve the snakes segmentation method [53], [237], where the length of the snake was taken into account for the internal snake energy, $E_{int}$, calculation in (3.4.4). They have applied their methods on a number of artificial shapes, but results showed, that these were not better than the conventional snakes segmentation method initially proposed by Kass [243] and later by Williams&Shah [124]. Furthermore, prior knowledge about the shape of the object to be segmented was also required. Some other researchers included in their proposed snakes segmentation techniques, factors that attracted contours to regions using statistical models [244], or texture [245], to complement operators that combine edge detection with region growing. More specifically, in [245] a new region energy term was added to the snakes functional and the method was applied on one MRI image and two artificial images. The method was carried out successfully provided that both a small part of the snake overlapped the desired region and that the statistical parameters were appropriate. This makes the use of such a snake not suitable for our application as, the placement of the initial contour should be made in such a way, so that it crosses the boundary of interest. Furthermore prior knowledge of statistical parameters is needed for a statistical snake, which must be given empirically by the expert. Also the snake model can be generalized to higher dimensions generating for example 3D snake surfaces [246].

### *7.4.2 Evaluation of plaque segmentation methods*

The four plaque snakes segmentation methods were further investigated using the TPF, TNF, FPF, and FNF (see Table 6.16), the Williams index, and the overlap index, and showed that the Lai&Chin snakes segmentation method performed better. Therefore, it may be assumed that the Lai&Chin snakes segmentation method gave results, which were more comparable to the manual delineation procedure.

Specifically, the best TNF and TPF fractions were given by the Lai&Chin snakes segmentation method with 80.89%, and 82.70%, whereas the best FPF, and FNF, fractions were given by the Balloon snakes segmentation method [333], with 5.40% and 13.90% respectively. The similarity kappa index, KI, and the overlap index, were for the Lai&Chin snakes segmentation method, 80.66% and 69.30% respectively, which were satisfactory and better than the rest of the snakes segmentation methods, compared in Table 6.16. The GVF snakes segmentation method [116], gave the lowest similarity kappa index, KI, (77.25%), and the lowest overlap index (66.60%).

There were no other studies reported in the literature, where the TPF, TNF, FPF, and FNF fractions were used to investigate the performance of a plaque segmentation technique in longitudinal ultrasound images of the carotid artery.

The TPF, TNF, FPF, and FNF fractions were also used in other MRI and CT studies to evaluate the segmentation results. Specifically in [61] the FPF was used where, 22 MRI transversal carotid artery images were segmented with the mean-shift density estimation algorithm, in order to specify histological differences between tissue types in these images. The FPF values for the plaque tissue detected were 13.5% for plaque, where we have reported FPF values of 5.86% with the Lai&Chin snakes segmentation method. In [43] 77 CT images of pelvis from 11 patients were segmented using a watershed morphological transformation. The segmentation results were compared against those produced by five experts. The TPF, FPF, kappa index, and overlap index were 85%, 17%, 93% and 87% for the segmentation of the bladder. The results were better than in this study. This is because the images used were CT images, which have better resolution than ultrasound images, and the borders of the bladder were more clearly defined. Furthermore the experts were allowed to edit the final segmentation results. In [362], 22 CT bladder scans were segmented using image thresholding and then manually segmented by an expert. The TPF, TNF, FPF, FNF values were, 72.70%, 55.90%, 6.66%, and 8.90% respectively. Furthermore, a segmentation method using multiscale morphological operation and entropy thresholding was proposed in [42]. An unknown number of X-ray mammogram images were segmented and the results were evaluated and confirmed by an expert. The TPF, FPF, and FNF fractions were 93.75%, 6.25%, and 3.75% respectively.

The four different plaque snakes segmentation methods were further investigated, based on the sensitivity, R, specificity, Sp, precision, P, the effectiveness measure, F, and the results were presented in Table 6.17. The best sensitivity, R, and precision, P, was given by the Lai&Chin, whereas best values for specificity, Sp and F, were given by the Balloon snakes segmentation method. Furthermore in some other studies R, and Sp, were investigated using ROC analysis [10], [42], [177].

The evaluation of the four plaque snakes segmentation methods based on box plots (see Fig. 6.19), showed that the box plots of the TPF, in Fig. 6.19a, exhibited a negative skew distribution, as the median value was nearest to the upper quartile, and the lower whisker was larger. Some outliers were found for the Williams&Shah, Balloon, and GVF snakes segmentation methods, whereas the Lai&Chin exhibited no outliers. The smallest box in Fig. 6.19a, was for the Williams&Shah snakes segmentation that exhibited less distributed measurements than the others, and the largest box was the box for the Lai&Chin snakes segmentation method. The smallest box for the TNF, shown in Fig. 6.19b was found for the Lai&Chin snakes segmentation method, whereas the largest was found for the GVF snakes segmentation method. Figure 6.19b also showed that the GVF snakes segmentation method demonstrated no outliers. The smallest box for the FPF, in Fig. 6.19c was for the Balloon snakes segmentation method, where the largest box was demonstrated for the Williams&Shah snakes segmentation method. All boxes exhibited a negative skew distribution with the largest

demonstrated by the Williams&Shah, and the Lai&Chin snakes segmentation methods. No outliers were demonstrated for all four snakes segmentation methods for the FPF fraction. In the case of the FNF, shown in Fig. 6.19d, the smallest box was given by the Balloon snakes segmentation method, where no outliers were given for the Lai&Chin. The best box for the KI, and the overlap index, were given for the Lai&Chin snakes segmentation method (see Fig 6.21e, and Fig. 6.19d). Furthermore it was shown that the boxes for the GVF, and Williams&Shah snakes segmentation methods, in Fig. 6.19f, exhibited a larger distribution. Multiple comparisons from Fig. 6.19 showed that the Lai&Chin snakes segmentation method was better. Specifically a better TNF, (Fig. 6.19b), FPF, (Fig. 6.19c), Williams index, KI, (Fig. 6.19e), and overlap index, (Fig. 6.19f), were obtained by the Lai&Chin snakes segmentation method.

The evaluation of the four plaque snakes segmentation methods based on ROC curves (see Fig. 6.20), showed that the best ROC curve was obtained for the Lai&Chin snakes segmentation method. The area under this curve was larger than the others. There are no other studies reported in the literature, where the TPF, TNF, FPF, FNF, box plots, and ROC curves, were used to evaluate the segmentation performance of a plaque snakes segmentation algorithm in longitudinal ultrasound images of the carotid artery.

### *7.4.3 Summary findings on plaque segmentation*

The results of this study showed that the segmentation method of Lai&Chin is the most appropriate to segment the plaque from ultrasound longitudinal images of carotid artery after despeckle filtering with the *lsmv* filter and after image normalisation.

We have outlined in Chapter 5.8 some of the limitations using the blood flow image to estimate the initial plaque contour for the snakes segmentation algorithm, which was in some cases not satisfactory. In some images, however, the blood covers areas of the tissue and the colour does not always fill up regions where the blood has a low speed. In these cases, the initial contour was not correctly estimated and thus the outcome of the segmentation was greatly influenced. Some other limitations of the proposed method, include the presence of acoustic shadowing and speckle noise, which hinders the visual and automatic analysis in ultrasound images. Such images, with bad visual perception, were neither included in this study [358], nor were they delineated by the experts. We have also excluded from our segmentation experiments, type I and type V plaques [208], [322]. These plaques show extensive echolucency and calcification respectively as explained in Chapter 5.8. This problem is inherent to ultrasound and could be only resolved by using other techniques, like MRI [94]. Backscattered ultrasound is also angle dependent. During the recording of the images a standard recording technique was used to adjust the position of the probe so that the ultrasound beam was at right angles to the arterial wall. This improved IMT and plaque visualisation. Moreover, the new spatial compound imaging technique might optimise further carotid plaque imaging [14], [188], [193].

As discussed in this Chapter, not much research has been made towards the direction of the segmentation of carotid plaque from longitudinal ultrasound images, and there were only very few publications reported in this area, mainly for segmenting the plaque from transversal ultrasound images. Initial attempts, for segmenting the atherosclerotic carotid plaque, were made on IVUS images [72], [184], where the insertion of a catheter in the patients artery for acquiring the IVUS images, posed a certain risk to the patient. These approaches were based on graph searching, which required that the expert must provide the initial plaque border contour. Furthermore, a time consuming methodology based on the Balloon snake [333] was proposed in [100] for 3D ultrasound carotid artery images, by triangulating the image in a finite element mesh. The method proposed in [64], for transversal, as the one proposed in [41], for longitudinal images of the carotid artery, were time consuming and results were not that accurate. Furthermore, in recent studies [46], [47], where morphological processing was applied, the results were not accurate and the expert had no interaction with the system. Some attempts were made from other researchers to segment the carotid plaque in MRI by using a mean shift density estimation algorithm [61], the GVF field [191], active contours [191], dynamic programming [321], and morphology operations in CT scans [362]. In all of the above studies, the initial snake contour was placed manually, and a smaller number of images compared with this study were tested.

The method presented in this dissertation, is to the best of our knowledge the first computerized approach for plaque segmentation in longitudinal ultrasound images of the carotid artery. Such a computerized method cannot only reduce significantly the time required for the image analysis, but also it can reduce the subjectivity that accompanies manual delineations and measurements. The method will be further evaluated on a larger number of ultrasound images and on multiple experts' evaluation. Furthermore, it is expected that the segmentation method will be incorporated into an integrated system enabling the texture analysis of the segmented plaque, as documented in [10], providing an automated system for the early diagnosis and the assessment of the risk of stroke.

## 7.5 Proposed system

Based on the results obtained in this study an ultrasound processing and analysis system for the carotid artery is proposed. This system can be easily implemented based on the following procedure:

a) Acquiring an ultrasound image

b) Digitize the image with 576x768 (at least 16 pixels per mm) and 256 (at least) gray level distribution

c) Normalize the image

d) Despeckle the area of interest or the whole image with the *lsmv* filter

e) In the case of IMT segmentation

   i. Select the B-mode image

   ii. Mark the region of interest

   iii. Estimate an initial IMT snake contour

   iv. Apply the Lai&Chin snake to segment the IMT

   v. Measure and plot the IMT

   vi. Compute the $IMT_{mean}$, $IMT_{\min}$, $IMT_{\max}$, and $IMT_{median}$ statistics

f) In the case of the plaque segmentation

   i. Select the B-mode and the blood flow images

   ii. Cross correlate the two images (B-mode and blood flow images from point i above) and extract the edge borders of the blood flow area (edge image)

   iii. Mark a region of interest on the edge image

   iv. Estimate of the initial plaque contour

   v. Map the initial plaque contour on the B-mode image

   vi. Apply the Lai&Chin snake to segment the plaque

   vii. Measure and plot the final plaque contour.

The proposed system can easily be applied for the collection of more cases. In addition the proposed system could be an integrated part of a computer aided diagnostic system, where the plaque texture features are computed, that can subsequently be fed to a neural network or statistical classifier for computing the type or class of the plaque [10].

# *Chapter 8*

# *Conclusions and Future Work*

# CHAPTER 8: CONCLUSIONS AND FUTURE WORK

## 8.1 Conclusions

Stroke is one of the most important causes of death in the world and the leading cause of serious, long-term disability. It is usually caused by atherosclerosis, the hardening of the artery walls. There is therefore an urgent need for better techniques of diagnosing patients at risk of stroke, and deliver guidelines for the choice of treatment. Ultrasound measurements of the intima media thickness (IMT) and the atherosclerotic carotid plaque in the carotid artery are important factors to consider for a patient at risk of stroke, and are used today as validated measures for atherosclerosis.

The objective of this work was to carry out a comparative evaluation of despeckle filtering techniques and to develop a segmentation system for detecting the intima-media layer at the far wall of the CCA and the borders of the atherosclerotic carotid plaque in 2D longitudinal ultrasound images of the carotid artery. To the best of our knowledge, although a number of techniques have been proposed for IMT segmentation, no similar system has been developed for segmenting the atherosclerotic carotid plaque.

A total of 11 different despeckle filters were developed in this work based on local statistics, median filtering, linear scaling, pixel homogeneity, geometric filtering, homomorphic filtering, anisotropic diffusion, speckle anisotropic diffusion, non-linear coherence diffusion and wavelet filtering. We have evaluated despeckle filtering on 440 (220 asymptomatic and 220 symptomatic) ultrasound images of the carotid artery bifurcation, based on visual evaluation by two medical experts, texture analysis measures, and image quality evaluation metrics.

The IMT segmentation method developed in this work is based on the Williams&Shah snake, and utilizes an automatic initial contour estimation for the IMT and plaque borders. Segmentation was carried out on the original, despeckled, normalized and normalized despeckled images. The IMT segmentation technique was tested and validated on 100 longitudinal ultrasound images of the carotid bifurcation, based on manual measurements and visual perception made by two vascular experts, univariate statistical analysis, and correlation analysis.

Four different plaque snakes segmentation methods were developed based on the Williams&Shah, Balloon, Lai&Chin, and the GVF algorithms. The initial plaque contour was estimated using the B-mode and the blood flow images. The initial contour was mapped on the original B-mode image, which was despeckled and normalized. The contour was then deformed by the snake for best fit of the plaque boundaries. The method was tested on 80 longitudinal ultrasound images of the carotid artery. We have validated the four plaque snakes segmentation

methods using the manual measurements made by a vascular expert, the performance of the algorithms, and ROC analysis.

A despeckle filter based on local statistics (*lsmv*) improved the class separation between the asymptomatic and the symptomatic classes, gave only a marginal improvement in the percentage of correct classifications success rate based on texture analysis and the kNN classifier, and improved the visual assessment by the experts. It was also found that the *lsmv* despeckle filter can be used for despeckling asymptomatic images where the expert is interested mainly in the plaque composition and texture analysis, whereas a geometric despeckle filter (*gf4d*) can be used for despeckling of symptomatic images where the expert is interested in identifying the degree of stenosis and the plaque borders.

The IMT mean ± standard deviation snakes segmentation results were $0.7 \pm 0.14$ mm, $0.69 \pm 0.13$ mm, $0.67 \pm 0.13$ mm, $0.68 \pm 0.12$ mm, for the original, despeckled, normalized, and normalized despeckled images respectively. The manual ± standard deviation results for the first expert were, $0.67 \pm 0.16$ mm, $0.68 \pm 0.17$ mm, and for the second expert were, $0.65 \pm 0.18$ mm, $0.61 \pm 0.17$ mm on the original and normalized images respectively. The results showed that there was no significant difference between all the snakes segmentation measurements and the manual measurements. Furthermore, the snakes segmentation results were more reproducible than the manual measurements on the normalized despeckled ultrasound images.

The plaque segmentation results showed that, the Lai&Chin snakes segmentation method that is based on variable snake parameters, gave results closest to the manual delineation procedure, compared with the results given by the Williams&Shah, Balloon, and the GVF, snakes segmentation methods. Specifically the Lai&Chin segmentation method, gave a better true positive fraction (82.7%), and true negative fraction (80.9%), a better kappa index (80.7%), and overlap index (69.3%). The area below the ROC curve was 0.88, 0.85, 0.82, and 0.76 for the Lai&Chin, Balloon, Williams&Shah, and GVF snakes segmentation method respectively, with the largest area under the ROC curve obtained by the Lai&Chin snakes segmentation method.

The results of this study, suggest that the first order statistics despeckle filter *lsmv*, may be applied on ultrasound images to improve the visual perception and automatic image analysis, and the Lai&Chin snakes segmentation method for the IMT and plaque segmentation. These methods complement and assist the experts in the assessment of the structure and morphology of carotid artery.

The proposed despeckling and segmentation methods will be further evaluated on a larger number of ultrasound images collected from different neurovascular clinics and experts in the EU. Furthermore, it is expected that both methods will be incorporated into an integrated system

enabling the texture analysis of the segmented plaque, providing an automated system for the early diagnosis and the assessment of the risk of stroke.

## 8.2 Future work

Significant technical and clinical progress can still be made in the field of image despeckling and segmentation, to advance our understanding of the diagnosis and treatment of atherosclerosis. Future work is proposed in the following areas: snakes initialisation, snake parameters estimation, level sets and snakes, neural and fuzzy image processing, 3D imaging, video segmentation, and data mining.

*Snakes initialisation*: Another area where more work is required is the positioning of the initial snake contour. As explained in Chapter 5, the inaccurate positioning of the initial snake contour may lead to wrong segmentation results. Therefore a more accurate and robust snake initialisation method should be investigated. The initial snake contour estimation used in this work requires the blood flow and the B-mode image, as explained in section 5.8.2. A new snake initialisation procedure using only the B-mode image will be further investigated. Preliminary investigation has shown that this procedure can be implemented as follows. The expert selects a region of interest on the B-mode image including the plaque, the region is then despeckled, converted to binary, and dilated. The contour of the dilated region is extracted and mapped on the B-mode image to form the initial snake plaque contour. The snake could be adapted with any of the four segmentation techniques mentioned in this study.

*Snake parameters estimation*: Genetic algorithms (GAs) are stochastic global search and optimization methods that mimic the metaphor of natural biological evolution [267], [310], [311], [312]. GAs operate on a population of potential solutions applying the principle of survival of the fittest to produce successively better approximations to a solution [268]. The disadvantage of GAs is the time required for searching the optimum solution thus making such techniques not suitable for interactive application, such as image filtering and segmentation.

Generally the adjustments of the snakes functional parameters ($\alpha$, $\beta$, $\gamma$) are carried out by trial and error [241], [246], [252], [260]. This is a very difficult task. The use of GAs to estimate the optimal parameters, $\alpha$, $\beta$, and $\gamma$, for the snake model in (3.4.2) was investigated by [69], [306]. Other researchers applied GAs for the segmentation of 3D medical images [302], finding the parameters of a Balloon model [304], to optimize deformable surface meshes [305], to segment real world images [306], [307], and for function optimization [308], [309]. Furthermore, an active contour model for the segmentation of brain tumors was proposed [70], where GAs, were used to estimate the initial contour of the snake based on wavelet preprocessing. It would be therefore interesting to investigate further the use of GAs for

optimizing the parameters of the snakes segmentation algorithm and compare the optimization result with the solution proposed in this study using the Lai&Chin snakes segmentation method.

*Level sets and snakes*: As noted in Chapter 3 current level-set techniques have difficulties in representing open curves [97], [111]. They have also some advantages. First, they are independent of the parameterization of the evolving contour, thus there is no need to add or remove nodes on the evolving contour or adjust the spacing of the nodes [179]. The evolving contour can automatically change topology (split or merge), when multiple objects are to be segmented such as in the segmentation of blood vessels [221]. A level set approach may therefore be investigated for simultaneously segmenting the far and the near wall of the carotid artery. Additionally, for the segmentation of the IMT in the carotid artery, where open curves are required a level set approach may be further investigated.

*Neural and fuzzy image processing*: Neural networks have been used in a variety of image processing tasks, such as in image pre-processing [144], image reconstruction, image restoration, image enhancement [145], data reduction [195], feature extraction [62], image segmentation [158], object recognition [63], optimization [144], and image understanding [161]. Many neural network approaches have been presented that segment images based on feed forward neural networks, self-organising maps, probabilistic neural networks [144], and other [161], and also for the segmentation of MRI using active contour models [39].

Fuzzy logic poses the ability to mimic the human mind to effectively employ modes of reasoning that are approximate rather than exact. When information in ultrasound images is not well defined, inaccurate or ill defined, fuzzy logic may be employed [198]. Over the past years, a number of fuzzy segmentation approaches have been proposed to achieve tissue differentiation in MRI [122], and in the domain of natural images for edge detection and segmentation [118]. Fuzzy segmentation, based on a fuzzy-ruled based system, has been also applied for optical character recognition [224], and to white blood cells segmentation [276] for counting the different blood cells classes in bone marrow microscopic images. Furthermore, the fuzzy reasoning approach [113] was used to perform detection and tracking of moving objects for image segmentation, edge extraction and image enhancement using a probabilistic neural network classifier and optimised by GAs.

The use of neuro-fuzzy snakes segmentation of the carotid artery still remains to be investigated.

*3D Imaging*: Another interesting area of future research is to apply the methods proposed in this study in 3D ultrasound images, which may improve the diagnostic performance [55], [77]-[79], [96]. Although 3D vascular imaging is very promising in revealing vascular structure and pathology, more work is needed in the directions of fast and accurate free hand scanning, automated or semi-automated segmentation, real-time and user friendly visualisation [112], and

3D texture analysis [95]. Advances in these directions will enable the wide spread use of 3D imaging in clinical practise.

*Video segmentation*: The advent of powerful video systems nowadays allows medical video to supplement earlier imaging techniques, where medical video is used in various medical image analysis applications [4], [7]-[9]. Video imaging in medicine is important not only because it allows the expert to review the procedure and re-evaluate the initial diagnosis, but also because of its application in medical education [114], [135]. Another advantage of medical video imaging is the possibility of having multiple views. The multiple views allow a 3D reconstruction of the carotid artery (see also 3D imaging above) [95], [183], [230], [336]. To the best of our knowledge, video segmentation in carotid arteries has not yet been investigated. Specifically, video segmentation of the carotid artery may be used to estimate the motion, find and track the boundaries of the plaque, classifying the motion of the plaque in normal or abnormal, and thus finding normal and abnormal plaques [71].

Medical image video transmission remains the main drawback in mobile and wireless networks. Medical images are of high volume and have to be compressed in lossless (bit preserving) manner in order to maintain its diagnostic value unaffected. Different standards have been introduced and were applied for wireless video communication, where the most popular are the MPEG-2 and MPEG-4. In terms of bandwidth requirements, MPEG-4 was originally intended for very low bitrate video coding. It is important to note that despite the standardization of MPEG-4, any of the suggested functionalities are under intense development, and are thus not currently available. Progress in the implementation of MPEG-4 is primarily hindered due to the lack of effective video segmentation tools [173], thus video segmentation (incorporating ultrasound and video segmentation of the carotid) is one of the most interesting areas where further investigation and research is required.

*Data mining*: It is anticipated that the extraction of quantitative criteria for the identification of high and low risk subgroups of patients, will be a decisive factor for the selection of the therapy, either medical or surgical. Thus, only patients at high risk will be considered for surgery, (carotid endarterectomy), while patients at low risk will be spared from an unnecessary and expensive surgery that also carries a risk. In order to achieve the above task, an integrated database system must be developed taking into consideration important stroke related clinical risk factors, and non-invasive (paraclinical) parameters, i.e. high resolution ultrasound images of the carotid, and CT brain scans. This integration will facilitate the data mining analysis for the assessment of the risk of stroke.

Finally, we hope that the performed research will contribute towards the advancement of medical imaging and processing technologies.

# *Appendix I*

# *Statistics Of Speckle*

# APPENDIX I: STATISTICS OF SPECKLE

## I.1 The statistics of fully developed speckle

Given the stochastic nature of the speckle noise, we may describe this noise pattern statistically. Each of the diffused scatterer, as shown in Fig. 2.2a (see Chapter 2), contributes a component to the echo signal in a sum known as a random walk in the complex plane and in the case of a large number of scatterers within the resolution cell (fully developed speckle), the real and the imaginary parts of the resulting complex field are Gaussian random variables [2], [18], [21], [24], [199], [339], [342].

This is shown schematically in Fig. I.1. If each step in this walk, as Fig. I.1a shows, is considered an independent random variable, over many such walks we can apply the central limit theorem to their sum. Therefore, in fully developed speckle, this complex radio frequency echo signal from diffuse scatterers alone has a zero mean, 2D Gaussian probability density function (PDF) in the complex plane [2], [199], [351].

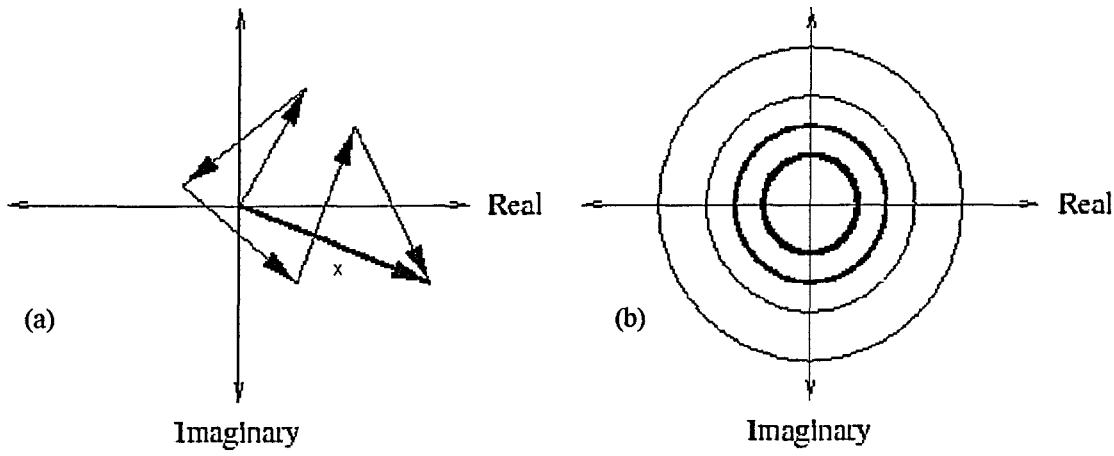


**Fig. I.1**: (a) Through superposition, each scatterer in a population of diffuse scatterers contributes an echo signal that adds one step in a random walk that constitutes the resulting receiving complex echo X, (b) a contour plot of the PDF of X, a 2D complex Gaussian centred at the origin.

Let $N$ be the number of scatterers within the resolution cell. If we denote by $X$ the reflected signal, then:

$$X = \frac{1}{\sqrt{N}} \sum_{i=0}^{N-1} \xi_i e^{j\alpha} \qquad \text{(I.1.1)}$$

where $\xi_i$ is the amount of signal backscattered by the scatterer $i$, $\theta_i$ is the phase shift relative to the reflected wave, and $\frac{1}{\sqrt{N}}$ a normalization term.

Now, we assume $\xi_i$, and $\theta_i$, to be independent and identically distributed, and the number of scatterers to be large ($N \to \infty$), then it can be calculated that, using the central limit theorem, the joint intensity distribution of $X_r$, and $X_i$, the real and the imaginary parts of the complex phasor, will be Gaussian with no cross correlation term (as they are uncorrelated):

$$p_{X_r X_i}(X_r, X_i) = \frac{1}{2\pi\sigma^2} e^{-(X_r^2 + X_i^2)/2\sigma^2} \tag{I.12}$$

with $\sigma^2$, the variance of the signal X. Since the transducer is pressure sensitive, we are interested in the statistics of $X := |X|$, the amplitude of the complex phasor. We have:

$$X = |X| = \sqrt{X_r^2 + X_i^2} \,. \tag{I.13}$$

Introducing polar coordinates, we eventually find as probability distribution of $X$ [351]:

$$p_X(X) = \frac{X}{\sigma^2} e^{-\frac{X^2}{2\sigma^2}} \,. \tag{I.14}$$

This distribution function in (I.1.4) is known as a Rayleigh distribution [351], named after Lord Rayleigh and it is shown in Fig. I.2.

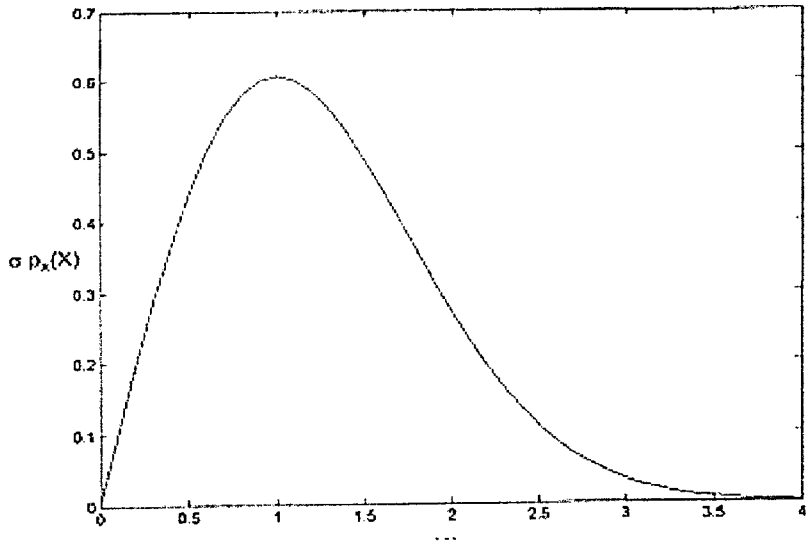


**Fig. I.2**: Rayleigh Distribution (from [351]).

In general, we can write any arbitrary moment as [2], [199]:

$$E\{A^{\nu}\} = \int_0^{\infty} A^{\nu} p(A) dA. \tag{I.15a}$$

with $\nu \in \Re^{+}$.

If we apply this to (I.14), we get:

$$E\{X^{\nu}\} = (2\sigma^2)^{\nu/2} \int_0^{\infty} X^{\nu/2} e^{-X} dX, \tag{I.15b}$$

which can be simplified using the Gamma function to:

$$E\{X^{\nu}\} = (2\sigma^2)^{\nu/2} \Gamma(1+\frac{\nu}{2}). \tag{I.15c}$$

Using (I.15c) we can calculate the signal-to-noise ratio (SNR), $\gamma$, which is defined to be the ratio of the mean, $\mu$, to the standard deviation, $\sigma$, as [2], [355]:

$$\gamma = \frac{\mu}{\sigma} = \frac{E\{X\}}{\sqrt{E\{X^2\} - E^2\{X\}}} = \frac{\sigma\sqrt{\frac{\pi}{2}}}{\sigma\sqrt{2-\frac{\pi}{2}}} \cong 1.91, \tag{I.16}$$

which is constant and independent of the backscattered energy. As one would expect, this value of the SNR is much lower than in most images of natural scenes. The speckle that is formed under these conditions, i.e. spatially uniformly distributed scatterers with uniformly distributed backscattered amplitude and a high scatterer density (>10 per resolution cell) is called fully developed speckle. It has been observed [351], [355], that when the scatterer density falls, the SNR becomes much smaller than 1.91. Similarly, the presence of periodically located (structural) scatterers next to the randomly located diffuse scatterers increases the SNR [21].

# *Appendix II*

# *Optical Perception Testing Procedure Evaluations*

# APPENDIX II: OPTICAL PERCEPTION TESTING PROCEDURE EVALUATIONS

Subjective evaluations represent the point of reference in the first hand together with quality metrics in the second hand. However, different applications require different testing procedures. Psychophysics provides the tools for measuring the perceptual performance of subjects [295].

Two kinds of decision tasks may be distinguished, namely adjustment and judgment [296], where in the first the expert is given a classification and provides a stimulus, and in the second the expert is given a stimulus and provides the classification. Adjustment tasks include setting the threshold amplitude of a stimulus, cancelling a distortion, or matching a stimulus to a given one. Judgment tasks on the other hand include yes or no decisions, forced choices between two alternatives, and magnitude estimation on a rating scale.

It is evident from the definition of adjustment and judgment tasks that most of them are focusing on threshold measurements. Traditionally, the concept of the threshold has played an important role in Psychophysics. This has been motivated by the desire to minimize the influence of perception and knowledge by using simple criteria and tasks. Signal detection theory has provided the statistical framework for such measurements [297]. While such threshold experiments are well suited to the investigation of low-level sensory mechanisms, a simple yes or no answer is not sufficient to capture the expert's experience in may cases, including visual quality assessment. This has stimulated a great deal of experimentation in recent years.

Subjective testing for visual quality assessment has been formalised in ITU-R Recommendation BT.500-10 (2000) [316], which suggests standard viewing conditions criteria for the selection of experts and test material, assessment procedures, and data analysis methods. The three most commonly used procedures are the following:

a) Double Stimulus Continuous Quality Scale (DSCQS) [316]. The presentation sequence for a DSCQS trial is shown in Fig. 4.1a (see Chapter 4). Experts are shown multiple sequence pairs consisting of a reference (Ref.) and a test sequence (Test), which are rather short (typically 10 seconds). The reference and test sequence are presented twice in alternating fashion, with the order of the two chosen randomly for each trial. Experts are not informed which is the reference and which is the test sequence. They rate each of the two separately on a continuous quality scale ranging from bad to excellent as shown in Fig. II.1b. Analysis is based on the difference in rating for each pair, which is calculated from an equivalent numerical scale from 1 to 100. This differencing removes a lot of the subjectivity with respect to scene content and experience.

b) Double Stimulus Impairment Scale (DSIS) [316]. The presentation sequence for a DSIS trial is illustrated in Fig. II.1a. As opposed to the DSCQS method, the reference (original) is always shown before the test (despeckle) sequence, and neither is repeated. Experts rate the amount of impairment in the test sequence on a discrete five-level scale ranging from very annoying to imperceptible as shown in Fig. II.1b.

c) Single Continuous Stimulus Quality Evaluation (SSCQE) [298]. Instead of seeing separate short sequence pairs, experts watch a program of typically 20 to 30 minutes duration which has been processed by the system under test, where the reference is not shown. Using a slider, the experts continuously rate the instantaneously perceived quality on the DSCQS scale from bad to excellent.

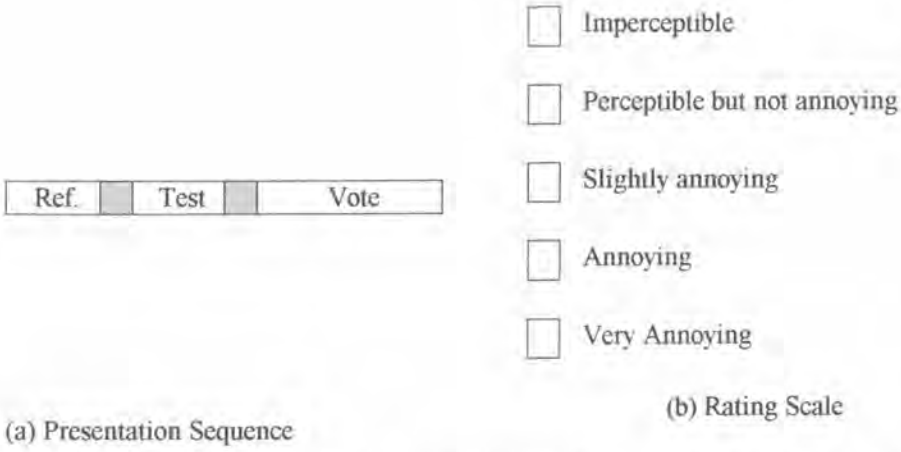


**Fig. 4.2**: DIS Method, (a) the reference and the test sequence are shown only once, (b) experts rate the amount of impairment in the test sequence on a discrete five-level scale ranging from very annoying to imperceptible (Modified from [316] pp. 38, Fig. 3.6, Fig. 3.7).

The above three methods generally have different applications. DSCQS is the preferred method, when the quality of the test and the reference sequence are similar, because the test is quite sensitive to small differences in quality. The DSIS method is better suited for evaluating clearly visible impairments like artefacts caused by transmission errors. However, both DSCQS and DSIS method share a common drawback. Changes in scene complexity, statistical multiplexing, or transmission errors can produce substantial quality variations. They are not evenly distributed over time, severe degradations may appear only once every few minutes. The standard DSCQS, and DSIS methods with their single rating are not suited to the evaluation of such long sequences because of the recency phenomenon, a bias in the ratings towards the final 10 to 20 seconds due to limitations of human working memory [299]. Furthermore it has been argued that the presentation of a reference as well as the repetition of the sequences in the DSCQS method puts the experts in a situation too removed from the home viewing environment

by allowing them to become familiar with the material under investigation [298]. SSCQE has been designed with these problems in mind, as it relates well to the time varying quality of today's compressed digital video systems. On the other hand, program content tends to have a significant influence on SSCQE scores. Also, SSCQE of different tests are harder to compare because of the lack of a reference.

# *Appendix III*

# *Texture Measures*

# APPENDIX III: TEXTURE MEASURES

In this study a total of 56 different texture features [10], [128] were considered, which were extracted from the original and the despeckled images. The tested feature sets were also successfully used in previous work in texture analysis [10], [129], [214]. To evaluate the performance of each filter the following texture feature sets were used:

*(i)* Statistical Features (SF) [93]: In this category the parameters are derived from the gray level histogram. They describe the gray level distribution without considering spatial independence (neighbouring relationship between the pixels); as a result, they can only describe echogenisity of texture and the overall variation of characteristics with the region of interest. The parameters used for this category are:

a. Mean gray level, which is defined as the average gray level of pixels with gray levels $g_1,...g_N$ in an area as:

$$\mu = \frac{1}{N}\sum_{j=1}^{N} g_j \,. \tag{III.1}$$

b. Median, which is the median gray level of image gray levels, above and below which 50% of the overall number of pixels is spread.

c. Standard deviation ($\sigma$), which describes the histogram, width or an estimation of the intensity changes with respect to the mean intensity value as:

$$\sigma = \sqrt{\frac{1}{N-1}\sum_{j=1}^{N}(g_j - \overline{g})^2} \,. \tag{III.2}$$

d. Skewness ($\sigma^3$), which describes the degree of asymmetry of a distribution around its mean.

$$\sigma^3 = \frac{1}{N}\sum_{j=1}^{N}\left[\frac{g_j - \overline{g}}{\sigma}\right]^3 \,. \tag{III.3}$$

e. Kurtosis ($\sigma^4$), which measures the flatness of a distribution in relation to a normal distribution.

$$\sigma^4 = \left\{\frac{1}{N}\sum_{j=1}^{N}\left[\frac{g_j - \overline{g}}{\sigma}\right]^4\right\} - 3 \,. \tag{III.4}$$

f. The speckle index $C = \sigma / \mu$.

*(ii)* The SGLDM or co-occurrence matrices method as proposed by Haralick et al. [128] are based on the estimation of the second-order joint conditional probability density functions, $f(i,j,d,\theta)$. The $f(i,j,d,\theta)$, is the probability that two pixels $(k,l)$,

and $(m,n)$, with distance, $d$, in direction specified by the angle, $\theta$, have intensities of gray level, $i$, and gray level, $j$, [213]. In order to create the co-occurrence matrix, first a distance, $d$, and an angle, $\theta$, between pixels is chosen. For each texture measure, an average angle measure was calculated by averaging the values from the measures calculated at angles 0, 45, 90 and 135. If not otherwise stated, the $d$ value, used in this work is 1. The estimated values for these probability density functions will be denoted by, $P(i,j,d\theta)$. In an $N_x xN_y$ image, let, $L_x = \{1,2,...,N_x\}$, be the horizontal spatial domain, $L_y = \{1,2,...,N_y\}$, be the vertical spatial domain and $g(x,y)$, be the image intensity at pixel $(x,y)$. Formally, for angles quantized at 45° intervals the un-normalised probability density functions are defined by:

$$P(i, j, d, 0^\circ) = \#\{((k,l),(m,n)) \in (L_y \times L_x) \times (L_y \times L_x) : k - m = 0, |l - n| = d, g(k,l) = i, g(m,n) = j\} \quad \text{(III.5)}$$

$$P(i, j, d, 45^\circ) = \#\{((k,l),(m,n)) \in (L_y \times L_x) \times (L_y \times L_x) : (k - m = d, |l - n| = d) \text{ or } (k - m = -d, l - n = d), g(k,l) = i, g(m,n) = j\} \quad \text{(III.6)}$$

$$P(i, j, d, 90^\circ) = \#\{((k,l),(m,n)) \in (L_y \times L_x) \times (L_y \times L_x) : |k - m| = d, l - n = 0, g(k,l) = i, g(m,n) = j\} \quad \text{(III.7)}$$

$$P(i, j, d, 135^\circ) = \#\{((k,l),(m,n)) \in (L_y \times L_x) \times (L_y \times L_x) : (k - m = d, l - n = d) \text{ or } (k - m = -d, l - n = -d), g(k,l) = i, g(m,n) = j\} \quad \text{(III.8)}$$

where # denotes the number of elements in the set.

Haralick et al. [128] proposed the following texture measures, which can be, extracted from the SGLDM:

*Notation:*

$p(i,j)$ $(i,j)th$ entry in the normalised spatial gray level dependence matrix,

$= P(i,j)/R,$

where $R$ is a normalising constant.

$p_x(i)$ $ith$ entry in the marginal probability matrix obtained by summing the rows of $p(i,j)$,

$$= \sum_{j=1}^{N_g} p(i,j) \tag{III.9}$$

$N_g$ Number of distinct gray levels in the quantized image.

$\sum_i$ means $\sum_{i=1}^{N_g}$, and $\sum_j$ means $\sum_{j=1}^{N_g}$.

$$p_y(i) = \sum_{i=1}^{N_g} p(i,j) \tag{III.10}$$

$$p_{x+y}(k) = \sum_{\substack{i=1 \\ i+j=k}}^{N_g} \sum_{j=1}^{N_g} p(i,j), \qquad k = 2,3,\ldots 2N_g \tag{III.11}$$

$$p_{x-y}(k) = \sum_{\substack{i=1 \\ |i-j|=k}}^{N_g} \sum_{j=1}^{N_g} p(i,j), \qquad k = 0,1,\ldots N_g - 1. \tag{III.12}$$

*a.* ASM, which is a measure of the inhomogeneity of the image. Homogeneous images have very few dominant gray-tone transmissions, which results into higher readings.

$$f_1 = \sum_i \sum_j (p(i,j))^2. \tag{III.13}$$

*b.* Contrast, which is a measure of the amount of local variations in an image. Images with large neighbouring gray level differences are associated with high contrast, as defined in NGTDM [214].

$$f_2 = \sum_{i=1}^{N_g - 1} n^2 \Big( \sum_{\substack{i=1 \\ |i-j|=n}}^{N_g} \sum_{j=1}^{N_g} p(i,j) \Big). \tag{III.14}$$

*c.* Correlation, which is a measure of gray-tone-linear dependencies in the image and heterogeneity. Heterogeneous images have higher correlation values [128].

$$f_3 = \frac{\sum_i \sum_j (i,j)p(i,j) - \mu_x \mu_y}{\sigma_x \sigma_y} \quad \text{(III.15)}$$

where $\mu_x, \mu_y$, and $\sigma_x, \sigma_y$, are the mean and standard deviation values of $p_x$ and $p_y$. Correlation is a measure of gray tone linear dependencies.

*d.* Sum of squares: variance

$$f_4 = \sum_i \sum_j (i-\mu)^2 p(i,j) \ . \quad \text{(III.16)}$$

*e.* IDM, which is a measure of local homogeneity (neighbouring gay level transitions). Values of IDM range between 0 (for complete heterogeneous plaques) and 1 (for perfectly homogeneous plaques).

$$f_5 = \sum_i \sum_j \frac{1}{1+(i-j)^2} p(i,j) \ . \quad \text{(III.17)}$$

*f.* Sum average.

$$f_6 = \sum_{i=2}^{2N_g} i p_{x+y}(i) \ . \quad \text{(III.18)}$$

*g.* Sum variance, a measure of image heterogeneity.

$$f_7 = \sum_{i=2}^{2N_g} (i - f_6)^2 p_{x+y}(i) \ . \quad \text{(III.19)}$$

*h.* Sum entropy, a measure of image homogeneity.

$$f_8 = \sum_{i=2}^{2N_g} p_{x+y}(i) \log(p_{x+y}(i)) \ . \quad \text{(III.20)}$$

*i.* Entropy, which is a measure of image complexity, with larger values observed in heterogeneous and complex images.

$$f_9 = \sum_i \sum_j p(i,j) \ \log(p(i,j)) \ . \quad \text{(III.21)}$$

*j.* Difference variance, a measure of image heterogeneity.

$$f_{10} = \text{variance of } p_{x-y} \ . \quad \text{(III.22)}$$

*k.* Difference entropy, a measure of image homogeneity.

$$f_{11} = \sum_{i=0}^{N_g - 1} p_{x-y}(i) \log(p_{x-y}(i)) \ . \quad \text{(III.23)}$$

*l.* Information measures of correlation-1.

*m.* Information measures of correlation-2.

For each feature the mean values and the range of values were computed, and were used as two different feature sets.

$$f_{12} = \frac{HXY - HXY1}{\max(HX, HY)}. \quad \text{(III.24)}$$

$$f_{13} = (1\text{-}\exp[-2.0(HXY2 - HXY)])^{1/2}. \quad \text{(III.25)}$$

$$HXY = -\sum_i \sum_j p(i,j)\ \log(p(i,j)). \quad \text{(III.26)}$$

where $HX$ and $HY$ are entropies of $p_x$ and $p_y$, and

$$HXY1 = -\sum_i \sum_j p(i,j)\log(p_x(i)p_y(j)).$$

$$HXY2 = -\sum_i \sum_j p_x(i)p_y(j)\log(p_x(i)p_y(j)). \quad \text{(III.27)}$$

For a chosen distance, $d$, we have four angular gray level dependence matrices, i.e. we obtain four values for each of the above 13 texture measures. The mean and the range of the four values of each of the 13 texture measures comprise a set of 26 texture features, which can be used for classification. Some of the 26 features are strongly correlated with each other, and a feature selection procedure may be applied in order to select a subset or linear combinations of them. In this work, the mean values and the range of values were computed for each feature for, $d$=1, and they were used as two different feature sets.

*(iii)* The GLDS algorithm [129], use first order statistics of local property values based on absolute differences between pairs of gray levels or of average gray levels in order to extract texture measures. Let $g(x,y)$, be the image intensity function and for any given displacement, $\delta \equiv (\Delta x, \Delta y)$, let $g_\delta(x,y) = |g(x,y)\text{-}g(x+\Delta x, y+\Delta y)|$ . Let $p_\delta$ be the probability density of $g_\delta(x,y)$. If there are $m$ gray levels, this has the form of an $m$-dimensional vector whose $i$th component is the probability that $g_\delta(x,y)$ will have value $i$. The probability density $p_\delta$ can be easily computed by counting the number of times each value of $g_\delta(x,y)$ occurs, where $\Delta x$ and $\Delta y$ are integers. In a coarse texture, if the $\delta$ is small, $g_\delta(x,y)$ will be small, i.e. the values of $p_\delta$ should be concentrated near $i = 0$. Conversely in a fine texture the values of $p_\delta$ should be more spread out. Thus, a good way to analyse texture coarseness would be to compute, for various magnitudes of $\delta$, some measure of the spread of values in $p_\delta$ away from the origin. The GLDS [129] algorithm is based on the assumption that useful texture information can be extracted using first order statistics of an image. Coarse texture features result in low gray level difference values, whereas, fine texture images result in pixel gray level differences with great variances. The features belonging in this category are:

*a.* Contrast:

$$CON = \sum_i i^2 p_\delta(i). \tag{III.28}$$

This is the second moment of $p_\delta$ i.e. its moment of inertia about the origin.

*b.* ASM-Homogeneity:

$$ASM = \sum_i p_\delta(i)^2. \tag{III.29}$$

*ASM* is small when the $p_\delta(i)$ values are very close and large when some values are high and others low.

*c.* Entropy:

$$ENT = -\sum_i p_\delta(i)\log(p_\delta(i)). \tag{III.30}$$

This is largest for equal $p_\delta(i)$ values and small when they are very unequal.

*d.* Mean:

$$MEAN = (1/m)\sum_i i\ p_\delta(i). \tag{III.31}$$

This is small when the $p_\delta(i)$, are concentrated near the origin and large when they are far from the origin. The above features were calculated for $\delta$ = (0, 1), (1, 1), (1,0), (1,-1) and their mean values were taken.

*e.* Energy.

Features a, b, c are similar with the corresponding SGLDM features and carry about the same information.

*(iv)* Amadasun and King (1989) [214] proposed the NGTDM in order to extract textural features, which correspond to visual properties of texture. Let $g(k,l)$ be the gray tone of a pixel at $(k,l)$ having gray tone value $i$. Then we can find the average gray-tone over a neighbourhood cantered at, but excluding $(k,l)$:

$$\overline{A}_i = \overline{A}(k,l) = \frac{1}{W-1}\left[\sum_{m=-d}^{d}\sum_{n=-d}^{d} g(k+m,l+n)\right] \tag{III.32}$$

where $(m,n)\neq(0,0)$, $d$, specifies the neighbourhood size and $W=(2d+1)^2$.

Then the $i$th entry in the NGTDM is:

$$s(i) = \sum |i - \overline{A}_i| \quad \text{for } i \in N_i \text{ if } N_i \neq 0, \tag{III.33}$$

$$= 0,$$

otherwise

where $\{ N_i \}$ is the set of all pixels having gray tone $i$.

The following textural features are defined as:

*a.* Coarseness:

$$f_{\cos} = \left[ \varepsilon + \sum_{i=0}^{g_{\max}} p_i s(i) \right]^{-1} \tag{III.34}$$

where $g_{\max}$ is the highest gray-tone value present in the image and ε is a small number to prevent $f_{cos}$ to get infinite. For an *N*x*N* image, $p_i$ is the probability of occurrence of Gray-tone value *i*, and is given by:

$$p_i = N_i / n^2 \text{, where } n = N - 2d \text{.} \tag{III.35}$$

Amadasun and King (1989) define an image as coarse when the primitives composing the texture are large and texture tends to possess a high degree of local uniformity in intensity for fairly large areas. Large values of $f_{cos}$ represent areas where gray-tone differences are small.

*b.* Contrast:

$$f_{con} = \left[ \frac{1}{N_g(N_g - 1)} \sum_{i=0}^{g_{\max}} \sum_{j=0}^{g_{\max}} p_i p_j (i-j)^2 \right] \left[ \frac{1}{n^2} \sum_{i=0}^{g_{\max}} s(i) \right] \tag{III.36}$$

where $N_g$ is the total number of different gray levels present in the image. High contrast means that the intensity difference between neighbouring regions is large.

*c.* Business:

$$f_{bus} = \left[ \sum_{i=0}^{g_{\max}} p_i s(i) \right] / \left[ \sum_{i=0}^{g_{\max}} \sum_{j=0}^{g_{\max}} i p_i - j p_j \right] , \quad p_i \neq 0, p_j \neq 0 \text{.} \tag{III.37}$$

A busy texture is one in which there are rapid changes of intensity from one pixel to its neighbour.

*d.* Complexity:

$$f_{com} = \sum_{i=0}^{g_{\max}} \sum_{j=0}^{g_{\max}} \{ (|i-j|)/(n^2(p_i + p_j)) \} \{ p_i s(i) + p_j s(j) \}, \quad p_i \neq 0, p_j \neq 0. \tag{III.38}$$

A texture is considered complex when the information content is high i.e. when there are many primitives in the texture, and more so when the primitives have different average intensities.

*e.* Strength:

$$f_{str} = \left[ \sum_{i=0}^{g_{\max}} \sum_{j=0}^{g_{\max}} (p_i + p_j)(i-j)^2 \right] \left[ \varepsilon + \sum_{i=0}^{g_{\max}} s(i) \right] , \quad p_i \neq 0, p_j \neq 0 \text{ .} \tag{III.39}$$

A texture is generally referred to as strong when the primitives that comprise it are easily definable and clearly visible.

*(v)* The SFM [211], [213] measures the statistical properties of pixel pairs at several distances within an image, which are used for statistical analysis. Let $g(x,y)$ be the intensity at point $(x,y)$, and let $\delta=(\Delta x,\Delta y)$ represent the intersample spacing distance vector, where $\Delta x$ and $\Delta y$ are integers. The $\delta$ contrast, $\delta$ covariance and $\delta$ dissimilarity are defined as:

$$CON(\delta) \equiv E\{[g(x,y) - g(x+\Delta x, y+\Delta y)]^2\}, \quad \text{(III.40)}$$

$$COV(\delta) \equiv E\{[g(x,y) - \eta]\,[g(x+\Delta x, y+\Delta y) - \eta]\}, \quad \text{(III.41)}$$

$$DSS(\delta) \equiv E\{[g(x,y) - g(x+\Delta x, y+\Delta y)]\}, \quad \text{(III.42)}$$

where $E\{\ \}$ denotes the expectation operation and $\eta$ is the average gray level of the image.

An SFM ($M_{sf}$), is an $(L_r+1)\text{x}(2L_c+1)$ matrix whose $(i,j)$ element is the $d$ statistical feature of the image, where $d = (j-L_c, i)$ is an intersample spacing distance vector for $i=0,1,\ldots, L_r$, $j=0,1,\ldots, L_c$, and $L_r$ , $L_c$ are the constants which determine the maximum intersample spacing distance. In a similar way, the contrast matrix ($M_{con}$), covariance matrix ($M_{cov}$) and dissimilarity matrix ($M_{dss}$) can be defined as the matrices whose $(i,j)$ elements are the $d$ contrast, $d$ covariance and $d$ dissimilarity, respectively. Based on the SFM the following texture features can be computed:

*a.* Coarseness:

$$F_{CRS} = c / \sum_{(i,j)\in N_r} DSS(i,j) / n. \quad \text{(III.43)}$$

where $c$ is a normalising factor, $N_r$ is the set of displacement vectors defined as $N_r=\{(i,j) : |i|, |j|\le r\}$ and $n$ is the number of elements in the set. A pattern is coarser than another when they differ only in scale with the magnified one to be the coarser and having a larger $F_{CRS}$ value. The definition of coarseness given here is different than the definition given by NGTDM in (III.34).

*b.* Contrast:

$$F_{CON} = \left[ \sum_{(i,j)\in N_r} CON(i,j) / 4 \right]^{1/2}. \quad \text{(III.44)}$$

Contrast measures the degree of sharpness of the edges in an image.

*c.* Periodicity:

$$F_{PER} = \frac{\overline{M}_{dss} - M_{dss}(valley)}{\overline{M}_{dss}}. \quad \text{(III.45)}$$

where $\overline{M}_{dss}$ is the mean of all elements in $M_{dss}$ and $M_{dss}(valley)$ is the deepest valley in the matrix. Periodicity measures the appearance of periodically repeated patterns in the image.

*d.* Roughness:

$$F_{RGH} = (D_f^{(h)} + D_f^{(v)})/2. \quad \text{(III.46)}$$

where $D_f$ is the fractal dimension (see section (vii)) in horizontal and vertical directions. $D_f$ = 3 - $H$ and $E\{|\Delta I|\} = k(\delta)^H$ where $H$ can be estimated from the dissimilarity matrix since the $(i, j+L_c)$ element of the matrix is $E\{|\Delta I|\}$ with $\delta=(j,i)$. The larger the $D_f$ the rougher is the image. In this study an intersample spacing distance vector $\delta$=(4,4) was used.

*(vi)* Laws TEM [211] are derived from three simple vectors of length 3, *L3*=(1,2,1), *E3*=(-1,0,1) and *S3*=(-1,2,-1), which represent the one dimensional operations of center-weighted local averaging, symmetric first differencing for edge detection, and second differencing for spot detection. If these vectors are convolved with themselves, we obtain new vectors of length 5, *L5*=(1,4,6,4,1), *E5*=(-1,-2,0,2,1) and *S5*=(-1,0,2,0,-1). By further self-convolution we obtain new vectors of length 7, *L7*=(1,6,15,20,15,6,1), *E7*=(-1 -4,-5, 0, 5,4,1), *S7*=(-1 -2, 1, 4, 1 -2 -1) where *L7* again performs local averaging, *E7* acts as edge detector and *S7* acts as spot detector. If we multiply the column vectors of length *l* by row vectors of the same length, we obtain Laws *lxl* masks. In this work the following combinations were used to obtain 7x7 masks:

$LL = L7^t L7,\ LE = L7^t E7,\ LS = L7^t S7,\ EL = E7^t L7,\ EE = E7^t E7,\ ES = E7^t S7,$

$SL = S7^t L7,\ SE = S7^t E7,\ SS = S7^t S7.$

In order to extract texture features from an image, these masks are convoluted with the image and statistics (e.g. energy) of the resulting image are used to describe texture. The following texture features were extracted:

*a.* LL - texture energy (TE) from LL kernel

*b.* EE - TE from EE kernel

*c.* SS - TE from SS kernel

*d.* LE - average TE from LE and EL kernels

$$LE=(LE+EL)/2 \quad \text{(III.47)}$$

*e.* ES - average TE from ES and SE kernels

$$ES=(ES+SE)/2 \tag{III.48}$$

*f.* LS - average TE from LS and SL kernels

$$LS=(LS+SL)/2 \tag{III.49}$$

The averaging of matched pairs of energy measures gives rotational invariance.

*(vii)* FDTA [210], [211]: $H^{(k)}$ parameter (Hurst coefficient) for resolutions $k$=1, 2, 3, 4.

In 1828 the Scottish biologist Robert Brown (1773-1858) observed, while looking through his microscope at small particles floating in a liquid, that they made tiny, random, unpredictable movements [210]. He attributed this phenomenon to physical causes. The explanation for this Brownian motion was given later by Einstein based on the thermal motions of molecules. Mandelbrot [210] developed the fractional Brownian motion model in order to describe the roughness of nature surfaces. It considers naturally occurring surfaces as the end result of random walks. Such random walks are basic physical processes in our universe [211]. An important parameter to represent a fractal dimension is the fractal dimension $D_f$ estimated theoretically by the equation [211]:

$$E\{\Delta g^2\} = c(\Delta r)^{(6-2D_f)} \tag{III.50}$$

where $E\{\ \}$ denotes the expectation operator, $\Delta g$ is the intensity difference between two pixels, $c$ is a constant and $\Delta r$ is the distance between two pixels.

A simpler method is to estimate the $H$ parameter (Hurst coefficient) from:

$$E(|\Delta I|) = k(\Delta r)^H \tag{III.51}$$

where $k = E(|\Delta I|)_{\Delta r=1}$ .

By applying the log function we obtain:

$$\log E(|\Delta I|) = \log k + H \log(\Delta r)\ . \tag{III.52}$$

From the above equation the $H$ parameter can be estimated and the fractal dimension $D_f$ can be computed from the relationship:

$$D_f = 3 - H\ . \tag{III.53}$$

A smooth surface is described by a small value of the fractal dimension $D_f$ (large value of the parameter $H$) where the reverse applies for a rough surface.

Given an $M$x$M$ image the intensity difference vector is defined as:

$$IDV \equiv [\, id(1), id(2), \ldots id(s) \,] \tag{III.54}$$

where $s$ is the maximum possible scale, $id(k)$ is the average of the absolute intensity difference of all pixel pairs with vertical or horizontal distance $k$. The value of the parameter $H$ can be obtained by using least squares linear regression to estimate the slope of the curve of $id(k)$ versus $k$ in log - log scales.

If the image is seen under different resolutions then the multiresolution fractal ($MF$) feature vector is defined as:

$$MF \equiv (H^{(m)}, H^{(m-1)}, \ldots, H^{(m-n+1)}) \tag{III.55}$$

where $M = 2^m$ is the size of the original image, $H^{(k)}$ is the $H$ parameter estimated from image $g^{(k)}$, and $n$ is the number of resolutions chosen. The multiresolution fractal ($MF$) feature vector describes also the lacunarity of the image. It can be used for the separation of textures with the same fractal dimension $D_f$ by considering all but the first components of the $MF$ vectors. In this work $H$ was computed for four different resolutions.

*(viii)* FPS [211]: The estimation of power spectrum of an image using Fourier transform provides useful information about texture [129]. Coarse texture will produce results concentrated near the origin, while in images with smooth texture values will be more spread out. The features are:

*a.* Radial sum, and

*b.* Angular sum.

# *Appendix IV*

# *Complete Snake Implementation*

# Appendix IV: Complete Snake Implementation (Kass)

The snake method iterates around the snake point to find local minimum energy at snake points. This is an approximation, since it does not necessarily determine the best local minimum in the region of the snake points. A complete snake implementation of Kass, solves for all snake points in one step to ensure that, the snake moves to the best local energy minimum [243].

We seek therefore to choose snake points, $v(s)=(x(s),y(s))$, in such a manner that the energy functional (3.4.2) is minimized with $\frac{dE_{snake}}{dv}=0$. By the calculus of variations [111], [97], (3.4.2) may be solved and results in a set of equations that iteratively provide new sets of contour points. The entire derivation may be found in [155], [243] and the result is:

$$\frac{-d}{ds}(\alpha(s)\frac{dv(s)}{ds})+\frac{d^2}{ds^2}(\beta(s)\frac{d^2v(s)}{ds^2})+\frac{dE_{image}}{dv}=0, \qquad \text{(IV.1)}$$

with $v(s)=(x(s),y(s))$.

This vector-valued partial differential equation expresses the balance of internal and external forces when the contour rests at equilibrium. The first two terms represent the internal stretching and bending respectively, while the third term represents the image forces that couple the snake to the image data. The usual approach to solving (IV.1) is through the application of numerical algorithms, which will be derived later. By applying the principles of Lagrangian mechanics this leads to a dynamic deformable model that unify the description of shape and motion, making it possible to quantify not just static shape, but also shape evolution through time. To find a solution to (IV.1), the snake is made dynamic snake and can be represented by introducing a time varying contour, $v(s,t)=(x(s,t),y(s,t))$, with a mass density, $\mu(s)$, and a damping density, $\delta(s)$, from a medium surrounding the snake. The Lagrange equation of motion for a snake with the internal energy given by (3.4.4) and the image energy given by (3.4.10) is [155]:

$$\mu\frac{d^2v}{dt^2}+\delta\frac{dv}{dt}-\frac{d}{ds}(\alpha\frac{dv}{ds})+\frac{d^2}{ds^2}(\beta\frac{d^2v}{ds^2})=-\nabla P(v(s,t)). \qquad \text{(IV.2)}$$

This is the Newton's law of motion for a snake with mass, $\mu$, driven by external and internal forces. The first two terms of the left-hand side of this partial differential equation represent inertial and damping forces. Note that in mechanical systems the first two terms represents force and velocity. However, in our system force and velocity are equivalent and therefore only the velocity term will be taken into consideration. Referring to (IV.1), the remaining terms in (IV.2) represent the internal stretching and bending forces, while the right hand-side represents

the image forces. Equilibrium (stabilization) is achieved when the image and external forces balance and the contour comes to rest, $(dv/dt = 0, d^2v/dt^2 = 0)$, which yields the equilibrium condition in (IV.1). Equation (IV.2) has reformulated the original energy minimization framework in (3.4.2) into a pair of differential equations. Active contour models can be applied statistically with (IV.1), to single images or dynamically, to temporal image sequences with (IV.2).

To implement a complete snake, we seek a solution to (IV.2). By the method of finite differences, we substitute, as illustrated with (3.4.5) and (3.4.6), for the first-order difference, $\frac{dv(s)}{ds} \cong v_{s+1} - v_s$, and for the second order difference, $\frac{d^2v(s)}{ds^2} \cong v_{s+1} - 2v_s + v_{s-1}$, which by substitution to (IV.2), for a contour discretised into $s$ points equally spaced at intervals of an *arc* length, $h$, gives:

$$\frac{dv(s)}{ds} = v_{s+1} - v_s, \quad \frac{d^2v(s)}{ds^2} = v_{s+1} - 2v_s + v_{s-1}, \tag{IV.3}$$

$\frac{-d}{ds}\frac{1}{h}\{\alpha_{s+1}(v_{s+1} - v_s)\} + \frac{d^2}{ds^2}\frac{1}{h^2}\{\beta_{s+1}(v_{s+1} - 2v_s + v_{s-1})\} + \frac{dE_{image}}{dv} = 0$, with $h$ the spatial sampling distance.

$$\Rightarrow -\frac{1}{h}\{\alpha_{s+1}(v_{s+1} - v_s) - \alpha_s(v_s - v_{s-1})\} + \frac{1}{h^2}\{\beta_{s+1}(v_{s+2} - 2v_{s+1} + v_s) - 2\beta_s(v_{s+1} - 2v_s + v_{s-1}) + \beta_{s-1}(v_s - 2v_{s-1} + v_{s-2})\} + \frac{dE_{image}}{dv} = 0. \tag{IV.4}$$

This will result to:

$$\frac{v_\tau - v_{\tau-1}}{\tau} - \frac{1}{h}\left\{a_{s+1}\frac{(v_{s+1} - v_s)}{h} - a_s\frac{(v_s - v_{s-1})}{h}\right\} + \frac{1}{h^2}\left\{\beta_{s+1}\frac{(v_{s+2} - 2v_{s+1} + v_s)}{h^2} - 2\beta_s\frac{(v_{s+1} - 2v_s + v_{s-1})}{h^2} + \beta_{s-1}\frac{(v_s - 2v_{s-1} + v_{s-2})}{h^2}\right\} = -\nabla P(v), \tag{IV.5}$$

with the first term of (IV.2) to be zero and while $\delta\frac{dv}{dt}$ tends to zero after some iterations when a stable state would be obtained and the snake stops.

By collecting the coefficient of different points, above equation can be expressed as:

$$f_s = a_s x_{s-2} + b_s x_{s-1} + c_s x_s + d_s x_{s+1} + e_s x_{s+2}, \quad \text{where,} \tag{IV.6a}$$

$$f_s = -\frac{1}{2}\frac{dE_{edge}}{dv}, \tag{IV.6b}$$

$$a_s = \frac{\beta_{s-1}}{h^4}, \tag{IV.6c}$$

$$b_s = -2\frac{(\beta_s - \beta_{s-1})}{h^4} - \frac{a_s}{h^2}, \tag{IV.6d}$$

$$c_s = \frac{(\beta_{s+1} + 4\beta_s + \beta_{s-1})}{h^4} - \frac{a_{s+1} + \alpha_s}{h^2}, \tag{IV.6e}$$

$$d_s = -2\frac{(\beta_{s+1} + \beta_s)}{h^4} - \frac{a_{s+1}}{h^2}, \tag{IV.6f}$$

$$e_s = \frac{\beta_{s+1}}{h^4}, \tag{IV.6g}$$

The above is now in the form of a linear matrix equation:

$$Ax = f_x(x, y), \tag{IV.7}$$

where $f_x(x, y)$ is the first order differential of the edge magnitude along the $x-axis$ and A is a pentavector, which may be described as follows:

$$A^T = \left[\frac{\beta}{h^4}, -\frac{4\beta}{h^4} - \frac{\alpha}{h^2}, \frac{6\beta}{h^4} + \frac{2\alpha}{h^2}, -\frac{\alpha}{h^2} - \frac{4\beta}{h^4}, \frac{\beta}{h^4}\right]. \tag{IV.8}$$

The parameter $h$ used in $A$ denotes the spatial sampling distance, which is defined in this study as 1. Moreover, $\alpha$, and $\beta$, are initially set to 0.6 and 0.4 respectively and then estimated with (3.4.7). The above equation may be solved to provide a new vector $v_{i+1}$ from an initial vector $v_i$ where $i$ is an evolution index. The iterative solution is finally given by:

$$\frac{v_{i+1} - v_i}{\Delta} + Av_{i+1} = fv(x_i, y_i), \tag{IV.9}$$

with $\Delta$ as a control scalar factor chosen to control convergence. It controls the rate of evolution of the snake. Large values make the snake move quickly, where low values make the snake move slowly. Fast movement implies that the snake may pass over features of interest without noticing them. Slow movement can be rather tedious. Therefore the appropriate choice of $\Delta$ is a compromise, between selectivity and time. The problem may be avoided by manual tuning and the image force is modified to limit the updating step. According to (IV.9), $A$ is a high-pass filter with amplification. The next iteration of the snake is computed by filtering out the high-frequency component, from the current state, and combining the image force with a factor, $\tau$. An appropriate choice of the time constant, $\tau$, is given in [241], and suggests that, $\tau$A, should be a unit high-pass filter without amplification, i.e $\tau$, is the reciprocal of the maximum absolute value of the frequency response of A:

$$\tau = \frac{1}{\max(|H(A)|}, \tag{IV.10}$$

where $H(\mathrm{A})$ denotes the frequency response of vector A. Based on this definition the snake does not converged and the choice of time constant becomes easy to handle. The final equation that may be used to evolve a contour is then:

$$v_{i+1} = (A + \frac{1}{\Delta} I)(\frac{1}{\Delta} v_i + f_v(x_i, y_i)), \tag{IV.11}$$

where $I$ is the identity matrix.

Equation (IV.11) implies that the new set of coordinates, $v_s(x_s, y_s)$, is a weighted sum of the initial set of contour points and the image information. The new set of contour points becomes the starting set for the next iteration. This is a continuous formulation, as opposed to the discrete implementation. One penalty is the need for a matrix inversion, affecting speed. The benefits are that coordinates are calculated as real functions, and the complete set of new contour points is provided at each iteration.

By observing (IV.9) it is clear that a different solution could be obtained by using different values for the snake parameters. In real applications the choice of values for $\alpha$, $\beta$, and $\gamma$, together with the scalar factor, $\Delta$, must be made carefully. In fact this is part of the difficulty in using snakes for practical feature extraction [55], [178], [185], [220], [241]. A further difficulty is that the result depends on where the initial contour is placed [55], [241], but this may be solved by an initial contour detection as proposed in Chapter 3.6. These difficulties are called parameterization and initialization respectively and have motivated much research and development. Another difficulty reported in the literature is the convergence of the algorithm.

By using (3.4.8)-(3.4.10) the external force may be defined as, gradient and additional forces given by the user or based on the application:

$$E_{image}(v(s)) = -\int_{\Omega} c(|G\sigma * g| + D * g)ds = -\int_{\Omega} F(v)ds, \tag{IV.12}$$

where

$$D = c_2 \begin{bmatrix} 0 & -1 & 0 \\ 0 & 0 & 0 \\ 0 & 1 & 0 \end{bmatrix}. \tag{IV.13}$$

The parameter, $G\sigma$, represents a Gaussian function (or the Macleod operator) [12], $g$ denotes the raw image, $c$ is the gravity constant, $c_2$ is a positive weighting factor ($c_2 = 1.5$ in this

study) and the operator * represents the convolution operation [241]. In ultrasound images of the carotid artery the noisy boundary of the sub-intima as seen in Fig. 3.1, is observed and makes the detection of the intima and adventitia layers difficult. Therefore a criterion to enhance the border is chosen where the Macleod operator is implemented and the gradient is considered as the image force. An additional criterion to enhance the adventitia and reduce the effect of the sub-intima may be used by introducing a vector $[-1,0,1]^T$ having a black region above and a white region below as in (IV.13) [241]. From (IV.72) we may see that the image force may have negative values, thus representing a repulsive force, which may repels the snake from the sub-intimal region to the adventitia. The image force may further cause the snake to become unstable if it is not normalized. Thus the image force is modified according to calculate the gradient only within a given searching region. Therefore (IV.12) can be modified as:

$$E_{image}(v_i) = \frac{c}{\overline{g_i}} \sum_{p \in W(v)} q(p) \frac{pv_i}{\|pv_i\|^2 + a^2}, \tag{IV.14}$$

with

$$q(p) = |G\sigma * g(p)| + D * g(p), \text{ and } \overline{g_i} = \frac{1}{W_i^2} \sum_{p \in W(v)} q(p), \tag{IV.15}$$

where $c$ is a gravity constant defined by the user, and $\overline{g_i}$, is the mean gray value for the searching region. This normalization form prevents the snake from diverging and oscillating during the updating process. In addition the constant $a$, is a non-zero parameter thereby avoiding a zero solution of the denominator.

An additional vertical force may be added to the image force of the (IV.14) [241], which may attract the snake downward to trace the boundary for the intima layer. It is useful, when the initial snake contour is placed closed to the boundary of interest. This force vanishes when no layer is found in a short period of time. The vertical force is defined as:

$$F_v = [0,1/\exp(Index/Step)]^T, \tag{IV.16}$$

where $Index$, is the iteration index, and $Step$, is a positive parameter to prolong or shorten the searching period. Results in [241] showed that a $Step = 20$, for the detection of the intima layer boundary and a $Step = 100$, for the detection of the adventitia layer boundary may be chosen. Therefore (IV.14) may be modified as:

$$E_{image}(v_i) = \frac{c}{\overline{g_i}} \sum_{p \in W(v)} \left[ |G\sigma * g(p)| + D * g(p) \right] \frac{pv_i}{\|pv_i\|^2 + a^2} + F_v. \tag{IV.17}$$

# *Appendix V*

# *List of Publications*

# Appendix V: List of Publications

## *Book Contributions*

1. C.S. Pattichis, E. Kyriakou, C.I. Christodoulou, M.S. Pattichis, C.P. Loizou, M. Pantziaris, and A. Nicolaides, "Cardiovascular: Ultrasound imaging in vascular cases," in Wiley Encyclopaedia of Biomedical Engineering, Wiley, 2004.

## *Journal Publications*

1. C.P. Loizou, C.S. Pattichis, C.I. Christodoulou, R.S.H. Istepanian, M. Pantziaris, A. Nicolaides, Comparative evaluation of despeckle filtering in ultrasound imaging of the carotid artery, *IEEE Trans. Ultrasonics Ferroelectrics and Frequency Control*, accepted, 2005.

## *Papers Published in Refereed Conference Proceedings*

1. C.P. Loizou, C.S. Pattichis, R.S.H. Istepanian, M. Pantziaris, A. Nicolaides, "Atherosclerotic carotid plaque segmentation," *Proc. of the 26th annual Int. conf. IEEE EMBS,* San Francisco, California, USA, Sept. 1-5, pp. 1403-1406, 2004.
2. C.P. Loizou, C.S. Pattichis, R.S.H. Istepanian, M. Pantziaris, "Intima media segmentation of the carotid artery," *IEEE* X *Med. Conf. Medical, Biological Engineering, "Health in the Information Society," MEDICON,* July 31-Aug. 5, Ischia, Naples-Italy, POS-03, 499, pp. 1-4, 2004.
3. C.P. Loizou, C.S. Pattichis, R.S.H. Istepanian, M. Pantziaris, "Atherosclerotic carotid plaque segmentation," *II EFOMP Mediterranean conf. on Medical Physics*, Limassol-Cyprus, pp. W2-3 (6 pages), April 28-30, 2004.
4. C.P. Loizou, C.S. Pattichis, R.S.H. Istepanian, M. Pantziaris, T. Tyllis, A. Nicolaides, "Quality evaluation of ultrasound imaging in the carotid artery," *IEEE Int. conf. Melecon*, Dubrovnik-Croatia, vol. I, pp. 395-398, May 12-15, 2004.
5. C.P. Loizou, C.S. Pattichis, R.S.H Istepanian, M. Pantziaris, E. Kyriakou, T. Tyllis, A. Nicolaides, "Ultrasound image quality evaluation," *ITAB 2003, Proc of the 4th annual IEEE conf. on Int. Technology Applications in Biomedicine*, Birmingham UK, pp.138-141, 24-26 April, 2003.

6. C.I. Christodoulou, C.P. Loizou, C.S. Pattichis, M. Pantziaris, E. Kyriakou, M.S. Pattichis, C.N. Schizas, A. Nicolaides, "De-speckle filtering in ultrasound imaging of the carotid artery", *Second joint EMBS/BMES conf. of the IEEE Engineering in Medicine and Biology Society and the Biomedical Engineering Society*, Houston, TX, USA, pp. 1027-1028, 23-26 Oct., 2002.

7. C.P. Loizou, C.H. Christodoulou, C.S. Pattichis, R.S.H Istepanian, M. Pantziaris, A. Nicolaides, "Speckle reduction in ultrasound images of atherosclerotic carotid plaque," *DSP-2002, 14th Int. IEEE conf. on Digital Signal Processing*, Santorini-Greece, pp. 525-528, July 1-3, 2002.

8. C.P. Loizou, C.H. Christodoulou, C.S. Pattichis, M. Patziaris, A. Nicolaides, "Ultrasonic imaging De-speckling and texture analysis for the assessment of atherosclerotic carotid," *1st Medit. Congress of Neurology*, Limassol-Cyprus, pp. 1-4, April 25-28, 2002.

# Comparative Evaluation of Despeckle Filtering In Ultrasound Imaging Of The Carotid Artery

*C. P. Loizou[1], C. S. Pattichis[2], C. I. Christodoulou[3],
R.S.H. Istepanian[4], M. Pantziaris[3], A. Nicolaides[3,5]

[1] Dep. of Computer Science, Intercollege, P. O. Box 51604, CY-3507 Limassol- Cyprus, e-mail: christosl@lim.Intercollege.ac.cy

[2] Dep. of Computer Science, University of Cyprus, Nicosia-Cyprus, e-mail: pattichi@ucy.ac.cy

[3] Cyprus Institute of Neurology and Genetics, Nicosia-Cyprus, e-mail: cschr2@ucy.ac.cy

[4] Mobile Information and Network Technologies Research Center (MINT@K), School of Computing and Information Systems, Kingston University, Penrhyn road, Kingston-Upon-Thame, London KT1 2EE, UK. e-mail: r.Istepanian@kingston.ac.uk

[5] Department of Vascular Surgery, Imperial College London-U.K

To be published in the IEEE Transactions in Ultrasonics Ferroelectrics and Frequency Control

*Corresponding Author: Intercollege, 92 Ayias Phylaxeos Str., P.O.Box 3507, Limassol-Cyprus. Phone (+357) 25-381180, Fax: (+357) 25-386982, e-mail: christosl@lim.Intercollege.ac.cy

**Permission to publish the abstract separately is granted**

**Abstract**—It is well known that speckle is a multiplicative noise that degrades the visual evaluation in ultrasound imaging. The recent advancements in ultrasound instrumentation and portable ultrasound devices necessitate the need of more robust despeckling techniques for enhanced ultrasound medical imaging for both routine clinical practice and tele-consultation. The objective of this work was to carry out a comparative evaluation of despeckle filtering based on texture analysis, image quality evaluation metrics, and visual evaluation by medical experts, in the assessment of 440 (220 asymptomatic and 220 symptomatic) ultrasound images of the carotid artery bifurcation. In this paper a total of 10 despeckle filters were evaluated based on local statistics, median filtering, pixel homogeneity, geometric filtering, homomorphic filtering, anisotropic diffusion, non-linear coherence diffusion and wavelet filtering. The results of this study suggest that the first order statistics filter *lsmv*, gave the best performance, followed by the geometric filter *gf4d*, and the homogeneous mask area filter *lsminsc*. These filters improved the class separation between the asymptomatic and the symptomatic classes based on the statistics of the extracted texture features, gave only a marginal improvement in the classification success rate, and improved the visual assessment carried out by the two experts. More specifically filters *lsmv* or *gf4d* can be used for despeckling asymptomatic images, where the expert is interested mainly in the plaque composition and texture analysis, whereas filters *lsmv* or *gf4d* or *lsminsc* can be used for the despeckling of symptomatic images where the expert is interested in identifying the degree of stenosis and the plaque borders. In conclusion, the proper selection of a despeckle filter is very important in the enhancement of ultrasonic imaging of the carotid artery. Further work is needed to evaluate at a larger scale and in clinical practice the performance of the proposed despeckle filters in the automated segmentation, texture analysis and classification of carotid ultrasound imaging.

*Index Terms*—**Speckle, despeckle filtering, ultrasound imaging, texture analysis, carotid artery.**

## I. INTRODUCTION

The use of ultrasound in the diagnosis and assessment of arterial disease is well established because of its non-invasive nature, its low cost, and the continuing improvements in image quality [1]. Speckle, a form of locally correlated multiplicative noise corrupts medical ultrasound imaging making visual observation difficult [2], [3]. The presence of speckle noise in ultrasound images has been documented since the early 1970's where researchers such as Burckhardt [2], Wagner [3], and Goodman [4], described the fundamentals and the statistical properties of the speckle noise. Speckle is not truly a noise in the typical engineering sense, since its texture often carries useful information about the image being viewed. It is the primary factor, which limits the contrast resolution in diagnostic ultrasound imaging, thereby limiting the detectability of small, low contrast lesions and making the ultrasound images generally difficult for the non-specialist to interpret [2], [3], [5], [6]. Due to the speckle presence, ultrasound experts with sufficient experience may not often draw useful conclusions from the images [6]. Speckle noise also limits the effective application of image processing and analysis algorithms (i.e. edge detection, segmentation) and display in 2D and volume rendering in 3D. Therefore, speckle is most often considered a dominant source of noise in ultrasound imaging and should be filtered out [2], [5], [6] without affecting important features of the image. The objective of this paper was to carry out a comparative evaluation of despeckle filtering techniques based on texture analysis, image quality evaluation metrics as well as visual assessment by experts on 440 ultrasound images of the carotid artery bifurcation. Preliminary results of this study were published in [7] and [8].

The wide spread of mobile and portable telemedicine ultrasound scanning instruments also necessitates the need for better image processing techniques, in order to offer a clearer image to the medical practitioner. This makes the use of efficient despeckle filtering a very important task. Early attempts to suppress speckle noise were implemented by averaging of uncorrelated images of the same tissue recorded under different spatial positions [5], [9], [10]. While these methods are effective for speckle reduction, they require multiple images of the same object to be obtained [11]. Speckle reducing filters originated from the synthetic aperture radar (SAR)

community [9]. These filters have then later been applied to ultrasound imaging since the early 1980's [12]. Filters that are used widely in both SAR and ultrasound imaging include the Frost [13], Lee [9], [14], [15], and Kuan [11], [16].

Table I summarizes the despeckle filtering techniques that are investigated in this study, grouped under the following categories: local statistics, median filtering, homogeneity, geometric, homomorphic, anisotropic diffusion and wavelet filtering. Furthermore, in Table I the main investigators, the methodology used and the corresponding filter names are given. These filters are briefly introduced in this Section, and presented in greater detail in Section II.

Some of the local statistic filters are the Lee [9], [14], [15], the Frost [13], and the Kuan [11], [16]. The Lee and Kuan filters have the same structure, whereas the Kuan is a generalization of the Lee filter. Both filters form the output image by computing the central pixel intensity inside a filter-moving window, which is calculated from the average intensity values of the pixels and a coefficient of variation inside the moving window. Kuan considered a multiplicative speckle model and designed a linear filter, based on the minimum-mean-square error (MMSE) criterion that has optimal performance when the histogram of the image intensity is Gaussian distributed. The Lee [9] filter is a particular case of the Kuan filter based on a linear approximation made for the multiplicative noise model. The Frost [13] makes a balance between the averaging and the all-pass filters. It was designed as an adaptive Wiener filter that assumed an autoregressive exponential model for the image.

TABLE I [here]

In the homogeneity group the filtering is based on the most homogeneous neighbourhood around each image pixel [8]. Geometric filters [10] are based on non-linear iterative algorithms, which increment or decrement the pixel values in a neighbourhood based upon their relative values. The method of homomorphic filtering [17], [18] is similar to the logarithmic point operations used in histogram improvement, where dominant bright pixels are de-emphasised. In the homomorphic filtering, the FFT of the image is calculated, then denoised, and then the inverse FFT is calculated.

Some other despeckle filtering methods, such as anisotropic diffusion [2], [19], [20]-[23] speckle reducing anisotropic diffusion [5] and coherence anisotropic diffusion [24] presented recently in the literature, are non-linear filtering techniques for simultaneously performing contrast enhancement and noise reduction by utilising the coefficient of variation [5]. Furthermore, in the wavelet category, filters for suppressing the speckle noise were documented. These filters are making use of a realistic distribution of the wavelet coefficients [2], [15], [25]-[30] where only the useful wavelet coefficients are utilised. Different wavelet shrinkage approaches were investigated, usually based on Donoho's work [29].

The majority of speckle reduction techniques have certain limitations that can be briefly summarised as follows:

1) They are sensitive to the size and shape of the window. The use of different window sizes greatly affects the quality of the processed images. If the window is too large over smoothing will occur, subtle details of the image will be lost in the filtering process and edges will be blurred. On the other hand, a small window will decrease the smoothing capability of the filter and will not reduce speckle noise thus making the filter not effective.
2) Some of the despeckle methods based on window approaches require thresholds to be used in the filtering process, which have to be estimated empirically. The inappropriate choice of a threshold may lead to average filtering and noisy boundaries thus leaving the sharp features unfiltered [7], [10], [14].
3) Most of the existing despeckle filters do not enhance the edges but they only inhibit smoothing near the edges. When an edge is contained in the filtering window, the coefficient of variation will be high and smoothing will be inhibited. Therefore, speckle in the neighbourhood of an edge will remain after filtering. They are not directional in the sense that in the presence of an edge, all smoothing is precluded. Instead of inhibiting smoothing in directions perpendicular to the edge, smoothing in directions parallel to the edge is allowed.

4) Different evaluation criteria for evaluating the performance of despeckle filtering are used by different studies. Although most of the studies use quantitative criteria like the mean-square error (MSE) and speckle index (C), there are additional quantitative criteria, like texture analysis and classification, image quality evaluation metrics and visual assessment by experts that could be investigated.

To the best of our knowledge there is only one study which investigated despeckle filtering on ultrasound images of the carotid artery and proposed speckle reducing anisotropic diffusion as the most appropriate method [5]. This technique was compared with the Frost [13], Lee [14], and the homomorphic filtering [18] and documented that anisotropic diffusion performed better.

In this study, we compare the performance of 10 despeckle filters on 440 ultrasound images of the carotid artery bifurcation. The performance of these filters was evaluated using, texture analysis, the kNN classifier, image quality evaluation metrics, and visual evaluation by two experts. The results of our study, show that despeckle filtering improves the class separation between asymptomatic and symptomatic ultrasound images of the carotid artery.

In the following Section, a brief overview of despeckle filtering techniques is presented, whereas in Section III the methodology is presented, covering the material, recording of ultrasound images, texture and statistical analysis, the kNN classifier, image quality evaluation metrics and the experiment carried out for visual evaluation are described. Sections IV and V present the results, and discussion respectively.

## II. DESPECKLE FILTERING

In order to be able to derive an efficient despeckle filter, a speckle noise model is needed. The speckle noise model may be approximated as multiplicative, if the envelope signal which is received at the output of the beamformer of the ultrasound imaging system, is captured before logarithmic compression and may be defined as

$$y_{i,j} = x_{i,j} n_{i,j} + a_{i,j} \tag{1}$$

where $y_{i,j}$ represents the noisy pixel in the middle of the moving window, $x_{i,j}$ represents the noise-free pixel, $n_{i,j}$ and $a_{i,j}$ represent the multiplicative and additive noise, respectively, and

$i, j$ are the indices of the spatial locations that belong in the 2D space of real numbers, $i, j \in \Re^2$. Logarithmic compression is applied to the envelope detected echo signal in order to fit it in the display range [24], [31]. It has been shown, that the logarithmic compression, affects the speckle noise statistics in such a way that the local mean becomes proportional to the local variance rather than the standard deviation [24], [26], [28], [31] (see also (8)). More specifically, logarithmic compression affects the high intensity tail of the Rayleigh and Rician probability density function (PDF) more than the low intensity part. As a result the speckle noise becomes very close to white Gaussian noise corresponding to the uncompressed Rayleigh signal [31]. Since the effect of additive noise is considerably smaller compared with that of multiplicative noise, equation (1) may be written as

$$y_{i,j} \approx x_{i,j} n_{i,j} . \tag{2}$$

Thus the logarithmic compression transforms the model in (2) into the classical signal in additive noise form as

$$\log(y_{i,j}) = \log(x_{i,j}) + \log(n_{i,j}), \tag{3a}$$

$$g_{i,j} = f_{i,j} + nl_{i,j} . \tag{3b}$$

For the rest of the paper the term $\log(y_{i,j})$, which is the observed pixel on the ultrasound image display after logarithmic compression, is denoted as $g_{i,j}$, and the terms $\log(x_{i,j})$, $\log(n_{i,j})$ which are the noise free pixel and noise component after logarithmic compression, as $f_{i,j}$ and $nl_{i,j}$ respectively (see Eq. 3b).

*A. Local Statistics Filtering*

Most of the techniques for speckle reduction filtering in the literature use local statistics. Their working principle may be described by a weighted average calculation using sub region statistics to estimate statistical measures over different pixel windows varying from 3x3 up to 15x15. All these techniques assume that the speckle noise model has a multiplicative form as given in (2) [7]-[15], [24], [26].

*1) First Order Statistics Filtering (lsmv, wiener)*

The filters utilizing the first order statistics such as the variance and the mean of the neighbourhood may be described with the model as in (3). Hence the algorithms in this class may be traced back to the following equation [5], [7]-[16]

$$f_{i,j} = \overline{g} + k_{i,j}(g_{i,j} - \overline{g}) \tag{4}$$

where $f_{i,j}$, is the estimated noise-free pixel value, $g_{i,j}$, is the noisy pixel value in the moving window, $\overline{g}$, is the local mean value of an $N_1 x N_2$, region surrounding and including pixel $g_{i,j}$, $k_{i,j}$, is a weighting factor, with $k \in [0..1]$, and $i, j$, are the pixel coordinates. The factor $k_{i,j}$, is a function of the local statistics in a moving window. It can be found in the literature [9], [11], [14] and may be derived in different forms that

$$k_{i,j} = (1 - \overline{g}^2\sigma^2)/(\sigma^2(1+\sigma_n^2)) \tag{5}$$

$$k_{i,j} = \sigma^2/(\overline{g}^2\sigma_n^2 + \sigma^2) \tag{6}$$

$$k_{i,j} = (\sigma^2 - \sigma_n^2)/\sigma^2 . \tag{7}$$

The values $\sigma^2$, and $\sigma_n^2$, represent the variance in the moving window and the variance of noise in the whole image respectively. The noise variance may be calculated for the logarithmically compressed image, by computing the average noise variance over a number of windows with dimensions considerable larger than the filtering window. In each window the noise variance is computed as

$$\sigma_n^2 = \sum_{i=1}^{p} \sigma_p^2 / \overline{g}_p \tag{8}$$

where $\sigma_p^2$, and $\overline{g}_p$, are the variance and mean of the noise in the selected windows respectively and $p$, is the index covering all windows in the whole image [24], [25], [31]. If the value of $k_{i,j}$, is 1 (in edge areas) this will result to an unchanged pixel, whereas a value of 0 (in uniform areas) replaces the actual pixel by the local average, $\overline{g}$, over a small region of interest

(see (4)). In this study the filter *lsmv* uses equation (5). The filter *wiener* uses a pixel-wise adaptive Wiener method [2]-[6], [13] implemented as given in (4), with the weighting factor $k_{i,j}$, as given in (7). For both despeckle filters *lsmv* and *wiener* the moving window size was 5x5.

*2) Homogeneous Mask Area Filtering (lsminsc)*

The *lsminsc* is a 2D filter operating in a 5x5 pixel neighbourhood by searching for the most homogenous neighbourhood area around each pixel, using a 3x3 subset window [32]. The middle pixel of the 5x5 neighbourhood is substituted with the average gray level of the 3x3 mask with the smallest speckle index, C, where C for log-compressed images is given by

$$C = \sigma_s^2 / \bar{g}_s \tag{9}$$

where $\sigma_s^2$, and $\bar{g}_s$, represents the variance and mean of the 3x3 window. The window with the smallest C is the most homogenous semi-window, which presumably, does not contain any edge. The filter is applied iteratively until the gray levels of almost all pixels in the image do not change.

*B. Median Filtering (median)*

The filter *median* [33] is a simple nonlinear operator that replaces the middle pixel in the window with the median-value of its neighbours. The moving window for the *median* filter was 7x7.

*C. Maximum Homogeneity Over a Pixel Neighbourhood Filtering (homog)*

The *homog* filter is based on an estimation of the most homogeneous neighbourhood around each image pixel [34]. The filter takes into consideration only pixels that belong in the processed neighbourhood (7x7 pixels) using (10), under the assumption that the observed area is homogeneous. The output image is then given by

$$f_{i,j} = (c_{i,j} g_{i,j}) / \sum_{i,j} c_{i,j}, \text{ with } \quad c_{i,j} = 1 \text{ if } (1-2\sigma_n)\overline{g} \le g_{i,j} \le (1+2\sigma_n)\overline{g} \tag{10}$$

$$c_{i,j} = 0 \text{ otherwise}.$$

The *homog* filter does not require any parameters or thresholds to be tuned, thus making the filter suitable for automatic interpretation.

*D. Geometric Filtering (gf4d)*

The concept of the geometric filtering is that speckle appears in the image as narrow walls and valleys. The geometric filter, through iterative repetition, gradually tears down the narrow walls (bright edges) and fills up the narrow valleys (dark edges), thus smearing the weak edges that need to be preserved.

The *gf4*d filter [10] investigated in this study, uses a non-linear noise reduction technique. It compares the intensity of the central pixel in a 3x3 neighbourhood with those of its 8 neighbours and, based upon the neighbourhood pixel intensities it increments or decrements the intensity of the central pixel such that it becomes more representative of its surroundings. The operation of the geometric filter *gf4d* may be described with Fig. 1 and has the following form:

*i) Select direction and assign pixel values*
Select the direction be NS and the corresponding three consecutive pixels be *a*, *b*, *c* (see Fig. 1a and 1b respectively).

*ii) Carry out central pixel adjustments*
Do the following intensity adjustments (see Fig. 1b)

if $a \ge b+2$ then $b = b+1$,

if $a \succ b$ and $b \le c$ then $b = b+1$,

if $c \succ b$ and $b \le a$ then $b = b+1$,

if $c \ge b+2$ then $b = b+1$,

if $a \le b-2$ then $b = b-1$,

if $a \prec b$ and $b \ge c$ then $b = b-1$,

if $c \prec b$ and $b \ge a$ then $b = b-1$,

if $c \leq b-2$ then $b = b-1$.

*iii) Repeat*

Repeat steps 1 and 2 for directions west-east (WE) direction, west-north to south-east (WN-SE) and north-east to west-south direction (NE to WS) (see Fig. 1a).

FIGURE 1 [here]

*E. Homomorphic Filtering (homo)*

The *homo* filter performs homomorphic filtering for image enhancement, by calculating the Fast Fourier Transform (FFT) of the logarithmic compressed image, applying a denoising homomorphic filter function $H(.)$, and then performing the inverse FFT of the image [17], [18]. The homomorphic filter function $H(.)$, maybe constructed either using a band-pass Butterworth or a high-boost Butterworth filter. In this study, a high-boost Butterworth filter was used with the homomorphic function [17]

$$H_{u,v} = \gamma_L + \frac{\gamma_H}{1+(D_0 / D_{u,v})^2} \tag{11a}$$

with

$$D_{u,v} = \sqrt{(u-N/2)^2 + (v-N/2)^2} \tag{11b}$$

where $D_0 = 1.8$, is the cut of frequency of the filter, and $\gamma_L = 0.4$, $\gamma_H = 0.6$, are the gains for the low and high frequencies respectively, $u$, $v$, are the spatial coordinates of the frequency transformed image, and $N$ the dimensions of the image in the $u$, $v$, space.

This form of filtering sharpens features and flattens speckle variations in an image.

*F. Diffusion Filtering*

Diffusion filters remove noise from an image by modifying the image via solving a partial differential equation (PDE). The smoothing is carried out depending on the image edges and their directions. Anisotropic diffusion is an efficient nonlinear technique for simultaneously performing contrast enhancement and noise reduction. It smoothes homogeneous image regions but retains image edges [5], [22], [23] without requiring any information from the image power

spectrum. It may thus directly be applied to logarithmic compressed images. Consider applying the isotropic diffusion equation given by $dg_{i,j,t}/dt = div(d\nabla g)$ using the original noisy image, $g_{i,j,t=0}$, as the initial condition, where $g_{i,j,t=0}$ is an image in the continuous domain, $i, j$, specifies spatial position, $t$, is an artificial time parameter, $d$, is the diffusion constant, and $\nabla g$, is the image gradient. Modifying the image according to this linear isotropic diffusion equation is equivalent to filtering the image with a Gaussian filter. In this Section we will present conventional anisotropic diffusion (*ad*) and coherent nonlinear anisotropic diffusion (*nldif*).

*1) Anisotropic Diffusion Filtering (ad)*

Perona and Malik [23] replaced the classical isotropic diffusion equation, as described above, by the introduction of a function, $d_{i,j,t} = f(|\nabla g|)$, that smoothes the original image while trying to preserve brightness discontinuities with

$$\frac{dg_{i,j,t}}{dt} = div\left[d_{i,j,t}\nabla g_{i,j,t}\right] = \left[\frac{d}{di}d_{i,j,t}\frac{d}{di}g_{i,j,t}\right] + \left[\frac{d}{dj}d_{i,j,t}\frac{d}{dj}g_{i,j,t}\right] \qquad (12\text{ a})$$

where $|\nabla g|$, is the gradient magnitude, and $d(|\nabla g|)$, is an edge stopping function, which is chosen to satisfy $d \to 0$ when $|\nabla g| \to \infty$ so that the diffusion is stopped across edges. This function, called the diffusion coefficient, $d(|\nabla g|)$, which is a monotonically decreasing function of the gradient magnitude, $|\nabla g|$, yields intra-region smoothing not inter-region smoothing [19], [20], [22], [23] by impeding diffusion at image edges. It increases smoothing parallel to the edge and stops smoothing perpendicular to the edge, as the highest gradient values are perpendicular to the edge and dilated across edges. The choice of $d(|\nabla g|)$, can greatly affect the extent to which discontinuities are preserved. For example if $d(|\nabla g|)$, is constant at all locations, then smoothing progresses in an isotropic manner. If $d(|\nabla g|)$, is allowed to vary according to the local image gradient, then we have anisotropic diffusion. A

basic anisotropic PDE is given in (12 a). Two different diffusion coefficients were proposed in [23] and also derived in [22]. The diffusion coefficient suggested were

$$d(|\nabla g|) = \frac{1}{1+(|\nabla g_{i,j}|/K)^2}, \tag{12 b}$$

where K, in (12 b) is a positive gradient threshold parameter, known as diffusion or flow constant [22]. In our study the diffusion coefficient in (12 b) was used as it was found to perform better in our images of carotid artery.

A discrete formulation of the anisotropic diffusion in (12 a) is [2], [22], [23]

$$\frac{dg_{i,j}}{dt} = \frac{\lambda}{|\eta_s|}\{d_{i+1,j,t}[g_{i+1,j}-g_{i,j}]+d_{i-1,j,t}[g_{i-1,j}-g_{i,j}]+d_{i,j+1,t}[g_{i,j+1}-g_{i,j}]+d_{i,j-1,t}[g_{i,j-1}-g_{i,j}]\} \tag{13 a}$$

where the new pixel gray value, $f_{i,j}$, at location $i,j$, is

$$f_{i,j} = g_{i,j} + \frac{1}{4}\frac{dg_{i,j}}{dt}, \tag{13 b}$$

where $d_{i+1,j,t}, d_{i-1,j,t}$, $d_{i,j+1,t}$, and $d_{i,j-1,t}$, are the diffusion coefficients for the west, east, north and south pixel directions, in a four pixel neighborhood, around the pixel $i,j$, where diffusion is computed respectively. The coefficient of variation leads to the largest diffusion where the nearest-neighbor difference is largest (largest edge), while the smallest diffusion is calculated where the nearest-neighbor difference is smallest (the weakest edge). The constant, $\lambda \in \Re^+$, is a scalar that determines the rate of diffusion, $\eta_s$, represents the spatial neighborhood of pixel, $i,j$, and $|\eta_s|$, is the number of neighbors (usually four except at the image boundaries). Perona and Malik [23] linearly approximated the directional derivative in a particular direction as, $\nabla g_{i,j} = g_{i+1,j} - g_{i,j}$, (for the east direction of the central pixel $i,j$). Modifying the image according to the above equation in (13), which is a linear isotropic diffusion equation, is equivalent to filtering the image with a Gaussian filter. The parameters for the anisotropic diffusion filter used in this study were, $\lambda = 0.25$, $\eta_s = 8$, and the parameter $K = 30$, which was used for the calculation of the edge stopping function $d(|\nabla g|)$, in (12b).

*2) Coherent Nonlinear Anisotropic Diffusion Filtering (nldif)*

The applicability of the *ad* filter (12) is restricted to smoothing with edge enhancement, where $|\nabla g|$, has higher magnitude at edges. In general, the function $d(|\nabla g|)$, in (12) can be put into a tensor form that measures local coherence of structures such that the diffusion process becomes more directional in both the gradient and the contour directions, which represent the directions of maximum and minimum variations, respectively. Therefore, the *nldif* filter will take the form

$$\frac{dg_{i,j,t}}{dt} = div[D\nabla g] \tag{14}$$

where $D \in \Re^{2x2}$, is a symmetric positive semi-definite diffusion tensor representing the required diffusion in both gradient and contour directions and, hence, enhancing coherent structures as well as edges. The design of $D$, as well as the derivation of the coherent nonlinear anisotropic diffusion model may be found in [24] and is given as

$$D = (\omega_1 \;\; \omega_2) \begin{pmatrix} \lambda_1 & 0 \\ 0 & \lambda_2 \end{pmatrix} \begin{pmatrix} \omega_1^T \\ \omega_2^T \end{pmatrix} \tag{14a}$$

with

$$\lambda_1 = \begin{cases} \alpha\left(1 - \dfrac{(\mu_1 - \mu_2)^2}{s^2}\right) & if \;\; (\lambda_1 - \lambda_2)^2 \le s^2 \\ 0, & else \end{cases}, \tag{14b}$$

$$\lambda_2 = \alpha.$$

where the eigenvectors $\omega_1$, $\omega_2$ and the eigenvalues $\lambda_1$, $\lambda_2$ correspond to the directions of maximum and minimum variations and the strength of these variations, respectively. The flow at each point is affected by the local coherence, which is measured by $(\mu_1 - \mu_2)$ in (14b).

The parameters used in this study for the *nldif* filter were, $s^2 = 2$, and $\alpha = 0.9$, which were used for the calculation of the diffusion tensor $D$, and the parameter step size $m = 0.2$, which defined the number of diffusion steps performed. The local coherence is close to zero in very

noisy regions and diffusion must become isotropic ($\mu_1 = \mu_2 = \alpha = 0.9$), whereas in regions with lower speckle noise the local coherence must correspond to $(\mu_1 - \mu_2)^2 > s^2$ [24].

*G. Wavelet Filtering (waveltc)*

Speckle reduction filtering in the wavelet domain, used in this study, is based on the idea of the Daubenchies Symlet wavelet and on soft-thresholding denoising. It was first proposed by Donoho [29] and also investigated by [25], [26], [38]. The Symmlets family of wavelets, although not perfectly symmetrical, were designed to have the least asymmetry and highest number of vanishing moments for a given compact support [29]. The *waveltc* filter, implemented in this study is described as follows

i) Estimate the variance of the speckle noise, $\sigma_n^2$, from the logarithmic transformed noisy image, with (8).

ii) Compute the discrete wavelet transform (DWT), using the Symlet wavelet for two scales.

iii) For each sub-band

a. Compute a threshold [27], [29]

$$T = \begin{cases} (T_{\max} - \alpha(j-1))\sigma_n & \text{if } T_{\max} - \alpha(j-1) \succ T_{\min} \\ T_{\min}\sigma_n, & \text{else} \end{cases} \quad (15)$$

where $\alpha$, is a decreasing factor between two consecutive levels, $T_{\max}$, is a maximum factor for $\sigma_n$, while $T_{\min}$, is a minimum factor. The threshold $T$, is primarily calculated using, $\sigma_n$, and a decreasing factor, $T_{\max} - \alpha(j-1)$.

b. Apply the thresholding procedure in a. on the wavelet coefficients in (ii).

iv) Invert the multiscale decomposition to reconstruct the despeckled image, $f$.

## III. METHODOLOGY

### A. Material

A total of 440 ultrasound images of the carotid artery bifurcation, 220 asymptomatic and 220 symptomatic were investigated in this study. Asymptomatic images were recorded from patients at risk of atherosclerosis in the absence of clinical symptoms, whereas symptomatic images were recorded from patients at risk of atherosclerosis, which have already developed clinical symptoms, such as a stroke episode.

### B. Recording of Ultrasound Images

In this study ultrasound images of the carotid artery bifurcation were acquired using the ATL HDI-3000 ultrasound scanner. The ATL HDI-3000 ultrasound scanner is equipped with 64 elements fine pitch high-resolution, 38 mm broadband array, a multi element ultrasound scan head with an operating frequency range of 4-7 MHz, an acoustic aperture of 10x8 mm and a transmission focal range of 0.8-11 cm [39]. In this work all images were recorded as they are displayed in the ultrasound monitor, after logarithmic compression. The images were recorded digitally on a magneto optical drive, with a resolution of 768x756 pixels with 256 gray levels. The image resolution was 16.66 pixels/mm.

### C. Despeckle Filtering

Ten despeckle filters were investigated as presented in Section II, and were applied on the 440 logarithmically compressed ultrasound images.

### D. Texture Analysis

Texture provides useful information for the characterization of atherosclerotic plaque [40]. In this study a total of 56 different texture features were extracted both from the original and the despeckled images as follows [40], [41]:

*(i) Statistical Features (SF):* 1) Mean, 2) Median, 3) Variance ($\sigma^2$), 4) Skewness ($\sigma^3$), 5) Kurtosis ($\sigma^4$), and 6) Speckle index ($\sigma/m$). *(ii) Spatial Gray Level Dependence Matrices*

*(SGLDM)* as proposed by Haralick et al. [41]: 1) Angular second moment, 2) Contrast, 3) Correlation, 4) Sum of squares: variance, 5) Inverse difference moment, 6) Sum average, 7) Sum variance, 8) Sum entropy, 9) Entropy, 10) Difference variance, 11) Difference entropy, 12), and 13) Information measures of correlation. Each feature was computed using a distance of one pixel. Also for each feature the mean values and the range of values were computed, and were used as two different feature sets. *(iii) Gray Level Difference Statistics (GLDS)* [42]: 1) Contrast, 2) Angular second moment, 3) Entropy, and 4) Mean. *(iv) Neighbourhood Gray Tone Difference Matrix (NGTDM)* [43]: 1) Coarseness, 2) Contrast, 3) Business, 4) Complexity, and 5) Strength. *(v) Statistical Feature Matrix (SFM)* [44]: 1) Coarseness, 2) Contrast, 3) Periodicity, and 4) Roughness. *(vi) Laws Texture Energy Measures (TEM)* [44]: For the laws TEM extraction, vectors of length $l = 7$, $L = (1,6,15,20,15,6,1)$, $E = (-1,-4,-5,0,5,4,1)$ and $S = (-1,-2,1,4,1-2,-1)$ were used, where $L$ performs local averaging, $E$ acts as an edge detector and $S$ acts as a spot detector. The following TEM features were extracted: 1) LL - texture energy (TE) from LL kernel, 2) EE - TE from EE kernel, 3) SS - TE from SS kernel, 4) LE - average TE from LE and EL kernels, 5) ES - average TE from ES and SE kernels, and 6) LS - average TE from LS and SL kernels. *(vii) Fractal Dimension Texture Analysis (FDTA)* [44]: Hurst coefficient, $H^{(k)}$, for resolutions $k$=1, 2, 3, 4. *(viii) Fourier Power Spectrum (FPS)* [44]: 1) Radial sum, and 2) Angular sum.

*E. Distance Measures*

In order to identify the most discriminant features separating asymptomatic and symptomatic ultrasound images, before and after despeckle filtering the following distance measure was computed for each feature [40]

$$dis_{zc} = |m_{za} - m_{zs}| / \sqrt{\sigma_{za}^2 + \sigma_{zs}^2} \tag{16}$$

where $z$ is the feature index, $c$ if $o$ indicates the original image set and if $f$ indicates the despeckled image set, $m_{za}$ and $m_{zs}$ are the mean values and $\sigma_{za}$ and $\sigma_{zs}$ are the standard deviations of the asymptomatic and symptomatic classes respectively. The most discriminant

features are the ones with the highest distance values [40]. If the distance after despeckle filtering is increased i.e.

$$dis_{zf} > dis_{zo} \tag{17}$$

then it can be derived that the classes may be better separated.

For each feature, a percentage distance was computed as

$$feat_dis_z = (dis_{zf} - dis_{zo})100. \tag{18}$$

For each feature set, a score distance was computed as

$$Score_Dis = (1/N)\sum_{z=1}^{N}(dis_{zf} - dis_{zo})100 \tag{19}$$

where N is the number of features in the feature set. It should be noted that for all features a larger feature distance shows improvement.

*F. Univariate Statistical Analysis*

The Wilcoxon rank sum test was used in order to detect if for each texture feature a significant (S) difference or not (NS) exists between the original and the despeckled images at $p<0.05$.

*G. kNN Classifier*

The statistical k-nearest-neighbour (kNN) classifier using the Euclidean distance with k=7 was also used to classify a plaque image as asymptomatic or symptomatic [40]. The leave-one-out method was used for evaluating the performance of the classifier, where each case is evaluated in relation to the rest of the cases. This procedure is characterized by no bias concerning the possible training and evaluation bootstrap sets. The kNN classifier was chosen because it is simple to implement and computationally very efficient. This is highly desired due to the many feature sets and filters tested [44].

*H. Image Quality Evaluation Metrics*

Differences between the original, $g_{i,j}$, and the despeckled, $f_{i,j}$, images were evaluated using image quality evaluation metrics. The following measures, which are easy to compute and have clear physical meaning, were computed

a) The MSE

$$MSE = \frac{1}{MN}\sum_{i=1}^{M}\sum_{j=1}^{N}(g_{i,j} - f_{i,j})^2 \tag{20}$$

which measures the quality change between the original and processed image in an $MxN$ window [45].

b) The root MSE (RMSE), which is the square root of the squared error averaged over an $MxN$ window [46]

$$RMSE = \sqrt{\frac{1}{MN}\sum_{i=1}^{M}\sum_{j=1}^{N}(g_{i,j} - f_{i,j})^2}\,. \tag{21}$$

c) The error summation in the form of the Minkowski metric, which is the norm of the dissimilarity between the original and the despeckled images [47]

$$Err = \left(\frac{1}{MN}\sum_{i=1}^{M}\sum_{j=1}^{N}\left|g_{i,j} - f_{i,j}\right|^{\beta}\right)^{1/\beta} \tag{22}$$

computed for $\beta = 3$ ($Err_3$) and $\beta = 4$ ($Err_4$). For $\beta = 2$, the $RMSE$ is computed as in (21), whereas for $\beta = 1$, the absolute difference, and for $\beta = \infty$ the maximum difference measure.

d) The Geometric Average Error ($GAE$) is computed as follows [48]. The $GAE$ is approaching zero, if there is a very good transformation (small differences) between the original and the despeckled image, and high vice versa. This measure is also used for tele-ultrasound, when transmitting ultrasound images and is defined as

$$GAE = \left(\prod_{i=1}^{M}\prod_{j=1}^{N}\sqrt{g_{i,j} - f_{i,j}}\right)^{1/MN}. \tag{23}$$

e) The SNR is given by [49]

$$SNR = 10\log_{10}\frac{\sum_{i=1}^{M}\sum_{j=1}^{N}(g_{i,j}^2 + f_{i,j}^2)}{\sum_{i=1}^{M}\sum_{j=1}^{N}(g_{i,j} - f_{i,j})^2}. \tag{24}$$

f) The peak SNR (PSNR) is computed using [49]

$$PSNR = -10\log_{10}\frac{MSE}{g_{\max}^2} \tag{25}$$

where $g_{\max}^2$, is the maximum intensity in the unfiltered image. The $PSNR$ is higher for a better-transformed image and lower for a poorly transformed image. It measures image fidelity that is how closely the despeckled image resembles the original image.

g) The mathematically defined universal quality index [50] models any distortion as a combination of three different factors, which are: loss of correlation, luminance distortion, and contrast distortion and is derived as

$$Q = \frac{\sigma_{gf}}{\sigma_f\sigma_g}\cdot\frac{2\bar{f}\bar{g}}{(\bar{f})^2+(\bar{g})^2}\cdot\frac{2\sigma_f\sigma_g}{\sigma_f^2+\sigma_g^2}, \qquad -1<Q<1 \tag{26}$$

where $\bar{g}$, and $\bar{f}$ represent the mean of the original and despeckled values with their standard deviations, $\sigma_g$, and $\sigma_f$, of the original and despeckled values of the analysis window, and $\sigma_{gf}$ represents the covariance between the original and despeckled windows. Q is computed for a sliding window of size 8x8 without overlapping. Its highest value is 1 if $g_{i,j} = f_{i,j}$, while its lowest value is –1 if $f_{i,j} = 2\bar{g} - g_{i,j}$.

h) The structural similarity index between two images [47], which is a generalization of (26) is given by

$$SSIN = \frac{(2\bar{g}\bar{f} + c_1)(2\sigma_{gf} + c_2)}{(\bar{g}^2 + \bar{f}^2 + c_1)(\sigma_g^2 + \sigma_f^2 + c_2)}, \qquad -1 < SSIN < 1. \tag{27}$$

where $c_1 = 0.01dr$ and $c_2 = 0.03dr$, with $dr = 255$ representing the dynamic rage of the ultrasound images. The range of values for the SSIN lies between –1, for a bad and 1 for a good similarity between the original and despeckled images respectively. It is computed, similarly to the Q measure, for a sliding window of size 8x8 without overlapping.

It is noted that a new image quality metric based on natural scene statistics, and mutual information between the original and the filtered images has recently been proposed by Sheikh, Bovik, and Veciana [51]. This metric will be investigated in a future study.

*I. Visual Evaluation by Experts*

Visual evaluation can be broadly categorized as the ability of an expert to extract useful anatomical information from an ultrasound image. The visual evaluation varies of course from expert to expert and is subject to the observer's variability [52]. The visual evaluation, in this study, was carried out according to the ITU-R recommendations with the Double Stimulus Continuous Quality Scale (DSCQS) procedure [48]. A total of 100 ultrasound images of the carotid artery bifurcation (50 asymptomatic and 50 symptomatic) were evaluated visually by two vascular experts, a cardiovascular surgeon, and a neurovascular specialist before and after despeckle filtering. For each case, the original and the despeckled images (despeckled with filters *lsmv, lsminsc, median, wiener, homog, gf4d, homo, ad, nldif, and waveltc*) were presented without labelling at random to the two experts. The experts were asked to assign a score in the one to five scale corresponding to low and high subjective visual perception criteria. Five was given to an image with the best visual perception. Therefore the maximum score for a filter is 500, if the expert assigned the score of five for all the 100 images. For each filter, the score was divided by five to be expressed in percentage format. The experts were allowed to give equal scores to more than one image in each case. For each class and for each filter the average score was computed.

The two vascular experts evaluated the area around the distal common carotid, 2-3 cm before the bifurcation and the bifurcation. It is known that measurements taken from the far wall of the carotid artery are more accurate than those taken from the near wall [53]. Furthermore, the experts were examining the image in the lumen area, in order to identify the existence of a plaque or not.

## IV. RESULTS

In this Section we present the results of the 10 despeckle filters described in Section II, applied on 220 asymptomatic and 220 symptomatic ultrasound images of the carotid artery bifurcation. A total of 56 texture features were computed and the most discriminant ones are presented. Furthermore the performance of these filters is investigated for discriminating between asymptomatic and symptomatic images using the statistical kNN classifier. Moreover, nine different image quality evaluation metrics were computed, as well as visual evaluation scores carried out by two experts.

### *A. Evaluation of Despeckle Filtering on a Symptomatic Ultrasound Image*

Figure 2 shows an ultrasound image of the carotid together with the despeckled images. The best visual results as assessed by the two experts were obtained by the filters *lsmv* and *lsminsc*, whereas the filters *gf4d*, *ad*, and *nldif* also showed good visual results but smoothed the image considerably and thus edges and subtle details may be lost. Filters that showed a blurring effect are the *median*, *wiener*, *homog*, and *waveltc*. Filters *wiener*, *homog*, and *waveltc* showed poorer visual results.

FIGURE 2 [here]

### *B. Texture Analysis: Distance Measures, Table II*

Despeckle filtering and texture analysis were carried out on 440 ultrasound images of the carotid. Table II tabulates the results of $feat_dis_z$ (18), and $Score_Dis$ (19), for SF, SGLDM range of values and NGTDM feature sets for the 10 despeckle filters. The results of these feature sets are presented only, since were the ones with the best performance. The filters are categorized in local statistics, median, maximum homogeneity (HF), geometric (GF), homomorphic (HM), diffusion and wavelet filters, as introduced in Sections I and II. Also the number of iterations (Nr. of It.) for each filter is given, which was selected based on C and on the visual evaluation of the two experts. When C was minimally changing then the filtering process was stopped. The bolded values represent the values that showed an improvement after

despeckle filtering compared to the original. The last row in each sub-table shows the $Score_Dis$ for all features, where the highest value indicates the best filter in the sub-table. Additionally, a total score distance $Score_Dis_T$ was computed for all feature sets shown in the last row of Table II. Some of the despeckle filters, shown in Table II, are changing a number of texture features, by increasing the distance between the two classes, (positive values in Table II), and therefore making the identification and separation between asymptomatic and symptomatic plaques more feasible. A positive feature distance shows improvement after despeckle filtering, whereas a negative shows deterioration.

In the first part of Table II the results of the SF features are presented, where the best $Score_Dis$ is given for the filter *homo* followed by the *lsminsc, lsmv, homog, nldif, waveltc, median,* and *wiener*, with the worst $Score_Dis$ given by *gf4d*. All filters reduced the speckle index, C. Almost all filters reduced significantly the variance, $\sigma^2$, and the kurtosis, $\sigma^3$, of the histogram, as it may be seen from the bolded values in the first part of Table II.

In the second part of the Table II the results of the SGLDM-Range of values features set are tabulated. The filters with the highest $Score_Dis$ in the SGLDM range of values features set, are *homo*, *lsminsc*, *median, ad,* and *homog,* whereas all other the filters (*nldif, wiener, waveltc, gf4d, lsmv)* are presenting a negative $Score_Dis$. Texture features, which improved in most of the filters, are the contrast, correlation, sum of squares variance, sum average, and sum variance.

In the third part of Table II, for the NGTDM feature set almost all filters showed an improvement in $Score_Dis$. Best filters in the NGTDM feature set were, the *homo, lsminsc, homog*, and *lsmv*. Texture features improved at most were the completion, coarseness and contrast. The completion of the image was increased by all filters.

Finally, in the last row of Table II, the total score distance, $Score_Dis_T$, for all feature sets is shown, where best values were obtained by the filters *homo*, *lsminsc*, *median*, *lsmv*, *homog*, and *ad*.

TABLE II [here]

*C. Texture Analysis: Univariate Statistical Analysis, Table III*

Table III shows the results of the rank sum test, which was performed on the SGLDM range of values features set of Table II, for the 10 despeckle filters. The test was performed to check if significant differences exist between the features computed on the 440 original and the 440 despeckled images. Filters that resulted with the most significant number of features after despeckle filtering as shown with the score row of Table III were the following: *lsmv, gf4d, lsminsc* and *nldif*. The rest of the filters gave a lower number of significantly different features. Features that showed a significant difference after filtering were the inverse difference moment, IDM, angular second moment, ASM, sum of entropy, contrast, correlation, sum of squares variance, SOSV, and sum variance, $\sum Var$. These features were mostly affected after despeckle filtering and they were significantly different.

TABLE III [here]

*D. Texture Analysis: kNN Classifier, Table IV*

Table IV shows the percentage of correct classifications score for the kNN classifier with k=7 for classifying a subject as asymptomatic or symptomatic. The classifier was evaluated using the leave one out method [44], on 220 asymptomatic, and 220 symptomatic images on the original, and despeckled images. The percentage of correct classifications score is given for the following feature sets: Statistical Features, SF, Spatial Gray Level Dependence Matrix Mean Values, SGLDMm, Spatial Gray Level Dependence Matrix Range of Values, SGLDMr, Gray Level Difference Statistics, GLDS, Neighborhood Gray Tone Difference Matrix, NGTDM, Statistical Feature Matrix, SFM, Laws Texture Energy Measures, TEM, Fractal Dimension Texture Analysis, FDTA, and Fourier Power Spectrum, FPS. Filters that showed an improvement in classifications success score compared to that of the original image set, were in average (last row of Table IV) the filter *homo* (3 %), *gf4d* (1%), and *lsminsc* (1%).

TABLE IV [here]

Feature sets, which benefited mostly by the despeckle filtering were the SF, GLDS, NGTDM, and TEM when counting the number of cases that the correct classifications score was

improved. Less improvement was observed, for the feature sets FDTA, SFM, SGLDMm, FPS and SGLDMr. For the feature set SGLDMr better results are given for the *lsminsc* filter with an improvement of 2%. This is the only filter that showed an improvement for this class of features. For the feature set TEM the filter *lsmv* shows the best improvement with 9%, whereas for the FPS feature set the filter *lsminsc* gave the best improvement with 5%. The filter *lsminsc* showed improvement in the GLDS and NGTDM feature sets, whereas the filter *lsmv* showed improvement for the feature sets SF and TEM.

*E. Image Quality Evaluation Metrics, Table V*

Table V tabulates the image quality evaluation metrics presented in Section III.H, for the 220 asymptomatic and 220 symptomatic ultrasound images between the original and the despeckled images respectively. Best values were obtained for the *nldif*, *lsmv* and *waveltc* with lower MSE, RMSE, Err3, and Err4 and higher SNR and PSNR. The GAE was 0.00 for all cases, and this can be attributed to the fact that the information between the original and the despeckled images remains unchanged. Best values for the universal quality index, Q, and the structural similarity index, SSIN were obtained for the filters *lsmv* and *nldif*.

TABLE V [here]

*F. Visual Evaluation by Experts, Table VI*

Table VI shows the results of the visual evaluation of the original and despeckled images made by two experts, a cardiovascular surgeon and a neurovascular specialist. The last row of Table VI presents the overall average percentage (%) score assigned by both experts for each filter.

TABLE VI [here]

For the cardiovascular surgeon, the average score, showed that the best despeckle filter is the *lsmv* with a score of 62%, followed by *gf4d*, *median*, *homog* and *original* with scores of 52%, 50%, 45% and 41% respectively. For the neurovascular specialist, the average score showed that the best filter is the *gf4d* with a score of 72%, followed by *lsmv*, *original*, *lsminsc*

and *median* with scores of 71%, 68%, 68% and 66% respectively. The overall average % score shows that the highest score was given to the filter *lsmv* (67%), followed by *gf4d* (62%), *median* (58%), and *original* (54%). It should be emphasized that the despeckle filter *lsmv* is the only filter that was graded with a higher score than the original by both experts for the asymptomatic and symptomatic image sets.

We may observe a difference in the scorings between the two vascular specialists and this is because, the cardiovascular surgeon is primarily interested in the plaque composition and texture evaluation whereas the neurovascular specialist is interested to evaluate the degree of stenosis and the lumen diameter in order to identify the plaque contour. Filters *lsmv* and *gf4d* were identified as the best despeckle filters, by both specialists as they improved visual perception with overall average scores of 67% and 62% respectively. The filters *waveltc* and *homo* were scored by both specialists with the lowest overall average scores of 28% and 29% respectively.

By examining the visual results of Fig. 2, the statistical results of Tables II-V and the visual evaluation of Table VI we can conclude that the best filters are *lsmv* and *gf4d*, which may be used for both plaque composition enhancement and plaque texture analysis, whereas the filters *lsmv, gf4d* and *lsminsc* are more appropriate to identify the degree of stenosis and therefore may be used when the primary interest is to outline the plaque borders.

## V. DISCUSSION

Despeckle filtering is an important operation in the enhancement of ultrasound images of the carotid artery, both in the case of texture analysis, and in the case of image quality evaluation and visual evaluation by the experts. In this study a total of 10 despeckle filters were comparatively evaluated on 440 ultrasound images of the carotid artery bifurcation, and the validation results are summarised in Table VII.

As given in Table VII, filters *lsmv, lsminsc,* and *homo*, improved the class separation between the asymptomatic and the symptomatic classes (see also Table II). Filters *lsmv*, *lsminsc*, and *gf4d* gave a high number of significantly different features (see Table III). Filters *lsminsc*,

*gf4d*, and *homo*, gave only a marginal improvement in the percentage of correct classifications success rate (see Table IV). Moreover, filters *lsmv*, *nldif*, and *waveltc*, gave better image quality evaluation results (see Table V). Filters *lsmv*, and *gf4d*, improved the visual assessment carried out by the experts (see Table VI). It is clearly shown that filter *lsmv* gave the best performance, followed by filters *lsminsc*, and *gf4d* (see Table VII). Filter *lsmv* or *gf4d* can be used for despeckling asymptomatic images where the expert is interested mainly in the plaque composition and texture analysis. Filters *lsmv* or *gf4d* or *lsmnsc* can be used for despeckling of symptomatic images where the expert is interested in identifying the degree of stenosis and the plaque borders. Filters *homo*, *nldif*, and *waveltc* gave poorer performance.

Filter *lsmv* gave very good performance, with respect to: (i) preserving the mean and the median as well as decreasing the variance and the speckle index of the image, (ii) increasing the distance of the texture features between the asymptomatic and the symptomatic classes, (iii) significantly changing the SGLDM range of values texture features after filtering based on the Wilcoxon rank sum test, (iv) marginally improving the classification success rate of the kNN classifier for the classification of asymptomatic and symptomatic images in the cases of SF, SMF and TEM feature sets, and (v) improving the image quality of the image. The *lsmv* filter, which is a simple filter, is based on local image statistics. It was first introduced in [14], [9], [15] by Jong-Sen Lee and co-workers and it was tested on a few SAR images with satisfactory results. It was also used for SAR imaging in [13] and image restoration in [16], again with satisfactory results.

TABLE VIII [here]

Filter *lsminsc* gave the best performance with respect to: (i) preserving the mean, as well as decreasing the variance and the speckle index and increasing the contrast of the image, (ii) increasing the distance of the texture features between the asymptomatic and the symptomatic classes, (iii) significantly changing the SGLDM texture features after filtering based on the Wilcoxon rank sum test, (iv) improving the classification success rate of the kNN classifier for the classification of asymptomatic and symptomatic images in the cases of SF, SGLDMr, GLDS, NGTDM, FDTA and FPS feature sets. Filter *lsminsc* was originally introduced by

Nagao in [32] and was tested on an artificial and a SAR image with satisfactory performance. In this study the filter was modified, by using the speckle index instead of the variance value for each sub window (as described in Section II.A.2, equation (9)).

Filter *gf4d* gave very good performance with respect to: (i) decreasing the speckle index, (ii) marginally increasing the distance of the texture features between the asymptomatic and the symptomatic classes, (iii) significantly changing the SGLDM range of values texture features after filtering based on the Wilcoxon rank sum test, (iv) improving the classification success rate of the kNN classifier for the classification of asymptomatic and symptomatic images in the cases of SGLDMm, GLDS, NGTDM, SFM and TEM feature sets. The geometric filter *gf4d* was introduced by Crimmins [10], and was tested visually on a few SAR images with satisfactory results.

Filters used for speckle reduction in ultrasound imaging by other investigators include: *median* [33] *wiener* [13], *homog* [8], *homo* [17], [18], *ad* [5], and *waveltc* [29]. However, these filters were evaluated on a small number of images, and their performance was tested based only on the mean, median, standard deviation and speckle index of the image before and after filtering.

The *median* and the *wiener* filters were originally used by many researchers for suppressing the additive and later for suppressing the multiplicative noise in different types of images [2]-[9], [13], [33]. The results of this study showed that the *wiener* and *median* filters were not able to remove the speckle noise and produced blurred edges in the filtered image (see Fig. 2). In this study the *median* filter performed poorer as shown in Tables II and III, and IV.

The *homog* [8] and *homo* [2], [17], [18] filters, were recently used by some researchers for speckle reduction but our results in Tables II and III, V and the visual evaluation of the experts in Table VI showed poor performance especially for the *homo* filter.

Anisotropic diffusion is an efficient nonlinear technique for simultaneously performing contrast enhancement and noise reduction. It smoothes homogeneous image regions but retains image edges [23]. Anisotropic diffusion filters usually require many iteration steps compared with the local statistic filters. In a recent study [5], speckle reducing anisotropic diffusion

filtering was proposed as the most appropriate filter for ultrasound images of the carotid artery. However, in this study, *ad*, as shown in Tables II, III, IV, V and VI performed poorer compared to *lsmv*, *gf4d* and *lsminsc*.

Furthermore, wavelet filtering proposed by Donoho in [29], was investigated for suppressing the speckle noise in SAR images [15], [35], real world images [25] and ultrasound images [26] with favourable results. In this study, it is shown that the *waveltc* filter gave poorer performance for removing the speckle noise from the ultrasound images of the carotid artery (Tables II, III).

In conclusion, despeckle filtering is an important operation in the enhancement of ultrasonic imaging of the carotid artery. In this study it was shown that simple filters based on local statistics (*lsmv* and *lsminsc*) and geometric filtering (*gf4d*) could be used successfully for the processing of these images. In this context, despeckle filtering can be used as a pre-processing step for the automated segmentation of the IMT [54] and the carotid plaque, followed by the carotid plaque texture analysis, and classification. This field is currently being investigated by our group [55]. Initial findings show promising results, however, further work is required to evaluate the performance of the suggested despeckle filters at a larger scale as well as their impact in clinical practise. In addition, the usefulness of the proposed despeckle filters, in portable ultrasound systems and in wireless telemedicine systems still has to be investigated.

## ACKNOWLEDGMENT

This work was partly funded through the project *Integrated System for the Support of the Diagnosis for the Risk of Stroke (IASIS),* of the 5th Annual Program for the Financing of Research of the Research Promotion Foundation of Cyprus 2002-2005, as well as, through the project *Integrated System for the Evaluation of Ultrasound Imaging of the Carotid Artery (TALOS)*, of the Program for Research and Technological Development 2003-2005, of the Research Promotion Foundation of Cyprus.

## REFERENCES


[1] D. Lamont, L. Parker, M. White, N. Unwin, et al., "Risk of cardiovascular disease measured by carotid intima-media thickness at age 49-51: life course study," *BMJ*, vol. 320, pp. 273-278, 29 Jan. 2000.

[2] C.B. Burckhardt, "Speckle in ultrasound B-mode scans," *IEEE Trans. Sonics and Ultrasonics*, vol. SU-25, no. 1, pp. 1-6, 1978.

[3] R.F. Wagner, S.W. Smith, J.M. Sandrik, and H. Lopez, "Statistics of speckle in ultrasound B-scans," *IEEE Trans. Sonics Ultrasonics*, vol. 30, pp. 156-163, 1983.

[4] J.W. Goodman, "Some fundamental properties of speckle," *J. of Optical Society of America*, vol. 66, no. 11, pp. 1145-1149, 1976.

[5] Y. Yongjian and S.T. Acton, "Speckle reducing anisotropic diffusion," *IEEE Trans. Image Processing*, vol. 11, no. 11, pp. 1260–1270, Nov. 2002.

[6] R.W. Prager, A.H. Gee, G.M. Treece, and L. Berman, "Speckle detection in ultrasound images using first order statistics," University of Cambridge, Dept. of Engineering, GUED/F-INFENG/TR 415, pp. 1-17, July 2002.

[7] C. Loizou, C. Christodoulou, C.S. Pattichis, R. Istepanian, M. Pantziaris, and A. Nicolaides, "Speckle reduction in ultrasound Images of atherosclerotic carotid plaque," DSP 2002, Proc. *IEEE 14th Int. Conf. on Digital Signal Processing*, vol. 2, pp. 525-528, July 2002.

[8] C.I. Christodoulou, C. Loizou, C.S. Pattichis, M. Pantziaris, E. Kyriakou, M.S. Pattichis, C.N. Schizas, and A. Nicolaides,"Despeckle filtering in ultrasound imaging of the carotid artery," *Second Joint EMBS/BMES Conference*, Houston, TX, USA, pp. 1027-1028, Oct. 23-26, 2002.

[9] J.S. Lee, "Speckle analysis and smoothing of synthetic aperture radar images," *Computer Graphics and Image Processing*, vol. 17, pp. 24-32, 1981.

[10] L. Busse, T.R. Crimmins, and J.R. Fienup, "A model based approach to improve the performance of the geometric filtering speckle reduction algorithm," *IEEE Ultrasonic Symposium*, pp. 1353-1356, 1995.

[11] D.T. Kuan, A. A. Sawchuk, T. C. Strand, and P. Chavel, "Adaptive restoration of images with speckle," *IEEE Trans. Acoustic Speech and Signal Processing*, vol. ASSP-35, pp. 373-383, 1987.

[12] M. Insana, et al., "Progress in quantitative ultrasonic imaging," *SPIE Vol. 1090 Medical Imaging III, Image Formation*, pp. 2-9, 1989.

[13] V.S. Frost, J.A. Stiles, K.S. Shanmungan, and J.C. Holtzman, "A model for radar images and its application for adaptive digital filtering of multiplicative noise," *IEEE Trans. Pattern Analysis and Machine Intelligence*, vol. 4, no. 2, pp.157-165, 1982.

[14] J.S. Lee, "Digital image enhancement and noise filtering by using local statistics," *IEEE Trans. Pattern Analysis and Machine Intelligence*, PAMI-2, no. 2, pp. 165-168, 1980.

[15] J.S. Lee, "Refined filtering of image noise using local statistics," *Computer Graphics and Image Processing*, vol. 15, pp. 380-389, 1981.

[16] D.T.Kuan and A.A.Sawchuk, "Adaptive noise smoothing filter for images with signal dependent noise," *IEEE Trans. Pattern Analysis and Machine Intelligence*, vol. PAMI-7, no. 2, pp. 165-177, 1985.

[17] S. Solbo, and T. Eltoft, "Homomorphic wavelet based-statistical despeckling of SAR images," *IEEE Trans. Geosc. Remote Sensing*, vol. 42, no. 4, pp. 711-721, 2004.

[18] J. Saniie, T. Wang, and N. Bilgutay, "Analysis of homomorphic processing for ultrasonic grain signal characterization," *IEEE Trans. Ultrasonics, Ferroelectrics and Frequency Control*, vol. 3, pp. 365-375, 1989.

[19] S. Jin, Y. Wang, and J. Hiller, "An adaptive non-linear diffusion algorithm for filtering medical images," *IEEE Trans. Information Technology in Biomedicine*, vol. 4, no. 4, pp.298-305, Dec. 2000.

[20] J. Weickert, B. Romery, and M. Viergever, "Efficient and reliable schemes for nonlinear diffusion filtering," *IEEE Trans. Image Processing*, vol. 7, pp. 398-410, 1998.

[21] N. Rougon and F. Preteux, "Controlled anisotropic diffusion," *Conference on Nonlinear Image Processing VI*, IS&T/SPIE Symposium on Electronic Imaging, Science and Technology, San Jose, California, pp. 1-12, 5-10 Feb. 1995.

[22] M. Black, G. Sapiro, D. Marimont, and D. Heeger, "Robust anisotropic diffusion," *IEEE Trans. Image Processing*, vol. 7, no. 3, pp. 421-432, March 1998.

[23] P. Rerona and J. Malik, "Scale-space and edge detection using anisotropic diffusion," *IEEE Trans. Pattern Analysis and Mach. Intelligence*, vol. 12, no. 7, pp. 629-639, July 1990.

[24] K. Abd-Elmoniem, A.-B. Youssef, and Y. Kadah, "Real-time speckle reduction and coherence Enhancement in ultrasound imaging via nonlinear anisotropic diffusion," *IEEE Trans. Biomed. Eng.*, vol. 49, no. 9, pp. 997-1014, Sept. 2002.

[25] S. Zhong and V. Cherkassky, "Image denoising using wavelet thresholding and model selection," *Proc. of IEEE Int. Conf. Image Processing*, Vancouver, Canada, pp.1-4, Nov. 2000.

[26] A. Achim, A. Bezerianos and P. Tsakalides, "Novel Bayesian multiscale method for speckle removal in medical ultrasound images," *IEEE Trans. Medical Imaging*, vol. 20, no. 8, pp. 772-783, 2001.

[27] X. Zong, A. Laine, and E. Geiser, "Speckle reduction and contrast enhancement of echocardiograms via multiscale nonlinear processing," *IEEE Trans. Medical Imaging*, vol. 17, no. 4, pp. 532-540, 1998.

[28] X. Hao, S. Gao, and X. Gao, "A novel multiscale nonlinear thresholding method for ultrasonic speckle suppressing," *IEEE Trans. Medical Imaging*, vol. 18, no. 9, pp. 787-794, 1999.

[29] D. L. Donoho, "Denoising by Soft Thresholding," *IEEE Trans. Inform. Theory*, vol. 41, pp. 613, 627, 1995.

[30] A.M. Wink and J.B.T.M. Roerdink, "Denoising functional MR images: A comparison of wavelet denoising and Gaussian smoothing", *IEEE Trans. Medical Imaging*, vol. 23, no. 3, pp. 374-387, 2004.

[31] V. Dutt, "Statistical analysis of ultrasound echo envelope," Ph.D. dissertation, Mayo Graduate School, Rochester, MN, 1995.

[32] M. Nagao and T. Matsuyama, "Edge preserving smoothing," *Computer Graphic and Image Processing*, vol. 9, pp. 394-407, 1979.

[33] T. Huang, G. Yang, and G. Tang, "A fast two-dimensional median filtering algorithm," *IEEE Trans. Acoustics, Speech and Signal Processing*, vol. 27, no. 1, pp. 13-18, 1979.

[34] S.M. Ali and R.E. Burge, "New automatic techniques for smoothing and segmenting SAR images," *Signal Processing*, North-Holland, vol. 14, pp. 335-346, 1988.

[35] F.N.S Medeiros, N.D.A. Mascarenhas, R.C.P Marques, and C.M. Laprano, "Edge preserving wavelet speckle filtering," *5th IEEE Southwest Symposium on Image Analysis and Interpretation*, Santa Fe, New Mexico, pp. 281-285, 7-9 April 2002.

[36] P. Moulin, Multiscale image decomposition and wavelets, *in Handbook of Image & Video Processing*, Ed. by A. Bovik, Academic Press, pp. 289-300, 2000.

[37] P. Scheunders, "Wavelet thresholding of multivalued images," *IEEE Trans. Image Processing*, vol. 13, no. 4, pp. 475-483, 2004.

[38] S. Gupta, R.C. Chauhan, S.C. Sexana, "Wavelet-based statistical approach for speckle reduction in medical ultrasound images," *Medical & Biological Engineering & Computing*, vol. 42, pp. 189-192, 2004.

[39] A Philips Medical System Company, "Comparison of image clarity, SonoCT real-time compound imaging versus conventional 2D ultrasound imaging," *ATL Ultrasound, Report*, 2001.

[40] C. Christodoulou, C. Pattichis, M. Pantziaris, and A. Nicolaides, "Texture-Based Classification of Atherosclerotic Carotid Plaques," *IEEE Trans. Medical Imaging*, vol. 22, no. 7, pp. 902-912, 2003.

[41] R.M. Haralick, K. Shanmugam, and I. Dinstein, "Texture Features for Image Classification," *IEEE Trans. Systems, Man., and Cybernetics*, vol. SMC-3, pp. 610-621, Nov. 1973.

[42] J.S Weszka., C.R. Dyer, and A. Rosenfield, "A comparative study of texture measures for terrain classification," *IEEE Trans. Systems, Man. & Cybernetics*, vol. SMC-6, pp. 269-285, April 1976.

[43] M. Amadasun and R. King, "Textural features corresponding to textural properties," *IEEE Trans. Systems, Man, & Cybernetics*, vol. 19, no. 5, pp. 1264-1274, Sept. 1989.

[44] C.M. Wu, Y.C. Chen, and K.-S. Hsieh, "Texture features for classification of ultrasonic images," *IEEE Trans. Med. Imaging*, vol. 11, pp. 141-152, June 1992.

[45] T.J. Chen, K.S. Chuang, Jay Wu, S.C. Chen, I.M. Hwang, M.L. Jan, "A novel image quality index using Moran I statistics," *Physics in Medicine and Biology*, vol. 48, pp. 131-137, 2003.

[46] R. Gonzalez and R. Woods, Digital image processing, Second Edition, Prentice-Hall Inc., 2002, pp. 419-420.

[47] Z. Wang, A. Bovik, H. Sheikh, and E. Simoncelli, "Image quality assessment: From error measurement to structural similarity," *IEEE Trans. Image Processing*, vol. 13, no. 4, pp. 600-612, Apr. 2004.

[48] S. Winkler, "Vision models and quality metrics for image processing applications," PhD, University of Lausanne-Switzerland, Dec. 21, 2000.

[49] D. Sakrison, "On the role of observer and a distortion measure in image transmission," *IEEE Trans. Communication*, vol. 25, pp. 1251-1267, Nov. 1977.

[50] Z. Wang and A. Bovik, "A Universal quality index," *IEEE Signal Processing Letters*, vol. 9, no. 3, pp. 81-84, March 2002.

[51] H.R. Sheikh, A.C. Bovik, G.de Veciana, "An information fidelity criterion for image quality assessment using natural scene statistics," *IEEE Trans. Image Proces.*, to be published.

[52] E. Krupinski, H. Kundel, P. Judy, and C. Nodine, "The medical image perception society, key issues for image perception research," *Radiology*, vol. 209, pp. 611-612, 1998.

[53] T. Elatrozy, A. Nicolaides, T. Tegos, A. Zarka, M. Griffin, and M. Sabetai, "The effect of B-mode ultrasonic image standardization of the echodensity of symptomatic and asymptomatic carotid bifurcation plaque," *Int. Angiology*, vol. 17: 179-186, no. 3, Sept.1998.

[54] C. Loizou, C. Pattichis, R. Istepanian, and M. Pantziaris, "Intima media segmentation of the carotid artery," *Medicon X Mediterranean Conf. on Medical and Biological Engineering, Health in the Information Society,* July 31-August 5, Ischia, Naples-Italy, POS-03, 499, 4 pages, 2004.

[55] C.S. Pattichis, E. Kyriakou, C. Christodoulou, M.S. Pattichis, C. Loizou, M. Pantziaris, and A. Nicolaides, "Cardiovascular: Ultrasound imaging in vascular cases," in Wiley Encyclopaedia of Biomedical Engineering, Wiley, to be published in 2005.

## LIST OF FIGURES

Fig. 1. (a) Directions of implementation of the *gf4d* geometric filter, (b) pixels selected for the NS direction (intensity of central pixel b is adjusted based on the values of intensities of pixels a, b and c).

Fig. 2. Original ultrasound image of the carotid artery (2-3 cm proximal to bifurcation) given in (a), and the despeckled filtered images given in (b)-(k).

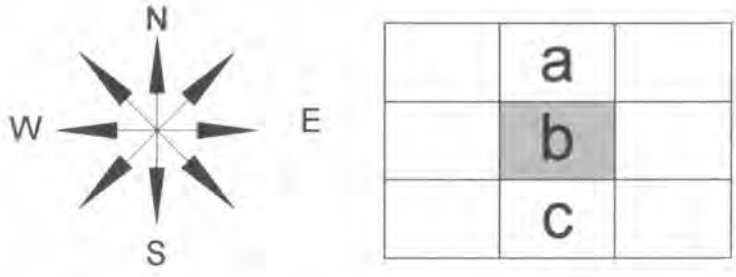


(a) (b)

Fig. 1. (a) Directions of implementation of the *gf4d* geometric filter, (b) pixels selected for the NS direction (intensity of central pixel b is adjusted based on the values of intensities of pixels a, b and c).

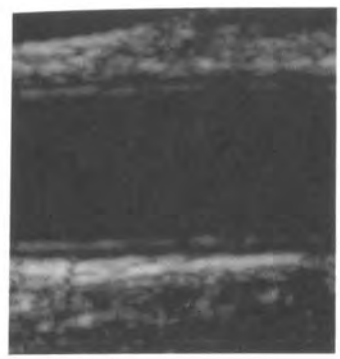

*(a) original image*

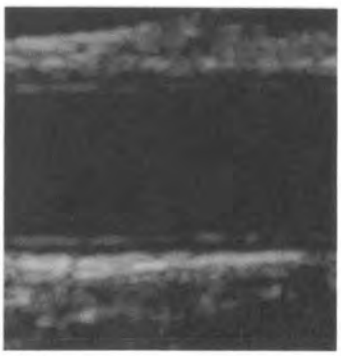

*(b) lsmv*

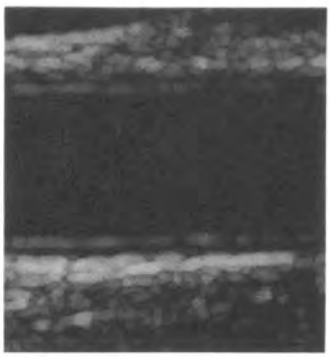

*(c) lsminsc*

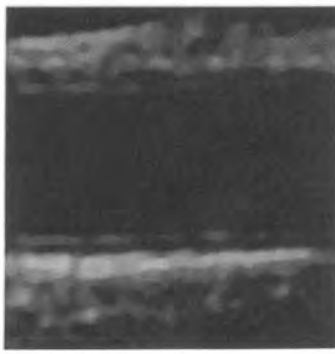

*(d) median*

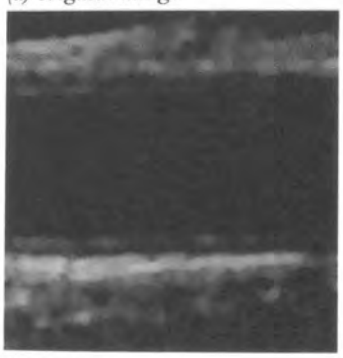

*(e) wiener*

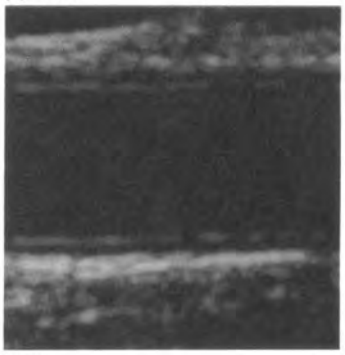

*(f) homog*

*(g) gf4d*

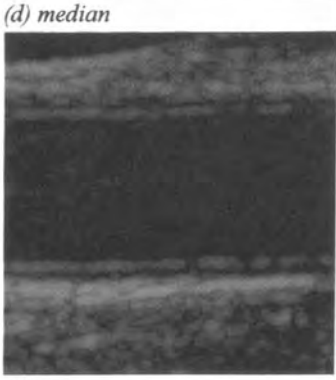

*(h) homo*

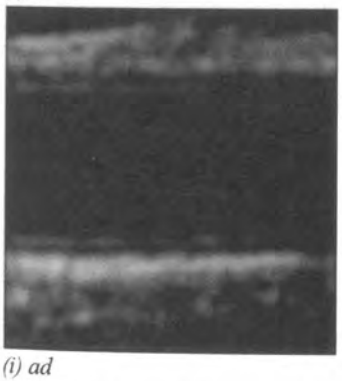

*(i) ad*

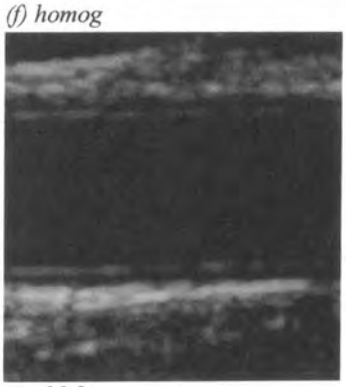

*(j) nldif*

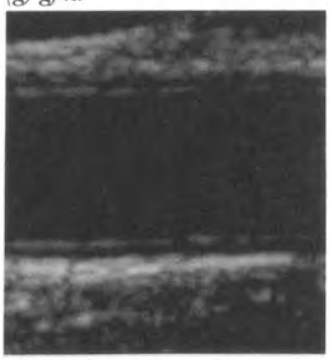

*(k) waveltc*

Fig. 2. Original ultrasound image of the carotid artery (2-3 cm proximal to bifurcation) given in (a), and the despeckled filtered images given in (b)-(k).

## LIST OF TABLES

TABLE I: AN OVERVIEW OF DESPECKLE FILTERING TECHNIQUES

TABLE II: FEATURE DISTANCE (EQ. 17) AND SCORE_DIS (EQ. 18) FOR SF, SGLDM RANGE OF VALUES, AND NGTDM TEXTURE FEATURE SETS BETWEEN ASYMPTOMATIC AND SYMPTOMATIC CAROTID PLAQUE ULTRASOUND IMAGES. BOLDED VALUES SHOW IMPROVEMENT AFTER DESPECKLE FILTERING

TABLE III: WILCOXON RANK SUM TEST FOR THE SGLDM RANGE OF VALUES TEXTURE FEATURES APPLIED ON THE 440 ULTRASOUND IMAGES OF CAROTID PLAQUE BEFORE AND AFTER DESPECKLE FILTERING. THE TEST SHOWS WITH S AND NS, THE FEATURES THAT ARE AND ARE NOT SIGNIFICANTLY DIFFERENT AFTER FILTERING AT $p<0.05$ RESPECTIVELY

TABLE IV: PERCENTAGE OF CORRECT CLASSIFICATIONS SCORE FOR THE kNN CLASSIFIER WITH k=7 FOR THE ORIGINAL AND THE FILTERED IMAGE SETS. BOLDED VALUES INDICATE IMPROVEMENT AFTER DESPECKLING

TABLE V: IMAGE QUALITY EVALUATION METRICS COMPUTED FOR THE 220 ASYMPTOMATIC AND 220 SYMPTOMATIC IMAGES

TABLE VI: PERCENTAGE SCORING OF VISUAL EVALUATION OF THE ORIGINAL AND DESPECKLED IMAGES (50 ASYMPTOMATIC (A) AND 50 SYMPTOMATIC (S)) BY THE EXPERTS

TABLE VII: SUMMARY FINDINGS OF DESPECKLE FILTERING IN ULTRASOUND IMAGING OF THE CAROTID ARTERY

TABLE I
AN OVERVIEW OF DESPECKLE FILTERING TECHNIQUES

| Speckle Reduction Technique | Investigator | Method | Filter Name |
|---|---|---|---|
| Local Statistics | [7]-[14], [13]-[16] | Moving window utilising local statistics<br>a) mean (m), variance ($\sigma^2$) | *lsmv* |
| | [7]-[14] | b) mean, variance, 3rd and 4th moments (higher moments) and entropy | |
| | [32] | c) Homogeneous mask area filters | *lsminsc* |
| | [2]-[14], [15] | e) Wiener filtering | *wiener* |
| Median | [33] | Median filtering | *median* |
| Homogeneity | [8] | Based on the most homogeneous neighbourhood around each pixel | *homog* |
| Geometric | [10] | Non linear iterative algorithm | *gf4d* |
| Homomorphic | [2], [17], [18] | The image is logarithmically transformed, the Fast Fourier transform (FFT) is calculated, denoised, the inverse FFT is calculated and finally exponentially transformed back | *homo* |
| Anisotropic Diffusion | [2], [5], [12], [13], [19], [20]-[23], | Non-linear filtering technique for simultaneously performing contrast enhancement and noise reduction. Exponential damp kernel filters utilising diffusion | *ad* |
| | [24] | Coherence enhancing diffusion | *nldif* |
| Wavelet | [15], [25]-[28], [29], [35] | Only the useful wavelet coefficients are utilised | *waveltc* |

TABLE II

FEATURE DISTANCE (EQ. 17) AND SCORE_DIS (EQ. 18) FOR SF, SGLDM RANGE OF VALUES, AND NGTDM TEXTURE FEATURE SETS BETWEEN ASYMPTOMATIC AND SYMPTOMATIC CAROTID PLAQUE ULTRASOUND IMAGES. BOLDED VALUES SHOW IMPROVEMENT AFTER DESPECKLE FILTERING

| | *Local Statistics* | | | | *HF* | *GF* | *HM* | *Diffusion* | | *Wavelet* |
|---|---|---|---|---|---|---|---|---|---|---|
| Feature | *lsmv* | *lsminsc* | *wiener* | *median* | *homog* | *gf4d* | *homo* | *ad* | *nldif* | *waveltc* |
| Nr. of It. | 4 | 1 | 2 | 2 | 1 | 3 | 2 | 20 | 5 | 5 |
| SF-Statistical Features | | | | | | | | | | |
| Mean | **14** | **22** | **19** | **4** | **11** | **3** | **164** | **18** | **5** | **15** |
| Median | -5 | -17 | -26 | -5 | -5 | -15 | **110** | -29 | -6 | -15 |
| $\sigma^2$ | **18** | **38** | **18** | **7** | **13** | -2 | **140** | **9** | **7** | **18** |
| $\sigma^3$ | **12** | **16** | **5** | **9** | **7** | -0.1 | **149** | **17** | **7** | **8** |
| $\sigma^4$ | -12 | -14 | -7 | -6 | -4 | -3 | **117** | -21 | **6** | -9 |
| C | 0.4 | 0.3 | 0.3 | 0.4 | 0.3 | 0.4 | 0.08 | 0.3 | 0.4 | 0.3 |
| *Score_dis* | 27 | 45 | 9 | 9 | 22 | -17 | 680 | -6 | 19 | 17 |
| SGLDM Range of Values–Spatial Gray Level Dependence Matrix | | | | | | | | | | |
| ASM | -21 | -0.5 | -29 | **2** | -4 | -8 | -47 | -25 | -17 | -20 |
| Contrast | **47** | **107** | **14** | **64** | **32** | -3 | **165** | **104** | **13** | **22** |
| Correlation | **12** | **59** | **15** | **24** | -5 | **2** | **10** | **54** | -4 | -4 |
| SOSV | **9** | **40** | **18** | **10** | **16** | -2 | **101** | **9** | **8** | **20** |
| IDM | -50 | -11 | -48 | **2** | -29 | -8 | **94** | -54 | -34 | -43 |
| SAV | **17** | **24** | **23** | **7** | **15** | **3** | **169** | **22** | **6** | **18** |
| $\sum Var$ | **19** | **38** | **18** | **9** | **15** | -2 | **90** | **9** | **8** | **20** |
| $\sum Entr$ | -34 | -14 | -49 | **3** | -19 | -4 | -11 | -47 | -30 | -36 |
| *Score_dis* | -1 | 243 | -38 | 121 | 21 | -22 | 571 | 72 | -50 | -23 |
| NGTDM–Neighbourhood Gray Tone Difference Matrix | | | | | | | | | | |
| Coarseness | **30** | **87** | **4** | **9** | -16 | -7 | **72** | -36 | -37 | -33 |
| Contrast | **7** | -0.3 | -9 | **8** | **0.4** | -4 | **105** | **5** | -27 | -15 |
| Busyness | **17** | **26** | -30 | **8** | **1** | -4 | **48** | -14 | -39 | **8** |
| Completion | **64** | **151** | **21** | **53** | **80** | **2** | **150** | **63** | **18** | **27** |
| *Score_dis* | 118 | 264 | -14 | 78 | 66 | -13 | 375 | 18 | -85 | -13 |
| *Score_dis*$-T$ | 144 | 551 | -43 | 208 | 108 | -52 | 1626 | 84 | -116 | -19 |

ASM: Angular 2nd moment, SOSV: Sum of squares variance, IDM: Inverse difference moment, SAV: Sum average, $\sum Var$ : Sum Variance

HF: Homogeneity, GF: Geometric, HM: Homomorphic

TABLE III
WILCOXON RANK SUM TEST FOR THE SGLDM RANGE OF VALUES TEXTURE FEATURES APPLIED ON THE 440 ULTRASOUND IMAGES OF CAROTID PLAQUE BEFORE AND AFTER DESPECKLE FILTERING. THE TEST SHOWS WITH S AND NS, THE FEATURES THAT ARE AND ARE NOT SIGNIFICANTLY DIFFERENT AFTER FILTERING AT $p<0.05$ RESPECTIVELY

| | *Local Statistics* | | | *Median* | *HF* | *GF* | *HM* | *Diffusion* | | *Wavelet* | Score |
|---|---|---|---|---|---|---|---|---|---|---|---|
| Feature | *lsmv* | *lsminsc* | *wiener* | *median* | *homog* | *gf4d* | *homo* | *ad* | *nldif* | *waveltc* | |
| ASM | S | S | NS | NS | S | S | NS | S | S | S | 7 |
| Contrast | S | NS | NS | NS | NS | S | NS | NS | S | NS | 3 |
| Correlation | S | S | NS | NS | NS | S | NS | NS | NS | NS | 3 |
| SOSV | S | NS | NS | NS | NS | S | NS | NS | NS | NS | 2 |
| IDM | S | S | NS | S | S | S | S | NS | S | S | 8 |
| SAV | NS | NS | NS | NS | NS | NS | NS | NS | NS | NS | 0 |
| $\sum Var$ | S | S | NS | NS | NS | NS | NS | NS | NS | NS | 2 |
| $\sum Entropy$ | S | S | NS | NS | NS | S | NS | NS | S | S | 5 |
| Score | 7 | 5 | 0 | 1 | 2 | 6 | 1 | 1 | 4 | 3 | |

ASM: Angular 2nd moment, SOSV: Sum of squares variance, IDM: Inverse difference moment, SAV: Sum average, $\sum Var$ : Sum Variance

HM: Homomorphic, HF: Homogeneity, GF: Geometric, HM: Homomorphic. Score: illustrates the number of S

TABLE IV
PERCENTAGE OF CORRECT CLASSIFICATIONS SCORE FOR THE kNN CLASSIFIER WITH k=7 FOR THE ORIGINAL AND THE FILTERED IMAGE SETS. BOLDED VALUES INDICATE IMPROVEMENT AFTER DESPECKLING

| *Feature set* | *No. of Feat.* | | *Local Statistics* | | | *Median* | *HF* | *GF* | *HM* | *Diffusion* | | *Wavelet* |
|---|---|---|---|---|---|---|---|---|---|---|---|---|
| | | *original* | *lsmv* | *lsminsc* | *wiener* | *median* | *homog* | *gf4d* | *homo* | *ad* | *nldif* | *waveltc* |
| SF | 5 | 59 | **62** | **61** | **61** | 57 | **63** | 59 | **65** | **60** | 52 | **61** |
| SGLDMm | 13 | 65 | 63 | 64 | 62 | 63 | **69** | **67** | **68** | 61 | **66** | 63 |
| SGLDMr | 13 | 70 | 66 | **72** | 64 | 66 | 65 | 70 | 69 | 64 | 65 | 65 |
| GLDS | 4 | 64 | 63 | **66** | 61 | **69** | 64 | **66** | **72** | 59 | 58 | 62 |
| NGTDM | 5 | 64 | 63 | **68** | 60 | **69** | 63 | **65** | 57 | 60 | 61 | 62 |
| SFM | 4 | 62 | 62 | 60 | 62 | 58 | 55 | **65** | **68** | 59 | 56 | 55 |
| TEM | 6 | 59 | **68** | 52 | **60** | 59 | **66** | **60** | **65** | 53 | **60** | **60** |
| FDTA | 4 | 64 | 63 | **66** | 53 | **68** | 53 | 62 | **73** | 55 | 54 | 62 |
| FPS | 2 | 59 | 54 | **64** | 59 | 58 | 59 | 59 | 59 | 52 | 48 | 55 |
| Average | | 63 | 63 | **64** | 60 | 63 | 62 | **64** | **66** | 58 | 58 | 61 |

SF: Statistical Features, SGLDMm: Spatial Gray Level Dependence Matrix Mean Values, SGLDMr: Spatial Gray Level Dependence Matrix Range of Values, GLDS: Gray Level Difference Statistics, NGTDM: Neighborhood Gray Tone Difference Matrix, SFM: Statistical Feature Matrix, TEM: Laws Texture Energy Measures, FDTA: Fractal Dimension Texture Analysis, FPS: Fourier Power Spectrum.

HF: Homogeneity, GF: Geometric, HM: Homomorphic

TABLE V
IMAGE QUALITY EVALUATION METRICS COMPUTED FOR THE 220 ASYMPTOMATIC AND 220 SYMPTOMATIC IMAGES

| | *Local Statistics* | | | *Median* | *HF* | *GF* | *HM* | *Diffusion* | | *Wavelet* |
|---|---|---|---|---|---|---|---|---|---|---|
| *Feature set* | *lsmv* | *lsminsc* | *wiener* | *median* | *homog* | *gf4d* | *homo* | *ad* | *nldif* | *waveltc* |
| Asymptomatic Images | | | | | | | | | | |
| MSE | 13 | 86 | 19 | 131 | 42 | 182 | 758 | 132 | 8 | 11 |
| RMSE | 3 | 9 | 4 | 10 | 6 | 13 | 27 | 11 | 2 | 3 |
| Err3 | 7 | 17 | 5 | 25 | 14 | 25 | 38 | 21 | 5 | 4 |
| Err4 | 11 | 26 | 7 | 41 | 24 | 40 | 49 | 32 | 10 | 5 |
| GAE | 0 | 0 | 0 | 0 | 0 | 0 | 0 | 0 | 0 | 0 |
| SNR | 25 | 17 | 23 | 16 | 21 | 14 | 5 | 14 | 28 | 25 |
| PSNR | 39 | 29 | 36 | 29 | 34 | 27 | 20 | 28 | 41 | 39 |
| Q | 0.83 | 0.78 | 0.74 | 0.84 | 0.92 | 0.77 | 0.28 | 0.68 | 0.93 | 0.65 |
| SSIN | 0.97 | 0.88 | 0.92 | 0.94 | 0.97 | 0.88 | 0.43 | 0.87 | 0.97 | 0.9 |
| Symptomatic Images | | | | | | | | | | |
| MSE | 33 | 374 | 44 | 169 | 110 | 557 | 1452 | 374 | 8 | 23 |
| RMSE | 5 | 19 | 6 | 13 | 10 | 23 | 37 | 19 | 3 | 5 |
| Err3 | 10 | 33 | 9 | 25 | 20 | 43 | 51 | 31 | 5 | 6 |
| Err4 | 16 | 47 | 11 | 38 | 30 | 63 | 64 | 43 | 7 | 8 |
| GAE | 0 | 0 | 0 | 0 | 0 | 0 | 0 | 0 | 0 | 0 |
| SNR | 24 | 13 | 22 | 16 | 17 | 12 | 5 | 12 | 29 | 25 |
| PSNR | 34 | 23 | 33 | 26 | 28 | 21 | 17 | 23 | 39 | 36 |
| Q | 0.82 | 0.77 | 0.7 | 0.79 | 0.87 | 0.75 | 0.24 | 0.63 | 0.87 | 0.49 |
| SSIN | 0.97 | 0.85 | 0.89 | 0.81 | 0.94 | 0.85 | 0.28 | 0.81 | 0.97 | 0.87 |

MSE: Mean square error, RMSE: Randomised mean square error, Err3, Err4: Minowski metrics, GAE: Geometric average error, SNR: Signal to noise radio, PSNR: Peak signal to noise radio, Q: universal quality index, SSIN: structural similarity index

TABLE VI
PERCENTAGE SCORING OF VISUAL EVALUATION OF THE ORIGINAL AND DESPECKLED IMAGES (50 ASYMPTOMATIC (A) AND 50 SYMPTOMATIC (S)) BY THE EXPERTS

| | | | *Local Statistics* | | *Median* | *HF* | *GF* | *HM* | *Diffusion* | *Wavelet* |
|---|---|---|---|---|---|---|---|---|---|---|
| Experts | *A/S* | *original* | *lsmv* | *lsminsc* | *median* | *homog* | *gf4d* | *homo* | *nldif* | *waveltc* |
| Cardiovascular | A | 33 | 75 | 33 | 43 | 47 | 61 | 19 | 43 | 32 |
| Surgeon | S | 48 | 49 | 18 | 57 | 43 | 42 | 20 | 33 | 22 |
| Average % | | 41 | 62 | 26 | 50 | 45 | 52 | 19 | 38 | 27 |
| Neurovascular | A | 70 | 76 | 73 | 74 | 63 | 79 | 23 | 52 | 29 |
| Specialist | S | 66 | 67 | 63 | 58 | 45 | 65 | 55 | 41 | 28 |
| Average % | | 68 | 71 | 68 | 66 | 54 | 72 | 39 | 47 | 28 |
| Overall Average % | | 54 | 67 | 47 | 58 | 50 | 62 | 29 | 43 | 28 |

HF: Homogeneity, GF: Geometric, HM: Homomorphic

TABLE VII
SUMMARY FINDINGS OF DESPECKLE FILTERING IN ULTRASOUND IMAGING OF THE CAROTID ARTERY

| Despeckle Filter | Statistical and Texture Features Table II | Statistical Analysis Table III | kNN Classifier Table IV | Image Quality Evaluation Table V | Optical Perception Evaluation Table VI |
|---|---|---|---|---|---|
| Local Statistics | | | | | |
| *lsmv* | ✓ | ✓ | | ✓ | ✓ |
| *lsminsc* | ✓ | ✓ | ✓ | | |
| Geometric Filtering | | | | | |
| *gf4d* | | ✓ | ✓ | | ✓ |
| Homomorphic Filtering | | | | | |
| *homo* | ✓ | | ✓ | | |
| Diffusion Filtering | | | | | |
| *nldif* | | | | ✓ | |
| Wavelet Filtering | | | | | |
| *waveltc* | | | | ✓ | |

BRITISH LIBRARY

IMAGING SERVICES NORTH
Boston Spa, Wetherby
West Yorkshire, LS23 7BQ
www.bl.uk

# PAGE/PAGES EXCLUDED UNDER INSTRUCTION FROM THE UNIVERSITY

# *References*

# References

[1] K.R. Castleman, Digital image processing, Prentice Hall Inc., 1996.

[2] C. Loizou, Speckle reduktion in medizinischer ultraschallbildern, University of Kaisserslautern, Germany, Masters Thesis, pp. 1-157, 1990.

[3] R. Gonzalez, R. Woods, Digital image processing, Second edition, Prentice-Hall Inc., 2002.

[4] S. Stergiopoulos, Advanced signal processing handbook, Theory and implementation for radar, sonar, and medical imaging real-time systems, CRC Press LLC, 2001.

[5] A. Kokaram, Motion picture restoration, Springer Verlag, 1998.

[6] A. Watt, 3-D Computer graphics, Addison-Wesley, 2000.

[7] M. Sonka, J.M. Fitzpatrik, Handbook of medical imaging, vol. 2, Medical image processing and analysis, SPIE, 2000.

[8] A. Bovik, Handbook of image & video processing, Academic Press, 2000.

[9] I.N. Bakman, Handbook of medical imaging, processing and analysis, Academic Press, © 2000.

[10] C.I. Christodoulou, C.S. Pattichis, M. Pantziaris, A. Nicolaides, "Texture based classification of atherosclerotic carotid plaques," *IEEE Trans. Med. Imag.*, vol. 22, no. 7, pp. 902-912, July 2003.

[11] V. Grau A.U.J. Mewes, M. Alcaniz, S.K. Warfield, "Improved watershed transform for medical image segmentation using prior information," *IEEE Trans. Med. Imag*, vol. 23, no. 4, pp. 447-458, 2004.

[12] V. Metzler, M. Puls, T. Aach, "Restoration of ultrasound images by non-linear scale-space filtering," Institute of signal processing, Medical university of Luebeck, D-23538 Luebeck, Germany, 1999.

[13] L. Gagnon, Wavelet filtering of speckle noise – Some numerical results, "Vision interface," Trois-Rivieres, Canada, pp. 336-343, 19-21 May 1999.

[14] J.E. Wilhjelm, S.K. Jespersen, J.U. Hansen, T. Brandt, K. Gammelmark, H. Sillensen, "In vitro imaging of the carotid artery with spatial compound imaging," Dept. of Vascular surgery, Gentofe University Hospital, DK-2900 Hellerup, Denmark, pp. 9-14, 1999.

[15] N. Otsu, "A Threshold Selection Method from Gray-Level Histograms," *IEEE Trans. on Systems, Man, and Cybernetics*, vol. 9, no. 1, pp. 62-66, 1979.

[16] E. Nezry, F.Y.-Simen, "Family of distribution-entropy filters for polarimetric SAR data, and for single or multi-channel detected and complex SAR images," *Private Experts in Remote Sensing*, Great Bay Marina, Netherlands Antiles, 2000.

[17] D. Guo, "Intra vascular ultrasound speckle statistics," *IEEE BioMedical DiVision*, Hong Kong Institute of Engineering, 1998.

[18] N.D.A. Maskarenhas, L.F. Costa, F.N.S. Medeiros, "Speckle noise filtering in SAR images by MAP approach," *Cybernetic Vision Group,* IFSC-University of Sao Paulo, Caixa Postal, 369, SP, Brasil, 1991.

[19] L.J. Busse, T.R. Crimmins, J.R. Fienup, "A model based approach to improve the performance of the geometric speckle reduction algorithm," *IEEE Ultrasonic Symposium*, pp. 1353-1356, 1995.

[20] A.N. Evans, M.S. Nixon, "Biased motion-adaptive temporal filtering for Speckle reduction in EchoCardiography," *IEEE Trans. Med. Imag*, vol. 15, no. 1, February 1996.

[21] T. Greiner, C. Loizou, M. Pandit, J. Mauruschat, F.W. Albert, "Speckle reduction in ultrasonic imaging for medical applications," *Proc. of the ICASSP91, 1991 Int. Conf. acoustic Signal speech and Processing*, Toronto Canada, May 14-17, pp. 2993-2996, 1991.

[22] J.-S. Lee, "Digital image enhancement and noise filtering by use of local statistics," *IEEE Trans. on Pattern Analysis and Machine Intelligence*, PAMI-2, no. 2 pp. 165-168, 1980.

[23] J.-S. Lee, "Refined filtering of image noise using local statistics," *Comp. Graph.Image Proces.*, vol. 15, pp. 380-389, 1981.

[24] J.-S. Lee, "A simple speckle-smoothing algorithm for synthetic aperture radar images," *IEEE Trans. System Man and Cybernetics*, vol. SMC-13, no.1, pp. 85-89, 1983.

[25] J.-S. Lee, "Digital image smoothing and the sigma Filter," *Comp. Graph.Image Proces*, vol. 24, pp. 255-269, 1983.

[26] J.-S. Lee, "Speckle suppression and analysis for synthetic aperture radar," *SPIE Int. Conf. Speckle*, vol. 556, pp. 170-179, 1985.

[27] V.S. Frost, J.A. Stiles, K.S. Shanmungan, J.C. Holtzman, "Edge detection for synthetic aperture radar and other noisy images," *Proc. of the Int. Geoscience and Remote Sensing symposium (IGARSS'82)*, Sec. FA2, pp.4.1-4.9, 1982.

[28] V.S. Frost, J.A. Stiles, K.S. Shanmungan, J.C. Holtzman, "A model for radar images and its application for to adaptive digital filtering of multiplicative noise," *IEEE Trans. on Pattern Analysis Mach. Intellig.*, vol. PAMI-4, no.2, 1982, pp.157-165.

[29] D.T. Kuan, A.A. Sawchuk, "Adaptive noise smoothing filter for images with signal dependent noise," *IEEE Trans. on Pattern Analysis and Mach. Intellig.*, vol. PAMI-7, no.2, pp.165-177, 1985.

[30] D.T. Kuan, A.A. Sawchuk, T.C. Strand, P. Chavel, "Adaptive restoration of images with speckle," *IEEE Trans. on Acoustic speech and Signal Processing*, vol. ASSP-35, no.3, pp.373-383, 1987.

[31] A. Lopes, E. Nezry, R. Touzi, H. Laur, "Maximum A posteriori speckle filtering and first order texture model in SAR images," *Proc. of the Int. Geoscience and Remote Sensing Symposium (IGARSS'90)*, pp. 2409-2412, 1990.

[32] A. Lopes, E. Nezry, R. Touzi, H. Laur, "Structure detection and statistical adaptive speckle filtering in SAR images," *Int. J. Remote Sensing*, vol.14, no.9, pp. 1735-1758, 1993.

[33] Y. Huang, J.L. van Genderen, B.S. van Veen, ITC Filter, "A new adaptive filter for SAR speckle reduction," *Int. Institute for AeroSpace survey and earth science (ITC)*, 1996.

[34] R. Fjortoft, A. Lopes, Frederic Adragna, "Radiometric and spatial aspects of speckle filtering," *Proc. IGARSS*, Honolulu, Hawaii, 24-28 July, pp. 1-3, 2000.

[35] F. Sery, D.D.-Gambart, A. Lopes, R. Fjortoft, E.C.-Castan, P. Marthon, "Multisource classification of SAR images with the use of segmentation, Polarimetry, Texture and Multitemporal Data," *Society of Photo-Optical Instrumentation Engineers*, 1996.

[36] J.S. Won, J.H. Ryu, H.Y Kim, "Radarsat SAR investigation over the south coast of Korea: Coastal zone management perspective," *Dept. of Earth System Sciences*, Yonsei University, Seodaemun-Ku, Shinchon-dong 134, Seoul, Korea, 1996.

[37] N. Rougon, F. Preteux, "Controlled anisotropic diffusion," Dept. Signal et Image, Institute National des Telecommunications, Evry, France, *Conference on Non-linear Image Processing VI at IS&T/SPIE Symposium on Electronic Imaging*, Science and Technology 95.

[38] Y. Yongjian, S.T. Acton, "Speckle reducing anisotropic diffusion," *IEEE Trans. on Image Proces.*, vol. 11, no. 11, pp. 1260-1270, Nov. 2002.

[39] I. Middleton, R.I. Damper, "Segmentation of magnetic resonance images using a combination of neural networks and active contour models," *Medical Engineering & Physics*, vol. 26, pp. 71-86, 2004.

[40] G. Hamarneh, "Image segmentation with constrained snakes," *Swedish society for Image Analysis Newsletter,* SSABlaskan, no. 8., 2000.

[41] P. Abolmaesumi, M.R. Sirouspour, S.E. Salcudean, "Real-time extraction of carotid artery contours from ultrasound images," *IEEE Computer Society*, pp.1-3, 22-24 June 2000.

[42] M. Melloul, L. Joskowicz, "Segmentation of micro calcifications in X-ray mammograms using entropy thresholding," *Proc. Of the 16th Int. Congress on Computer Assisted Radiology and Surgery*, CARS 2002, pp. 490-495, 2002.

[43] G. Bueno, M. Fischer, K. Burnham, J. Mills, O. Haas, "Automatic segmentation of clinical structures for RTP: Evaluation of a morphological approach," *Medical Image Understand. and Analysis MIUA*, pp. 73-76, 16-17 July 2001.

[44] A.S.-Trucksaess et al., "Computerised analysis system using the active contour in ultrasound measurement of carotid artery intima-media thickness," *Clinical Physiology 21*, vol. 5, pp. 561-569, 2001.

[45] L.E. Shields, C. Lowery, C. Deforge, D. Gustfson, "Technology and early clinical experience with real time 3D ultrasound," *Electromedica 66*, no.2, pp. 84-88, 1998.

[46] A.R.Abdel-Dayen, M.R. El.-Sakka, "A novel morphological-based carotid artery contour extraction," *Canadian Conf. Electrical and Computer Engin.*, vol. 4, pp. 1873-1876, 2-5 May 2004.

[47] A. Hamou, M.El.-Sakka, "A novel segmentation technique for carotid ultrasound images," *Int. Conf. on Acoustic Speech and Signal Processing*, ICASSP 2004, pp. III-521-III-524, May 2004.

[48] C.K. Zarins, C.Xu, S. Glagov, "Atherosclerotic enlargement of the human abdominal aorta," *Atherosclerosis,* vol. 155, no. 1, pp.157-164, 2001.

[49] G. Nergizog, K. Keven, M.A. Gurses, O.A.S. Ertuk, "Carotid intima media thickness and ACE-gene polymorphism in hemodialysis patients," *Nephrology Journal*, vol.12, no. 4, pp.261-265, 1999.

[50] A.M. Kupinski, "The utility of duplex ultrasound in the management of stroke patients," *Electromedica 68*, Karmody Vascular Laboratory, Albany, USA, Neuro-2000.

[51] G. Geroulakos, M. Sabetai, "Ultrasonic carotid plaque morphology," *Archives of Hellenic Medicine*, vol. 17, no. 2, pp. 141-145, 2000.

[52] J.E. Wilhjelm, M.L.M. Gronholdt, S. Rasmussen, K. Martinsen, H. Sillensen, "Centre of arteriosclerosis detection with ultrasound CADUS," *IEEE Ultrasonic Symposium,* pp.1-4, 1996.

[53] A. Dimitras, A. Venetsanopoulos, "A comparative study of snake models with application to object shape description in BI-level and gray-level images," *Proc. IEEEE-EURASIP Workshop on nonlinear signal and image processing*, June 3-6, pp. 1-5, 2001.

[54] J.F. Carpenter, F.J. Lexa, J.T. Davis, "Determination of doppler ultrasound criteria appropriate to the North American Symptomatic carotid endarterectomy," *Trial Stroke*, vol. 27, pp. 695-9, 1996.

[55] A. Zahalka, A. Fenster, "An automated segmentation method for three-Dimensional carotid ultrasound images," *Physics in Med. and Biology,* vol. 46, pp. 1321-1342, 2001.

[56] R. Kagawa, K. Moritake, T. Shima, Y. Okada, "Validity of B-ultrasound findings in patients undergoing carotid endarterectomy in comparison with angiographic and clinicopathologic features," *Stroke*, vol. 27, pp. 700-705, 1996.

[57] P.H. Arbeille, C. Desombre, B. Aesh, M. Phillipot, F. Lappierre, "Quantification and assessment of carotid artery lesions: Degree of stenosis and plaque volume," *J. Clin. Ultrasound*, vol.123, pp. 113-24, 1995.

[58] J. Kaufhold, R. Chan, W.C. Karl, D.A. Castanon, H.H. Pien, " Ultrasound tissue analysis and characterization," *Battlefield Biomedical Technologies*, (ed.), *Proc. SPIE V 3712*, Orlano, pp. 1-10, April 5-9, 1999.

[59] T. McInerney, D. Terzopoulos, "Deformable models in medical image analysis: A survey," *Med. Imag. Anal.*, vol. 1, no. 2, pp. 91-108, 1996.

[60] J.V. Miller, D.E. Breen, W.E. Lorensen, R.M. Bara, M.J. Wonzy, "Geometrically deformed models: a method for extracting closed geometric models form volume data," *Proc. Comp. Graph. SIGGRAPH'91 Conf. (Las Vegas*, NV), vol. 25, pp. 217-26, 1991.

[61] D. Xu, J.-N. Hwang, C. Yuan, "Atherosclerotic plaque segmentation at human carotid artery based on multiple contrast weighting MR images," *IEEE ICIP 2001*, pp. 849-852, 2001.

[62] G.A. Carpenter, S. Grossberg, G.W. Lesher, "The what-and-where filter-a spatial mapping neural network for object recognition and image understanding, " *Computer Vision and Image Understanding*, vol. 69, no. 1, pp. 1-22, 1998.

[63] C.I. Christodoulou, "Neural network pattern recognition in bioSignal analysis," Queen Mary and Westfield University of London, PhD Thesis, March 1999.

[64] F. Mao, J. Gill, D. Downey, Aaron Fenster, "Segmentation of carotid artery in ultrasound images: Method development and evaluation technique," *Med. Phys.*, vol.27, no. 8, pp. 1-10, August 2000.

[65] S.A. Godwin, "Introduction to emergency ultrasound, A review of justifications, indications and significant findings," Dept. of emergency medicine, University of Florida Health Science Center, Jacksonville, 1999.

[66] G. Kampmann, "Bildgebende Verfahren bei der Diagnostik der Karotisstenose: Is der Angiogram Veraltet? ," *Schweiz Med Wochenschr*, vol. 130, pp. 1231-1236, 2000.

[67] W. Lang, W. Lalouschek, "Abschaetzung der Relation von nutzen und risiko einer Karotisendarterektomie," *Neurologie Phychiatric*, vol. 1, pp.17-21, 2000.

[68] J. Dnacan, "Medical image analysis: Progress over two decades and the challenges ahead," *IEEE Trans. Pattern Anal. Mach. Intellig.*, vol.22, no.1, pp.85-101, Jan. 2000.

[69] N. Vincent, J-J. Rousselle, "Determination of optimal coefficients in active contour method for contour extraction," *11th Int. Colloquium on Numerical Analysis and Computer Sciences with Applications*, Plodiv, Bulgaria, August 12-17, pp. 79-82, 2002.

[70] K.-J. Mun, H.T. Kang, H.-S. Lee, Y.-S. Yoon, C.-M. Lee, J.H. Park, "Active contour model based object detection using genetic algorithm with wavelet based image processing," *Int. Journal of Control and Systems*, vol. 2, no. 1, pp. , March 2004.

[71] J.S. Suri, S. Laxaminarayan, "Angiography and plaque Imaging," CRC press LLC, 2003.

[72] X. Zhang, C.R. McKay, M. Sonka, "Tissue characterization in intravascular ultrasound images," *IEEE Trans. Med. Imag.*, vol. 17, no. 6, pp. 889-899, 1998.

[73] J.D. Klingensmith, R. Shekhar, D.G. Vince, "Identification of luminal and medial-adventitial borders in IVUS images," *IEEE Trans. Med. Imag.*, vol. 19, no. 10, pp. 996-1011, 2000.

[74] Y. Yu, J.A. Molloy, S.T. Acton, "Generalized speckle reducing anisotropic diffusion for ultrasound imagery," *Proc. Of the 17th IEEE Symposium on Computer-Based Medical Systems (CBMS'04)*, pp. 1-6, June 24-25, 2004.

[75] R.N. Czerwinski, D.L. Jones, W.D. O'Brien, "Detection and boundaries in speckle images-Application to medical ultrasound," *IEEE Trans. Med. Imag.*, vol. 18, no.2, pp. 126-136, Feb. 1999.

[76] R.N. Czerwinski, D.L. Jones, W.D. O'Brien, "Line and boundary detection in speckle images", *IEEE Trans. Image Proces.*, vol. 7, no. 12, pp. 1700-1714, Dec. 1998.

[77] J.D. Gill, H.M. Ladak, D.A. Steinman, A. Fenster, J.P. Robarts, "Development and evaluation of semi-automatic 3D segmentation technique of the carotid artery from 3D ultrasound images," Research Institute and University of western Ontario, London Canada, 2000.

[78] F. Mao, J. Gill, A. Fenster, "Technique for evaluation of semi-automatic segmentation methods," *SPIE Conf. Imag. Proces.*, San Diego-California, pp. 1027-1036, Feb. 1999.

[79] J.D. Gill, H. M. Ladak, D.A. Steinman, A. Fenster, "Accuracy and variability assessment of a semi-automatic technique for segmentation of the carotid arteries from three dimensional ultrasound images," *Med. Phys.*, vol.27 no. 6, pp.1333-1342, June 2000.

[80] H. M. Ladak,, D.A. Steinman, A. Fenster, "Prostate boundary segmentation from 2D ultrasound images," *Med. Phys.*, vol. 27, no. 8, pp. 1777-1788, August 2000.

[81] P. Slomka, J. Mandel, A. Fenster, D. Downey, "Automated 3-D registration of magnetic resonance angiography, 3D Power Doppler, and 3D B-Mode ultrasound images of carotid bifurcation," *Med. Imag. Proc. SPIE*, vol. 3979, pp. 332-341, 2000.

[82] D.-C. Cheng, A. Schmidt, K.-Sheng, M. Sandrock, "Automatic detection of the intimal and the adventitial layers of the common carotid artery wall in ultrasound B-Mode images using snakes," *Proc. ICIAP*, pp.1-6, 1999.

[83] E. Izquierdo, M. Ghanbari, "Nonlinear Gaussian filtering approach for object segmentation," *IEEE Proc. Vision, Image and Signal Proces.*, vol. 146, no. 3, pp. 137-143, 1999.

[84] P. Ying, R. Wang, D. Liang, "A new image segmentation approach based on linked pyramid," *Proc. 3rd Int. Conf. on Signal Processing*, vol. 2, pp. 1118-1121, 1996.

[85] T. Gustavsson, R.A.-Gharbieh, G. Hammarneh, Q. Liang, "Implementation and comparison of four different boundary detection algorithms for quantitative ultrasonic measurements of the human carotid artery," IEEE *Comp. In Cardiology*, vol. 24, pp. 1-4, 1997.

[86] H. Farid, "Blind inverse gamma correction," *IEEE Trans. Imag. Proces.*, vol.10, no. 2, 2001, pp. 1-9.

[87] R.W. Prager, A.H. Gee, G.M. Treece, L. Berman, "Speckle detection in ultrasound images using first order statistics," University of Cambridge, Department of Engineering, Internal Report, *CUED/F-INFENG/TR 415*, pp. 1-17, 2001.

[88] A. Achim, P. Tsakalides, A. Bezerianos, "SAR image denoising via Bayesian wavelet shrinkage based on heavy-tailed modelling," *IEEE Trans. Geosc. Remote Sens.*, vol. 41, no. 8, pp. 1773-1784, 2003.

[89] H. Xie, L. Pierce, F. Ulaby, "Statistical properties of logarithmically transformed speckle," *IEEE Trans. Geosc. Remote Sens.*, vol. 40, no. 3, pp. 721-727, 2002.

[90] A. Aldroubi, M. Unser, Wavelets in Medicine and Biology, CRC Press, 1996.

[91] J.-S. Lee, S.R. Cloude, K.P. Papthanassiou, M.R. Grunes, I.H. Woodhouse, "Speckle filtering and coherence estimation of polarimetric SAR interferometry data for forest applications," *IEEE Trans. Geosc. Remote Sens.*, vol. 41, no. 10, pp. 2254-2263, 2003.

[92] G.D. Grandi, J.-S. Lee, D. Schuler, E. Nerzy, "Texture and speckle statistics in polarimetric SAR synthesized Images," *IEEE Trans. Geosc. Remote Sens.*, vol. 41, no. 9, pp. 2070-2088, 2003.

[93] J.E. Wilhjelm, M.L. Gronholdt, B. Wiebe, S.K. Jespersen, L.K. Hansen, H. Sillesen, "Quantitative analysis of ultrasound B-Mode images of carotid atherosclerotic plaque: Correlation with visual classification and histological examination," *IEEE Trans. on Med. Imag.*, vol. 17, no. 6, pp. 910-922, Dec. 1998.

[94] J.M. Cai, T.S. Hatsukami, M.S. Ferguson et al., "Classification of human carotid atherosclerosis lesions with in vivo multicontrast MR imaging," *Circulation*, vol. 106, pp. 1368-1373, 2002.

[95] A. Wahle, P.M. Prause, S. Dejong, M. Sonka, "Geometrically correct 3D reconstruction of IntraVascular ultrasound images by fusion with biplane angiography-methods and validation," *IEEE Trans. Med. Imag.*, Final Manuscript #187/98, pp.1-14, June 30 1999.

[96] A. Fenster, D. Lee, S. Sherebrin, R. Rankin, D. Downey, "Three-dimensional ultrasound imaging of the vasculature," *Ultrasonics*, vol. 36, pp. 629-633, 1998.

[97] S. Oscher, R. Fedkiw, Level set methods and dynamic implicit surfaces, in applied sciences 153, Springer Verlag, New York Inc, 2003.

[98] E. Trouve, Y. Chambenoit, N. Classeau, P. Bolon, "Statistical and operational performance assessment of multi-temporal SAR image filtering," *IEEE Trans. Geosc. Remote Sens.*, vol. 41, no. 11, pp. 2519-2539, 2003.

[99] D. Lamont, L. Parker, M. White, N. Unwin, S.M.A. Bennett, M. Cohen, D. Richardson, H.O. Dickinson, A. Adamson, K.G.M.M. Alberti, A.W. Graft, "Risk of cardiovascular disease measured by carotid intima-media thickness at age 49-51: Life course study," *British Medical Journal (BMJ)*, vol. 320, pp. 273-278, 29 Jan. 2000.

[100] J.D. Gill, H.M. Ladak, D.A. Steinman, A. Fenster, "Segmentation of ulcerated plaque: A semi-automatic method for tracking the progression of carotid atherosclerosis," *World congress on Med.l Phys. and Biomed. Eng.*, Chicago, IL, pp. 1-4, July 2000.

[101] P. Brigger, J. Hoeng, M. Unser, "B-Spline snakes: A flexible tool for parametric contour detection," *IEEE Trans. Image Proces.*, vol. 9, no. 9, pp. 1484-1496, Sept. 2000.

[102] H.M. Ladak, J. S. Milner, D.A. Steinman, "Rapid-three dimensional segmentation of the carotid bifurcation from serial MR images," *J. BioMedical Eng.*, Techn. Briefs, vol. 122, pp. 96-99, Feb. 2000.

[103] H.M. Ladak J.B. Thomas, J.R. Mitchell, B.K. Rutt, D.A. Steinman, "A semi-automatic technique for measurement of arterial wall from black blood MRI," *Med. Physics*, vol. 28, no 6, pp. 1098-1107, Jun. 2001.

[104] Y. Wang, E.K. Teoh, D. Sheh, "Structure adaptive B-snake for segmenting complex objects," *IEEE ICIP Thessaloniki*, Greece, pp. 769-772, 2001.

[105] M. Pardas, M. Losada, "Facial parameter extraction system based on active contours," *IEEE ICIP*, Thessaloniki-Greece, pp. 1058-1061, 2001.

[106] B. Marendic, N. Galatsanos, D. Bless, "A new active contour algorithm for tracking vibrating vocal folds," *IEEE ICIP*, Thessaloniki-Greece, pp. 397-400, 2001.

[107] A. Pizurica, W. Philips, I. Lemahieu, M. Acheroy, "Despeckling SAR images using wavelets and a new class of adaptive shrinkage estimators," *IEEE ICIP*, Thessaloniki-Greece, pp. 233-236, 2001.

[108] F.L. Valverde, N. Guil, J. Munoz, Q. Li, M. Aoyama, K. Doi, "A deformable model for image segmentation in noisy medical images," *IEEE ICIP*, Thessaloniki-Greece, pp. 8285, 2001.

[109] G. Stippel, I. Duskunovic, W. Philips, A. Zedic, P. Govaert, I. Lemahieu, "A new filtering method for ultrasound images incorporating prior statistics concerning medical features," *IEEE ICIP*, Thessaloniki-Greece, pp. 821-824, 2001.

[110] D. Schilling, P.C. Cosman, "Image quality evaluation based on recognition times for fast browsing image applications," *IEEE Trans. on Multimedia*, vol. 4, no. 3, pp. 320-331, Sept. 2002.

[111] S. Oscher, N. Paragios, Geometric level set methods in imaging vision and graphics, Springer Verlag, New York Inc, 2003.

[112] C.S. Pattichis, E. Kyriakou, C. Christodoulou, M.S. Pattichis, C. Loizou, M. Pantziaris, A. Nicolaides, Cardiovascular: Ultrasound imaging in vascular cases, in Wiley Encyclopedia of Biomedical Engineering, Wiley, 2004.

[113] J. Dominguez, S. Klinko, "Image analysis via fuzzy reasoning approach: Prototype applications at NASA," *IEEE Int. Conf. On Fuzzy Systems*, pp. 1-4, 25-29 July 2004.

[114] F. Precioso, M. Barlaud, "B-Spline active contours for fast video segmentation," *IEEE ICIP Thessaloniki*-Greece, pp. 777-780, 2001.

[115] C.P. Loizou, C.S. Pattichis, C.I. Christodoulou, R.S.H Istepanian, M. Pantziaris, A. Nicoliades, "Comparative evaluation despeckle filtering in ultrasound imaging of the carotid artery," accepted, *IEEE Trans. of Ultras. Ferroel. and Frequency. Control*, 2005.

[116] C. Xu, J. Prince, "Gradient vector flow: A new external force for snakes," *IEEE Proc. Conf. on Comp. Patt. Recognition (CVPR'97)*, pp. 66-71, 1997.

[117] C. Xu, J. Prince, "Snake, shapes, and gradient vector flow," *IEEE Trans. on Imag. Proces.*, pp. 1-23, 1997.

[118] V. Boskovitz, H. Guterman, "An adaptive neuro-fuzzy system for automatic image segmentation and edge detection," *IEEE Trans. Fuzzy Systems*, vol. 10, no. 2, pp. 247-262, 2002.

[119] G. Hamarneh, T. McInerney, D. Terzopoulos, "Deformable organisms for automatic medical image analysis," *Med. Image Computing and Computer-Assisted Intervention, MICCAI*, Utrecht, The Netherlands, October 14-17, pp. 66-75, 2001

[120] G. Hamarneh, T. McInerney, "Controlled shape deformations via medial profiles," *Vision Interface 2001*, Ottawa, Canada, pp. 252-258, June 7-9, 2001.

[121] G. Hamarneh, T. Gustavsson, "Statistically constrained snake deformations," *IEEE Int. Conf. Systems, Man, Cybernetics*, Nashville, USA, Oct. 8-11, vol.3, pp.1610-1615, 2000.

[122] M.N. Ahmed, S.M. Yamany, N. Mohamed, A.A. Farag, T. Moriarty, "A modified c-means algorithm to bias field estimation and segmentation of MRI data," *IEEE trans. Med. Imag.*, vol. 21, no.3, pp. 193-199, March 2003.

[123] G. Gilboa, Y.Y. Zevi, N. Sochen, "Image enhancement segmentation and de-noising by time dependent non-linear diffusion process," *ICIP 2001*, Thessaloniki-Greece, pp. 134-137, 2001.

[124] D.J. Williams, M. Shah, "A fast algorithm for active contours and curvature estimation," *CVGIP: Image Understanding*, vol. 55, no. 1, pp. 14-26, 1992.

[125] C. Pattichis, C. Christodoulou, M. Pattichis, "Feature extraction and classifier design for the CARRS system," Report to Kerstel Corp., pp. 1-18, Dec. 2001.

[126] C. Pattichis, C. Christodoulou, M. Pattichis, M. Pantziaris, A. Nicolaides, "An integrated system for the assessment of US imaging atherosclerotic carotid plaques," *IEEE Int. Conf. Image Proces., ICIP 2001*, Thessaloniki, Greece, pp. 325-328, 7-10 October,2001.

[127] C. Christodoulou et al, "MultiFeature -texture analysis for the classification of carotid plaques, in CD-ROM," *Proc. VIII Mediter. Conf. Med. Biolog. Engin. Comp.*, University of Cyprus, Limassol-Cyprus, CD-ROM, 1998.

[128] R.M. Haralick, K. Shanmugam, I. Dinstein, "Texture features for image classification," *IEEE Trans. Systems, Man., Cybernetics,* vol. SMC-3, no. 6, pp. 610-621, Nov. 1973.

[129] J.S. Weszka, C.R. Dyer, A. Rosenfield, "A comparative study of texture measures for terrain classification," *IEEE Trans. Systems, Man. & Cybernetics,* vol. SMC-6, no. 4, pp. 269-285, April 1976.

[130] Loyola university medical center, Loyola university Chicago Stritch school of medicine, Chicago, USA, http://www.meddean.luc.edu/lumen/MedEd/Neuro/index.htm.

[131] C. Loizou , C. Christodoulou, C.S. Pattichis, R. Istepanian, M. Pantziaris, A. Nicolaides, "Speckle reduction in ultrasound images of atherosclerotic carotid plaque," *DSP 2002, Proc., IEEE 14th Int. Conf. Digital Signal Proces.*, Santorini-Greece, pp. 525-528, July 1-3, 2002.

[132] C.I. Christodoulou, C. Loizou, C.S. Pattichis, M. Pantziaris, E. Kyriakou, M.S. Pattichis, C.N. Schizas, A. Nicolaides, "De-speckle filtering in ultrasound imaging of the carotid artery," *Second Joint Conf. Engineering in Medicine and Biology and Biomedical Engineering Society (EBMS/BMES), Houston*, TX USA, pp. 1027-1028, Oct. 23-26, 2000.

[133] K.T. Dussik, "On the possibility of using ultrasound waves as a diagnostic aid," *Neurol. Psychiat.*, vol. 174, pp. 153-168, 1942.

[134] American stroke association, 2002 Heart disease and stroke statistics update, Dallas, Tex: American heart association, 2002, © 2002, American Heart Association.

[135] I. Patras, E.A. Hendriks and R.L. Lagendijk, "Video segmentation by MAP Labeling of watershed segments," *IEEE Trans. Pattern Anal. and Mach. Intellig.*, pp. 326-332, vol. 23, no. 3, March 2001.

[136] P.N.T. Wells, "Current status and future technical advances of ultrasonic imaging," Center for physics and engineering research in medicine, University of Bristol, *J. IEEE Eng. Med. Biol.*, pp. 14-20, Sept-Oct. 2000.

[137] S. Beucher, M. Bilodeau, X. Yu, "Road segmentation by watershed algorithms," *Proc. of the Pro-art vision group Prometheus workshop*, Sophia-Antipolis, France, April 1990.

[138] F. Rakebrandt et al., "Relation between ultrasound texture classification images and histology of atherosclerotic plaque," *Journal of Ultrasound in Med. & Biology*, vol. 26, no. 9, pp. 1393-1402, 2000.

[139] D.G. Vince, K.J. Dixon, R.M. Cothren, J.F. Cornhill, "Comparison of texture analysis methods for the characterisation of coronary plaques in intravascular ultrasound," *J. of Computerised Medical Imag. and Graphics*, vol. 24, pp. 221-229, 2000.

[140] L. Najman, M. Schmidt, "Geodesic saliency of watershed contours and hierarchical segmentation," *IEEE Trans. Pattern analysis and Machine Intelligence*, PAMI-18, vol. 12, 1996.

[141] A. Achim, A. Bezerianos, P. Tsakalides, "Novel Bayesian multiscale method for speckle removal in medical ultrasound images," *IEEE Trans. Med. Imag.*, vol. 20, no. 8, pp. 772-783, 2001.

[142] G. Cincotti, G. Loi, M. Pappalardo, "Frequency decomposition of ultrasound medical images with wavelet packets," *IEEE Trans. Med.l Imag.*, vol. 20, no. 8, pp. 764-771, Aug. 2001.

[143] S. Beucher, F. Meyer, "The morphological approach to segmentation: The watershed transform," Mathematical morphology in Image processing, E.R. Dougherty, Ed. New York:Marcel Dekker, vol. 12, pp. 433-481, 1993.

[144] D.F. Specht, "Probabilistic neural networks," *INNS Neural Networks*, vol. 3, no. 1, pp. 109-118, 1990.

[145] M.Niranjan, E. Wilson, T. Constandinides, S.-Y. Kung, "Neural networks for signal processing," *VIII. Proc. of the 1998 IEEE Signal Processing society workshop*, pp. 557-556, 1998.

[146] M. Akay, "Time frequency and wavelets in biomedical signal processing," IEEE press series in biomedical engineering, 2000.

[147] C.I. Christodoulou, S.C. Michaelides, C.S. Pattichis, "Multi-feature texture analysis for the classification of clouds in satellite imagery," *IEEE Trans. Geoscience and Remote Sens.*, vol. 41, no. 11, pp. 2662-2668, Nov. 2003.

[148] S.-M. Wu, Y.-W. Shau, F.-C. Chong, F.-J. Hsieh, "Non-invasive assessment of arterial dimension waveforms using gradient-based Hough transform and power Doppler ultrasound imaging," *Journal of Medical & Biolog. Engin. & Computing*, vol. 39, pp. 627-632, 2001.

[149] T.J. Tegos, M.M. Sambetai, A.N. Nicolaides et al., "Comparability of the ultrasonic tissue characteristics of carotid plaques," *J. Ultrasound Med.*, vol. 19, pp. 399-407, 2000.

[150] B. Solainman, B. Burdsall, Ch. Roux, "Hough transform and uncertainty handling. Application to circular object detection in ultrasound medical images," *Proc. Int. Conf. Image Proces. (ICIP98)*, vol. 3, pp. 828-831, 1998.

[151] L.F.C Lew Yan Voon, P. Bolland, O. Laligant, P. Gorria, "Gradient-based Hough transform for the detection and characterization of defects during non-destructive inspection," *Proc. of SPIE*, vol. 3029, pp. 140-146, 1997.

[152] F.N.S Medeiros, N.D.A. Mascarenhas, R.C.P Marques, C.M. Laprano, "Edge preserving wavelet speckle filtering," *5th IEEE Southwest Sympos. on Image Anal. and Interpret.*, Santa Fe, New Mexico, pp. 281-285, 7-9 April 2002.

[153] Imaging department, Johns Hopkins Bayview medical center, 4940 Eastern Ave., Baltimore Maryland 21224, http://www.jhbmc.jhu.edu/Imaging/index.html.

[154] C.P. Loizou, C.S. Pattichis, R.S.H. Istepanian, M. Pantziaris, T. Tyllis, "Intima media segmentation of the carotid artery," To be submitted, *IEEE Trans. Information Tech. Biomedicine*, pp. 45, 2005.

[155] M. Nixon, A. Aguado, Feature extraction & image processing, Newnes, First edition, 2002.

[156] J.U. Quistgaard, "Signal acquisition and processing in medical diagnostic ultrasound," *IEEE Signal Proces. magazine*, pp. 67-74, January 1997.

[157] S. Zhong, V. Cherkassky, "Image denoising using wavelet thresholding and model selection," *Proc. of IEEE Int. Conf. Image Proces.*, Vancouver, Canada, pp.1-4, Nov. 2000.

[158] V.R. Newey, D.K. Nassiri, "Online artery diameter measurement in ultrasound images using artificial neural networks," *Ultrasound in Medicine & Biology*, vol., 28, no. 2, pp.209-216, 2002.

[159] J.-S. LEE, "Speckle analysis and smoothing of synthetic aperture radar images," *Computer Graph. and Imag. Proces.*, vol. 17, pp. 24-32, 1981.

[160] C.P. Loizou, C.S. Pattichis, R.S.H. Istepanian, M. Pantziaris, T. Tyllis, A. Nicolaides, "Quality evaluation of ultrasound imaging in the carotid artery," *IEEE Melecon Int. Conf.*, May 12-15, vol. I, pp. 395-398, 2004.

[161] M.E.-Petersen, D. de Ridder, H. Handels, "Image processing with neural networks-a review," *Journal of Pattern Recognition*, vol. 35, pp. 2279-2301, 2002.

[162] T. R. Crimmins, "Geometric filter for speckle reduction," *Applied optics*, vol. 24, no. 10, pp. 1438-1443, 1985.

[163] J. W. Goodman, "Some fundamental properties of Speckle," *Journal of Optical society of America*, vol. 66, no. 11, pp. 1145-1149, 1976.

[164] C. B. Burckhardt, "Speckle in ultrasound B-Mode scans," *IEEE Trans. on Sonics and Ultrasonics*, vol. SU-25, no. 1, pp. 1-6, 1978.

[165] M. Nagao, T. Matsuyama, "Edge preserving smoothing," *Comp. Graph. Image Proc.*, vol. 9, pp. 394-407, 1979.

[166] North American Symptomatic Carotid Endarterectomy Trial (NASCET) Steering Committee, "North American symptomatic carotid endarterectomy trial: Methods, patients, characteristics, and progress," *Stroke*, vol. 22, pp. 711-720, 1991.

[167] M.F. Insana, T.J. Hall, G.G. Cox, J.S. Rosenthal, "Progress in quantitative ultrasonic imaging," *Proc. SPIE, Medical Imag. III, Image Formation*, vol. 1090, pp. 2-9, 1989.

[168] J. Saniie, T. Wang, N. Bilgutay, "Analysis of homomorphic processing for ultrasonic grain signal characterization," *IEEE Trans. Ultrasonics, Ferroelectrics, Frequency Control*, vol. 3, pp. 365-375, 1989.

[169] H. Ueno, H. Hirosawa, "A filter for reducing speckle of synthetic aperture radar imagery," *Electronics and Communications in Japan*, Part 1, vol. 71, no. 3, pp. 92-100, 1988.

[170] S.M. Ali, R.E. Burge, "New automatic techniques for smoothing and segmenting SAR images," *Signal Proces.*, vol. 14, pp. 335-346, North-Holland, 1988.

[171] M. Pattichis, C. Pattichis, M. Avraam, A. Bovik, K. Kyriakou, "AM-FM texture segmentation in electron microscopic muscle imaging," *IEEE Trans. Med. Imag.*, vol. 19, no. 12, pp. 1253-1258, 2000.

[172] M. Giger. N. Karssemeijer, S. Armato, "Guest editorial computer-aided diagnosis in medical imaging," *IEEE Trans. Med. Imag.*, vol. 20, no. 12, pp. 1205-1208, 2001.

[173] L. Chiariglione, "Impact on MPEG standards on multimedia industry," *IEEE Trans. Circuits and Systems for Video Technology*, pp. 5-18, 1997.

[174] J. Cabral, D. Linker, Y. Kim, "Ultrasound telemedicine system supporting compression of pre-scan converted data," *Proc. SPIE, Med. Imag.: Image display and visualization*, Seong. K. Mun ed., vol. 3976, pp. 350-358, 2000.

[175] G. Jacob, A. Noble, C. Behrenbruch, A. Kelion, A. Banning, "A Shape-space-based approach to tracking myocardial borders and quantifying regional left-ventricular function applied in echocardiography," *IEEE Trans. Med. Imag.*, vol. 21, no. 3, pp. 226-238, 2002.

[176] F.L. Valverde, N. Guil, J. Munoz, "Segmentation of vessels from mammograms using a deformable model," *Computer methods and programs in Biomedicine*, vol. 73, pp. 233-247, 2003.

[177] Y. Hatanaka, T. Hara, H. Fujita, S. Kasai, T. Endo, T. Iwase, "Development of an automated method for detecting mammographic masses with a partial loss of region," *IEEE Trans. Med. Imag.*, vol. 20, no. 12, pp. 1209-1214, 2001.

[178] Q. Liang, I. Wendelhag, J. Wilkstrand, T. Gustavsson, "A multiscale dynamic programming procedure for boundary detection in ultrasonic artery images," *IEEE Trans. Med. Imag.*, vol. 19, no. 2, pp. 127-142, 2000.

[179] C. Xu, A. Yezzi, J. Prince, "A summary of geometric level set analogues for a general class of parametric active contour and surface models," *Proc. of 1st IEEE workshop on variational and Level Set Methods in Computer Vision*, pp. 104-111, 2001.

[180] P. Scheunders, "Wavelet thresholding of multivalued images," *IEEE Trans. Image Proces.*, vol. 13, no. 4, pp. 475-483, 2004.

[181] C.P. Loizou, C.S. Pattichis, R.S.H. Istepanian, M. Pantziaris, E. Kyriakou, T. Tyllis, A. Nicolaides, "Ultrasound image quality evaluation," *Proc. of the 4th Annual IEEE Conf. on Int. Technology Applications in Biomed., ITAB 2003*, Birmingham UK, 24-26 April, pp.138-141, 2003.

[182] H. Haseqawa, H. Kanai, Y. Koiwa, "Detection of lumen-intima interface of posterior wall for measurement of elasticity of the human carotid artery," *IEEE Trans. Ultrasonics, Feroelectrics, Freq. Control*, vol. 51, no. 1, pp. 93-108, 2004.

[183] K. Subramanian, M. Thubrikar, B. Fowler, M. Mostafani, M. Funk, "Accurate 3-D reconstruction of complex blood vessel geometries from intravascular ultrasound images: in vitro study," *Journal of Med. Engin. & Technology*, vol. 24 no. 4, pp. 131-140, July/August 2000.

[184] M. Sonka, X. Zhang, M. Siebes, S. DeJong, C. McKay, S. Collins, "Automated segmentation of coronary wall and plaque from intravascular ultrasound image sequences," *Computers in Cardiology*, pp. 281-284, 1994.

[185] G. Xiao, M. Brady, J. Noble, Y. Zhang, "Segmentation of ultrasound B-mode images with intensity inhomogeneity correction," *IEEE Trans. Med. Imag.*, vol. 21, no. 1, pp. 48-57, Jan. 2002.

[186] B. Fetics, et al, "Enhancement of contrast echocardiography by image variability analysis," *IEEE IEEE Trans. Med. Imag.*, vol. 20, no. 11, pp. 1123-1130, Nov. 2001.

[187] R.V. Cristerna, V.M. Banuelos, O.Y. Suarez, "Coupling of radial-based network and active contour model for multi-spectral brain MRI segmentation," *IEEE Trans. Biomed. Eng.*, vol. 51, no. 3, pp. 459-470, 2004.

[188] J.E. Wilhjelm, M.S. Jensen, S.K. Jespersen, B. Sahl, E. Falk, "Visual and quantitative evaluation of selected image combination schemes in ultrasound spatial compound scanning," *IEEE Trans. Med. Imag.*, vol. 23, no. 2, pp. 181-190, 2004.

[189] E. Angelini, A. Laine, S. Takuma, J. Holmes, S. Homma, "LV volume quantification via spatiotemporal analysis of real-time 3D echocardiography," *IEEE Trans. Med. Imag.*, vol. 20, no. 6, pp. 457-469, Jun. 2001.

[190] S. Mitchell, B. Lelieveldt, R. Geest, H. Bost, J. Reiber, M. Sonka, "Multistage hybrid active appearance model matching: Segmentation of left and right ventricles in cardiac MR images," *IEEE Trans. Med. Imag.*, vol. 20, no. 5, pp. 415-423, May 2001.

[191] G.J. Adams, G.W. Vick, C.M. Ballantyne, W. Insull, J.D. Morrisett, "Estimation of carotid atherosclerotic plaque volume in vivo magnetic resonance images," *Proc. EMBS/BMES Conf.*, pp. 1072-1073, 2002.

[192] R. Sharma, R.B. Singh, R.K. Gupta, "A segmentation method for carotid artery atherosclerosis plaque for MRI contrast and MRI features, oxidative stress, markers in coronary and carotid plaque," *Proc. Of the 16th IEEE Symposium on Computer based medical systems*," pp. 323-328, 26-27 June 2003.

[193] S. Jespersen, J. Wilhjelm, H. Sillesen, "In vitro spatial compound scanning for improved visualization of atherosclerosis," *Ultrasound in Med. and Biology*, vol. 26, no. 8, pp. 1357-1362, 2000.

[194] Executive committee for the asymptomatic carotid atherosclerosis study, "Endarterectomy for asymptomatic carotid stenosis," *J. Am. Med. Assoc.*, pp. 273:1421-8, 1995.

[195] Z. He, S. Chen, B. Luk, R. Istepanian, "Post processing for image coding applications using neural network visual model," *Proc. IEEE Workshop on Neural Networks for Signal Processing*, Cambridge, UK, pp. 557-566, Aug. 31-Sept 3, 1998.

[196] B. Dawant, A. Zijidenbos, R. Margolin, "Correction of intensity variations in MR images of computer-aided tissue classification," *IEEE Trans. Med. Imag.*, vol. 12, pp. 770-781, Dec. 1993.

[197] R. Burgul, F. Gilbert, P. Undrill, "Methods of measurement of image quality in tele-ultrasound," *The British Journal of Radiology*, vol. 73, pp. 1306-1312, 2000.

[198] J.C. Bezdek, S.K. Pal, Fuzzy models for pattern recognition, Piscataway, NJ,:IEEE Press, 1991.

[199] J.C. Dainty, Laser speckle and related phenomena, Springer-Verlag, Berlin Heidelberg, New York, 1974.

[200] A. Kurjak, "Ultrasound scanning - Prof. Ian Donald (1910-1987)," *Eur. Journal Obstet. Gynecol. Reprod. Biol.*, vol. 90, no. 2, pp. 187-189, Jun. 2000.

[201] N. Bennet, R. Burridge, N. Saoki, "A method to detect and characterise ellipses using the Hough transform," *IEEE Trans. Pattern Anal. Machine Intellig.*, vol. 21, no. 7, July 1999.

[202] M. Sonka, W. Liang, R. Lauer, "Automated analysis of brachial ultrasound image sequences: Early detection of cardiovascular disease via surrogates of endothelial function," *IEEE Trans. Med. Imag.*, vol. 21, no. 10, pp. 1271-1279, 2002.

[203] S.C. Jeng, W.H.Tsai, "Scale and orientation-Invariant generalized Hough transform-A new approach," *Pattern Recognition*, vol. 24, pp. 037-1051, 1991.

[204] J. Illingworth, J. Kittler, "A survey of the Hough transform," *Computer Vision Graphics and Image Proces.*, vol. 44, pp. 87-116, 1988.

[205] R.-F. Chang, W.-J. Wu, C.-C. Tseng, D.-R. Chen, W.K. Moon, "3-D Snake for US in margin evaluation for malignant breast tumor excision using mammotone," *IEEE Trans. Inform. Tech. Biomed.*, vol. 7, no. 3, pp. 197-201, 2003.

[206] J. Tang, S. Acton, "Vessel Boundary Tracking for intravital microscopy via multiscale gradient vector flow snakes," *IEEE Trans. Biome. Eng.*, vol. 51, no. 2, pp. 316-324, 2004.

[207] K.-Mi Lee, W. Nick Street, "Generalized Hough transforms with flexible templates," *Proc. of Int. Conf. Artificial Intellig. (IC-AI)*, Las Vegas, NV, pp. 1-7, June 2000.

[208] A. Nicolaides, M. Sabetai, S. K. Kakkos, S. Dhanjil, T. Tegos, et al., "The asymptomatic carotid stenosis and risk of stroke (ACSRS) study," *Int. Angiology*, vol. 22, no. 3, pp. 263-272, 2003.

[209] N.M. El-Barghouty et al., "The identification of high-risk carotid plaque," *Eur. J. Vasc. Surg.*, vol. 11, pp. 470-478, 1996.

[210] B.B. Mandelbrot, The Fractal Geometry of Nature, San Francisco, CA: Freeman, 1982.

[211] C.M. Wu, C.Y.-Chang, H.K.-Sheng, "Texture features for classification of ultrasonic liver images," *IEEE Trans. Med. Imag.*, vol. 11, no. 3, pp. 141-152, 1992.

[212] K.I. Laws, "Rapid texture identification," *SPIE, vol. 238*, pp. 376-380, 1980.

[213] C.M. Wu, Y.-C. Chen, "Statistical feature matrix for texture analysis," *CVGIP: Graphical Models and Image Process.*, vol. 54, no. 5, pp. 407-419, 1992.

[214] M. Amadasun, R. King, "Textural features corresponding to textural properties," *IEEE Trans. Systems, Man., and Cybernetics*, vol. 19, no. 5, pp. 1264-1274, 1989.

[215] C.J. Bouma et al., "Automated lumen definition from 30 MHz intravascular ultrasound images," *Med. Image Anal.*, vol. 1, pp. 363-377, 1997.

[216] D.N. Metaxas, "Physics-based deformable models," applications to computer vision, graphics and medical imaging, Kluwer Academic Publishers, © 1997.

[217] D.S. Meier et al., "Automated morphometry of coronary arteries with digital image analysis of intra-vascular ultrasound," *Am. Heart J.*, vol. 133, pp. 681-690, 1997.

[218] S. Malassiotis, M. Strintzis, "Tracking the left ventricle in echocardiographic images by learning heart dynamics," *IEEE Trans. Med. Imag.*, vol. 18, no. 3, pp. 282-290, 1999.

[219] P.M. Morse, and H. Feshbach, Methods of theoretical physics, McGraw-Hill Company, New 1953.

[220] A. Mojsilovic, M. Popovic, N. Amodaj, R. Babic, M. Ostojic, "Automatic segmentation of intravascular ultrasound images: A texture-based approach," *Annals of Biomedical Engin.*, vol. 25, pp. 1059-1071, 1997.

[221] P. Martin, P. Refregier, F. Goudail, F. Guerault, "Influence of the noise model on level set active contour segmentation," *IEEE Trans. Pattern Anal. Mach. Intellig.*, vol. 26, no. 6, pp. 799-803, 2004.

[222] C.-M. Chen, H.H.-S. Lu, Y.-C. Lin, "A new ultrasound image segmentation algorithm based on an early vision model and discrete snake model," *SPIE Conf. on Image Proces.*, San Diego, California, pp. 959-970, Feb. 1998.

[223] X. Xie, M. Mirmehdi, "RAGS: Region-aided geometric snake," *IEEE Trans. Image Proc.*, vol. 13, no. 5, pp. 640-652, 2004.

[224] R.Al-Alawi, "A Hybrid n-tuple neuro-fuzzy classifier for handwritten numerals recognition," *Int. Joint Conf. Neural Networks-IJCNN*, W066, pp. 1-5, 25-29 July 2004.

[225] A. Yezzi et al, "A geometric snake model for segmentation of medical imagery," *IEEE Trans. Med. Imag.*, vol. 16, no. 2, pp. 199-209, Apr. 1997.

[226] B.L.-Obadia, A. Gee, "Adaptive segmentation of ultrasound images," *Image and Vision computing*, vol. 17, pp. 583-588, 1999.

[227] S. Graf, J. Gariery, M. Massonneau, R. Armentano, S, Mansour, J. Barra, A. Simon, J. Levenson, "Experimental and clinical validation of arterial diameter waveform and intimal media thickness obtained form B-mode ultrasound image processing," *Ultras. in Medic. & Biology*, vol. 25, no. 9, pp. 1353-1363, 1999.

[228] A.M. Wink, J.B.T.M. Roerdink, "Denoising functional MR images: A comparison of wavelet denoising and Gaussian smoothing," *IEEE Trans. Med. Imag.*, vol. 23, no. 3, pp. 374-387, 2004.

[229] S. Solbo, T. Eltoft, "Homomorphic wavelet based-statistical despeckling of SAR images," *IEEE Trans. Geosc. Remote Sensing*, vol. 42, no. 4, pp. 711-721, 2004.

[230] D.C. Barratt, B.B. Ariff, K.N. Humphries, S.A. McG. Thom, A.D. Hughes, "Reconstruction and quantification of the carotid artery bifurcation form 3-D ultrasound images," *IEEE Trans. Med. Imag.*, vol. 23, no. 5, pp. 567-583, 2004.

[231] C.-M. Chen , H.H.-S. Lu, "An adaptive snake model for ultrasound image segmentation: Modified trimmed mean filter, ramp integration and adaptive weighting parameters," *Ultrasonic Imag.*, vol. 22, pp. 214-236, 2000.

[232] N. Mudigonda, R. Rangayyan, J. Desautels, "Detection of breast masses in mammograms by density slicing and texture flow-field analysis," *IEEE Trans. Med. Imag.*, vol. 20, no. 12, pp. 121-1227, Dec. 2001.

[233] R.E. Zierler, D. Phillips, K. Beach, J. Primozich, "Non-invasive assessment of normal carotid bifurcation homodynamics with colour-flow ultrasound imaging," *Ultrasound in Medicine & Biology*, vol. 13, no. 8, pp. 471-476, 1987.

[234] M.A. Bottalico, A. Starita, "Ecostudio: a Computer tool to support carotid ultrasound images analysis," *Proc. of the 22nd annual EMBS Int. Conf.*, Chicago, IL, pp. 2428-2430, July 23-28, 2000.

[235] S.K. Jespersen, M. Gronholdt, J. Wilhjelm, B. Wiebe, L. Hansen, H. Sillesen, "Correlation between ultrasound B-mode images of carotid plaque and histological examination," *IEEE Ultrasonics Symposium*, pp. 1068-1096, 1996.

[236] J.M. Thijssen, B.J. Oosterveld, P.C. Hartman et. al, "Correlations between acoustic and texture parameters from RF and B-mode liver echograms," *Ultrasound Med. Biol.*, vol. 19, pp. 13-20, 1993.

[237] M.O. Berger, "Towards dynamic adaptation of snake contours," *Proc. 6th Int. Conf. Imag. Analysis and Processing*, Como, Italy, pp. 47-54, 1991.

[238] C. Loizou, C. Pattichis, R. Istepanian, M. Pantziaris, A. Nicolaides, "Atherosclerotic carotid plaque segmentation," *Proc. Of the 26th Annual Int. Conf. IEEE EMBS,* San Francisco, California, USA, Sept. 1-5, pp. 1403-1406, 2004.

[239] C. Baillard, C. Barillot, P. Bouthemy, "Robust adaptive segmentation of 3D medical images with level sets," Internal report, Institute national de recherché en informatique et en automatique, no. 4071, pp. 1-26, Nov. 2002.

[240] L. Sarry, J.-Y. Boire, "Three-dimensional tracking of coronary arteries from biplane angiographic sequences using parametrically deformable models," *IEEE Trans. Med. Imag.*, vol. 20, no. 12, pp. 1341-1351, Dec. 2001.

[241] D.-C. Cheng, A. S.-Trucksaess, K.-S. Cheng, H. Burkhardt, "Using snakes to detect the intimal and adventitial layers of the common carotid artery wall in sonographic images," *Computer Methods and Programs in Biomedicine*, vol. 67, pp. 27-37, 2002.

[242] S.R. Gunn, M.S. Nixon, "A robust snake implementation: a dual active model," *IEEE Trans. on Pattern Anal. and Mach. Intellig.*, vol. 19, no. 1, pp. 63-68, 1997.

[243] M. Kass, A. Witkin, D. Terzopoulos, "Snakes: Active contour models," *Int. Journal Compt. Vision*, vol. 1, pp. 321-331, 1988.

[244] R. Ronfard, "Region based strategies for active contour models," *Int. Journal of Computer Vision*, vol. 13, no. 2, pp. 229-251, 1994.

[245] J. Ivins, J. Porrill, "Active region models for segmenting textures and colors," *Image and Vision computing*, vol. 13, no. 5, pp. 431-437, 1995.

[246] I. Cohen, L.D. Cohen, N. Ayache, "Using deformable surfaces to segment 3D images and infer differential structures," *CVGIP: Image Underst.*, vol. 56 (2), pp. 242-263, 1992.

[247] N. Peterfreund, "Robust tracking of position and velocity," *IEEE Trans. on PAMI*, vol. 21 (6), pp. 564-569, 1999.

[248] K.F. Lai, R.T. Chin, "Deformable contours-modeling and extraction," *IEEE Trans. on PAMI*, vol. 17, no. 11, pp. 1084-1090, 1995.

[249] S. Chandran, A.K. Potty, "Energy minimization of contours using boundary conditions," *IEEE Trans. Pattern Recogn. and Mach. Intellig.*, vol. 20, no. 5, pp. 546-549, 1998.

[250] W. Neuenschwander, P. Fua, L. Iverson, G. Szekely, O. Kuebler, "Ziplock snakes," *Int. Journal of Computer Vision*, vol. 25, no.3, pp. 191-201, 1997.

[251] P. Gouvignou, N. Papanikolopoulos, M. Sullivan, P. Khosla, "The use of active deformable Models in model-based robotic visual servoing" *Journal of Intellig. and Robotic Syst.*, vol. 17, pp. 195-221, 1996.

[252] P.C. Yuen, G.C. Feng, J.P. Zhou, "A contour detection method: Initialization and contour model," *Pattern Recogn. Letters*, vol. 20, pp. 141-148, 1999.

[253] I. Wendelhag, Q. Liang, T. Gustavsson, J. Wikstrand, "A new automated computerized analyzing system simplifies reading and reduces the variability in ultrasound measurement of intima media thickness," *Stroke*, vol. 28, pp. 2195-2200, 1997.

[254] I. Wendelhag, O. Wiklund, J. Wikstrand, "On quantifying plaque size and intima-media thickness in carotid and femoral arteries," *Arterioscler., Thrombos. and Vasc. Biology*, vol. 16, pp. 843-850, 1996.

[255] S. Kanters, A. Algra, M. van Leeuwen, J. Banga, "Reproducibility in vivo carotid intima-media thickness measurements," *Stroke*, vol. 28, pp. 665-671, 1997.

[256] D. Baldassare, E. Tremoli, M. Amato, F. Velgia, A. Bondioli, C. Sirtori, "Reproducibility validation study comparing analog and digital imaging technologies for the measurement of intima-media thickness," *Stroke*, pp. 1104-1110, 2000.

[257] R. Woodman et al., "Improved analysis of brachial artery ultrasound using a novel edge detection software system," *Journal of Applied Physiology*, vol. 91, pp. 929-937, 2001.

[258] C. Xu, J. Prince, "Generalized gradient vector flow external forces for active contours," *Signal Proces.*, vol. 71, pp. 131-139, 1998.

[259] A. Blake, M. Isard, Active contours, © Springer-Verlag, London Limited, 2000.

[260] J. Wang, X. Li, "Guiding ziplock snakes with a priori Information," *IEEE Trans. Image Proc.*, vol. 12, no. 2, pp. 176-185, 2003.

[261] J. Smilowitz, J. Balog, H. keller, G. Olivera, L.A. Dewerd, T.R. Mackie, "A new multipurpose quality assurance phantom for clinical tomotherapy," *Proc. Of the 22nd Annual EMBS Int. Conf.*, July 23-28, pp. 1191-1194, 2000.

[262] H.E. Kreyszig, "Texture descriptors based on co-occurrence matrices," *Computer Vision, Graph. and Image Proces.*, vol. 51, pp. 70-86, 1990.

[263] D.C. He, L. Wang, "Texture features based on texture spectrum," *Pattern Recognit.*, vol. 24, pp. 391-399, 1991.

[264] J.M. Bland, D.G. Altam, "Statistical methods for assessing agreement between two methods of clinical measurement," *Lancet I*, pp. 307-310, 1986.

[265] V. Chalana, Y. Kim, "A Methodology for evaluation of boundary detection algorithms on medical images," *IEEE Trans. Med. Imag.*, vol. 16, no. 5, pp. 642-652, Oct. 1997.

[266] J.F. Polak et al., "Hypoechoic plaque at US of the carotid artery: An independent risk factor for incident stroke in adults aged 65 years or older," *Radiology*, vol. 208, pp. 649-654, 1998.

[267] J. Holland, "Adaptation in natural and artificial systems," The University of Michigan Press, Ann Arbor, 1975.

[268] A.J. Chipperfield, P.J. Flemming, C.M. Fonseca, "Genetic algorithm tools for control systems engineering," *Proc. Adaptive Comput. in Engin. Design and Control*, Plymouth Engineering Design Center, 21-22 Sept., pp. 128-133, 1994.

[269] M. Gutierrez, P. Pilon, S. Lage, L. Kopel, R. Carvalho, S. Furuie, "Automatic measurement of carotid diameter and wall thickness in ultrasound images," *Computers in Cardiology*, vol. 29, pp. 359-362, 2002.

[270] C. Liguori, A. Paolillo, A. Pietrosanto, "An automatic measurement system for the evaluation of carotid intima-media thickness," *IEEE Trans. Instrument. and Measur.*, vol. 50, no. 6, pp. 1684-1691, 2001.

[271] M. Karaman, M. Alper Kutay, G. Bozdagi, "An adaptive speckle suppression filter for medical ultrasonic imaging," *IEEE Trans. Med. Imag.*, vol. 14, no. 2, pp. 283-292, 1995.

[272] Z. Wang, A. Bovik, "A universal quality index," *IEEE Signal Proces. Letters*, vol. 9, no. 3, pp. 81-84, March 2002.

[273] A. Pommert, K. Hoehne, "Evaluation of image quality in medical volume visualization: The state of the art," Takeyoshi Dohi, Ron Kikinis (eds.): Medical image computing and computer-assisted intervention, Proc., MICCAI, 2002, Part II, Lecture Notes in Computer Science 2489, pp. 598-605, Springer Verlag, Berlin 2002.

[274] J.M. DeBray, J.M. Baud, M. Dauzat, "Consensus on the morphology of carotid plaques," *Cerebrovasc. Dis.*, vol. 7, pp. 289-296, 1997.

[275] B. Widder et al., "Morphological characterization of carotid artery stenosis by ultrasound duplex scanning," *Ultrasound Med. Biol.*, vol. 16, pp. 349-354, 1990.

[276] E. Montseny, P. Sobrevilla, S. Romani, "A fuzzy approach to white blood cells segmentation in color bone marrow images," *IEEE Int. Conf. Fuzzy Systems*, #1407, pp. 1-4, 25-29 July 2004.

[277] A.C. Gray-Weale et al., "Carotid artery atheroma: comparison of preoperative B-mode ultrasound appearance with carotid endarterectomy specimen pathology," *J. Cardiovasc. Surg.*, vol. 29,pp. 676-681, 1998.

[278] Z. Wang, A. Bovik, H. Sheikh, E. Simoncelli, "Image quality assessment: From error measurement to structural similarity," IEEE *Trans. Image Proces.*, vol. 13, no. 4, pp. 600-612, Apr. 2004.

[279] S. Lee, M. Pattichis, A. Bovik, "Foveated video quality assessment," *IEEE Trans. Multimedia*, vol. 4, no. 1, pp. 129-132, March 2002.

[280] D. Altman, J. Bland, "Measurement in medicine: The analysis of method comparison studies," *The Statistician*, vol. 32, pp. 307-313, 1983.

[281] J.M. Johnson et al., "Natural history of asymptomatic carotid plaque," *Arch. Surg.*, vol. 120, pp. 1010-1012, 1985.

[282] J.M. Bland, D.G. Altman, "Comparing methods of measurement: Why plotting difference against standard method is misleading," *Lancet* 346, pp. 1085-1087, 1995.

[283] I. Aveibas, B. Sankur, K. Sayood, "Statistical evaluation of image quality measures," *Journal Electronic Imaging*, vol. 11, no. 2, pp. 206-223, April 2002.

[284] M. Eckert, "Perceptual quality metrics applied to still image compression," Canon information systems research, Faculty of engineering, Un. Of Technology, Sydney, Australia, pp. 1-26, 2002.

[285] H.-L. Eng, K.-K. Ma, "Noise adaptive soft-switching median filter," *IEEE Trans. Image Process.*, vol. 10, no. 2, pp. 242-251, 2001.

[286] A. Ahumada, C. Null, "Image quality: A multidimensional problem," *A. B. Watson, ed., Digital Images and Human Vision, (Bradford Press: Cambridge Mass.)*, pp. 141-148, 1993.

[287] A. Ahumada, "Computational image quality metrics: A review," J. Morreale, (ed.), Society of Inform. Display, Int. Sympos. of Techn. Papers, vol. 24, Playa Del Rey, California, SID, pp. 305-309, 1993.

[288] A. Ahumada, "Simplified vision models for image quality assessment," NASA Research Center, Moffet field CA, *SID Int. Digest of Technical Papers*, vol. XXVII, pp. 397-400, May 1996.

[289] Z. Wang, A. Bovik, "Why is image quality assessment so difficult?," *Proc. IEEE Int. Conf. On Acoustics, Speech and Signal Processing*, vol. 4, pp. 3313-3316, May 2002.

[290] A. Ahumada, "A simple vision model for inhomogeneous image quality assessment," SID digest of technical papers, vol. 29, pp. 40.1, 1998.

[291] M. Aanestad, B. Edwin, R. Marwik, "Medical image quality as a socio-technical phenomenon," *Methods in Medicine*, vol. 4, pp. 302-306, 2003.

[292] E.A. Fedorovskaya, H.de Ridder, F.J. Blomaert, "Chroma variations and perceived quality of color images and natural scenes," *Color Research and Application*, vol. 22, no. 2, pp. 96-110, 1997.

[293] M. Lund, "The influence of video image size and resolution on viewing-distance preferences," *SMPTE Journal*, vol. 102, no. 5, pp. 407-415, 1993.

[294] G. Deffner et al., "Evaluation of display image quality: Experts vs. non-experts," *In Society for Inform. Display Sympos. Digest*, vol. 25, pp. 475-478, 1994.

[295] G. Gescheider, "Psychophysics: The fundamentals," Lawrence Erlbaum Associates, 3rd ed. 1997.

[296] D. Pelli, D. Farell, "Psychophysical methods," In M. Bass et al. (ed.), Handbook of Optics: Fundamentals, Techniques, and Design, vol. 1, chap. 29, McGraw-Hill, 2nd ed., 1995.

[297] D. Green, J. Swets, "Signal detection theory and psychophysics," John Willey & Sons, 1996.

[298] N. Lodge, "An Introduction to advanced subjective assessment methods and the work of the MOSAIC consortium," MOSAIC Handbook, pp. 63-78, 1996.

[299] R. Aldridge et al., "Recency Effect in the subjective assessment of digitally coded television pictures," *Proc. Of the Int. Conf. on Image Proces. and its Applications*, pp. 336-339, 1995.

[300] T.-J. Chen, K.-S. Chuang, J. Wu, S.C. Chen, I.-M. Hwang, M.-L. Jan, "A novel image quality index using Moran I statistics," *Physics in Medic. and Biology*, vol. 48, pp. 131-137, 2003.

[301] T.C. Potdevin, J.B. Fowlkes, A.P. Moskalik, P.L. Carson, "Reticulated foam flow phantom ultrasound contrast studies," *IEEEE Ultrasonics Symposium*, pp. 1974-1976, 2002.

[302] S. Gagnoni, A.B. Dobrzeniecki, R. Poli, J.C. Yanch, "Genetic algorithm based interactive segmentation of 3D medical images," *J. of Image and Vision Comput.*, vol. 17, no. 12, pp. 881-896, 1999.

[303] L.M. Reilly et al., "Carotid plaque histology using real-time ultrasonography: clinical and therapeutic implications," *Am. J. Surg.*, vol. 146, pp. 188-193, 1983.

[304] J. Brendo, T. Lehmann, K. Spitzer, "Automatic parameter setting for balloon models," *Proc. of SPIE*, vol. 3979, pp. 1185-1207, 2000.

[305] J. Tohka, "Global Optimization of deformable surface meshes based on genetic algorithms," *Proc. of 11th Int. Conf. On Image Analysis and Proces.*, pp. 459-464, IEEE CS press, Sept. 2001.

[306] J-J. Rousselle, N. Vincent, "Design of experiments to set active contours," *6th Int. Conf. On Quality Control by Artificial Visio*n, pp. 1-4, 2003.

[307] J-J. Rousselle, N. Vincent, N. Verbeke, "Genetic algorithm to set active Contour," *10th Int. Conf. CAIP*, Groeningen, The Netherlands, Proceedings, pp. 345-352, 2003.

[308] C. Houck, J. Joines, M. Kay, "A genetic algorithm for function optimization: A Matlab implementation," *NCSU-IE TR 95-09*, pp. 1-14, 1995.

[309] A. Chipperfield, P. Fleming, C. Fonseca, "Genetic algorithm tools for control systems engineering," ImechE seminar on genetic algorithms in design optimization," pp. 1-631 Jan. 1996.

[310] A. Chipperfield, P. Fleming, "The Matlab genetic algorithm toolbox," IEE Colloquium applied control techniques using Matlab, pp. 10\1-10\4, 26 Jan. 1995.

[311] D. E. Goldenberg, Genetic algorithms, Addison-Wesley Publishing Co. Inc., 1989.

[312] Z. Michalewicz, Genetic algorithms + data structures=Evolution programs, Springer Verlag, 2nd Ed., 1996.

[313] P. Pignoli, E. Tremoli, A. Poli, P. Oreste, R. Paoletti, "Intima plus media thickness of the arterial wall: A direct measurement with ultrasound imaging," *Atheroscler.*, vol. 74, no. 6, pp. 1399-1406, Dec. 1986.

[314] E. Bernstein, "Arterial wall changes with Atherogenesis: Ultrasound measurement of asymptomatic atherosclerosis," *Vascular Diagnosis*, pp. 432-438, 1993.

[315] E.R. Rietzschel, M. L. Buyzere, D. A. Duprez, D. L. Clement, "Interchangeability of carotid and femoral intima-media thickness in risk stratification," *Internat. Angiology*, pp. 38-46, April 2, 2001.

[316] S. Winkler, Vision models and quality metrics for image processing applications," PhD, University of Lausanne-Switzerland, Dec. 21, 2000.

[317] F.A. Dinenno, P.P. Jones, D.R. Seals, H. Tanaka, "Age-associated arterial wall thickening is related to elevations in sympathetic activity in healthy humans," *American J. Physiol. Heart Circ. Physiol.*, vol. 278, issue 4, pp. 1205-1210, 2000.

[318] L. Kornet, A.P.G. Hoeks, J. Lambregts, R.S. Reneman, "In the femoral artery bifurcation, differences in mean wall shear stress within subjects are associated with different intima-media thickness, "*Arterioscler Thromb. Vasc. Biology*, vol. 19, pp. 2933-2939, 1999.

[319] A.S.-Trueckaess, D. Grathwohl, A. Schmid, R. Boragk, C. Upmeir, J. Keul, M. Huonker, "Structural functional, and hemodynamic changes for the common carotid artery with age in male subjects, "*Arterioscler Thromb. Vasc. Biology*, vol. 19, pp. 1091-1097, 1999.

[320] S. Ebrahim et al., "Carotid plaque, intima media thickness, cardiovascular risk factors, and prevalent cardiovascular disease in men and women," *Stroke*, vol. 30, pp. 841-850, 1999.

[321] F. Yang, G.A. Holzapfel, Ch.A.J. Schulze-Bauer, R. Stollberger, D. Thedens, L. Bolinger, A. Stolpen, M. Sonka, "Segmentation of wall and plaque in in-vitro vascular MR images," *The Int. J. of Cardiovascular Imaging*, vol. 19, pp. 419-428, 2003.

[322] T. Elatrozy, A. Nicolaides, T. Tegos, A. Zarka, M. Griffin, M. Sabetai, "The effect of B-mode ultrasonic image standardization of the echodensity of symptomatic and asymptomatic carotid bifurcation plaque," *Intern. Angiology*, vol.17, pp. 179-186, no.3, Sept.1998.

[323] P. Moulin, "A multiscale image decomposition and wavelets, in Handbook of image & video processing, Ed. By A. Bovik, Academic press, pp. 289-300, 2000.

[324] S. Acton, Diffusion based edge detectors, in Handbook of image & video processing, Ed. by A. Bovik, Academic press, pp. 433-447, 2000.

[325] S. Tang, "Experiment of image enhancement with homomorphic filtering," Computers science department, University of Nevada, Reno, NV 89557, internal report, e-mail: tang@cs.unr.edu.

[326] S. Jin, Y. Wang, J. Hiller, "An adaptive non-linear diffusion algorithm for filtering medical images," *IEEE Trans. on Inform. Technol. in Biomed.*, vol. 4, no.4, pp.298-305, Dec. 2000.

[327] C. Boncelet, Image noise models, in Handbook of Image & Video Processing, Ed. by A. Bovik, Academic Press, pp. 325-335, 2000.

[328] G. Belgaro et al., "Ultrasound morphology classification of the arterial wall and cardiovascular events in a 6-year follow-up study," *Atherioscler. Thromb. Vasc. Biol.*, vol. 16, pp. 851-856, 1996.

[329] E. Krupinski, H. Kundel, P. Judy, C. Nodine, "The medical image perception society," key issues for image perception research," *Radiology*, vol. 209, pp. 611-612, 1998.

[330] A Philips Medical System Company, "Comparison of image clarity, SonoCT real-time compound imaging versus conventional 2D ultrasound imaging," *ATL Ultrasound, Bothell, Washington USA, Report*, Report no. G55203r1, 2001.

[331] D. Sakrison, "On the role of observer and a distortion measure in image transmission," *IEEE Trans. Communication*, vol. 25, pp. 1251-1267, Nov. 1977.

[332] A.L. Yuille, Deformable templates for face recognition, *Journal of Cognitive Neuroscience*, vol. 3, no. 1, pp. 59-70, 1991.

[333] L.D. Cohen, "On active contour models and balloons," *Comput. Vision Graphics Image Processing Image Understanding*, vol. 53, no. 2, pp. 211-218, 1991.

[334] A. Amini, S. Tehrani, T. Weymouth, "Using dynamic programming for minimizing the energy of active contours in the presence of hard constraints," *Proc. Second Intern. Conf. on Computer Vision*, pp. 95-99, 1988.

[335] C. Loizou, C. Pattichis, R. Istepanian, M. Pantziaris, "Atherosclerotic carotid plaque segmentation," *II EFOMP Med. Int. Conf. On Medical Physics*, Limassol-Cyprus, W. 2-3 (6pages), April 28-30, 2004.

[336] D. Terzopoulos, A. Witkin, M. Kass, "Symmetry-seeking models for 3-D object reconstruction," *Int. J. Comput. Vision*, vol. 1, no. 3, pp. 211-221, 1987.

[337] T.J. Tegos et al., "Patterns of brain computed tomography infraction and carotid plaque echogenicity," *J. Vascs. Surg.*, vol. 33, pp. 334-339, 2001.

[338] C. Loizou, C. Pattichis, R. Istepanian, M. Pantziaris, "Intima media segmentation of the carotid artery," *IEEE Int. Conf. Medicon X Med. Conf. on Medical and Biological Eng.*, POS-03, 499, pp. 1-4, July 31-August 5, 2004.

[339] R.F. Wagner, S.W. Smith, J.M. Sandrik, H. Lopez, "Statistics of speckle in ultrasound B-scans," *IEEE Trans. Sonics. Ultrason.*, vol. 30, pp. 156-163, 1983.

[340] R.F. Wagner, M.F. Insana, D.G. Brown, "Unified approach to the detection and classification of speckle texture in diagnostic ultrasound," *Optical Engin.*, vol. 25, no. 6, pp. 738-742, June 1986.

[341] R.F. Wagner, M.F. Insana, S.W. Smith, "Fundamental correlation lengths of coherent speckle in medical ultrasonic images," *IEEE Trans. Ultrasonics, Feroelectrics and Frequency Control*, vol. 35, no. 1, pp. 34-44, Jan. 1988.

[342] M.F. Insana, R.F. Wagner, B.S. Garra, D.G. Brown, T. H. Shawker, "Analysis of ultrasound image texture via generalized Rician statistics," *Optical Engin.*, vol. 25, no. 6, pp. 743-748, June 1986.

[343] L.J. Porcello, N.G. Massey, R.B. Ines, J.M. Marks, "Speckle reduction in synthetic aperture radar images," *J. Opt. Soc. Am.*, vol. 66, no. 11, pp. 1305-1311, Nov. 1976.

[344] J. Weickert, B.M. ter H. Romery, M. Viergever, "Efficient and reliable schemes for nonlinear diffusion filtering," *IEEE Trans. Image Proc.*, vol. 7, no. 3, pp. 398-410, March 1998.

[345] K. Abd-Elmonien, A.-B. Youssef, Y. Kadah, "Real-time speckle reduction and coherence enhancement in ultrasound imaging via nonlinear anisotropic diffusion," *IEEE Trans. Biomed. Eng.*, vol. 49, no. 9, pp. 997-1014, Sept. 2002.

[346] M. Black, G. Sapiro, D. Marimont, D. Heeger, "Robust anisotropic diffusion," *IEEE Trans. Image Proc.*, vol. 7, no. 3, pp. 421-432, March 1998.

[347] P. Perona, J. Malik, "Scale-space and edge detection using anisotropic diffusion," *IEEE Trans. Pattern Anal. and Mach. Intellig.*, vol. 12, no. 7, pp. 629-639, July 1990.

[348] X. Zong, A. Laine, E. Geiser, "Speckle reduction and contrast enhancement of echocardiograms via multiscale nonlinear processing, "*IEEE Trans. Med. Imag.*," vol. 17, no. 4, pp. 532-540, 1998.

[349] X. Hao, S. Gao, X. Gao, "A novel multiscale nonlinear thresholding method for ultrasonic speckle suppressing," *IEEE Trans. Med. Imag.*, vol. 18, no. 9, pp. 787-794, 1999.

[350] D.L. Donoho, De-noising by soft thresholding, "*IEEE Trans. Inform. Theory*, vol. 41, pp. 613, 627, May 1995.

[351] V. Dutt, "Statistical analysis of ultrasound echo envelope," Ph.D. dissertation, Mayo Graduate School, Rochester, MN, 1995.

[352] S. Glagov, E. Weisenberg, C.K. Zarins, R. Stankunavicius, "Compensatory enlargement of human athrerosclerotic coronary arteries," *NEJM*, vol. 316, pp. 1371-1375, May 1987.

[353] ACAS Clinical advisory: carotid endarterectomy for patients with asymptomatic internal carotid artery stenosis, *Stroke*, vol. 25, no. 12, pp. 2523-2524, 1994.

[354] H. Paul, H.P. Schwann, "Mechanism of absorption of ultrasound in liver tissue," *Journal Acoustical Society of America*, vol. 50, pp. 692, 1971.

[355] P.M. Shankar, J. Reid, H. Ortega, C.W. Piccoli, B.B. Goldberg, "Use on non-Rayleigh statistics for the identification of tumors in ultrasound B-scan of the breast," *IEEE Trans. Med. Imag.*, vol. 12, no. 4, pp. 685-692, 1993.

[356] S.O. Rice, "Mathematical analysis of random noise," *Bell Systems Technical Journal*, vol. 24, pp. 46-158, 1945.

[357] E. Jakeman, R.J.A. Tough, "Generalized k-distribution: a statistical model for weak scattering," *Journal of Optical Society of America*, vol. 13, pp. 31-48, 1980.

[358] M.M. Sabetai et al., "Hemispheric symptoms and carotid plaque echo morphology," *J. Vasc. Surg.*, vol. 31, pp. 39-49, 2000.

[359] M.F. Insana, R.F. Wagner, D.G. Brown, T. Hall, "Describing small-scale structure in random media using pulse echo ultrasound," *Journal Acoustical Society of America*, vol. 87, no. 1, pp. 179-192, 1990.

[360] R.L. Engle Jr., "Attempts to use computers as diagnostic aids in medical decision making: a thirty year experience," *Perspectives in Biology and Medicine*, vol. 35, no. 2, pp. 207-217, 1992.

[361] D.L. Wilson, A.J. Baddeley, R.A. Owens, "A new metric for gray-scale image comparison," *Int. J. of Computer Vision*, vol. 24, no. 1, pp. 5-17, 1997.

[362] S. Jaume et al., "Tumor detection in the bladder wall with a measurement of abnormal thickness in CT scans," *IEEE Trans. Biomed. Eng.*, vol. 50, no.3, pp. 383-390, 2003.

[363] C. Metz, "Basic principles of ROC analysis," *Semin. Nuclear Medicine*, vol. 8, pp. 283-298, 1978.

[364] A. Zijdenbos, B. Dawant, R. Margolin, et al., "Morphometric analysis in white matter lesions in MR images: Method and validation," *IEEE Trans. Med. Imag.*, vol. 13, no. 4, pp. 716-724, Dec. 1994.

[365] A. Kelemen, G. Szekely, G. Gerig, "Elastic model-based segmentation of 3D neuroradiological data sets," *IEEE Trans. Med. Imag.*, vol. 18, no. 10, pp. 828-839, Oct. 1999.

[366] F.J. Polak, Doppler Sonography: *An Overview, In Peripheral Vascular Sonography: A Practical Guide*, Baltimore USA: Williams and Wilkins, 1992.

[367] D.E. Gutstein, V. Fuster, "Pathophysiology and clinical significance of atherosclerotic plaque rapture," *Cardiovasc. Res.*, vol. 41, pp.323-333, 1999.

[368] A.J. Zukowski et al., "The correlation between carotid plaque ulceration and cerebral infraction seen on CT scan," *J. Vasc. Surg.*, vol. 1, pp. 782-786, 1984.

[369] P. Libby, "Molecular basis of acute coronary syndromes," *Circulation*, vol. 91, pp. 2844-2850, 1995.

[370] S. Clinton et al., "Macrophage-colony stimulating factor gene expression in vascular cells and human atherosclerosis," *Am. J. Pathology*, vol. 140, pp. 301-316, 1992.

[371] M.J. Davies et al., "Risk of thrombosis in human atherosclerotic plaques: role of extra cellular lipid, macrophage and smooth muscle cell content," *Br. Heart J.*, vol. 69, pp. 377-38, 1993.

[372] A.N. Nicolaides et al., "Ultrasound plaque characterization, genetic markers and risks," *Pathophysiol. Haemost. Thromb.*, vol. 32, (supl. 1), pp. 1-4, 2002.